The Electrochemical Oxidation Of Hydrogen Peroxide On Platinum Electrodes At Phosphate Buffer Solutions

A thesis presented in partial fulfilment of the
requirements for the degree of
Doctor of Philosophy
in
Chemistry
at Massey University, Palmerston North
New Zealand

Emad Aldeen Khudaish

September 1999

ABSTRACT

The kinetics and mechanism for the electrochemical oxidation of H_2O_2 on platinum electrodes in phosphate buffers were studied.

A mechanistic model for this reaction was developed that involves binding sites, on the surface of the electrode, that are thought to be based on some form of hydrous platinum oxide, initially identified as $Pt(OH)_2$. Hydrogen peroxide adsorbs onto the binding sites to form the complex $Pt(OH)_2{\cdot}H_2O_2$. The complex then undergoes internal electron transfer to form a reduced platinum site, Pt, with the release of the products water and oxygen. The binding sites regenerate electrochemically to give rise to an amperometric signal together with the release of protons.

Two side reactions were proposed, the first involved a competitive inhibition of the binding sites by oxygen to form the species $Pt(OH)_2{\cdot}O_2$. The second involved a non-competitive inhibition of the complex $Pt(OH)_2{\cdot}H_2O_2$ by protons.

A rate equation was derived to account for all electrode sites involved in the proposed mechanism, with kinetic parameters for electrode reactions, and was validated over a range of bulk $[H_2O_2]$, rotation rates, potentials, temperatures, buffer concentrations and pH.

The kinetic and equilibrium constants for the model were optimised using a SIMPLEX procedure. The equilibrium constants were found to be potential- and temperature-invariant ($K_1 = 6.38 \times 10^{-3}$ m^3 mol^{-1}, $K_4 = 0.128$ m^3 mol^{-1} and $K_5 = 0.053$ m^3 mol^{-1}). The diffusion coefficient for H_2O_2 was found to be in the range $0.55 - 0.66 \times 10^{-9}$ m^2 s^{-1}. These values were lower than those reported in the literature. The rate constants, k_2N and k_3N, were found to vary with potential and temperature, and pseudo-activation energies for k_2 were found to range from 70 – 40 kJ mol^{-1} (dependent on the potential).

The model was further developed to account for the formation of the platinum binding sites (labelled as Pt_{BS}) from precursor sites, Pt_{PS}. A series of experiments employing phosphate buffers with a range of concentration and pH were performed. It was found that steady-state responses for the oxidation of H_2O_2 increased with increasing phosphate concentration. In the absence of phosphate, an alternative binding mechanism was evident.

A maximum response was found at pH 6.8 and decreased markedly at more basic or acidic conditions. This pH-dependence suggested that $H_2PO_4^-$ was the species involved in the formation of the binding sites. The decrease in response at pH > 6.8 being caused by the decrease in $[H_2PO_4^-]$, whilst an inhibition of the precursor site by protons was proposed to account for the depression in electrode response at pH < 6.8.

The influence of chloride upon the kinetics of H_2O_2 oxidation was examined and described qualitatively in terms of the new model. It was found that the rate of oxidation was decreased markedly in the presence of chloride. Two possible inhibition modes for chloride were identified and it was established that a non-competitive inhibition of the precursor sites was likely to be the dominant cause for the chloride inhibition.

The work described in this thesis has not only identified a new and comprehensive mechanism for the oxidation of H_2O_2 at platinum electrodes, but also provides information that may prove useful when designing sensors that rely upon this reaction. In particular the important role of hydrodynamic conditions, buffer composition and concentration are clearly identified.

Publications arising from this work

i) Electrochemical oxidation of hydrogen peroxide at platinum electrodes. An adsorption-controlled mechanism. S. B. Hall, E. A. Khudaish and A. L. Hart, *Electrochim. Acta*, 1998 (43) 579.

ii) Electrochemical oxidation of hydrogen peroxide at platinum electrodes. Effect of potential. S. B. Hall, E. A. Khudaish and A. L. Hart, *Electrochim. Acta*, 1998 (43) 2015.

iii) Electrochemical oxidation of hydrogen peroxide at platinum electrodes. Effect of temperature. S. B. Hall, E. A. Khudaish and A. L. Hart, *Electrochim. Acta*, 1999 (44) 2455.

iv) Electrochemical oxidation of hydrogen peroxide at platinum electrodes. Phosphate buffer dependence. S. B. Hall, E. A. Khudaish and A. L. Hart, *Electrochim. Acta*, 1999 (44) 4573.

v) Electrochemical oxidation of hydrogen peroxide at platinum electrodes. Inhibitory effect by chloride ions. S. B. Hall, E. A. Khudaish and A. L. Hart, *Electrochim. Acta*, submitted for publication.

ACKNOWLEDGEMENTS

After three years of working towards this degree there are many people to whom I owe a great deal of thanks.

First, I offer my sincere thanks to my chief supervisor Dr Simon B. Hall for the expertise, assistance and guidance he provided during the course of this work. I also acknowledge his efforts in writing the computer software for this project. His enthusiasm for science, particularly electrochemistry, has been a great inspiration.

Thanks must also go to my second supervisor Dr Alan L. Hart (Sensor Group, AgResearch, Palmerston North) for his encouragement, valuable discussions and guidance during this project.

I gratefully acknowledge the Massey University Research Fund (MURF) for the funds supplied to my supervisor to buy most of the new equipment required to undertake my research, and Prof. Andrew Brodie (Head of Chemistry Department at the commencement of my study) for his encouragement.

I am obliged to the many people I have had the good fortune to work with for their skills, friendship and humour including Assoc. Prof. Roger Reeves, Assoc. Prof. Gavin Hedwig, Dr. Tony Wright, Dr. Kirstie Wild, Mr. Andy Trow, Mr. Rod McKenzie and the electroanalytical chemistry group members, Michael, Giovanna, Justin and Anthony.

I am grateful to Prof. K. Jadaan for support and encouraging me to commence post-graduate studies.

I thank my parents, sisters and brothers for their sincere, passionate and warm support which has come to me through their letters and telephone calls.

Lastly, and no means by last, I acknowledge the many sacrifices my wife Muna has made in encouraging me to work towards this degree and for my children Ghofran, Mohammed and Omer who have been very patient during the months of preparing this thesis.

TABLE OF CONTENTS

LIST OF FIGURES

LIST OF TABLES

LIST OF SYMBOLS

Symbol	Description	Unit
A	electrode geometric area	cm^2
A_o	true surface area of electrode	cm^2
[A]	concentration of species A at electrode surface	mol m^{-3}
$[A]_{bulk}$	concentration of species A in the bulk	mol m^{-3}
C_{dl}	double-layer capacitance	μF cm^{-2}
c	Concentration	mol L^{-1}
D	diffusion coefficient	m^2 s^{-1}
E	potential	mV
E^o	standard potential	mV
F	Faraday constant	C mol^{-1}
f	electrode rotation rate	rpm or rps
f	fraction of free surface sites	
ΔH	enthalpy change	kJ mol^{-1}
i	current density	mA cm^{-2}
i_L	limiting current	mA cm^{-2}
i_d	diffusion current	mA cm^{-2}
i_k	kinetic current	mA cm^{-2}
I	current	mA
I_{dl}	double-layer charging current	mA
I_f	faradaic resistance current	mA
j	heterogeneous rate	mol m^{-2} s^{-1}
j_{max}	maximum heterogeneous rate	mol m^{-2} s^{-1}
k_2	heterogeneous rate constant	m s^{-1}
k_3	heterogeneous rate constant	m s^{-1}
K_1	equilibrium constant	m^3 mol^{-1}
K_4	equilibrium constant	m^3 mol^{-1}
K_5	equilibrium constant	m^3 mol^{-1}

K_M	Michaelis constant	mol m^{-3}
m	molality	mol kg^{-1}
$\overline{m}$	average mass	g
n	number of electrons	
R_f	faradaic resistance	ohm
δ	thickness of diffusion layer	cm
η	absolute viscosity	kg m^{-1} s^{-1}
θ	fructional surface coverage	
ρ	density	kg m^{-3}
τ	efflux time	s
ν	kinematic viscosity	m^2 s^{-1}
ω	angular velocity	rad s^{-1}

LIST OF ABBREVIATIONS

A/D	analog/digital
CA	chronoamperometry
CE	counter electrode
CPE	carbon paste electrode
CV	cyclic voltammetry
FIA	flow-injection analysis
GOD	glucose oxidase
H_2O_2	hydrogen peroxide
ME	microelectrode
$Pt(OH)_2$	hydrous platinum oxide
RDE	rotating disc electrode
RE	reference electrode
rpm	revolutions per minute
SCE	saturated calomel electrode
SCP	staircase potentiometry
SHE	standard hydrogen electrode
WE	working electrode

CHAPTER ONE

INTRODUCTION

1.1 Introduction

When an electrode is placed in contact with a solution, a phase boundary or interface is created that differentiates the solute molecules in two ways, those at distance from the electrode and those sufficiently close to the interface to participate in the transfer of electrons to or from the electrode. These phenomena are known collectively as electrochemistry.

At the electrode–solution interface many phenomena can occur such as charge transfer, diffusional mass transport, adsorption, and chemical reactions. Accordingly, electrochemistry offers an effective tool for fundamental studies of these processes.

The selection of hydrogen peroxide (H_2O_2) as a targeted species in this work was due to its involvement as a product of the catalytic reaction in many biocatalytic sensors or biosensors, and for its importance in a wide range of chemistry.

The platinum electrode was selected to detect H_2O_2 as it is used in many biosensors. The nature and properties of the platinum electrode is given in the following sections.

The major emphasis on the reactions of H_2O_2 at platinum electrode in this work is on the anodic or oxidation reaction.

The electrochemical oxidation of H_2O_2 on platinum electrodes was usually studied in phosphate buffer solution close to neutral pH in order to maintain consistency with practical biosensors, which operate under physiological conditions.

1.2 Hydrogen Peroxide

Hydrogen peroxide was first identified by the French chemist Thènard in 1818 [1]. In 1885 hydrogen peroxide was manufactured by treating barium peroxide with acids such as phosphoric, hydrochloric and sulphuric [2,3].

$$BaO_2 + H_2SO_4 \longrightarrow H_2O_2 + BaSO_4 \qquad (1.1)$$

In these early days, the concentration of H_2O_2 was limited to about 3%, and for many years it was found to deteriorate badly on storage. At first it was thought that the H_2O_2

molecule was unstable, but further work showed that the instability was almost entirely due to metal ion impurities such as traces of iron or copper.

Hydrogen peroxide became a significant commercial item from about 1910 owing to the discovery of its bleaching and antiseptic properties based upon its behaviour as an oxidizing agent. Its importance is still increasing, both in chemical processes and for military uses in rockets and missiles [3] as an oxidant agent.

1.2.1 Production

Hydrogen peroxide is predominantly produced by the three processes listed below;

i) electrolysis of ammonium bisulphate,

ii) auto-oxidation of alkylanthraquinones,

iii) partial oxidation of secondary alcohols.

The main process for the large scale synthesis of hydrogen peroxide is the auto-oxidation of alkylanthraquinones, such as 2-ethylanthraquinone, in a cyclic continuous process [2–4].

$$\text{2-ethylanthraquinone} + H_2 \xrightarrow{Pd/Al_2O_3} \text{2-ethylanthrahydroquinone} \qquad (1.2)$$

$$\text{2-ethylanthrahydroquinone} + O_2 \longrightarrow \text{2-ethylanthraquinone} + H_2O_2 \qquad (1.3)$$

The production process needs only H_2, atmospheric oxygen, and water as major raw materials.

For this process, a solution of 2-ethylanthraquinone in a mixture of organic solvent, such as alkylbenzene, is catalytically hydrogenated to 2-ethylanthrahydro–quinone in the presence of a catalyst consisting of activated alumina coated with 0.7 % palladium. The reduction is typically carried out at 35 – 40 °C and under hydrogen pressure of 1 to 3 atm. [4].

Hydrogen peroxide is extracted from the oxidation product with a sufficient quantity of water to yield 20 to 25 % aqueous H_2O_2 solution. These dilute solutions are then concentrated by vacuum distillation to 28 – 35 %. Higher concentrations, 90 – 99 %, are commercially achieved by further multistage fractionation. Such concentrated materials are very susceptible to metal ion catalysed decomposition and it is necessary to add inhibitors such as sodium pyrophosphate or stannate prior to storage in pure aluminium (> 99.6 %) containers [2,4].

1.2.2 Structure

The molecule H_2O_2 has a skew, chain structure as shown in Fig. 1.1. There is only a low barrier to internal rotation about the O–O bond. In the liquid state H_2O_2 is even more highly associated via hydrogen bonding than is H_2O [5].

1.2.3 Properties

Hydrogen peroxide is a colourless liquid, miscible with water and glycerine in all proportions. Pure H_2O_2 boils at 150.2 °C, freezes at –0.43 °C and has a density of 1.44 g/ml at 25 °C. Since 100 % H_2O_2 is not usually available, the physical constants of pure H_2O_2 are of limited practical value.

The density of aqueous H_2O_2 solution increases with its concentration, (e.g. at 20 °C the density is 1.11 and 1.36 $g.ml^{-1}$ for 30 % and 85 %, respectively) [6].

In dilute aqueous solution, H_2O_2 is more acidic than water, with $K_{20\,°C} = 1.5 \times 10^{-12}$

$$H_2O_2 \rightleftharpoons H^+ + HO_2^- \qquad (1.4)$$

In the presence of impurities, such as traces of metal ions, H_2O_2 is decomposed into water and gaseous oxygen

$$2H_2O_2 \rightleftharpoons 2H_2O + O_2 \qquad \Delta H = -99\ kJmol^{-1} \qquad (1.5)$$

The decomposition of H_2O_2 may be considered self-oxidation, and is found to occur most rapidly in basic solutions [5].

Consequently, deionized water is used in all H_2O_2 production. Only a limited number of potential container materials, such as aluminium, pyrex-glass, quartz, and some plastics do not promote the decomposition of H_2O_2. High purity aluminium is now used widely in the production, storage and transportation of H_2O_2.

The redox chemistry of H_2O_2 in aqueous solution is summarised by the following half reactions and accompanying potentials vs the standard hydrogen electrode (SHE);

$$H_2O_2 + 2H^+ + 2e^- \rightleftharpoons 2H_2O \qquad E^\circ = 1.77\ V \qquad (1.6)$$

$$O_2 + 2H^+ + 2e^- \rightleftharpoons H_2O_2 \qquad E^\circ = 0.68\ V \qquad (1.7)$$

$$HO_2^- + H_2O + 2e^- \rightleftharpoons 3\ OH^- \qquad E^\circ = 0.87V \qquad (1.8)$$

These data indicate that H_2O_2 is a strong oxidizing agent in either acid or basic solution; only for the strongest oxidizing agents such as MnO_4^- will it behave as a reducing agent.

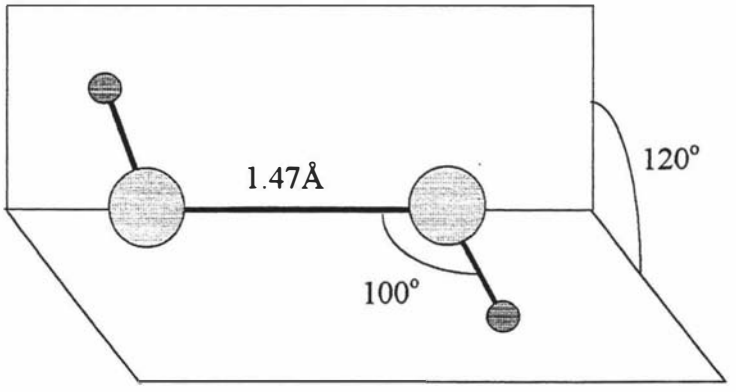

Fig. 1.1 The skew structure of the free H_2O_2 molecule. In crystalline solids such as $H_2O_{2(s)}$ and $Na_2C_2O_4 \cdot H_2O_2$, the parameters may vary.

In $H_2O_{2\,(s)}$ the O-O distance is 1.453Å with hydrogen bonding O-H····O at 2.8 Å versus 2.76 Å in $H_2O_{(s)}$.

The homogeneous oxidation of H_2O_2 in aqueous solution by Cl_2, MnO_4^-, and the catalytic decomposition caused by Fe^{3+}, I_2, MnO_2, have been studied using labelled H_2O_2. In both, oxidation and decomposition reactions, the oxygen produced was proposed to derive entirely from H_2O_2 and not from water [5]. This suggests that oxidizing agents do not break the O–O bond but remove electrons from the O_2^{2-} moiety. In the case of oxidation by chlorine, the following mechanism has been proposed that is consistent with the lack of exchange of ^{18}O between H_2O_2 and H_2O:

$$Cl_2 + H_2{}^{18}O_2 \longrightarrow H^+ + Cl^- + H^{18}O^{18}OCl \quad (1.9)$$

$$H^{18}O^{18}OCl \longrightarrow H^+ + Cl^- + {}^{18}O_2 \quad (1.10)$$

1.2.4 Commercial Usage and Importance

The greatest use of H_2O_2 is as a bleaching agent for textiles and paper pulp due to its decomposition to water and oxygen [7,8]. The advantage of this process arises from a final product which combines a high quality and stable whiteness, whilst maintaining its fabric strength for further finishing [1,9]. Furthermore, the products of decomposition, H_2O and O_2, are readily removed from the fabric. It is also used in waste water treatment for the control of hydrogen sulphide odours [4], which may be removed as SO_2.

Further points of interest are:

- It is often proposed that the toxicity of many drugs and chemicals results from excessive generation of superoxide (O_2^-) and H_2O_2, perhaps by exceeding the capacity of cellular enzyme systems to remove them efficiently. Therefore, measurement and control of H_2O_2 is of some interest [10]. Reactive oxygen intermediates may be generated in the lungs during various pathological processes. These intermediates and H_2O_2 itself are toxic to cells through their oxidizing effects on proteins, membranes and DNA. Consequently, detection of submicromolar concentration of H_2O_2 is vital because these peroxide levels can damage mammalian cells [10,11].
- The determination of very low concentrations of aqueous H_2O_2 has received great attention in atmospheric studies because it is believed that it rapidly oxidizes hydrogen sulphite ions in water at pH< 4.5 and thus contributes to the generation of sulphuric acid [12,13] in droplets and mist. Sulphur oxides (SO_x) and nitrogen oxides (NO_x), which are discharged at industrial areas, are the major causes of acid rain as

they are oxidized to sulphate ion and nitrate ion by H_2O_2 in the atmosphere (normally formed by a reaction of two $HO_2^{\bullet}$ free radicals, in turn produced in photochemical oxidation processes of hydrocarbon compounds). Therefore, H_2O_2 plays a part in the formation of acid rain.

- Currently, food regulations in some countries permit adding H_2O_2 to milk as a preservative. In the USA, 0.05% H_2O_2 may be added to milk used to manufacture certain cheeses [14]. In this process, normally called H_2O_2-catalase treatment, milk is treated with H_2O_2 (0.04 – 0.08 % H_2O_2, at 52–53 °C for 30 min.). This effectively reduces the total count of bacteria present in the milk [15].
- Dilute H_2O_2 possesses excellent bactericidal properties beside being well tolerated by the skin and tissues. A new approach is to use H_2O_2 as a disinfectant for swimming pool water in place of chlorine which has some disadvantages like irritation of eyes and mucous membrane, roughening skin and hair and a nuisance odour[16]. It is also used as an anti-bacterial agent in some pharmaceutical products [17]. In the dairy industry, H_2O_2 is circulated through equipment at a concentration of 1500 ppm to provide rapid sterilisation and it is necessary to ensure there is no peroxide carry-over into the first batch of sample [18].
- Considerable quantities of H_2O_2 are used as an energy source in aircraft jets, rockets and missiles in which concentrated H_2O_2 solutions (85 – 90 %) are required [3].

1.2.5 Determination

Many methods have been used in industry for the determination of H_2O_2. These include titrimetry [19], spectrophotometry [20,21], chemiluminescence [22] and fluorometry [23]. Such techniques typically suffer from a range of interferences, are time consuming and require expensive reagents. The electrochemical measurement of H_2O_2 has received significant attention since this technique potentially offers advantageous features such as rapid detection with high accuracy, lower detection limits (sub-micromolar), decreased interference (by selecting modified surfaces and specific catalytic reagents), measurements requiring small quantities of reagents, and sensors can be mass-produced commercially and inexpensively.

The electrochemical measurement of H_2O_2 and the construction of a range of sensors is given in the following section.

1.3 Biosensors Based on Detection of Hydrogen Peroxide

Electrochemical biosensors combine the analytical power of electrochemical techniques with the specificity of biological recognition processes. The aim is to produce an electrical signal which relates in a simple way to the concentration of the biological analyte. For this purpose, a biospecific reagent is either immobilised or retained at a suitable electrode, which converts the biological recognition process into a quantitative amperometric or potentiometric response.

A prime example of electrochemical biosensors is that of the glucose sensor. This amperometric device, first demonstrated by Clark [24] and developed by Updick and Hicks [25], represents the first reported use of an enzyme–based electrode.

The electrode is commonly based on the entrapment of glucose oxidase (GOD) between dialysis and permselective membranes on a platinum working electrode. When this device is immersed in a glucose–containing solution, glucose is first oxidised by the catalytic action of GOD

$$\text{glucose} + O_2 \xrightarrow{\text{GOD}} \text{gluconic acid} + H_2O_2 \qquad (1.11)$$

The liberation of H_2O_2 by the above enzymatic reaction is then monitored amperometrically at the surface of platinum electrode,

$$H_2O_2 \xrightarrow{\text{Platinum}} O_2 + 2H^+ + 2e^- \qquad (1.12)$$

In the absence of any deleterious processes the current is directly proportional to the glucose concentration in the analyte solution [26].

Since the electrochemical reaction of a molecule occurs at the electrode/solution interface, molecules must be transported from the bulk solution to the electrode surface. This mass transport is achieved mainly by hydrodynamics and diffusion [27]. The hydrodynamic mass transport is caused by the movement of matter by stirring the solution, rotating the electrode, or flowing the solution through a cell. Not only does this supply reactants to the reaction site but also removes products.

In the diffusion process, the matter is always transported from regions of high to low concentration. In other words, the diffusional mass transport must occur whenever there is a chemical change at an electrode surface where the concentration of the reactant is decreased and conversely the concentration of the electrogenerated product is increased.

In terms of the glucose biosensors described above, glucose molecules must be transported to the electrode surface continuously by one or both of diffusion and

hydrodynamic processes. The overall process must be analyte-controlled to afford an overall linear response, so that the rate of reaction 1.12 might be significantly faster than reaction 1.11 due to the electrochemical reaction of H_2O_2 at the electrode surface.

It should be noted here, that the enzymatic reaction requires another step involving the oxidation of the reduced enzyme by an electron acceptor (normally oxygen molecules). Therefore, the operation of this kind of biosensor depends mainly on molecular oxygen present in the solution. In the absence of oxygen, modified biosensors incorporate redox polymers [28,29] (termed a mediators) to act as an electron acceptor.

Galiasatos et al [30] prepared glucose sensors by depositing platinum electrochemically onto a graphite surface and GOD was inserted directly onto the platinized graphite surface. The enzymatically–generated H_2O_2 was detected amperometrically at +300 mV vs Ag/AgCl. Simultaneous electrodeposition of GOD and platinum particles onto a glassy carbon substrate was demonstrated by Gunasingham and Tan [31]. This glucose sensor showed a high dynamic response within the physiological–useful range for glucose in blood.

Selectivity or specificity among co-existing electroactive species may be enhanced by employing membrane electrodes generally constructed from polymers such as cellulose acetate, polyurethane, Nafion, and a variety of other materials [32-35].

More recently, sensors have been developed in which oxygen is not required as an electron acceptor. In these sensors, the electron transport from a redox enzyme can be facilitated by the incorporation of an electron transport mediator which acts as an electron shuttle between the redox centre of the enzyme and electrode surface. Accordingly, a number of reports on electrochemical biosensors are found using various types of mediators including ferrocenes [36], tetracano-quinodimethane [37], hexacyanoferrate [38], quinones [39], tetrathiafulvalene [40] and methylene blue [41].

1.4 The Nature of Platinum Electrode Surfaces

Platinum metal occupies a unique place in electrochemistry due to its relatively high chemical inertness, marked stability at positive potentials and its electrocatalytic properties.

Platinum surfaces dissociate large binding energy, diatomic molecules, such as oxygen, by forming strong Pt-O bonds, and holds the atoms in high surface concentrations [42].

Evidence from ^{195}Pt-NMR spectroscopy of a commercial graphite-supported nanoscale platinum electrode under different surface conditions at 80K [43], showed that the platinum surface is completely coated by oxygen. This was consistent with earlier evidence [44] that the low-field peak of the platinum surface coincides exactly with that of PtO_2.

Platinum has another feature arising from the tendency to adsorb many species, which follows from its electronic structure, designated as [Xe]$s^2p^6d^9$. Hence a partially unsaturated surface *d*-orbital facilitates adsorption of compounds with non-bonded electron pairs [45], and decreases the kinetic barriers (overpotential) for the oxidation of these species. Therefore, much interest arises from the presence of an oxide film at the electrode whose surface chemical composition and surface electronic structure determine the electrocatalytic properties of the solid/liquid interface [46,47].

Electrochemical species can undergo electrocatalytic oxidation through the reaction with oxygen, which may come from water or from surface oxides on the electrode formed primarily by anodic activation [48]. The anodic activation of the electrode can be achieved by application of cyclic voltammetry (CV), where the electrode is anodized by scanning the potential in the anodic region and/or holding the potential for some time at the anodic limit [49,50].

It is evident that adsorbed oxygen and most probably surface oxides are the oxygen species which are involved in the oxidation process [44,51].

It is thus recognized that the mechanism of electrochemical formation of surface oxide on a platinum electrode is an important subject of investigation in the electrocatalytic oxidation of H_2O_2 [52-54].

1.4.1 Formation of Platinum Oxide Films

The mechanism of electrochemical formation and reduction of surface oxides on platinum electrodes in acidic media have been studied [55-58] to account for the electrocatalytic behaviour of platinum.

According to Conway *et al* [56] the oxidation of the platinum surface is initiated by a process of electrodeposition of hydroxyl species commencing at about 0.75 V vs SHE,

$$Pt + H_2O \rightleftharpoons PtOH + H^+ + e^- \qquad (1.13)$$

It is followed by an irreversible electron-proton transfer reaction yielding surface oxygen species,

$$PtOH \longrightarrow PtO + H^+ + e^- \quad (1.14)$$

These studies indicate that platinum electrode is covered, depending on the polarization potential, either with adsorbed hydrogen or surface oxide. Only in a narrow potential interval from +0.4 to +0.8 V vs SHE, the so-called double layer region, is the platinum surface considered to be almost free from adsorbed species [59].

At potentials more positive than +0.8 V adsorbed oxygen begins to form, i.e. a surface oxide formation, where the reactivity towards oxidation reactions is mostly maintained up to +0.9 V and then decreases with increasing potential due to the formation of a greater quantity of stable oxide [60].

It was recognized that platinum electrodes exhibit reactivity even at more severe conditions [61], i.e. pre-treatment of the electrode with hot concentrated sulphuric acid and polarization at relatively high anodic potentials, where the thickness of the oxide increased rapidly.

When the direction of polarization is reversed, the oxide surface reduces gradually at potentials which are relatively more cathodic than those required for the corresponding oxidation process. The resolution (removal) of surface oxides appear in the cyclic voltammograms as a single sharp peak with current maxima at about +0.72 and +0.69 V in acidic and basic media, respectively [62].

The electrochemical charge transfer reactions mostly occur at the surface oxide rather than at the clean surface [63]. Therefore, the electrochemical oxidation reactions of most species are preferred at potentials close to those of the platinum oxide surface formation for greatest response [52].

The formation and reduction of the film give rise to anodic and cathodic residual currents. The nature of the electrode surface varies with potential and also depends on the prior history of the electrode. These variations usually affect the rate of electrode reactions, and in some cases may even alter their course.

The first detailed description of the effects of oxide formation and reduction on the residual current curve was given by Kolthoff and Tanaka [64] who recorded a small anodic wave when current-voltage curves were measured from negative to positive potentials at stationary and rotated platinum wire electrodes in supporting electrolytes

free of added oxidising or reducing agents over the entire pH range. However, when the potential was reversed to more negative potentials, a small cathodic wave was observed, commencing at a potential which approximately corresponds to the equilibrium value of the platinum-platinous hydroxide electrode, i.e close to the potential value of surface oxide formation [63].

A similar film was formed by placing the electrode in solutions of strongly oxidising agents. Lee *et al.* [65] studied the properties and the compositions of the oxide films of gold, platinum, and palladium electrodes in strongly oxidising aqueous solutions. They also examined the transient potential-time behaviour of reduced electrodes (electrodes which had been pre-treated cathodically to remove all oxidised material from the electrode surface) when immersed in strongly oxidising agents and compared this with the behaviour observed when these electrodes were oxidised anodically. They found that the same reactions were occurred at both sets of the electrodes. These reactions were attributed to oxide film formation since the reaction occurred at potentials that agreed well with the potential of known oxide-metal transitions.

Anson and Lingane [63] investigated the oxide film on platinum electrode and showed that the amount of oxidised platinum found by chemical analysis agrees with the amount of electrode oxidation as measured by chronoamperometric techniques. Chemical analyses indicated that both PtO and PtO_2 were present on the surface of an oxidised electrode, and the ratio of the two species was approximately the same regardless of whether the electrode had been oxidised by anodic polarisation or with various chemical oxidants [63].

More recently it has been suggested that the electrocatalytic behaviour of platinum electrodes involves pre-monolayer oxidation, i.e. low lattice co-ordination surface metal atoms oxidised to yield incipient hydrous oxide species that mediate oxidation processes [61,62,66,67]. Similar interpretations were used, in the case of gold, by Conway and coworkers [68,69] where they assumed that premonolayer oxidation involves formation of an anionic hydroxy species which mediates the oxidation process.

1.4.2 The Effect of an Oxide Film on Electrode Reactions

Many important consequences result from the existence of an oxide film on the surface of platinum electrodes. The presence of a fine oxide film represents the activated state of

oxygen species for the catalytic oxidation reaction [70] which can accelerate the electron transfer process. Accordingly, the electrochemical oxidation of many species are believed to occur concomitantly with the formation of platinum oxide, where the oxygen species is provided more easily from the oxide surface than from the bulk solution [50].

Earlier studies [71,72] were based on the oxygen-bridge theory which relates to the electrochemical reactions at an oxide-coated electrode, and are attributed to the formation of a bridge between an oxygen film and the species undergoing reaction.

Since this theory could not account for the decrease in the reaction rate constant when the electrode is fairly strongly oxidised, the theory was modified to state that oxygen-bridges can form only when a slight or very thin coating of oxide is present. Accordingly, this slight change in the theory can be used to explain the variations in the rate constants with the extent of electrode's oxidation. Apparently a heavy oxide film has the ability, to some degree, to suppress the electrode reactions, which has been indicated in several studies [63,73,74].

The electrochemical reactivity of platinum surface oxide was attributed also to the formation of finely divided platinum (a film of platinized platinum) on the electrode surface as a result of the reduction of platinum oxide [75,76].

1.5 Platinum Electrodes for H_2O_2 Oxidation

The detection of H_2O_2 is of practical importance in clinical and biological reactions as an important intermediate produced during the catalytic reaction of biomolecules. It is also important in environmental and in many industrial processes as a universal oxidant [77], so that its determination has received much attention [78,79]. Many composite electrodes containing platinum to accelerate the reaction rate of H_2O_2 have been utilized and a selection are described in the following sections.

1.5.1 Bare Platinum Electrodes

Direct electrochemical determination of H_2O_2 at bare electrodes is not suited for analytical applications due to the following reasons:

i) electrodes operating at large over-potentials lead to interference from other electroactive species that may be present in the analyte solution, such as uric and ascorbic acid [80,81],

ii) electrode fouling due to the adsorption of organic or/and biological materials may occur at the electrode surface [82,83], and

iii) bare Pt electrodes show irreproducible behaviour with time and a marked dependence on electrode pre-treatment [84,85].

Consequently, efforts have been made to develop modified electrocatalytic surfaces that do not exhibit these deleterous effects for the detection of H_2O_2.

These modifications rely mainly on the use of transition metals, their oxides, or their complexes as catalytic modifiers in different kinds of composite electrodes [86].

1.5.2 Metallized Carbon Electrodes

Carbon paste electrodes (CPE) were invented by Adams in 1958 [87], and consist of a matrix of graphite powder and an organic pasting liquid. This technique has been widely and successfully employed over the past three decades in electroanalysis and biosensors [88–90]. Such electrodes offer the advantages of very low background currents, a wide range of working potentials, are easily prepared, renewed, and have easily modified surfaces.

Despite these advantages, CPEs are limited for the following reasons;

i) they have weak mechanical properties due to their paste texture, which can easily lead to disintegration of the system,

ii) poor reproducibility of the electrode fabrication,

iii) leakage of mediator out of the carbon paste,

iv) failure of electron transfer from the biocatalytic site to graphite.

Despite these deleterious features, CPEs have been investigated for the feasibility of bulk modification of the electrode material with other catalytic components such as fine metal particles, enzymes, and mediators for the purpose of improving the electrode response and selectivity.

Particularly in this respect, electrodes have been made from carbon particles modified with platinum, palladium, and ruthenium microcrystallites [91]. These powders are characterized by a strong adhesion of the metal centre to the graphite substrate. The resulting electrodes fabricated by mixing the metallized graphite powder and organic pasting liquid, combine the inherent advantages of CPEs with the catalytic activity of the metallized sites.

Platinum has been the preferred choice of metals for many of these sensors. The purpose of using platinized carbon electrodes in the construction of biosensors is to create conditions in which the oxidation or reduction of enzymatically generated H_2O_2 can be achieved at less extreme potentials or lower overpotential compared with plain graphite electrodes [92-94]. This reduces the problems associated with the concurrent reaction of other electroactive species that may be present in a real sample.

Since the electrochemical response ultimately depends on electron transfer between the electrode material and a solution species, solid electrodes, particularly carbon, can have surface heterogeneity produced by adsorbed layers of impurities which leads to regions of slow electron transfer kinetics [95]. Platinized carbon overcomes this heterogeneity and offers a large active area for fast electron transfer that causes the electrode current density to increase markedly. Therefore, the electrical signal for the oxidation and reduction of H_2O_2 at platinized carbon electrodes can be increased (compared to solid carbon or platinum electrodes) as a result of the increased electrochemical active area.

Depositing finely divided platinum over a carbon substrate results in a highly catalytic surface [96] where a number of reactions can proceed at an accelerated rate. Studies indicate that platinum acts as an electron donor to carbon, where differences in the electronic work functions of platinum and carbon lead to an increase in electron density on platinum [97]. This increase in electron density can only be significant if the particle size of the dispersed metal (platinum) is comparable to the thickness of the electric double layer [97].

A number of glucose biosensors, based on the deposition of platinum at the surface of carbon electrode, have been described. Platinized carbon paper was used by Bennetto *et al* [98] with GOD immobilized directly onto the paper. Typically, these electrodes exhibited linear response up to 20 mM of glucose and operated with high precision and specificity.

The construction and operation of glucose biosensors based on finely divided platinum group metals and their oxides has also been described by Mullen [99] where the measurement of glucose was performed at a potential of +400 mV versus Ag/AgCl reducing the overpotential of electrochemical oxidation of H_2O_2 by about 200 mV.

The overpotential for both the oxidation and reduction of H_2O_2 can be decreased significantly for carbon electrodes modified by vapour or vacuum deposition of a thin

layer of a mixture of palladium and gold on the surface of the electrode [100-103], where the function of gold is to aid in the fine dispersion of palladium and to provide a conducting matrix for the sensor. Deposition conditions required optimization in preparing these electrodes. For example, it was found [101] that if the final palladium content of the film was greater than 35% the resultant electrode was nonconductive. Also the film thickness was very critical and must be controlled either by varying the deposition voltage and/or the evaporation time.

1.5.3 Screen-Printed Electrodes

There has been a great deal of interest in the production of a wide range of amperometric sensors amenable to mass production using established techniques such as screen-printing [104]. The technology is based on printing suitable pastes, differing in composition and electrical conductivity, onto substrates such as fired Al_2O_3 ceramics or plastics.

The fundamental steps are paste production, design and screen production, printing of the paste and finally drying. By manipulating the final compositions of the paste, i.e. enzyme and mediator content, it has been possible to fabricate sensors for a number of different analytes using this technique [105,106].

Cardosi and Birch [92] have reported a screen-printed sensor that employs a platinized carbon ink containing carbon particles that have been modified by covalent attachment of glucose oxidase.

More recently, a developed method to construct screen printed glucose biosensor for use in a flow injection analysis (FIA) was described by White *et al* [107]. The sensors were fabricated using a catalytic metallized carbon based ink, whereby H_2O_2 was oxidized at +350 mV vs Ag/AgCl. The promising feature of these sensors is that they are suitable for use over at least seven days.

1.6 Electrochemical Oxidation of H_2O_2

The anodic decomposition of H_2O_2 in solution to form oxygen has been a subject of continuing attention for over a century. The overall electrochemical oxidation of H_2O_2 was represented in reaction 1.12.

The most important studies were those related to the oxidation mechanism of H_2O_2 at metal electrodes [52,54,108-111] in the region of anodic potential. These studies proposed that the initial interaction with the metal moiety to form the metal oxide film was responsible for the oxidation reaction. Other studies [100,101] developed this concept by considering the surface binding sites and suggested a mechanistic model for the formation and reduction of oxidized surface.

The above mentioned studies are consistent in describing the oxidation of H_2O_2 on oxidized metal surface but did not include in the mechanism discussion of the mass transport and electron transfer kinetics. It is believed that the electrochemical oxidation of H_2O_2 can not be described by employing simple kinetic principles, especially when evaluating the kinetic parameters.

A detailed discussion for the oxidation of H_2O_2 on platinum electrode is given in Chapter 4 together with a model developed during this study.

1.7 The Scope of This Work

The principal objective of this research was to investigate the reaction mechanism for the electrochemical oxidation of H_2O_2 at platinum electrodes in phosphate buffer solutions and to evaluate the kinetic parameters quantitatively over a range of conditions.

A modified mechanism is proposed to extend and develop the existing schemes suggested by other workers [100,101]. The electrochemical oxidation of H_2O_2 was examined in light of this mechanism (publications arising from this work are indicated):

i) concentration and electrode rotation rate dependence [112] is described in Chapter 4,

ii) variation of rate with potential [113] is described in Chapter 5,

iii) the effect of temperature [114] is described in Chapter 6,

iv) the dependence of electrolyte concentration and pH [115] is described in Chapter 7, and

v) the inhibition by chloride ions [116] is described in Chapter 8.

The electrochemical methods used in this work have predominantly been chronoamperometry and staircase potentiometry techniques. Optimisation of experimental data was also developed to quantify and achieve good fits of all parameters identified in the reaction mechanism.

CHAPTER TWO

EXPERIMENTAL METHODS

2.1 Introduction

This chapter provides an overview of the electrochemical methods and experimental conditions used to study the oxidation of hydrogen peroxide at platinum working electrodes in phosphate buffer solutions over a range of concentrations, temperatures and pH. The electrochemical techniques employed in this work were cyclic voltammetry (CV), chronoamperometry (CA) and staircase potentiometry (SCP).

A range of platinum electrodes were used; planar rotating disc; microelectrode; and a thin layer flow cell with a planar electrode.

Details and comprehensive discussion of the results for CA experiments are given in Chapter 4, SCP experiments Chapters 5-8, whilst CA experiments on a thin layer flow cell attached to a sequential flow injection analysis (FIA) system are discussed in Chapters 7 and 8.

2.2 Instrumentation

2.2.1 Potentiostatic Equipment

The electrochemical cells used consisted of three electrodes, namely, the working electrode (WE), reference electrode (RE) and counter electrode (CE). The potential of the WE is controlled through the use of a potentiostat (or electrochemical analyzer) that controls the potential difference between the WE and RE by altering the current flowing the WE and CE [27].

Two kinds of potentiostat were used during this work:

i) a BAS 100B/W Electrochemical Analyzer and accompanying BAS 100B/W Version 2.0 software (Bioanalytical System Inc., West Lafayette, Indiana, USA) was used for the experiments with rotating disc electrode and microelectrodes, and

ii) a BAS CV-27 Voltammograph (Bioanalytical System Inc., West Lafayette, Indiana, USA) was used for the experiments with thin layer flow cells attached to

a flow injection analysis system, and also for experiments carried out to evaluate the electrode surface roughness.

In this thesis, the convention that oxidation produces a positive current is adopted. This is in contrast to the convention used in the BAS equipment where reduction processes are reported as positive currents.

2.2.2 Flow Injection Analysis System

This system combines hydrodynamic control with the sensing efficiency of electrochemistry by pumping liquid electrolyte through a thin layer cell.

The thin layer cell assembly with three electrodes located in a CC-5 cell compartment (Bioanalytical System Inc., West Lafayette, Indiana, USA) is shown in Fig. 2.1, where the WEs may be positioned in parallel or series. During this study, a single WE in the series position was subjected to a constant potential controlled by a BAS CV-27 Voltammograph.

The controlled flow of electrolyte was achieved using a Perstrop Analytical Environmental Instrument (Perstrop Analytical Inc., Wilsonville, Oregon, USA). This was fitted with a 120 position sample carousel, sample valve and sample loops of various sizes.

The operation of this FIA system was controlled by an accompanying software package (EnviroFlow 2.1, ALPKEM, Wilsonville, Oregon, USA) provided with the instrument. The analogue output from the CV-27 Voltammograph was connected to an A/D converter fitted in place of the usual optical detector in the Perstrop Analytical device.

This combination of electrochemical and analytical instrumentation converts the amperometric response to a signal proportional to the concentration of analyte entering the thin layer cell. The response for each H_2O_2–containing segment of solution entering the flow cell consisted of a well defined peak with little tailing.

Since the peak height was reported in arbitrary units by the EnviroFlow 2.1 software, it was necessary to relate this to the current response. For this purpose, a precision 0 to 1000 mV variable DC power supply (Institute of Fundamental Sciences Electronics Workshop, Massey University) was used to calibrate the A/D card.

Table 2.1 lists the potential applied to the A/D interface as a function of peak height reported by the ALPKEM software and Fig. 2.2 shows the graphical representation of

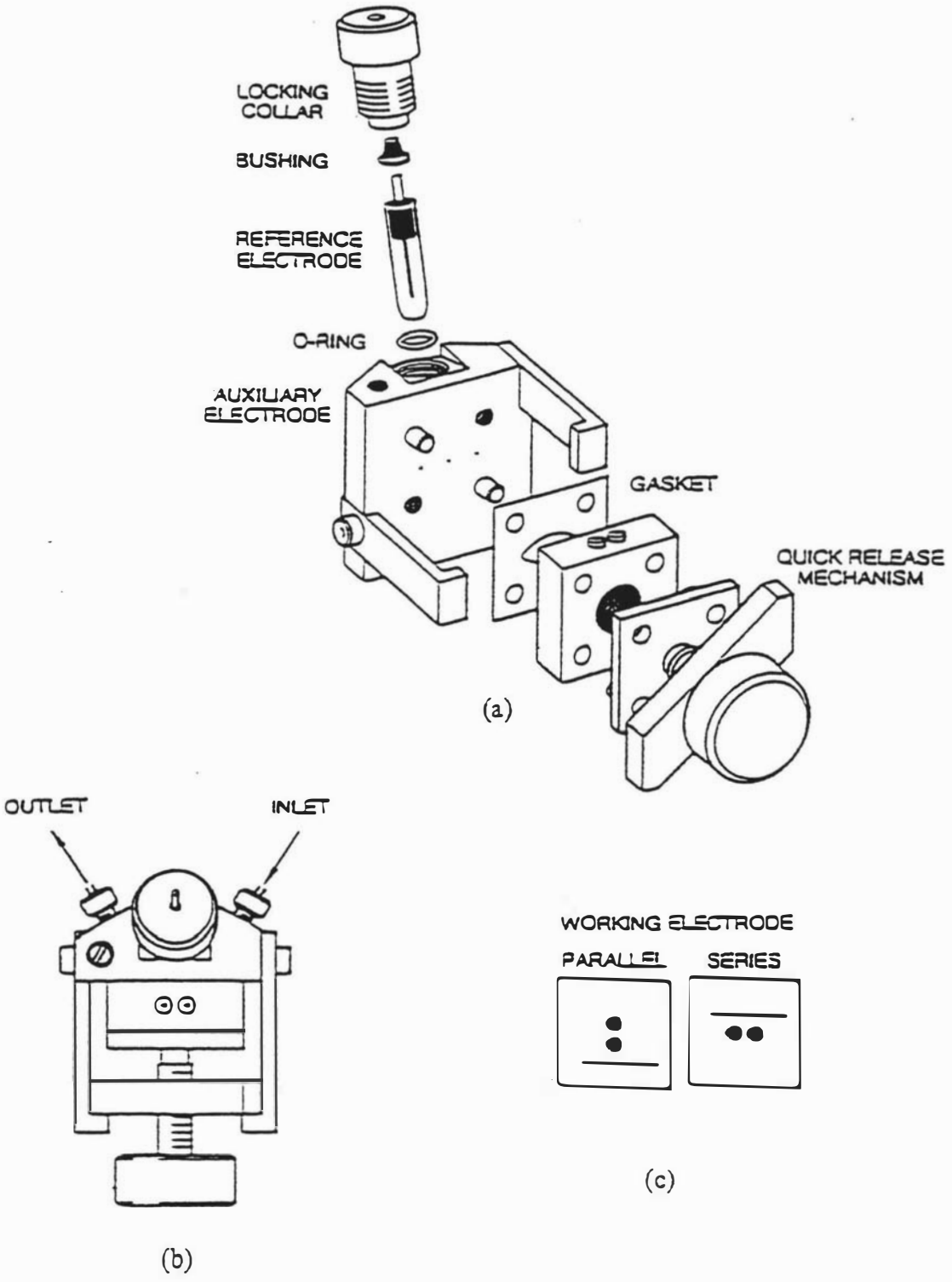

Fig. 2.1 The thin layer flow cell assembly. (a) the components, (b) the installed cell and (c) the position of working electrode.

Applied Potential mV	Peak Height 10^{12} counts
0	0.000
50	0.265
100	0.540
150	0.855
200	1.115
250	1.385
300	1.685
350	1.995
400	2.295
450	2.595
500	2.915
550	3.220
600	3.535
650	3.855
700	4.170
750	4.480
800	4.780
850	5.085
900	5.400
950	5.700
1000	6.000

Table 2.1 Peak height recorded by the FIA A/D card listed as a function of applied potential. Data are plotted in Fig. 2.2.

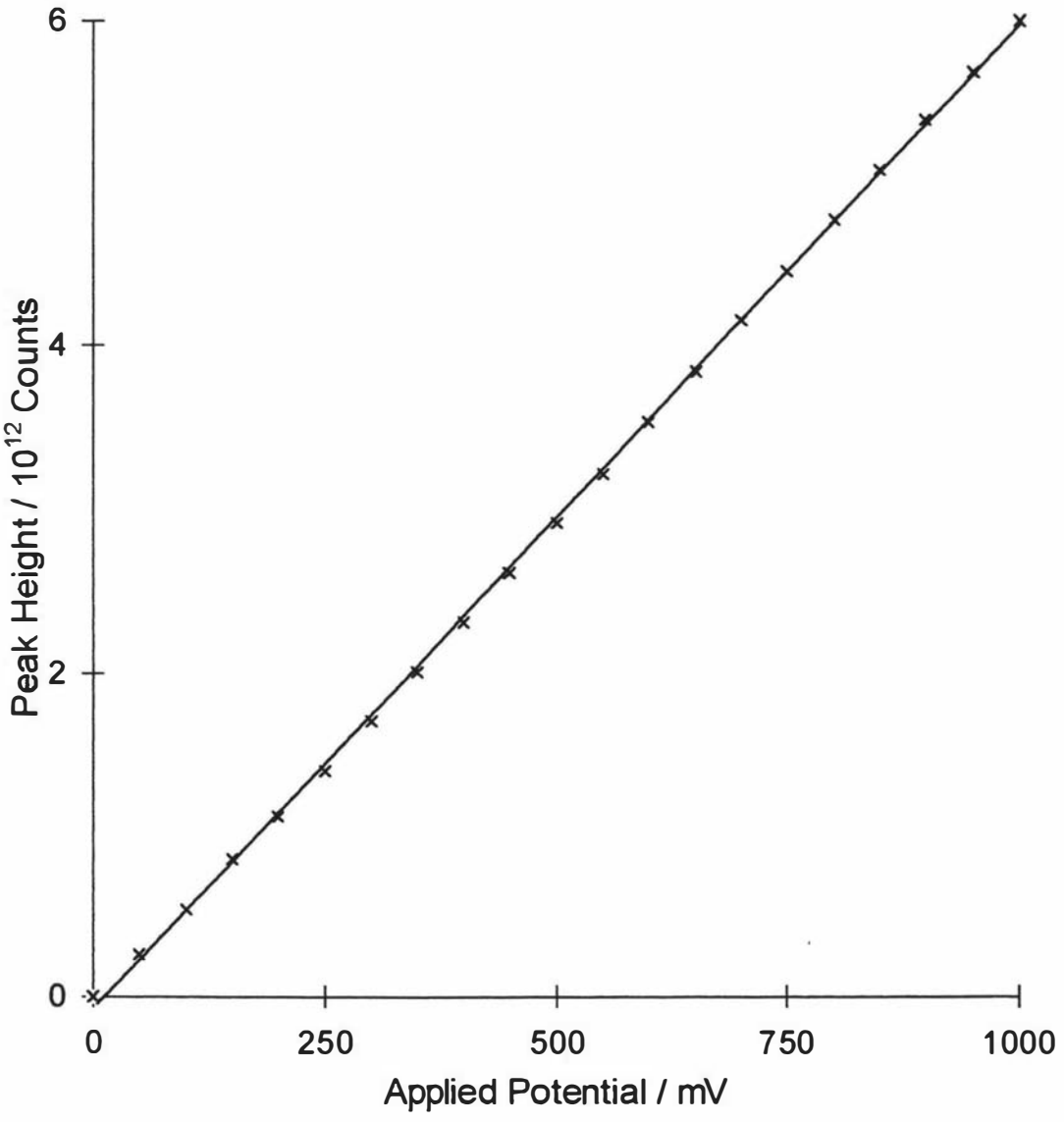

Fig. 2.2 Calibration of the FIA A/D card. The slope of this calibration plot was used in combination with Eq. 2.1 to convert peak height to current response for all thin layer flow cell experiments. Data are listed in Table 2.1.

these data. The A/D interface clearly demonstrates linear response over the range 0-1000 mV with insignificant bias. The slope was found to be 6.00×10^{12} counts V^{-1} and this was used together with the CV-27 current sensitivity setting to convert the peak height into a current response

$$\text{Current (mA)} = \frac{\text{peak height (counts)}}{6.00\times10^{12}\,(\text{counts V}^{-1})} \times \text{sensitivity (mA V}^{-1}) \qquad (2.1)$$

2.3 Electrode Systems

The electrochemical cells utilised during this study consisted of three electrodes where the electrochemical reaction of interest takes place at the WE with the generation of the amperometric signal or faradaic current due to an electron transfer processes. The CE is driven by the potentiostatic circuit to balance the faradaic process at the WE but in the opposite direction (e.g. if reduction takes place at the WE, oxidation will occur at the CE). Processes at the CE are typically not of interest, and in most experiments the small currents observed dictate that the electrolytic products at the CE have no influence on the process at the WE.

The reference electrode is an invariant potentiometric probe to monitor the potential change in the WE relative to its own potential by circuit combination with the potentiostat.

2.3.1 Rotating Disc Electrode

A platinum rotating disc electrode (RDE) with geometric area of 0.1195 cm^2 was used for the CV, CA and SCP experiments. For each experiment, the RDE was preconditioned prior to the electrochemical measurements by cycling the potential from 0 to +1000 mV vs Ag/AgCl at 100 mV s^{-1} for 50 continual cycles, with termination at the anodic potential limit on the final cycle. This is believed to increase the activity of the electrode by coating its surface with a coherent film of platinum oxide [52], this pre-treatment avoids the growth of a thick oxide layer which may decrease the activity of the electrode and alter its course by employing only an moderate potential excursion. All such pre-treatment was carried out in the appropriate phosphate buffer electrolyte in the absence of H_2O_2.

The RDE is vertically mounted on the shaft of a synchronous digitally controlled motor in the RDE-1 device (Bioanalytical System Inc., West Lafayette, Indiana, USA) and rotated with constant angular velocity (ω) in rad s^{-1} about an axis perpendicular to the plane disc surface as shown in Fig. 2.3.

The angular velocity is equal to $2\pi f$, where f is the rotation rate in revolutions per second. As a result of this motion, the fluid in an adjacent layer develops a radial velocity that moves it a way from the disc centre, and the fluid is replenished by a flow normal to the surface. Hence, the rotated disc can be viewed as a pump that draws a fresh solution up from the bulk solution [95].

A platinum coil with area of 1.90 cm^2 and an Ag/AgCl gel electrode (3M NaCl) with potential +197 mV vs the standard hydrogen electrode (SHE) (Bioanalytical System Inc., West Lafayette, Indiana, USA) were used as the CE and RE respectively, in the electrochemical cell.

The potential of the RE was checked periodically against a saturated calomel electrode (SCE) (Bioanalytical System Inc., West Lafayette, Indiana, USA) with potential +244 mV vs SHE at 20 °C. There was an insignificant change in the electrode potential over long periods.

The electrochemical measurements in the RDE system were made in 250 cm^3 of phosphate buffer solution in a specially designed water-jacketed cell (IFS Glassblower Workshop, Massey University) maintained at the desired temperature with a circulating water bath (Colora, Messtecknik, GMBH, Germany) and monitored with a calibrated thermocouple placed within the cell at the same height as the WE.

2.3.1.1 Calibration of Rotation Rate

The rotation rate of the RDE was calibrated routinely to ensure correct performance. The calibration procedure was carried out independently by use of an optical digital tachometer (Extech Instruments, Taiwan) by attachment of a reflective strip to the body of the RDE WE.

The rotation speed was set at the RDE-1 device through the RPM-adjust control over the range used in the course of this work, and compared with the rotation rate reported by the optical tachometer. A typical set of readings are given in Table 2.2, where good

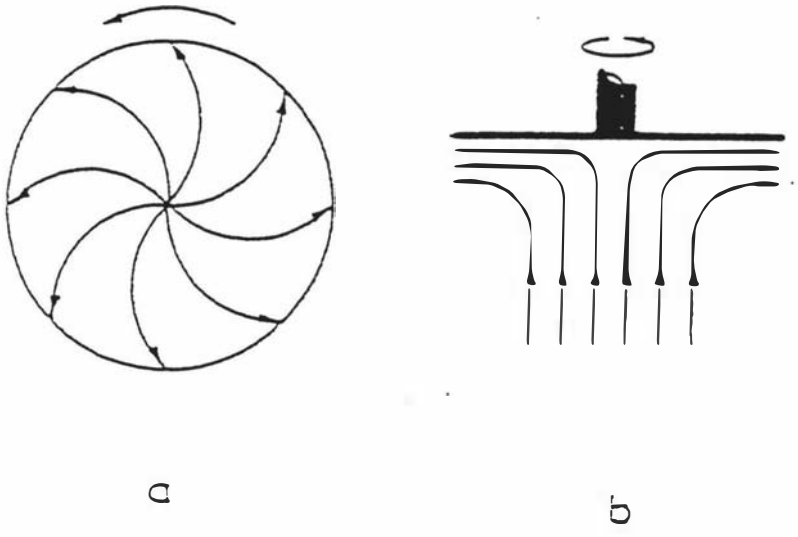

Fig. 2.3 The flow patterns created by the RDE, (a) solution flow close to the electrode surface, view from below and (b) view from side showing the pumped solution towards and outwards the disc.

RPM Adjust rpm	Tachometer rpm
1022	1022
2031	2032
3022	3025
4022	4024
5025	5025
6083	6085
7030	7032
8060	8060
9016	9022
9500	9503
9931	9930

Table 2.2 Rotation rate calibration for the RDE. The data in the first column represent the rotation rates set on the front panel of the RDE-1 whilst the second column lists the rotation rates detected with an Optical Tachmeter.

agreement between the RDE-1 setting and that given from the optical tachometer is evident.

2.3.1.2 Overcoming the Problem of Oxygen Bubbles

An important species produced during the catalytic oxidation of H_2O_2 is molecular oxygen which may accumulate at the electrode surface and hence disturb the detection of H_2O_2. The supporting electrolyte was purged with an inert gas, such as oxygen-free nitrogen, throughout the experiments to overcome the influence of dissolved oxygen. This practice was maintained for all experiments. The problem encountered with oxygen bubbles in this work was adherence of O_2 gas bubbles to the inverted RDE, thus decreasing the working area of the electrode and interrupting the hydrodynamic flow of electrolyte across the electrode surface. This was found to cause irreproducible and inaccurate results. To avoid these problems, the rotation rate of the WE was increased rapidly to the maximum rate possible (10000 rpm) immediately prior to all potential step and staircase potential experiments by application of an external analog signal to the rotation rate input of the RDE-1 device.

2.3.1.3 Electrode Rotation and the Levich Equation

Rotation of a planar electrode with constant angular velocity ω in rad s^{-1} results in the well-defined transport of electroactive species to the electrode surface [117] by forced diffusion. The current response has been derived according to Fick's first law and expressed in terms of the Nernst diffusion layer concept [118] as in Eq. 2.2

$$| i | = nFD \frac{c_b - c_s}{\delta} \tag{2.2}$$

where n is the number of electrons transferred in the reaction, F is the Faraday constant (96485 C mol^{-1}), D is the diffusion coefficient of the electroactive species, c_b and c_s are the bulk and surface concentrations of electroactive species respectively, and δ is the thickness of the Nernst diffusion layer. The sign of the current density is negative for a reduction reaction and positive for an oxidation reaction.

A limiting current, i_L, is reached when the surface concentration becomes effectively zero. Thus, substitution of $c_s = 0$ into Eq. 2.2 gives the relationship for limiting current density

$$i_L = \frac{nFDc_b}{\delta} \quad (2.3)$$

Equation 2.3 is qualitatively correct but neglects the hydrodynamics of the process, namely, the electrode rotation rate. Under laminar flow conditions and in a liquid medium of kinematic viscosity ν, the thickness of the diffusion layer decreases with increasing electrode angular velocity [95] according to the quantitative treatment described by Levich [119] and given in Eq. 2.4,

$$\delta = 1.61 D^{1/3} \omega^{-1/2} \nu^{1/6} \quad (2.4)$$

Combination of Eqs. 2.3 and 2.4 gives the well-known Levich equation [120] for the hydrodynamic process at rotating disc electrodes

$$i_L = 0.620 nFD^{2/3} \omega^{1/2} \nu^{-1/6} c_b \quad (2.5)$$

According to Eq. 2.5, the limiting current is proportional to the square root of the angular velocity.

Overall, the rotating disc electrode provides an efficient means for establishing reproducible mass transport, and hence analytical measurements may be made with high sensitivity and precision [121]. Provided the steady-state limiting current is controlled purely by diffusional mass transport, a plot of i_L vs. $\omega^{1/2}$ as a function of c_b should be linear and pass through the origin. If this is the case, then the diffusion coefficient of the electroactive species can be then evaluated from the slope of the linear plot according to Eq. 2.5.

2.3.2 Microelectrodes

A platinum microelectrode (ME) with diameter 10 μm (Bioanalytical System Inc., West Lafayette, Indiana, USA) was employed as a WE in the experiments of varying buffer concentrations and pH. The electrode was polished prior to each experiment with 1.0 μm diamond and 0.01 μm alumina powder (PK-4 polishing kit, Bioanalytical System Inc., Indiana, USA), and then washed with methanol to remove the traces of suspended particles and glycol in the slurries and dried in air. When dried, the WE was thoroughly washed with de-ionized water and sonicated in water for 1 min to assure the cleanliness of the electrode surface.

The electrochemical pre-treatment procedure described above for the RDE was also employed for the microelectrode. The CE and RE employed in the RDE experiments were also used in the microelectrode experiments.

Microelectrode systems have been used to minimize artefacts associated with ohmic potential drop. Due to the small working area of the ME, it generates extremely small currents and, thus, *iR* potential drop is minimized. Another feature of ME usage is that the double-layer capacitance is also reduced [122].

The current response at a ME as a consequence of diffusional mass transport limited reactions leads to an increase in the sensitivity of electroanalytical measurements. This is because the faradaic current density increases as a result of hemispherical diffusion of electroactive species to the electrode surface of small dimensions. Since the diffusion layer thickness is many multiples of the electrode diameter, many contributors to the residual current are proportional to the electrode area [123].

During this work, the microelectrode was employed to study the influence of phosphate buffer concentration and pH (Chapter 7) as well as the inhibitory effect of chloride ions (Chapter 8). The microelectrode was placed in a 60 cm^3 cell inside a Faraday cage (Cell Stand-C2) (Bioanalytical System Inc., Indiana, USA), to minimize noise from external electrical interferences that may distort the current-potential wave. The microelectrode was connected to a pre-amplifier (PA-1, Bioanalytical System Inc., Indiana, USA) to amplify the small currents, and controlled by the 100B/W electrochemical analyzer. All the electrochemical measurements of ME were performed with static electrodes in unstirred electrolytes at 20 °C.

2.3.3 Thin Layer Flow Cell

A platinum working electrode with geometric area of 0.1100 cm^2 was employed in the flow cell of the FIA system. For each experiment the WE was used directly without conditioning and was held at a constant potential of +600 mV vs Ag/AgCl.

However, in the experiments involving the chloride effect (Chapter 8), the electrode was polished with 1.0 μm diamond and 0.01 μm alumina to regenerate a bright and reproducible surface, since the electrode surface was tarnished and eroded with increasing concentration of chloride ions.

The cell compartment, and in particular the WE, was protected from any source of gas bubbles generating from the operation of the peristaltic pump of the FIA by connecting a de-bubbler immediately prior to the thin layer cell.

The stainless steel body of the thin layer cell was used as the CE and a gasket of 16 μm thickness was sandwiched between the CE and WE to fix the internal volume of the cell (2.9 μL) as shown in Fig. 2.1.

An Ag/AgCl electrode (3 M NaCl) with potential +197 mV vs SHE (Bioanalytical System Inc., Indiana, USA) was used as the RE, which was housed within the counter electrode block as shown in Fig. 2.1.

2.3.3.1 Measurement of Flow Rate

The electrochemical response for the oxidation of H_2O_2 in the thin layer flow cell was found to be influenced by the flow rate of electrolyte through the thin layer cell. The current was observed to increase with increasing the flow rate and was limited to some extent by the internal volume of the thin layer cell, diameter of the peristaltic tubes and the tightness of both sides of peristaltic pump rollers. The flow rate was routinely established after 30 min stabilization of peristaltic pumping of electrolyte through the flow cell before the commencement of each experiment. The flow rate determination was accomplished by collecting the eluted electrolyte in a small weighed beaker as a function of time using a stop watch. The ratio of weight to the density of eluted buffer solution, i.e. the volume of eluted buffer, divided by the elapsed time for collecting the eluted buffer gives the flow rate in unit of volume per unit time. The optimum flow rate with the 16 μm flow cell gasket was found to be 260 ± 10 μL min^{-1} and this was used in all experiments.

2.4 Reagents

All chemicals used were of the high purity and all electrolyte solutions were prepared in Millipore water (Nanopure II, Barnstead, Newton, Massachusetts, USA).

Hydrogen peroxide (30 % w/w) (Prolabo, France) was calibrated by titration against acidified solutions of $KMnO_4$ (Univar, Australia) which were prepared immediately prior to use and standardized against anhydrous disodium oxalate (Merck, Germany).

The electrolyte was degassed with stirring by purging with oxygen-free nitrogen gas for 15 min prior to all experiments. H_2O_2 was added to the electrolyte in successive small volume additions.

In the FIA experiments, the standard solutions of H_2O_2 were prepared by diluting with phosphate buffer of appropriate concentration. A phosphate buffer solution (Riedel-deHaèn, Germany) of 0.100 mol L^{-1} and pH of 7.28 was used as a carrier reagent and washing solution during these studies unless otherwise stated.

The electrochemical measurements in ME systems were made in 50 cm^3 of phosphate buffer solutions of various concentrations and pHs. The standardized concentrated H_2O_2 was diluted 10 times and added successively in 50 μL aliquot additions.

2.5 Determination of the pH of Phosphate Buffer Solutions

The pH of phosphate buffer solutions were measured using a high impedance pH-meter (Model 50, Denver Instrument Company, USA) calibrated in advance with standard buffer solutions at each specific temperature.

The pH-meter was fitted with a pH-Ag/AgCl (Denver Instrument Company, USA) combination glass membrane electrode, where the reference electrode compartment was filled with 4 M KCl saturated with AgCl.

The potential response of the glass electrode to pH is given by

$$E_{glass} = E^{\circ}_{glass} - \frac{2.303RT}{nF}\text{pH} \qquad (2.6)$$

where E_{glass} is the measured electrode potential and E°_{glass} is the standard potential of the glass electrode with respect to the internal Ag/AgCl reference electrode. The other symbols have their usual meanings.

A plot of E_{glass} versus pH should be linear with intercept equivalent to E°_{glass} and a slope given by

$$\text{slope} = -\frac{2.303RT}{nF} \qquad (2.7)$$

Equation 2.6 can thus be rewritten in the form

$$E_{glass} = \text{intercept} - \text{slope} \times \text{pH} \qquad (2.8)$$

In practice, however, the slope will vary slightly from that given by Eq. 2.7.

Consequently, standard buffers are used to calibrate E_{glass} and E°_{glass}.

The standard buffers with pH range from 3.0 to 11.0 were prepared [124] to enable construction of the calibration linear of best fit. The composition and the measured electrode potential of these standards at 20 °C and 25 °C are listed in Table 2.3, while Figs. 2.4 and 2.5 show the linear plots of electrode potential as a function of buffer pH. The experimental slopes of −58.573 and −59.120 mV decade^{-1} at 20 and 25 °C respectively are in good agreement with those given by Eq. 2.6 (−58.164 and −59.156 mV decade^{-1} respectively) indicating the good performance of the glass electrode/ reference electrode pair.

Therefore, the pH of a phosphate buffer solution can be evaluated by measuring the electrode potential and applying Eq. 2.8. This procedure was adopted to determination accurate pH of phosphate buffer solutions of varying compositions for a range of temperatures.

Table 2.4 lists the calculated pH using Eq. 2.8 for 0.100 mol L^{-1} phosphate buffer solutions as a function of temperature together with the experimental and theoretical slopes of the glass electrode. Figure 2.6, is a plot of the experimental and theoretical slopes over a range of temperatures, indicates that the linearity of experimental slopes plot deviates at temperatures above 25 °C and below 15 °C.

2.6 Preparation of Phosphate Buffer Solutions

The electrochemical measurements of all experiments covered in this thesis were made in 0.100 mol L^{-1} of phosphate buffer solution of pH 7.28 at controlled potentials and temperatures, except those involved in studying the effect of buffer concentration and pH which are given in Chapter 7.

2.6.1 Phosphate Buffer Solutions of Varying Concentrations

These buffers were prepared by maintaining the pH as close as possible to 7.28 to allow comparison with the studies of the 0.100 mol L^{-1} buffer, and to study the effect of total buffer concentration, $[PO_4^{3-}]_{tot}$, on the electrochemical oxidation of H_2O_2 in Chapter 7.

Table 2.5 lists the composition of these buffers with the glass electrode potential readings and the corresponding pH.

pH	Composition of Standard Buffer Solutions	E_{glass} / mV 20 °C	25 °C
3.0	50 ml of 0.1 mol L^{-1} ($KHC_8H_4O_4$) + 22.3 ml of 0.1 mol L^{-1} (HCl).	237.5	239.1
4.0	50 ml of 0.1 mol L^{-1} ($KHC_8H_4O_4$) + 0.1 ml of 0.1 mol L^{-1} (HCl).	175.4	181.0
5.0	50 ml of 0.1 mol L^{-1} ($KHC_8H_4O_4$) + 22.6 ml of 0.1 mol L^{-1} (NaOH).	119.9	121.6
6.0	50 ml of 0.1 mol L^{-1} (KH_2PO_4) + 5.6 ml of 0.1 mol L^{-1} (NaOH).	63.1	64.7
7.0	50 ml of 0.1 mol L^{-1} (KH_2PO_4) + 29.1 ml of 0.1 mol L^{-1} (NaOH).	2.7	2.6
8.0	50 ml of 0.1 mol L^{-1} (KH_2PO_4) + 46.7 ml of 0.1 mol L^{-1} (NaOH).	−54.5	−55.9
9.0	50 ml of 0.025 mol L^{-1} ($Na_2B_4O_7.10H_2O$) + 4.6 ml of 0.1 mol L^{-1} (HCl).	−114.2	−121.3
10.0	50 ml of 0.025 mol L^{-1} ($Na_2B_4O_7.10H_2O$) + 18.3 ml of 0.1 mol L^{-1} (NaOH).	−173.2	−174.6
11.0	50 ml of 0.05 mol L^{-1} (Na_2HPO_4) + 4.1 ml of 0.1 mol L^{-1} (NaOH).	−233.2	−229.4

Table 2.3 The composition of standard buffer solutions [124] over the pH range 3.0 to 11.0 together with the measured electrode potential at 20 °C and 25 °C.

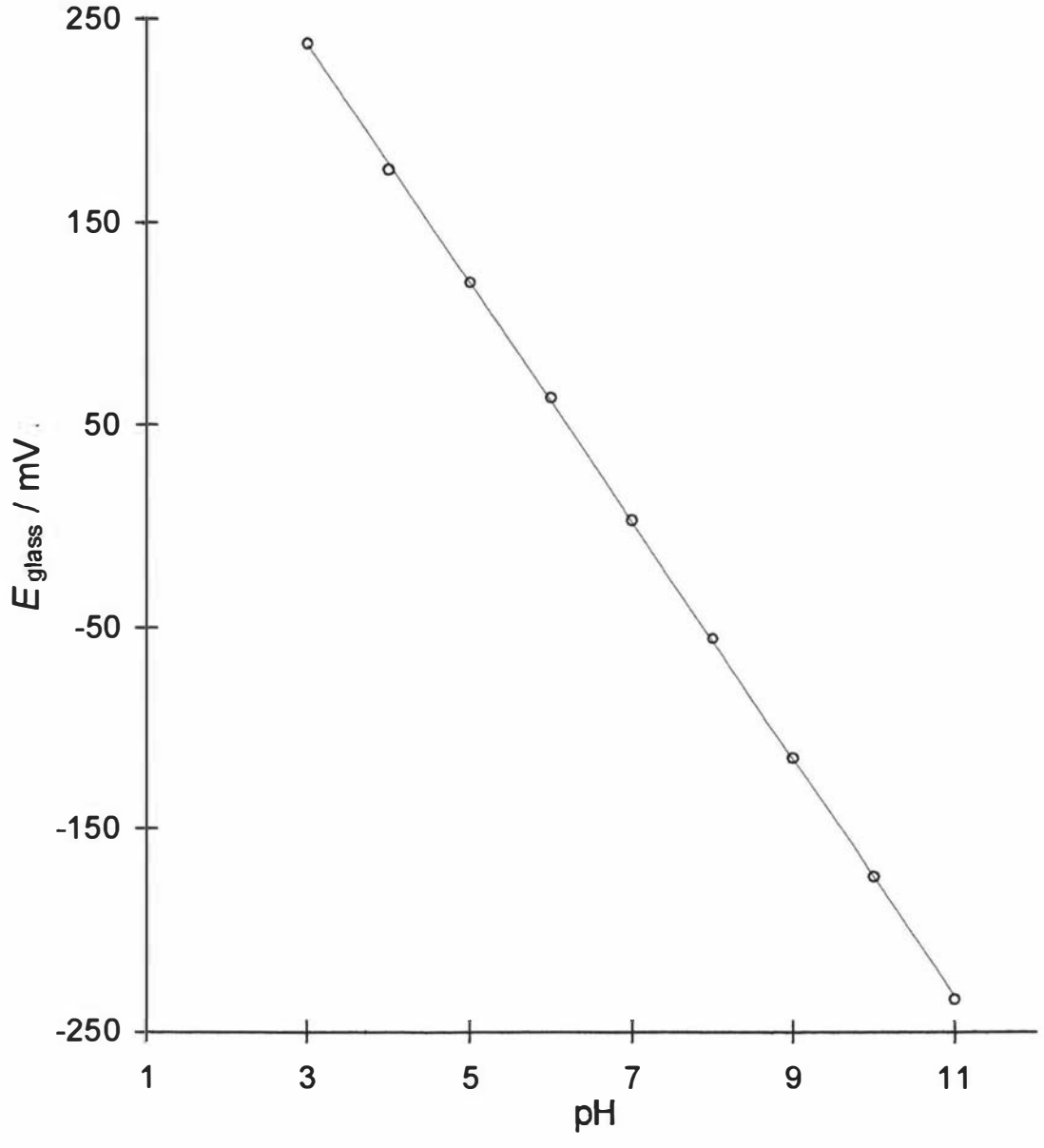

Fig. 2.4 Calibration line for the standard buffer solutions at 20 °C, data are listed in Table 2.3.

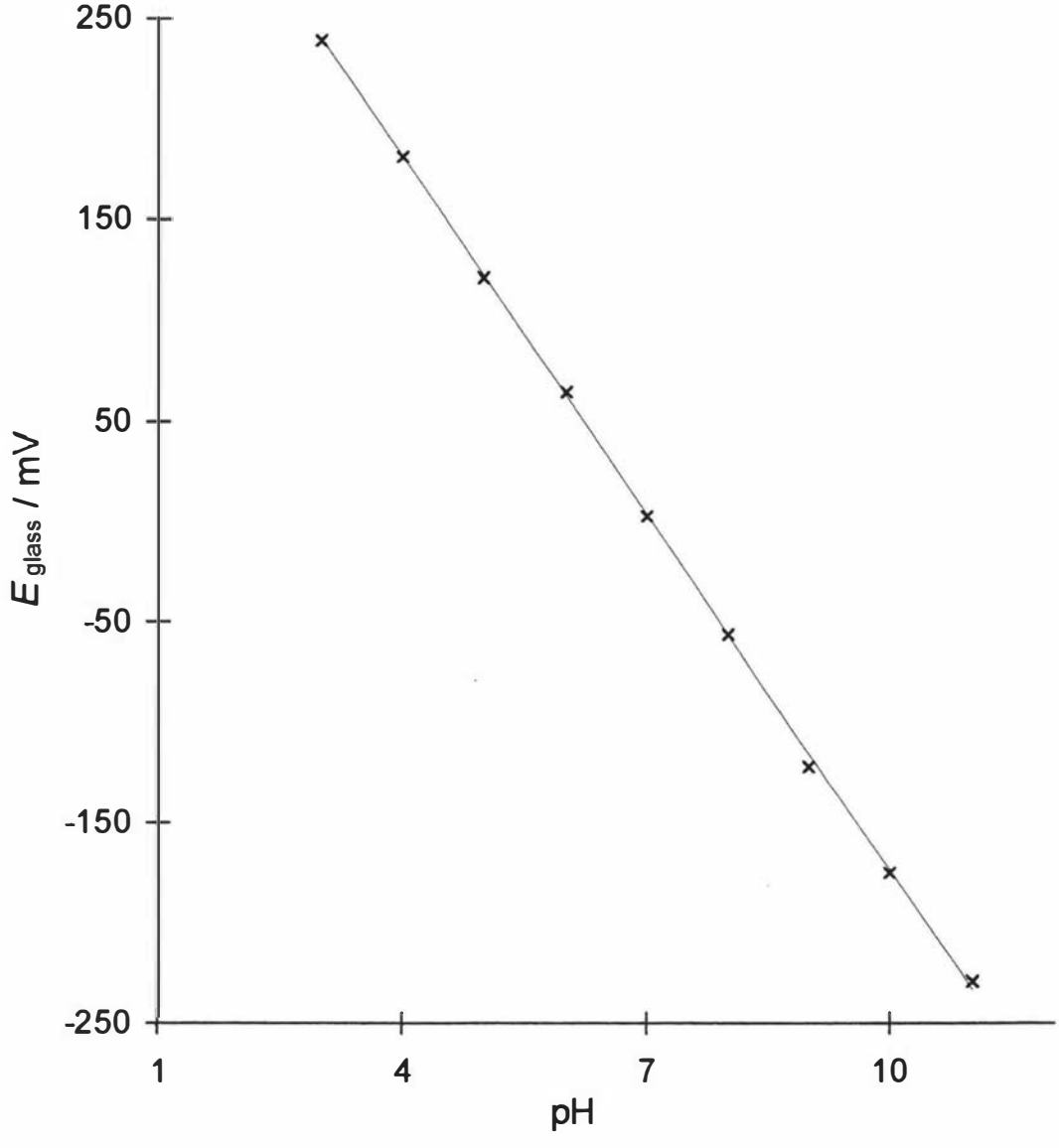

Fig. 2.5 Calibration line for the standard buffer solutions at 25 °C, data are listed in Table 2.3.

		Slope / mV decade^{-1}	
T / °C	pH	experimental	theoretical
5	7.242	−56.905	−55.188
10	7.254	−57.290	−56.180
15	7.269	−57.500	−57.172
20	7.282	−58.573	−58.164
25	7.287	−59.120	−59.156
30	7.294	−58.558	−60.148
35	7.301	−59.158	−61.140

Table 2.4 The pH of 0.100 mol L^{-1} phosphate buffer as a function of temperature together with the experimental and theoretical slopes.

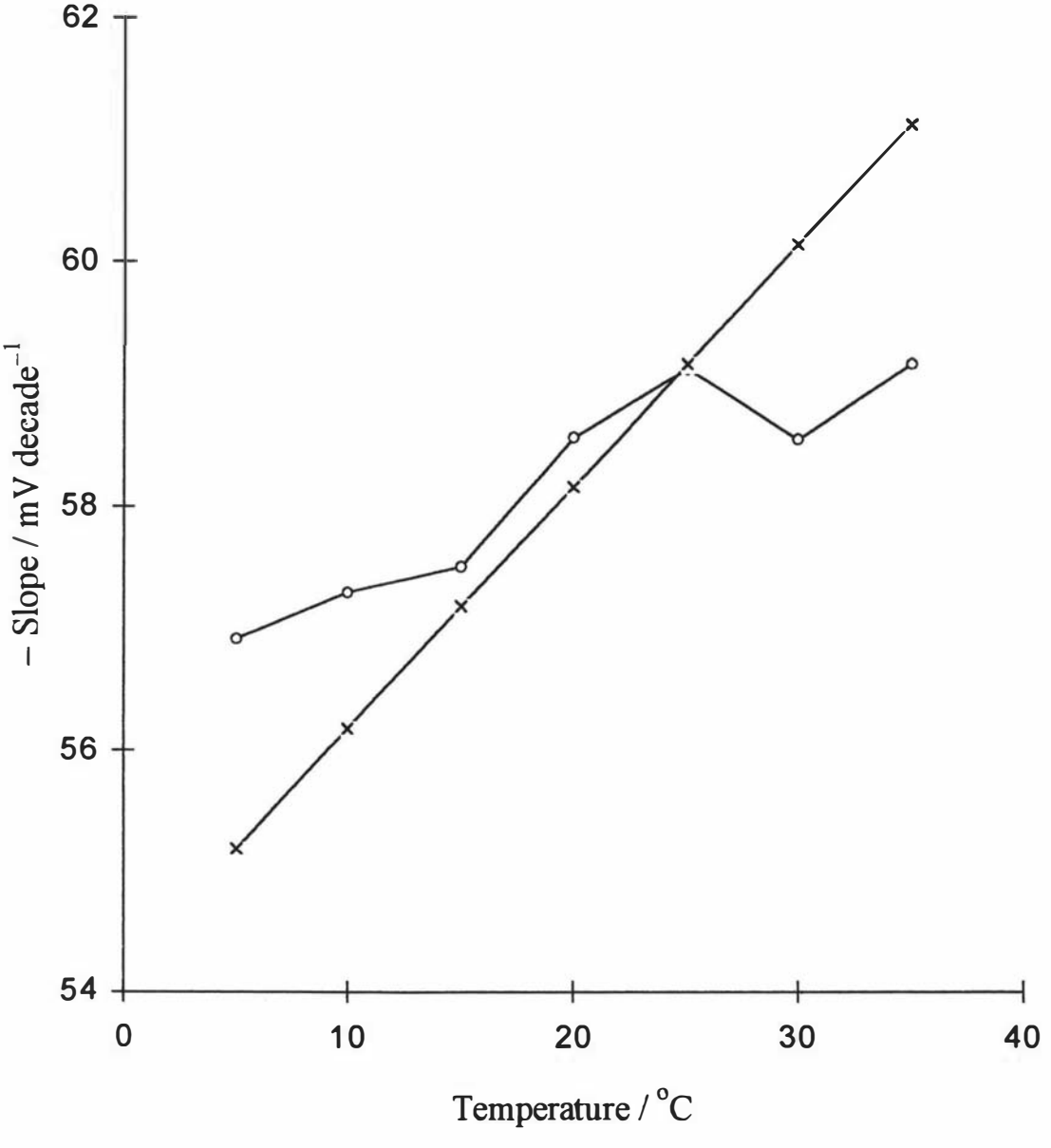

Fig. 2.6 Experimental (o) and theoretical (×) slopes for the glass electrode as a function of temperature as listed in Table 2.4. Theoretical slopes were calculated using Eq. 2.7.

$\frac{[PO_4^{3-}]_{tot}}{mol\ L^{-1}}$	$\frac{[KH_2PO_4]}{10^{-2}\ mol\ L^{-1}}$	$\frac{[K_2HPO_4]}{10^{-2}\ mol\ L^{-1}}$	$\frac{E_{glass}}{mV}$	pH
0.010	0.31	0.69	−17.7	7.347
0.025	0.80	1.70	−14.2	7.287
0.050	1.40	3.60	−16.2	7.321
0.075	2.10	5.40	−14.2	7.287
0.100	2.50	7.50	−13.9	7.282
0.125	3.40	9.10	−12.5	7.258
0.150	4.00	11.00	−12.3	7.255
0.175	4.70	12.80	−11.6	7.243
0.200	5.40	14.60	−10.6	7.226

Table 2.5 The composition of pH 7.3 phosphate buffer solutions for total phosphate concentration, $[PO_4^{3-}]_{tot}$, in the range, 0.010 to 0.200 mol L^{-1} with the glass electrode potential and calculated pH.

2.6.2 Phosphate Buffer Solutions of Varying pH

These buffers were prepared by maintaining the total phosphate concentration at 0.100 mol L^{-1} to study the effect of varying pH on the electrochemical oxidation of H_2O_2. Table 2.6 lists the composition of these buffers with the glass electrode potential and the accurate pH.

2.7 Viscosity and Density of Phosphate Buffer Solutions

The effect of temperature on the oxidation of H_2O_2 using phosphate buffer solution of 0.100 mol L^{-1} is described in Chapter 6. The diffusion coefficient for H_2O_2 is identified as an important factor in the overall reaction kinetic in Chapter 4. This parameter is affected by experimental temperature, since the viscosity of the working electrolyte also varies with temperature. Therefore, measuring the viscosity and density of phosphate buffer solution as a function of temperature was important in determining the diffusion coefficient for H_2O_2.

2.7.1 Viscosity Measurement

The viscosity of 0.100 mol L^{-1} phosphate buffer over the temperature range 5–35 °C in 5 °C intervals was determined using a calibrated Ostwald capillary viscometer (Cannon 50 I 317). The viscometer was placed in an insulated water bath with controlled temperature afforded by the combination of a circulating water bath controller (Colora, Messtechnik, GMBH, Germany) and a thermostated water pump (Thermomix 1440, Brann, Melsungen AG, Germany). The temperature of the insulated water bath was monitored with a calibrated thermocouple placed at the same depth as, and adjacent to, the viscometer capillary.

Table 2.7 lists the efflux time in seconds of both a 0.100 mol L^{-1} phosphate buffer solution and distilled water for a range of temperatures. The efflux times (200–400 s) were reproducible to better than ± 0.1 s.

The kinematic viscosity, ν_{buffer} (in m^2 s^{-1}), of phosphate buffer solution at each temperature was determined by the product of the literature values for the kinematic viscosity of water, ν_{water}, [125], and the ratio of efflux time for buffer, τ_{buffer}, and water, τ_{water}.

$[H_3PO_4]$ / mol L^{-1}	$[KH_2PO_4]$ / mol L^{-1}	$[K_2HPO_4]$ / mol L^{-1}	$[K_3PO_4]$ / mol L^{-1}	E_{glass} / mV	pH
0.020	0.08000	-	-	221.7	3.260
0.003	0.09700	-	-	174.1	4.072
-	0.09750	0.0025	-	103.0	5.286
-	0.08750	0.0125	-	62.4	5.979
-	0.02500	0.0750	-	−13.9	7.282
-	0.00400	0.0960	-	−65.7	8.166
-	0.09975		0.00025	−124.1	9.163
	0.04725	-	0.05275	−178.3	10.089
	0.03755	-	0.06245	−239.5	11.133

Table 2.6 The composition of 0.100 mol L^{-1} phosphate buffer solutions of different pH together with measured potential and calculated pH at 20 °C.

T / °C	Efflux time / s		η_{water} / 10^{-3} kg m^{-1}s^{-1}	ν_{buffer} / 10^{-6} m^2 s^{-1}
	Water	Buffer		
5	416.88	424.18	1.5190	1.5456
10	358.63	366.74	1.3070	1.3369
15	307.96	315.04	1.1390	1.1662
20	271.64	278.83	1.0020	1.0303
25	243.98	248.13	0.8904	0.9082
30	218.61	224.94	0.7975	0.8242
35	198.52	213.62	0.7194	0.7787

Table 2.7 Efflux time of both distilled water and 0.100 mol L^{-1} phosphate buffer solution as a function of temperature through an Ostwald capillary viscometer. The kinematic viscosity for the buffer was given by Eq. 2.9 in combination with the literature values for the absolute viscosity of water [125].

$$\nu_{buffer} = \frac{\tau_{buffer}}{\tau_{water}} \times \nu_{water} \quad (2.9)$$

2.7.2 Density Measurement

The densities of phosphate buffer solutions over the temperature range 5–35 °C in 5 °C intervals were determined using a 25 cm^3 density bottle (BS 733) immersed in a water bath (as in the previous section) to the level of the capillary stopper. After thermal equilibration (about 10 min), the bottle was removed and rapidly dried prior to weighing to 0.1 mg using a digital balance (Mettler, AE100).

Three replicate measurements were made for each of water and buffer and were reproducible in all cases to better than ± 1 mg. The average mass of the water and buffer are listed in Table 2.8 as a function of the experimental temperature.

The density of the buffer ρ_{buffer} at each temperature was given by the product of the literature value [125] for the density of water ρ_{water} and the ratio of the average mass of buffer, $\overline{m}_{buffer}$, to that for water, $\overline{m}_{water}$,

$$\rho_{buffer} = \frac{\overline{m}_{buffer}}{\overline{m}_{water}} \times \rho_{water} \quad (2.10)$$

2.8 Evaluation of Electrode Surface Roughness

The metal-solution interface is a region called the electric double-layer (dl) which arises when an electrode is immersed in an electrolyte solution. In this region the properties of the interface components are different to their bulk properties. One feature of the double-layer is the double-layer capacitance, C_{dl}, which is due to the allignment of counter-ions in solution parallel to the oppositely charged electrode surface. The double-layer capacitance may be determined by superimposition of a rapid triangular wave form upon a potentiostatically controlled potential.

The current response is a distorted square-wave which may be related to an equivalent circuit consisting of this capacitance and a resistor in parallel as shown in Fig. 2.7. The resistor being the faradaic resistance, R_f, which represents the barrier to charge transfer.

Thus, the current response is the combination of a double-layer capacitance, charging current, I_{dl}, and the faradaic resistance current, I_f.

The charging current is related to C_{dl} by

$\frac{T}{^{\circ}C}$	$\frac{\overline{m}_{water}}{g}$	$\frac{\overline{m}_{buffer}}{g}$	$\frac{\rho_{water}}{g\ ml^{-1}}$	$\frac{\rho_{buffer}}{g\ ml^{-1}}$
5	24.4794	24.8071	0.99999	1.01338
10	24.4656	24.7900	0.99973	1.01299
15	24.4556	24.7710	0.99913	1.01202
20	24.4317	24.7529	0.99823	1.01135
25	24.4060	24.7218	0.99707	1.00997
30	24.3799	24.6864	0.99567	1.00819
35	24.3436	24.6507	0.99406	1.00660

Table 2.8 The average weight for 25 cm^3 of both distilled water, $\overline{m}_{water}$, and 0.100 mol L^{-1} phosphate buffer, $\overline{m}_{buffer}$, as a function of temperature together with buffer density, ρ_{buffer}, calculated using Eq. 2.10 and litrature values for water density, ρ_{water}, [125].

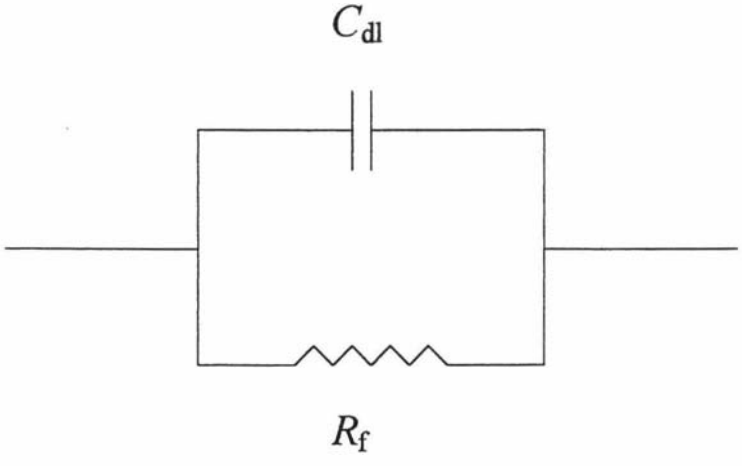

Fig. 2.7 The electrode-solution interface treated as capicitor and resistor in parallel.

$$I_{dl} = C_{dl} \frac{dE}{dt} \tag{2.11}$$

where dE/dt is the potential scan rate in V s^{-1} for the triangle wave

The faradaic resistance at any point in the distorted square-wave is given by

$$R_f = \frac{\Delta E}{\Delta I_f} \tag{2.12}$$

where ΔE is the potential excursion of the triangular wave form in volts, and ΔI_f is the corresponding change in I_f given in C s^{-1}. The form of the response is shown in Fig. 2.8.

The current density, i, typically reported in mA cm^{-2} throughout this thesis, is given by the observed current, I, divided by the geometric area, A, according to

$$i = \frac{I}{A} \tag{2.13}$$

The true area of the electrode surface, A_o, is affected by the microscopic roughening during polishing and electrochemical activity of the electrode. The surface roughness, γ, is the ratio of geometric and true surface area and is given by

$$\gamma = \frac{A_o}{A} \tag{2.14}$$

The true surface area can be estimated by assuming that platinum has double layer capacitance similar to that for the 'perfect' surface formed by liquid mercury. For mercury, C_{dl} is found to be 20 μF cm^{-2} [126]. Consequently, the true surface area can be given by

$$A_o = \frac{C_{dl}}{20\ \mu F\ cm^{-2}} \tag{2.15}$$

and the surface roughness can be calculated.

The surface roughness of platinum was evaluated by superimposition of a 5 mV peak to peak triangle wave at 300 Hz (Wave Function generator, Goldstar, FG-2002C, UK) at the open circuit potential (+240 mV vs Ag/AgCl at 25 °C) controlled by a BAS CV-27 potentiometer. The current response was captured using a computer based analogue to digital converter (MacLab V3.3 Program, Ad-Instrument, Australia).

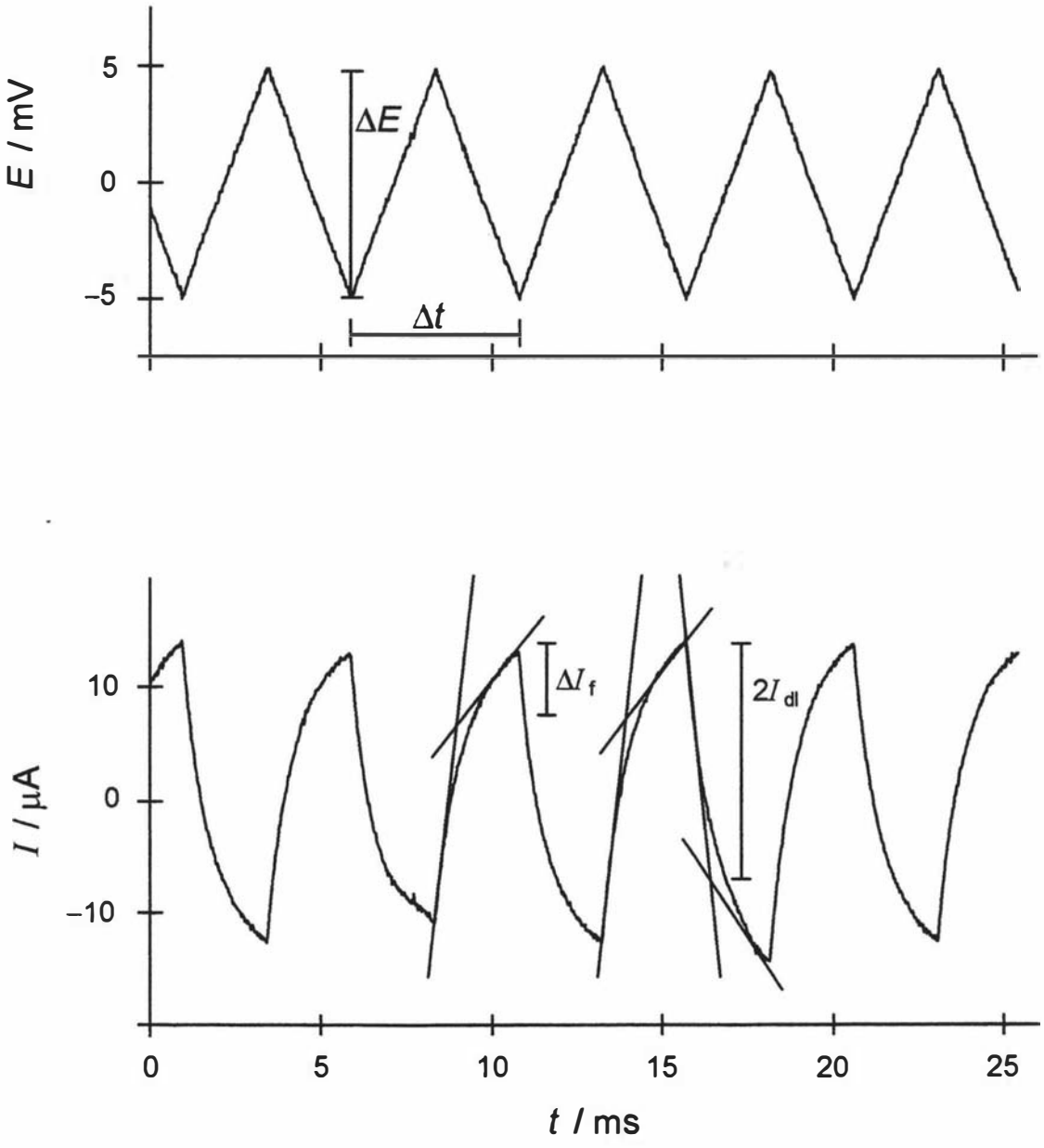

Fig. 2.8 The triangle potential waveform applied to a rotating disc electrode at $\omega = 0$ rad s^{-1} (upper plot) and the observed perturbed square wave current response (lower plot), employed to determine C_{dl} and R_f.

The resulting perturbed square waveforms were deconvoluted by line constructes as shown in Fig. 2.8. The average surface roughness for 50 measurements was found to be 2.25 with a standard deviation of 4 %.

2.9 Computer Software

A number of commercial software packages have already been identified in previous sections and relate to the operation of the BAS 100W/B potentiostat, FIA and the Maclab instrumentation. The other major commercial package used to a great extent in this project were Excel (version 5.0)† spreadsheets to visualise experimental results and compare these with optimized models. The cubic spline functions incorporated in the program Mathcad (Microsoft Inc., Massachusetts, USA) were used to interpolate activity coefficient and rate constant data in Chapter 6.

In addition to these commercial packages, a number of items of software were written for this project. For the most part, this software was developed by the project supervisor, S. B. Hall, using the programming language Turbo Pascal (Version 7.0)‡ on an IBM‡ PC-type computer. This software can be separated into two distinct classifications,

i) software written to manage, collate and transform the experimental data, and

ii) software developed to optimize the kinetic and thermodynamic parameters identified in the series of models.

2.9.1 Data Management and Collation

A series of software packages were developed to harvest appropriate data from the resulting files generated by the BAS 100B/W software package controlling the BAS 100B/W potentiostat. A summary of each is given below

(a) ESTEPAV: The last second of data for each of the CA experiments was averaged and used as the steady-state value in Chapter 4. This software opened each BAS 100B/W data file in turn, located the last second of the data (50 discrete points) and calculated the average and standard deviation current density. The resultant current density data was then arranged as a two-dimentional array,

† Excel is a registered trademark of Microsoft Corporation.
‡ Turbo Pascal is a registered trademark of Borland International Inc.
‡ IBM is a registered trademark of IBM Corporation.

seven columns (rotation rates) by 18 rows ($[H_2O_2]$), in an appropriate format as an input file for the optimization software ESTEPAV described in the following section.

(b) SCPAV: This software was an extension of ESTEPAV so that the results of SCP result files could be collated for each rotation rate, $[H_2O_2]$ and potential in Chapters 5 to 8. Two types of current density array files were generated by this software. The first involved one file for each potential step that listed current density as a function of rotation rate at each $[H_2O_2]$ (as did ESTEPAV). The second type produced a series of two-dimentional arrays for visualising in Excel spreadsheets.

2.9.2 Model Optimization

The primary optimization technique used in this research work was the SIMPLEX algorithm. This algorithm was developed by Box and Wilson [127] to permit the iterative optimization of numerous parameters such that a minimum is developed for the sum of differences squared between observed and experimental data. The goal-seeking of this technique was further refined by Spendley *et al.* [128] and Nedler and Mead [129]. The core of the code used in this study was written by A. Kucernak[†] in 1986 (whilst a postgraduate student at Auckland University). This code has been progressively modified over the last decade by S. B. Hall to enable the optimization of a diverse range of physicochemical systems including pharmaceutical formulations [130] and the binding of pyridyl ligands to zinc porphyrins [131].

The fundamental factors of this optimization can be illustrated by consideration of a relatively simple two variable system. Consider a series of experimentally derived data, y_{obs}, dependent on an experimental condition, x. Next, consider a model that attempts to provide a mathematical link between x and y_{obs} in terms of two fitting parameters m and c. In this example, a simple and familiar relationship is considered

$$y_{obs} = mx + c \tag{2.16}$$

where m and c represent the slope and intercept for a hypothetical linear relationship between x and y_{obs}. In this situation, optimum values for m and c may be calculated directly using the linear regression method. Instead an iterative method shall be

[†] Now lecturing at Imperial College, London.

considered here for location m and c to illustrate the approach if a direct method was not available. The iterative solution to this type of problem involves comparing a series of calculated responses, $y_{cal,i}$, for each value of x_i and comparing this with the observed result, $y_{obs,i}$, by calculating the sum of residuals, r_s, given by

$$r_s = \sum_{i=1}^{n} (y_{obs,i} - y_{cal,i})^2 \qquad (2.17)$$

The aim and conclusion of the iterative process is to minimize the sum of residuals by locating optimum m and c values. This optimization of two variables can be pictured as locating the lowest point on a three-dimensional surface as shown in Fig. 2.9.

Clearly, if a perfect fit were possible, as would be the case for the series of (x, y_{obs}) points: (0,1), (1,2), (2,3) etc., r_s would equal zero. In most real cases, however, $r_s > 0$.

The important feature of the SIMPLEX algorithm is how each successive choice for m and c is made efficiently. An example of a SIMPLEX optimization for the linear function given by Eq. 2.16 is shown in Fig. 2.10. Here a series of $y_{obs,i}$ data are used to determine m and c for the function

$$y_{obs,i} = 0.9\, x_i + 0.9 \qquad (2.18)$$

where x_i is an integral and equal to 0,1,2,....10. Clearly the optimum values for both m and c in this case are 0.9.

The optimization process is seeded with an estimate for each of m and c by the user. In this example these are labelled m_1 and c_1 and are both set at 0.10 (point 1) in Fig. 2.10. These are used to calculate the first sum of residuals, r_{s1}. The next attempt for each of m and c are at values of a set difference away from m_1 and c_1 and is labelled point 2 in Fig. 2.10 with coordinates m_2 and c_2. This first difference, or step, is also determined by the user. In the example shown in Fig. 2.10 the third point has as identical value for c whilst m is increased by a larger extent than the original step size. This larger increase in m was selected by the particular SIMPLEX algorithm used in this thesis based upon the relative change in the sum of residuals over the preceeding two attempts. In the fourth attempt the relative dependence is on the factor c which is tested together with further modifications to m. Note that the SIMPLEX will attempt to employ negative numbers. Consequently, in the kinetic studies presented in this thesis, the natural logarithm of the kinetic and thermodynamic parameters are optimized to prevent invalid results.

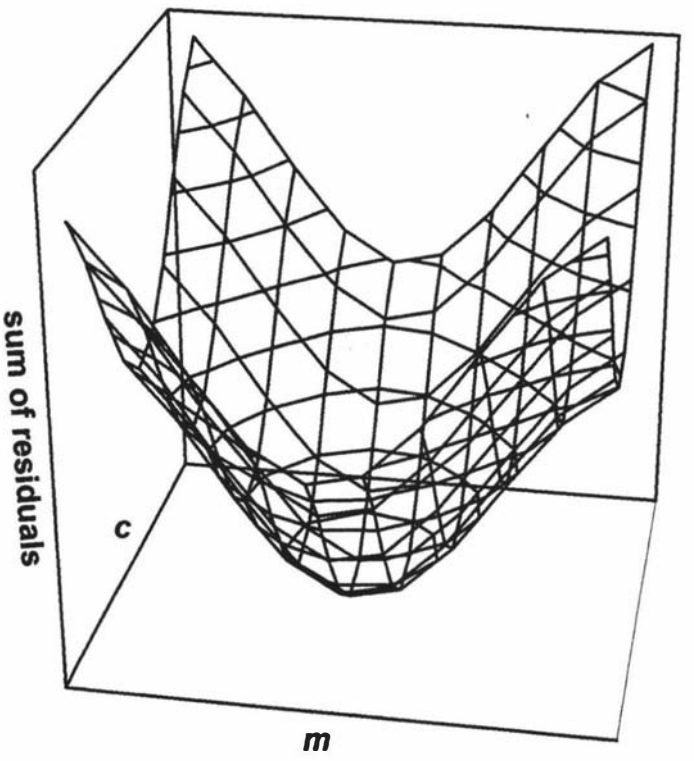

Fig 2.9 Schematic representation of the minima of the sum of residuals for the optimization of two variables *m* and *c*.

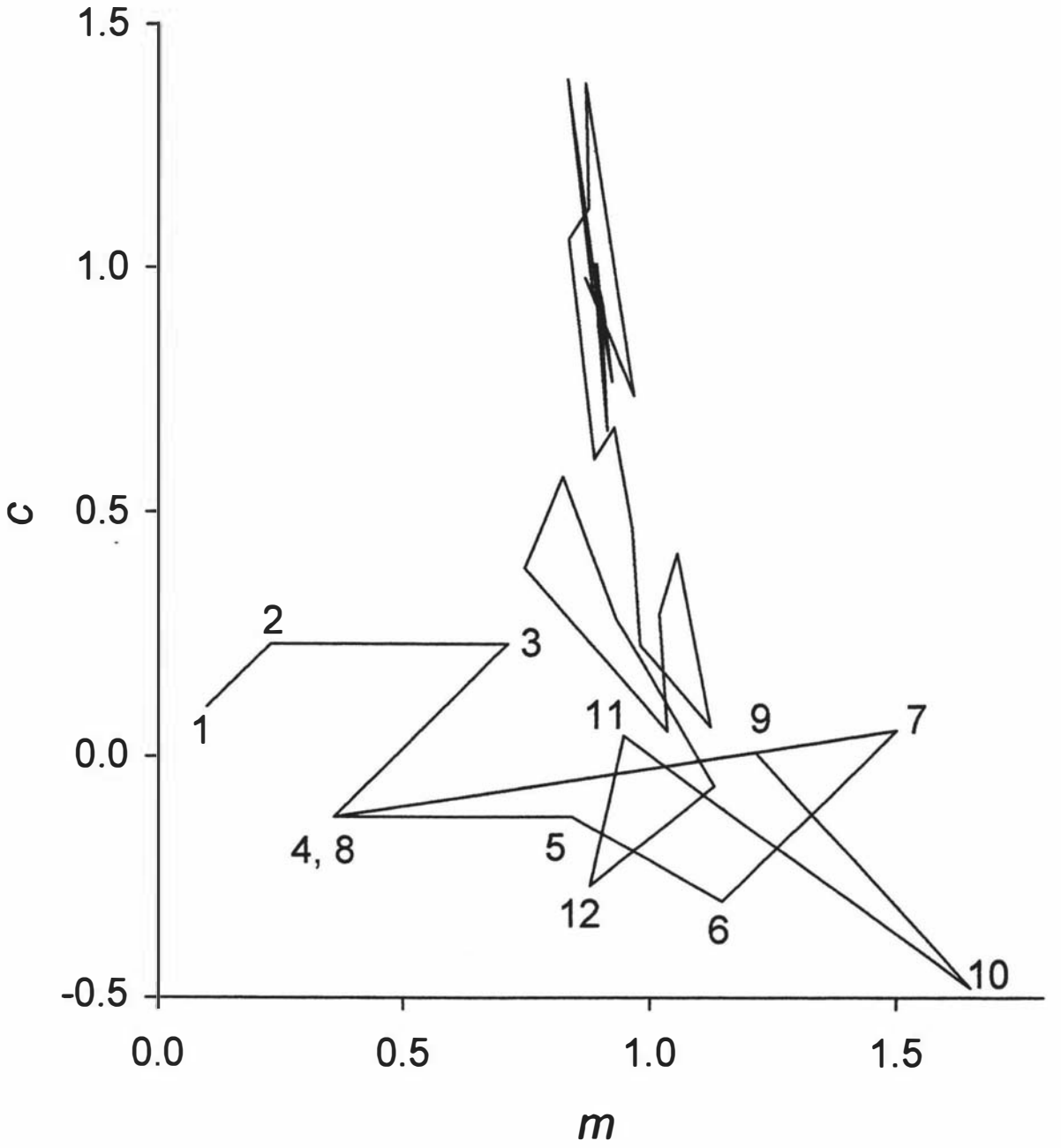

Fig. 2.10 Plot of successive attempts for m and c in the SIMPLEX optimization of Eq. 2.18 to give the optimum values $m = 0.9$ and $c = 0.9$. The first 12 attempts (of a total of 60) are indicated.

In the fifth attempt, m is increased again whilst holding c at the same value used in the fourth attempt. It is only after this fifth attempt that variation in both m and c is used between successive attemps.

The changes to each of m and c being made by the relative change in r_s with successive change to each variable. The logarithm plot of r_s as a function of iteration number is given in Fig. 2.11. This displays regular ratcheting in r_s with each successive iteration.

By the twelve attempt, the SIMPLEX has located the correct region for m whereas c is far from the ideal value of 0.9. This is as a consequence of Eq. 2.18 being intrinsically more sensitive to changes in slope than in the intercept. Further optimization locates the correct region for c and refines m. The optimization is terminated either once a set value for r_s is attained or when there is no significant change in r_s with successive steps. This is evident in Fig. 2.11 where r_s decreases to 4.0×10^{-13} and represents both m and c having been found to 7 significant figures.

Care must be taken to avoid inadvertant entrapment in a local minimum in r_s rather than the true minimum. This is usually avoided by confirming that for a series of optimization attempts using widely different initial values for m and c, the same optimum result is achieved.

In the models presented in this work the vector representation of the SIMPLEX process is far more complicated since in the initial model presented in Chapter 4 five fitting parameters are identified, for a rate function involving two main experimental conditions. With such a complicated system, it is impossible to draw schematic diagrams in the six dimensions required. Nevertheless, it is shown in this work that SIMPLEX is an extremely valuable tool for parameter optimization and without, which, the major interpretative outcomes would not have been achieved.

The SIMPLEX code formed the core of the three optimization programs developed for this work:

(a) ESTEP is used to describe the rotation rate and $[H_2O_2]$ dependence in Chapter 4,

(b) EVARY is used to describe the rotation rate, $[H_2O_2]$ and potential dependence in Chapter 5, and

(c) TVARY incorporates EVARY into a routine that describes the rotation rate, $[H_2O_2]$, potential and temperature dependence.

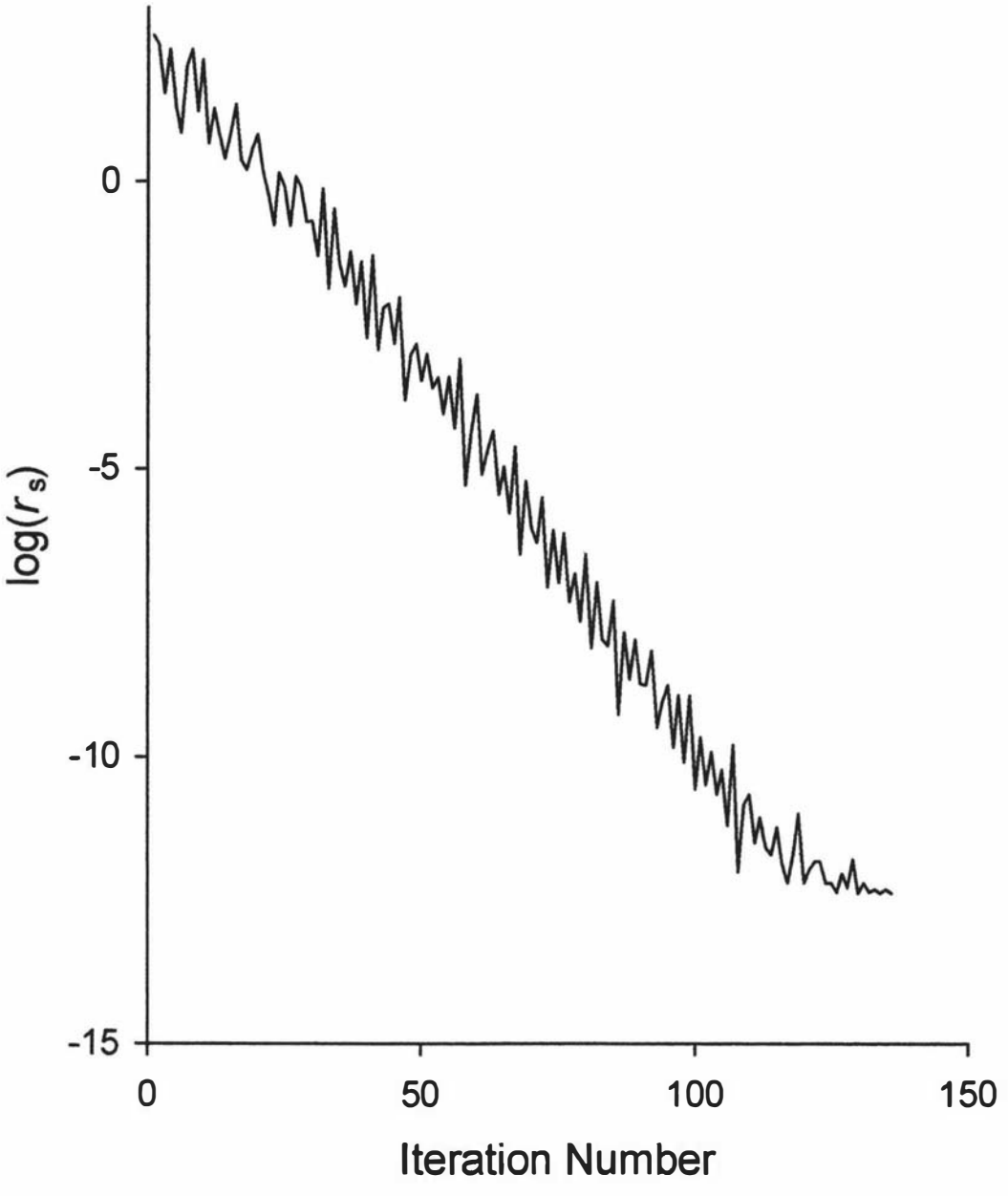

Fig. 2.11 A logarthmic plot of the sum of residuals as a function of iteration number for the SIMPLEX optimization of m and c in the function given by Eq. 2.18.

CHAPTER THREE

Overview of the Electrochemistry of Hydrogen Peroxide

3.1 Introduction

This chapter introduces the methodology that was used to study the electrochemistry of H_2O_2 at platinum electrodes.

Where appropriate, the theory underlying these methods is used to highlight various parameters associated with the models developed in this work. These include; current response as a function of time in potential step methods; potential scan rate in cyclic voltammetry; kinetics of electron transfer; mass transport of species to and from electrode surfaces; and rotation rate in rotating disc electrodes experiments.

An overview of the electrochemistry of H_2O_2 on Pt in phosphate media is also given.

3.2 Application of Electrochemical Techniques

3.2.1 Cyclic Voltammetry

Cyclic voltammetry (CV) is a potential-controlled technique where the potential is scanned linearly across the electrode-solution interface from an initial value E_i to a final value E_f at constant rate (mV s^{-1}). Having reached E_f the scan is reversed to complete a potential cycle. This technique may involve a single cycle or be repeated numerous times. The current through the WE is reported as a function of applied potential and the plot is frequently termed a voltammogram.

These voltammograms can provide both qualitative and quantitative information about electrode reactions [132].

3.2.1.1 Identification of the Oxidation Region for H_2O_2

The voltammogram in Fig. 3.1 shows the current-potential wave for 0.100 mol L^{-1} phosphate buffer solution at pH 7.28 in the absence (A) and in the presence of 2 mM H_2O_2 (B). It can be seen that whereas no significant redox wave was observed in (A), a well defined oxidation wave for H_2O_2 (B) commences at +250 mV and reaches a maximum at +600 mV vs Ag/AgCl.

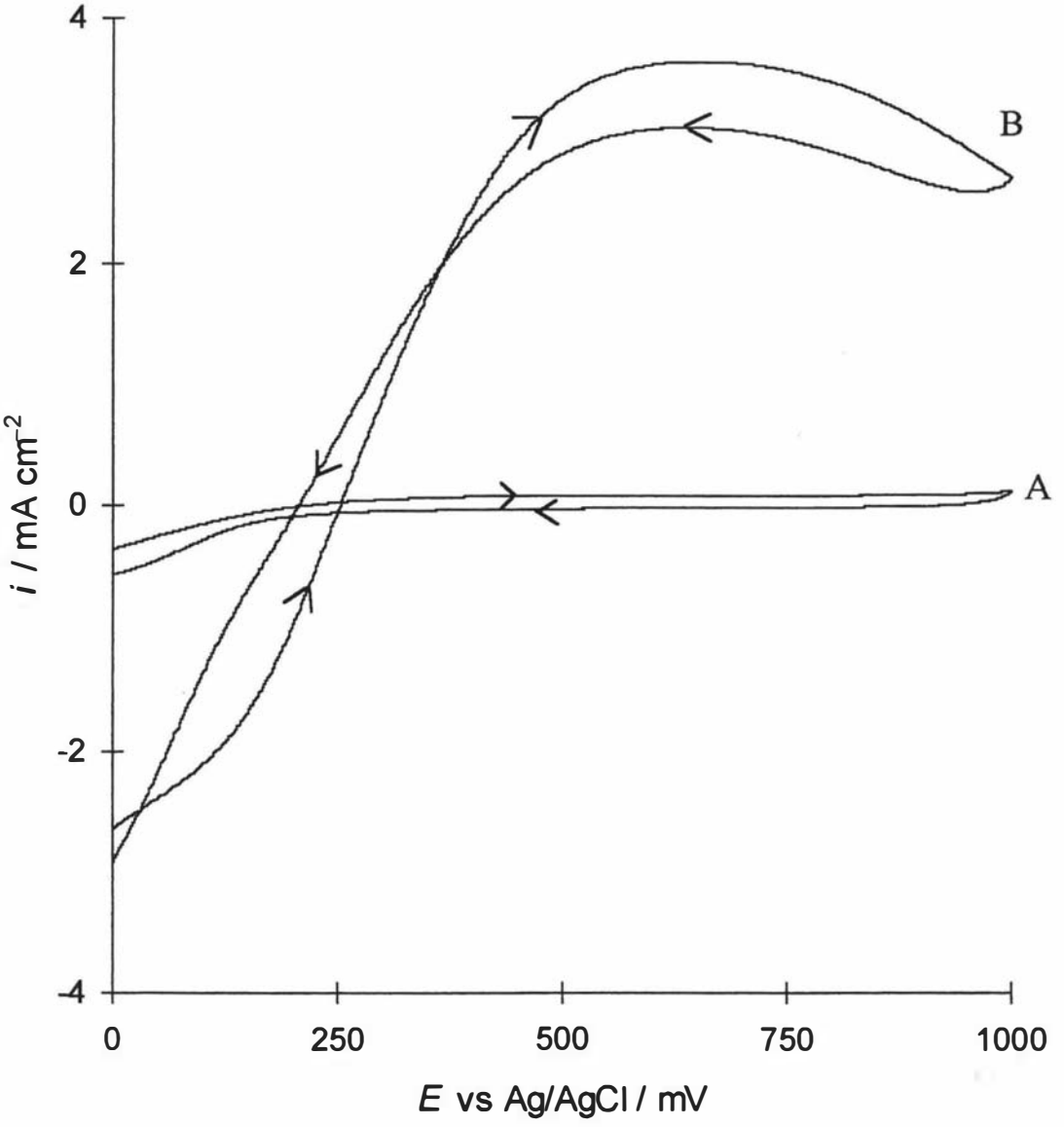

Fig. 3.1 The current-potential voltammogram of 0.100 mol L^{-1} phosphate buffer solution in the absence (A) and presence of 2 mM H_2O_2 (B) at a scan rate of 100 mV s^{-1} at 20 °C to identify the oxidation region for H_2O_2.

The technique was used during this study for identification of the appropriate potential regime to be adopted (beside those reported in the literature) for the oxidation of H_2O_2, and for the electrode pre-treatments to initiate the oxide film on the platinum electrode surface.

3.2.1.2 Repetitive Cycling

The electrode reproducibility was studied by maintaining the potential scan for ten cycles. Figure 3.2 shows of these, the first, fifth and tenth, cycles designated as 1, 5 and 10, respectively, for the oxidation of 10 mM H_2O_2 at a platinum rotating disc in 0.100 mol L^{-1} phosphate buffer solution cycled between –300 mV and +1400 mV vs Ag/AgCl. The system exhibits good reproducibility during these cycles and does not show any progressive change in the response.

During this study, repetitive cycles using CV experiments were carried out in phosphate buffer solution in the absence of H_2O_2 to establish the formation of a coherent oxide film on the platinum surface as stated in section 2.3.1.

3.2.1.3 Rotation Rate Dependence

Preliminary experiments to study the effect of electrolyte hydrodynamics were performed employing the CV technique. The voltammograms in Fig. 3.3 show the oxidation of 10 mM H_2O_2 in 0.100 mol L^{-1} phosphate buffer solution as a function of electrode rotation rates. The anodic current response (forward scans are only shown for clarity) increases with electrode rotation rate which can be attributed to the enhancement of mass transport of bulk H_2O_2 to the electrode surface with increasing rotation rate.

3.2.1.4 Concentration Dependence

The current-potential voltammogram for a range of $[H_2O_2]$ in a 0.100 mol L^{-1} phosphate buffer solution at 1000 rpm is shown in Fig. 3.4. Only the forward sweeps are shown for clarity. The anodic current response increases with $[H_2O_2]$ in the potential region between +750 and +1000 mV (while the oxidation potential at +600 mV, selected in Chapter 4 for mechanistic studies, the current response appeared to approach a limiting value at higher concentrations). In addition, the anodic wave shifts to more negative potentials with increasing $[H_2O_2]$.

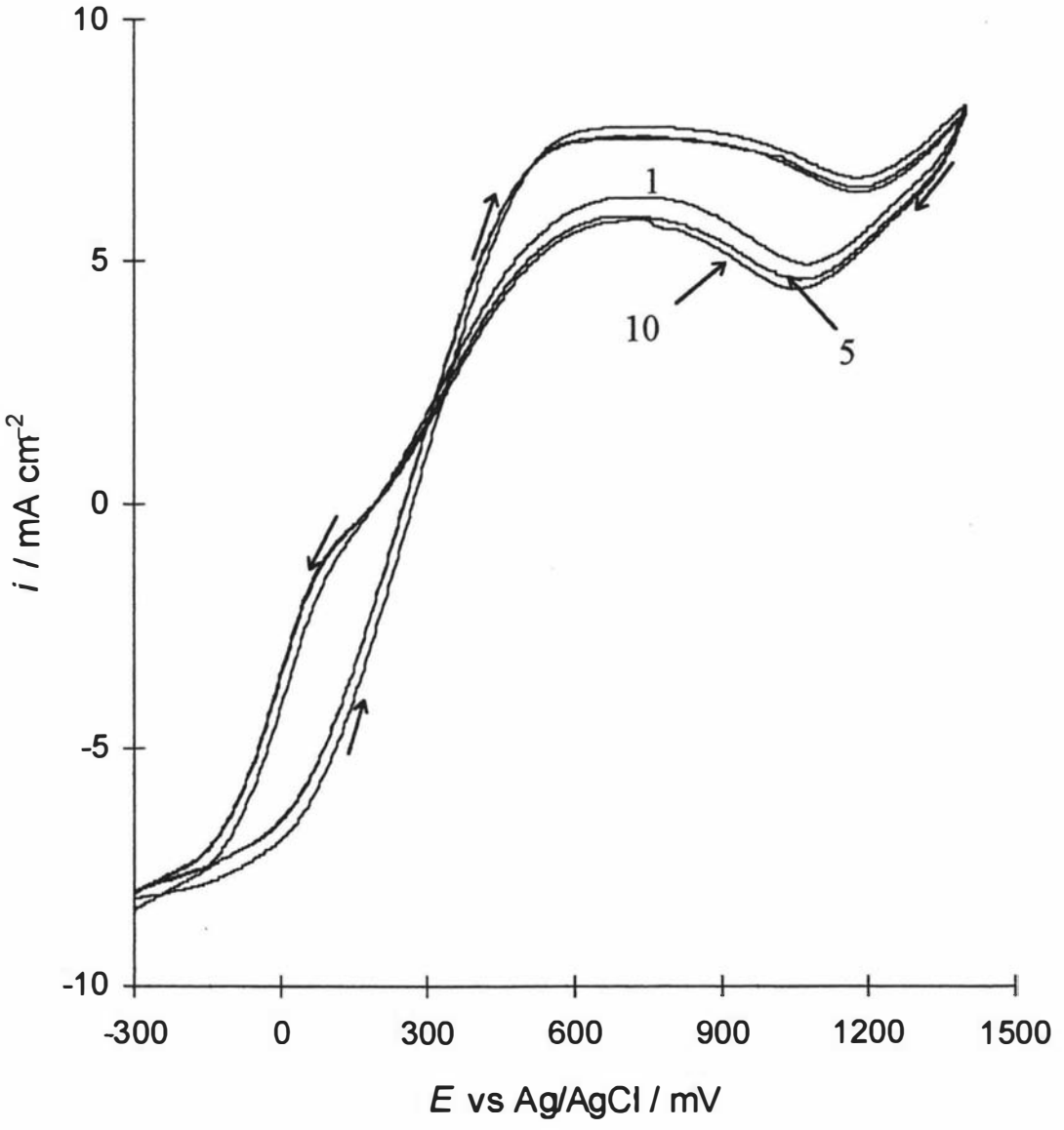

Fig 3.2 Voltammograms showing the first, fifth and tenth cycles for the oxidation of 2 mM H_2O_2 at a rotation rate of 1000 rpm and scan rate of 100 mV s^{-1} at 20 °C.

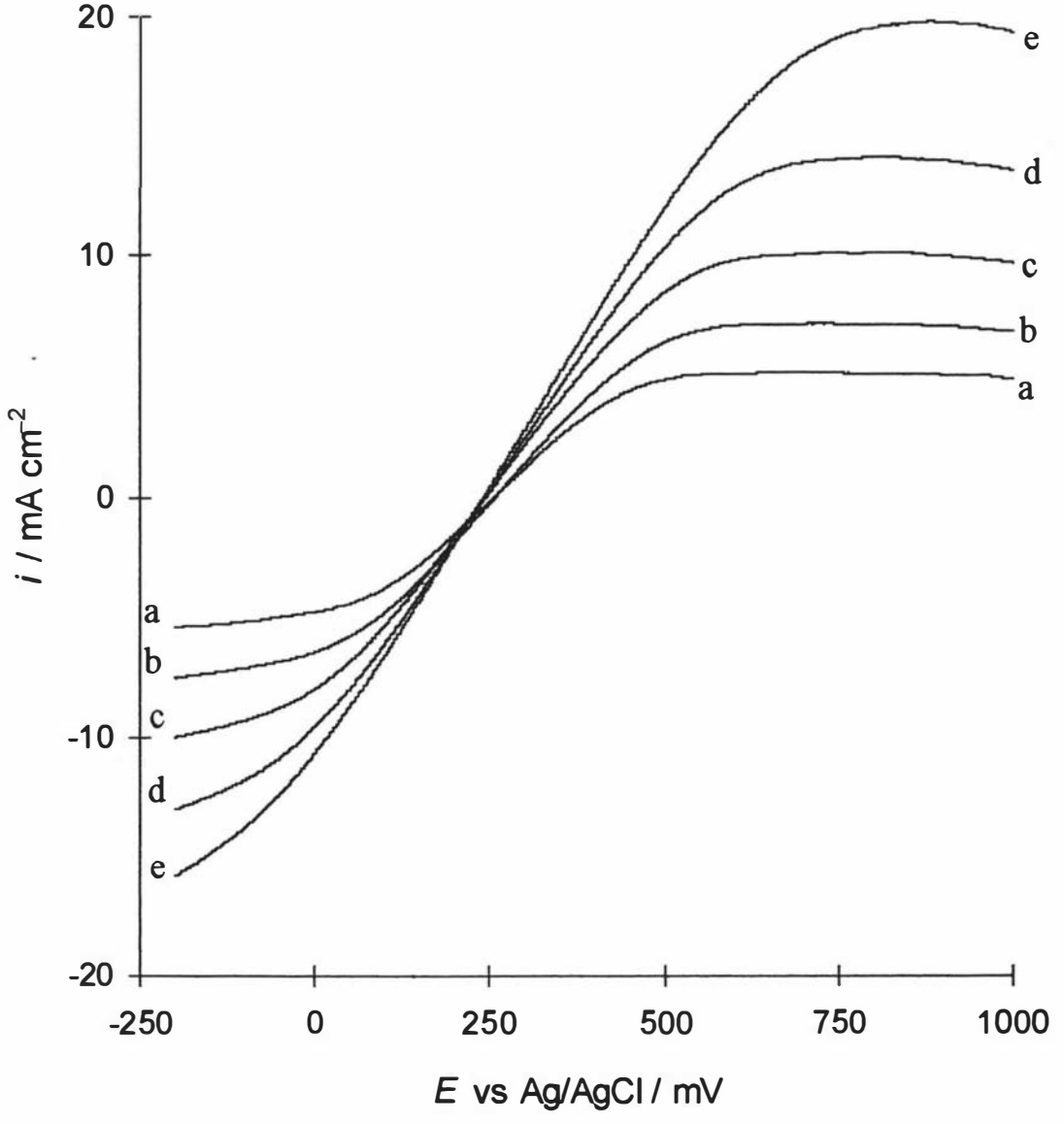

Fig. 3.3 Cyclic voltammogram of 10 mM H_2O_2 in 0.100 mol L^{-1} phosphate buffer solution with pH 7.28 at 20 °C with a scan rate of 100 mV s^{-1} as a function of rotation rate. Forward scans only are shown for clarity. Rotation rates from (a) to (e) are; 500, 1000, 2000, 4000 and 8000 rpm.

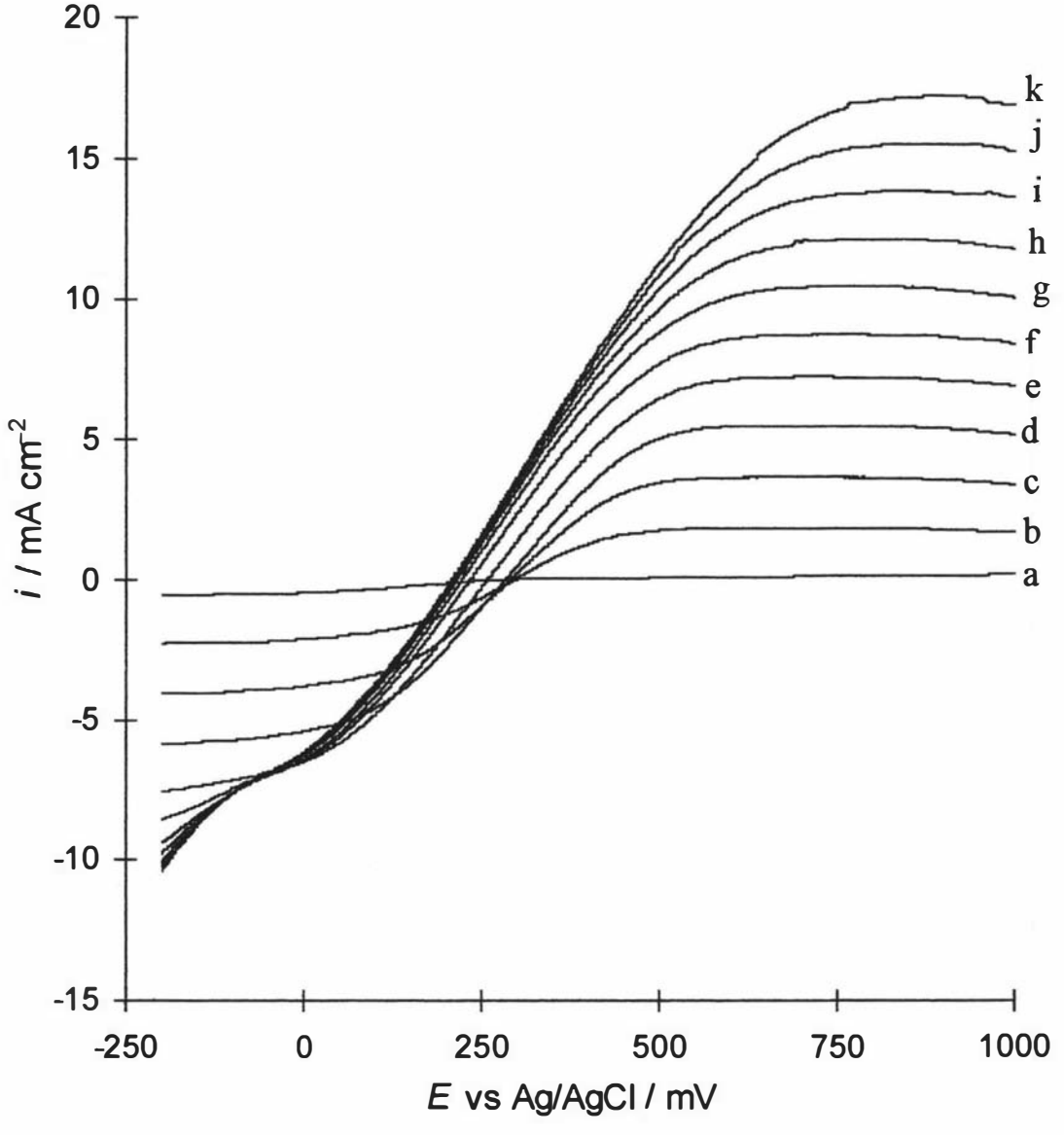

Fig. 3.4 Cyclic voltammogram for a range of $[H_2O_2]$ in 0.100 mol L^{-1} phosphate buffer solution with pH 7.28 at 20 °C. The scan rate is 100 mV s^{-1} and rotation rate is 1000 rpm. $[H_2O_2]$ from (a) to (k) as; 0, 2.5, 5.0, 7.5, 10.0, 12.5, 15.0, 17.5, 20.0, 22.5 and 25.0 mM.

3.2.2 Chronoamperometry

Chronoamperometry (CA) involves stepping the potential of the WE in a single step from a value at which no faradaic current occurs, E_1, to a potential, E_n, at which the current response for the oxidation of H_2O_2 can be recorded.

In this study the potential was stepped between +200 to +600 mV vs. Ag/AgCl at a rate of 100 mV s^{-1} and pulse width of 20 s, and the currents were recorded and averaged over the last 1 s.

The most important feature of this method is that the rate of oxidation attains a steady-state controlled by the diffusion of $[H_2O_2]$ to the electrode surface [27]. The rate of mass transport at a fixed point is termed the flux, j. This is defined as the number of molecules passing through a unit area of an imaginary plane (perpendicular to direction of movement) per unit of time, and has the units described by mol m^{-2} s^{-1}.

The current i is directly proportional to the flux according to

$$i = -nFj \tag{3.1}$$

where n is the number of electrons transferred in the reaction and F is the faraday constant (96485 C mol^{-1}).

According to Fick's first law, the rate of diffusion or the flux, is directly proportional to the concentration gradient,

$$j_{(x,t)} = -D\frac{\partial c_{(x,t)}}{\partial x} \tag{3.2}$$

D is the diffusion coefficient of electroactive species in m^2 s^{-1}, and $\partial c_{(x,t)} / \partial x$ is the concentration gradient at distance x from the electrode.

Combination of Eqs. 3.1 and 3.2 provides a general expression for the current response,

$$i = nFD\frac{\partial c_{(x,t)}}{\partial x} \tag{3.3}$$

Hence, the current at any time is proportional to the concentration gradient of the electroactive species.

As indicated by the above equations, the diffusional flux is time dependent, and such dependency is described by Fick's second law for linear diffusion

$$\frac{\partial c_{(x,t)}}{\partial t} = D\frac{\partial^2 c_{(x,t)}}{\partial t^2} \tag{3.4}$$

Accordingly, Fick's laws describe the flux and the concentration of electroactive species as a function of position and time.

When the mass transport is achieved by diffusion, the current-time curve reflects the change in concentration gradient in the vicinity of the electrode surface. This involves a gradual expansion of the diffusion layer associated with the depletion of reactant and hence decreased slope of the concentration profile as time progresses. Figure 3.5 is the chronoamperometric transients for a range of $[H_2O_2]$ at an electrode rotation rate of 2500 rpm. Here the current decays rapidly with time and adopts steady state conditions after ca. 15 s. In a similar fashion, the steady state current response of 7.88 mM $[H_2O_2]$ as a function of rotation rate is given in Fig. 3.6, in each case a steady state is rapidly adopted.

3.2.3 Stair-Case Potentiometry

Staircase potentiometry (SCP), first proposed by Barker [133], is a useful tool for the monitoring of faradaic current by applying successive potential steps of different heights for different times. The SCP used in this study involved constant step height (pulse amplitude) with constant depth (pulse width) and is shown schematically in Fig. 3.7.

The current is sampled for a short period of time at the end of each step (labelled I) and it is assumed that sufficient time has passed to attain steady-state conditions, with minimal non-faradaic charging current [134].

Thus, the results reported for an SCP experiment consist of a series discrete steady-state currents for a range of discrete potentials.

For this study, the potential was applied in a staircase waveform between +200 to +750 mV vs Ag/AgCl with a constant pulse amplitude of 32 mV and pulse width of 8 s, while the steady state current was recorded and averaged over the last 17 ms of each step. Figure 3.8 shows the steady-state responses for the oxidation of 2 mM H_2O_2 over a range of potentials and rotation rates employing SCP.

The electrode kinetics are affected greatly by applied potential, therefore, SCP was a useful technique to study the steady-state rate over a wide range of potential. Further details for these experiments are given in Chapter 5.

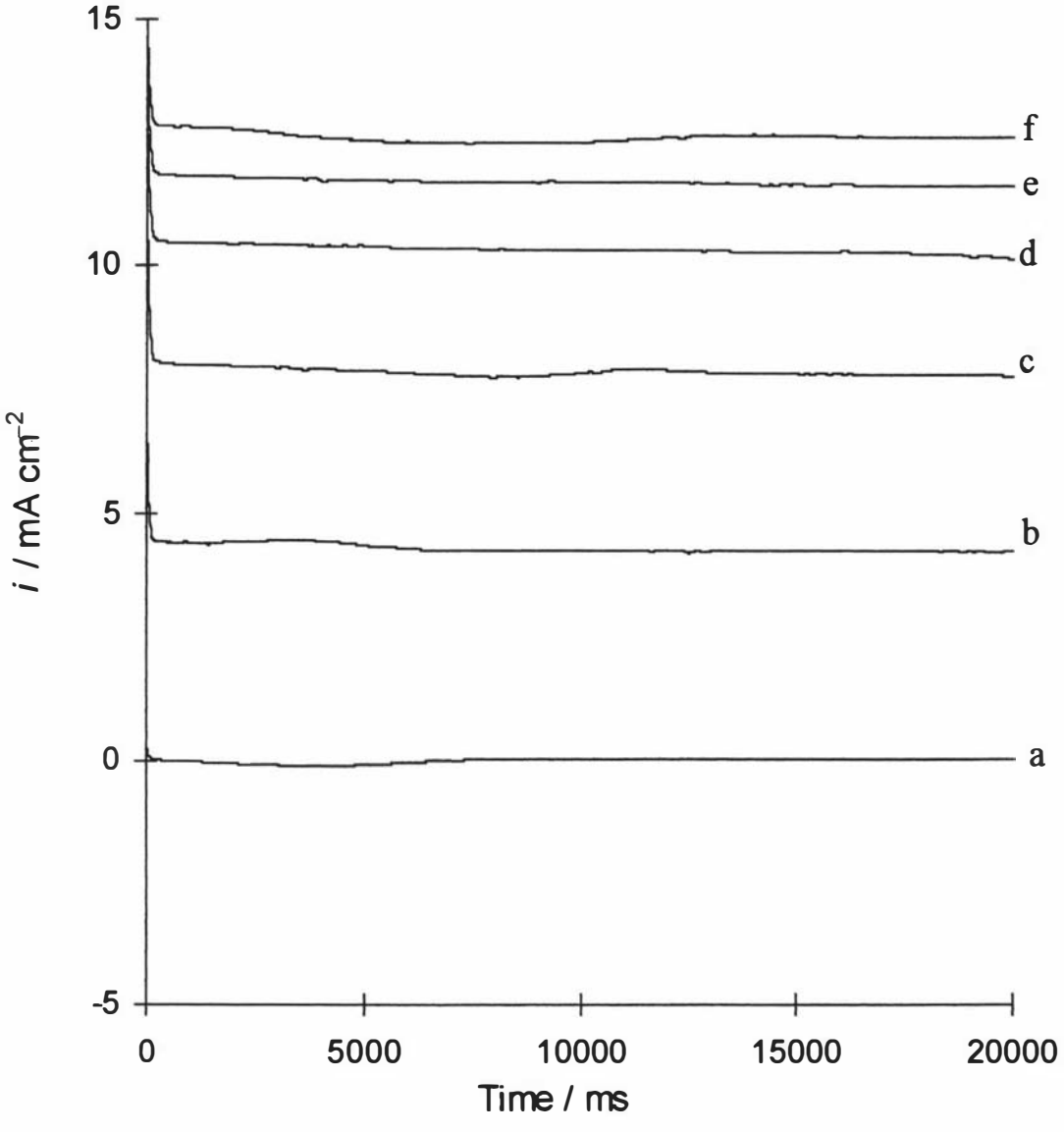

Fig. 3.5 Transient current response for potential steps between +200 to +600 mV vs. Ag/AgCl at 2500 rpm for the oxidation of H_2O_2 over a range of concentration. $[H_2O_2]$ from (a) to (f) are; zero, 3.94, 7.88, 11.82, 15.76 and 19.70 mM.

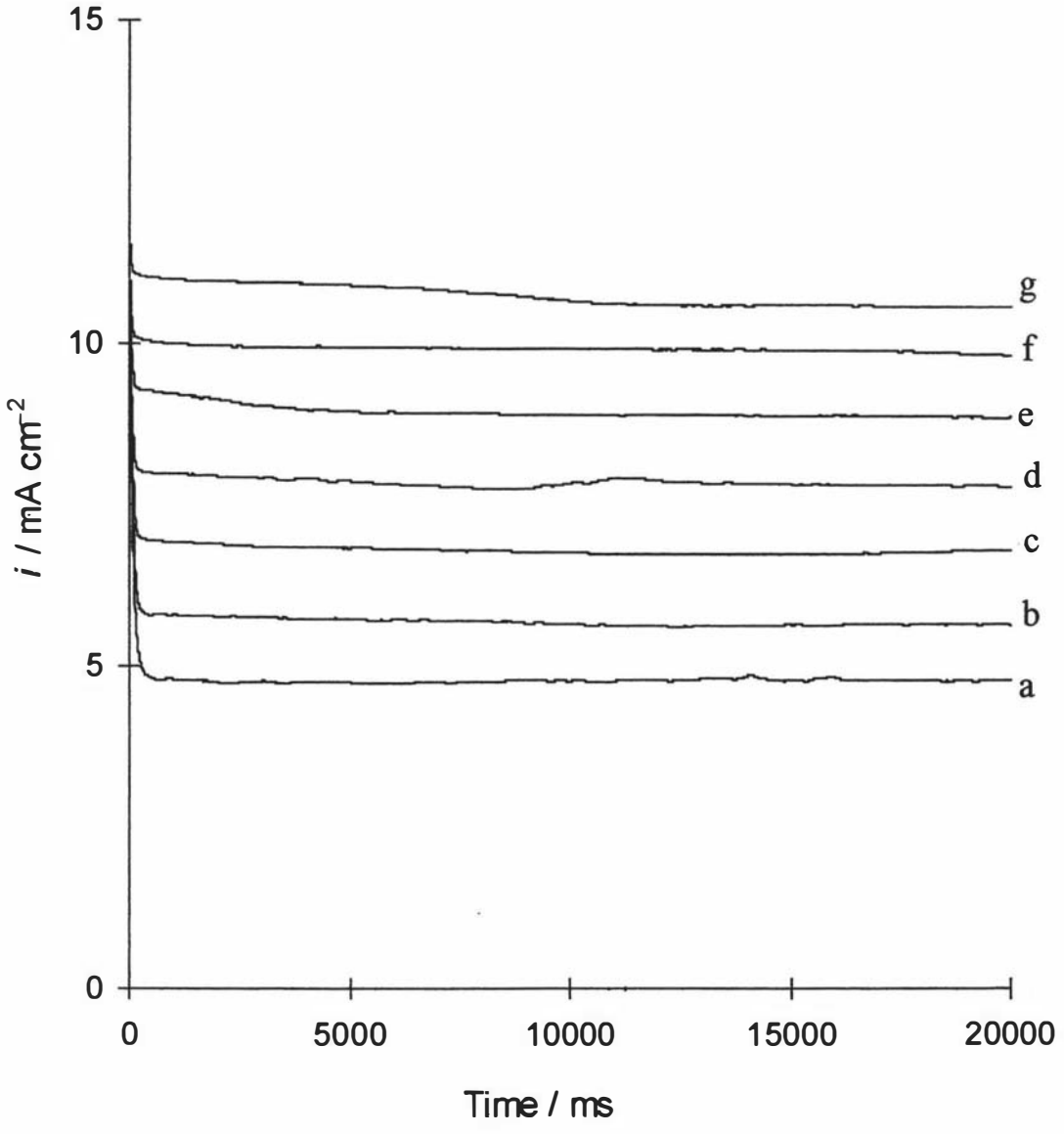

Fig. 3.6 Transient current for potential steps between +200 to +600 mV vs Ag/AgCl for the oxidation of 7.88 mM H_2O_2 as a function of rotation rates.
Rotation rates from (a) to (g) are; 630, 1000, 1585, 2500, 4000, 6300 and 10000 rpm.

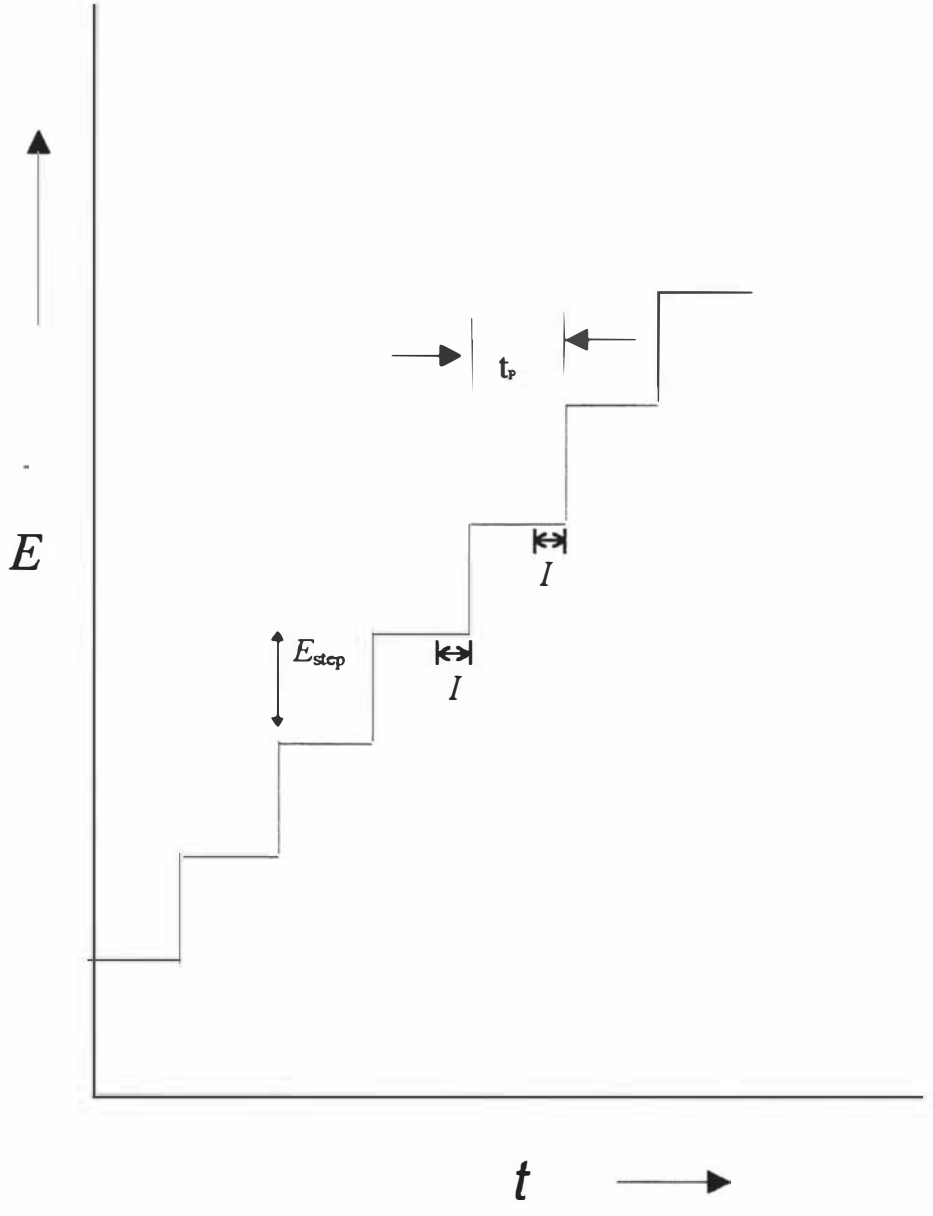

Fig. 3.7 The potential-time wave form of SCP indicating the pulse amplitude, E_{step}, and pulse width, t_p. The current is sampled and averaged over a short period of time at the end of each pulse indicated by *I*.

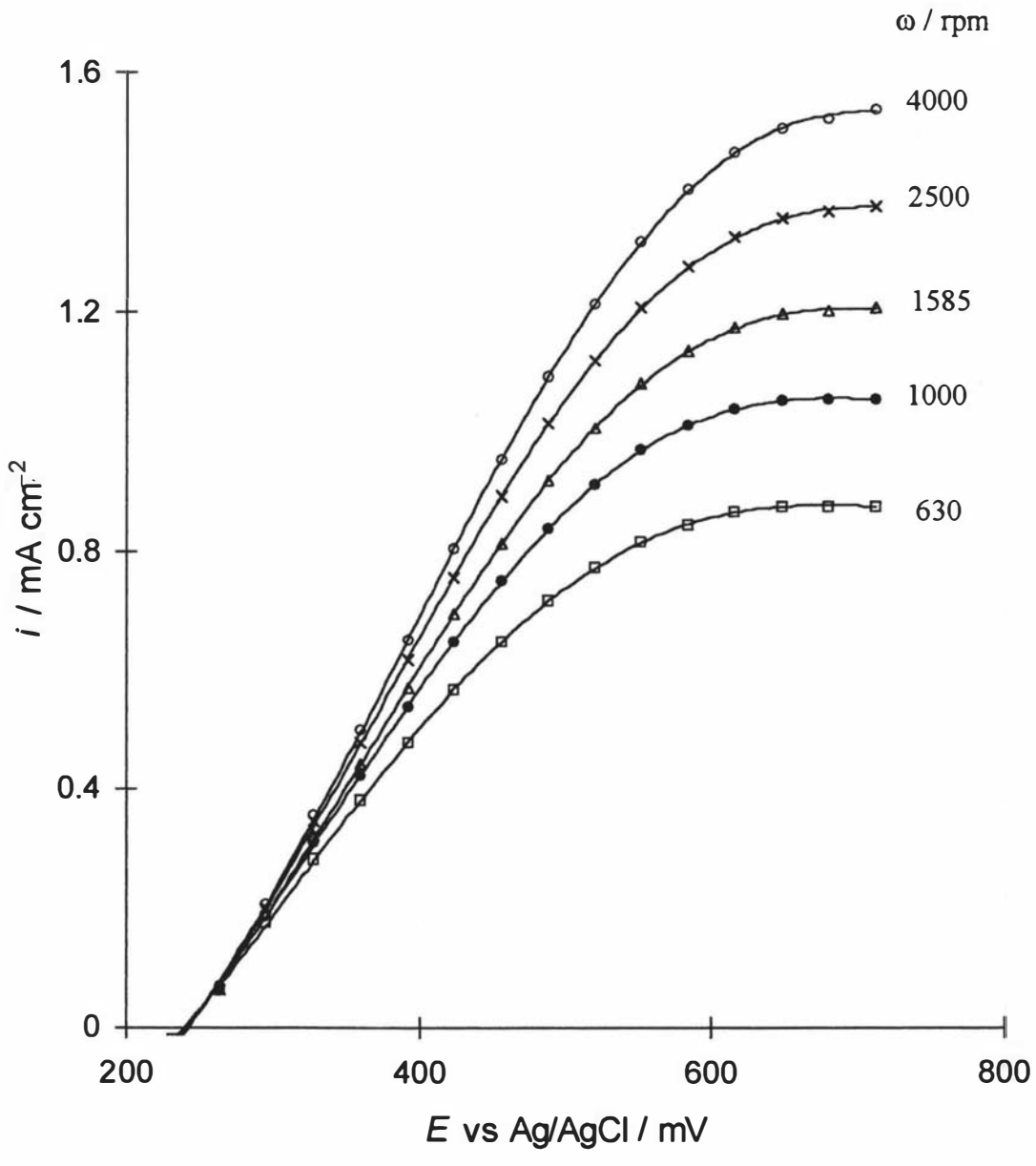

Fig. 3.8 Steady-state responses for the oxidation of 3 mM H_2O_2 over a range of potentials as a function of rotation rates employing the SCP technique.

3.3 The Reduction of H_2O_2 at Platinum Electrodes

A major problem associated with either direct reduction or oxidation of H_2O_2 at platinum electrodes is the relatively high operating overpotentials required, which under certain circumstances, can lead to unacceptable interference from other species [135].

The reduction of H_2O_2 has been interpreted to proceed by a number of different pathways [136,137].

The simplest mechanism is the direct reduction of H_2O_2 to water as in Eq. 3.5,

$$H_2O_2 + 2H^+ + 2e^- \longrightarrow 2H_2O \qquad (3.5)$$

At most electrodes this reaction forms part of a parallel mechanism for the direct four electron reduction of oxygen [137]

$$O_2 + 2H^+ + 2e^- \longrightarrow H_2O_2 \qquad (3.6)$$

The source of dissolved oxygen may be either from the catalytic decomposition of H_2O_2 itself at the electrode surface or in the bulk solution as,

$$H_2O_2 \longrightarrow H_2O + \frac{1}{2}O_2 \qquad (3.7)$$

or generated during the initial polarization of the electrode prior to the commencement of the cathodic sweep in cyclic voltammetry.

Another suggested route is the homolytic cleavage of H_2O_2 to hydroxyl radicals at the electrode surface prior to the electron transfer reaction with the formation of hydroxyl ions [111]. The overall reaction of this pathway can be written as,

$$H_2O_2 + 2e^- \longrightarrow 2OH^- \qquad (3.8)$$

A small series of experiments on the reduction of H_2O_2 at a platinum RDE were carried out using 0.100 mol L^{-1} phosphate buffer solution at pH 7.28. The WE was subjected to a SCP potential wave-form over the range +264 to – 450 mV vs Ag/AgCl with a constant pulse amplitude of 32 mV and pulse width of 8 s.

The current-potential wave in Fig. 3.9 shows the steady-state response of a Pt RDE for a range of potentials and rotation rates. The steady state reduction of H_2O_2 increases at all potentials for each rotation rate. At potentials more cathodic than −120 mV the reduction of oxygen (dissolved or generated by decomposition of H_2O_2) is thought to compete with the reduction of H_2O_2 [110].

Figure 3.10 shows the steady state response of a Pt RDE for a range of $[H_2O_2]$ and rotation rates at −120 mV. At each rotation rate the current exhibits linear dependence

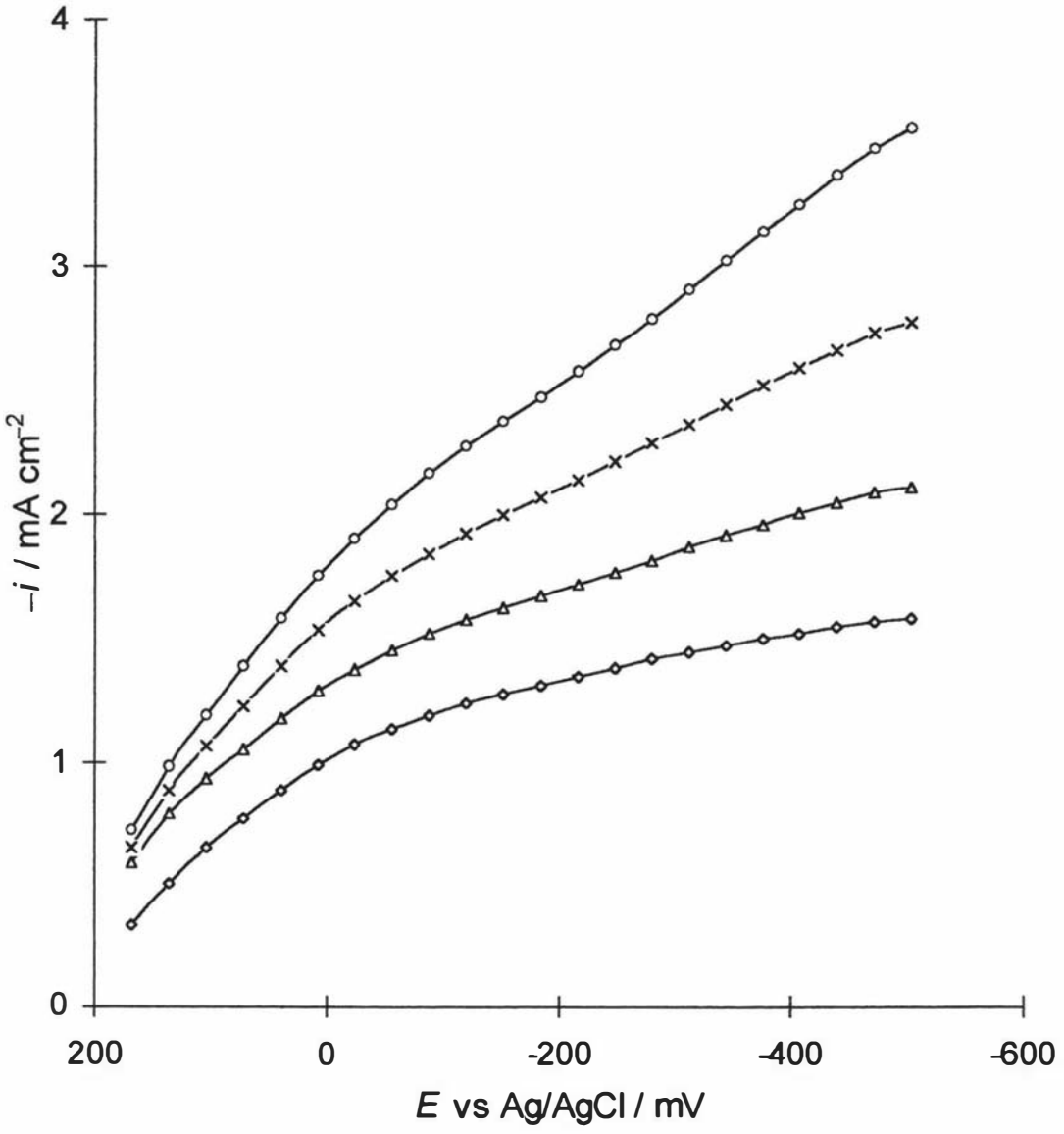

Fig. 3.9 Steady-state current response as a function of potential for the reduction of 2 mM H_2O_2 at different rotation rates; □ 1000, Δ 2000, × 4000 and O 8000 rpm.

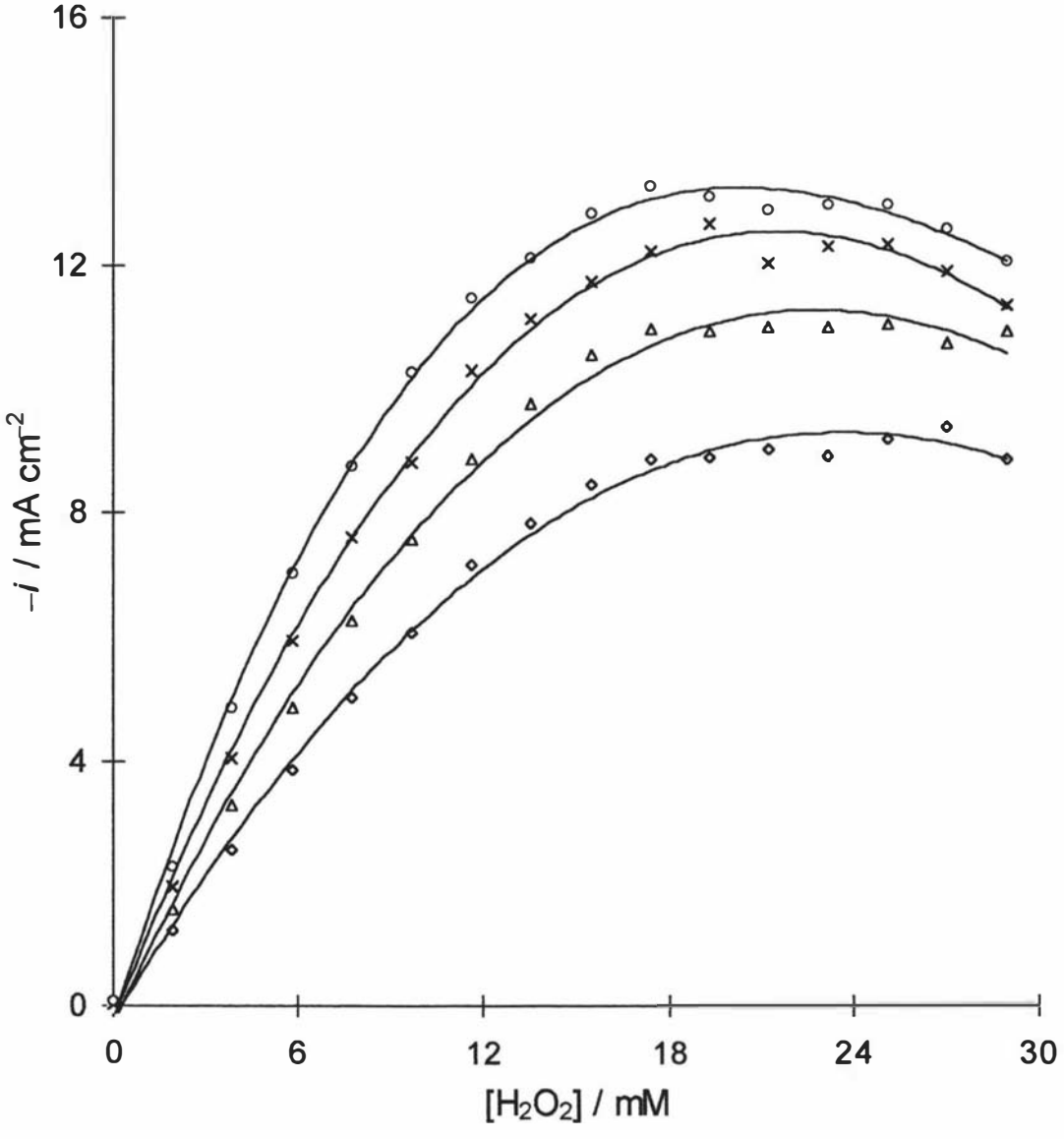

Fig. 3.10 Steady-state current responses as a function of bulk hydrogen peroxide at an electrode potential of −120 mV vs Ag/AgCl for a range of rotation rates; □ 1000, Δ 2000, × 4000 and O 8000 rpm.

on $[H_2O_2]$ up to 5 mM, but this dependence is progressively curtailed, so that for $[H_2O_2] > 15$ mM a limiting current is approached but this tends to decrease as $[H_2O_2]$ is further increased. This behaviour may be suggestive of the activity of binding sites at the electrode surface, which could be lowered due to the adsorption of inhibiting species produced during the reduction reaction.

The selected potential of −120 mV in Fig. 3.10 is believed to be appropriate for studying the reduction process since this would avoid the reduction of oxygen that occurs at more negative potentials.

In biocatalytic experiments, the reduction of H_2O_2 could not be usefully coupled to the functioning of an oxidase enzyme since the presence of oxygen could initiate a simultaneous side reaction resulting in formation of oxide surface that is thought to partially inhibit the reduction process [138], and perhaps for this reason the reaction has been little utilised in biosensors.

In the present study the reduction reaction was not investigated any further.

CHAPTER FOUR

An Adsorption-Controlled Mechanism for the Electrochemical Oxidation of Hydrogen Peroxide at Platinum Electrodes

4.1 Introduction

The detection of H_2O_2 by electrochemical techniques potentially offers an a valuable sensing tool for rapid, sensitive, selective and reproducible measurements [139].

One important approach has been the use of transition metals such as platinum as a catalytic material in the construction of amperometric sensors for the electrochemical measurement of H_2O_2 [140-143] generated during enzymatic reactions.

Many devices incorporate platinum (or other metals such as palladium or rhodium) as fine dispersions on carbon [91,94] which permits the mass-production of high surface area electrodes by screen-printing methods [144,145]. Here, highly catalytic surfaces are achieved so long as the particle size of the dispersed metal is comparable to that of the electric double layer [97].

Zhang and Wilson [146] examined the oxidation of H_2O_2 on platinum and platinum/iridium wire electrodes and found that a pronounced depression of response is evident for hydrogen peroxide concentrations above 1 mM, both in steady state measurements and in extrapolated kinetic currents for a series of Koutecky-Levich plots [120]. These workers explained this in terms of saturation of the electrode surface by H_2O_2 and O_2 based on earlier reports for potentiometric measurements [147]. They also suggested that slow electron transfer might impose kinetic control on the overall process so that the current is no longer proportional to the bulk H_2O_2 concentration.

One important factor that was found to influence the response of solid Pt electrodes was that the oxidation of H_2O_2 is favoured on oxidized Pt surfaces [52,148,149]. This finding was based on the potential at which H_2O_2 was observed to oxidize. This potential region (+750 to +900 mV vs SHE) had previously been shown to correspond to platinum oxide film formation [63]. Lingane and Lingane [52] supported the earlier suggestion by Hickling and Wilson [73] that the primary electron transfer reaction is the re-oxidation of platinum to platinum oxides, after the oxide film had previously been reduced by hydrogen peroxide.

It should be noted that there is a further complication as cathodic pre-treatment to remove adsorbed oxygen promotes the overall reaction [150].

A number of workers have explored the oxidation of H_2O_2 on thin palladium/gold layers. Gorton *et al* [100] found a non-linear steady-state response to H_2O_2 above 10 mM for vapour sputtered Pd/Au on carbon. Assuming that gold only acts to aid dispersion of palladium, they proposed that the oxidation mechanism was reliant on surface oxide films, in a similar manner to that found for Pt.

Johnston *et al*. [101] assembled Pd/Au thin-film electrodes by vacuum evaporation on PVC supports. These workers observed similar results to those of Gorton [100] and they explored the form of the deviation from linearity by consideration of a surface binding site model:

$$H_2O_{2\,bulk} \xrightarrow{k_D} H_2O_2 \tag{4.1}$$

$$H_2O_2 + Pd(OH)_2 \overset{K_1}{\rightleftharpoons} Pd(OH)_2 \cdot H_2O_2 \tag{4.2}$$

$$Pd(OH)_2 \cdot H_2O_2 \xrightarrow{k_2} Pd + 2H_2O + O_2 \tag{4.3}$$

$$Pd + 2H_2O \xrightarrow{k_3} Pd(OH)_2 + 2H^+ + 2e^- \tag{4.4}$$

where reaction 4.1 represents diffusion of hydrogen peroxide to the electrode surface and k_D is a mass transfer rate constant. It was assumed that the surface complex is in rapid equilibrium and sufficiently anodic potentials were applied (+650 mV vs SHE) so that reaction 4.4 was more rapid than 4.3, hence, the flux (mol cm^{-2} s^{-1}) was dependent on the slowest step and given by

$$j = k_2 N(1-f) \tag{4.5}$$

where N was defined as the number of binding sites on the electrode surface and f the fraction of free sites on the surface at any time.

Applying the steady-state approximation to the adsorbed species gave

$$\frac{d[N(1-f)]}{dt} = \{k_1[H_2O_2]Nf\} - \{k_{-1}N(1-f)\} - \{k_2N(1-f)\} = 0 \tag{4.6}$$

where k_1 and k_{-1} are the forward and backward rate constants, respectively, for reaction 4.2 and $[H_2O_2]$ is the surface concentration of H_2O_2 (dependent on the bulk concentration and stirrer speed). Solving for f and rearranging for j gave the derived rate equation

$$j = \frac{k_1 k_2 [H_2O_2] N}{k_1 [H_2O_2] + k_{-1} + k_2} \tag{4.7}$$

Taking the reciprocal of Eq. 4.7 yields the form

$$\frac{1}{j} = \frac{1}{k_2 N} + \frac{k_{-1} + k_2}{k_1 k_2 [H_2O_2] N} \tag{4.8}$$

Johnston *et al.* [101] demonstrated that for fixed cell geometry and stirring conditions (unspecified) that the double reciprocal form of Eq. 4.8 (equivalent to Lineweaver-Burk plots in enzyme kinetics) gave linear plots of $1/j$ against $1/[H_2O_2]$ with positive slope and positive intercept equivalent to $1/k_2N$. This is suggestive of the system obeying a form of Michaelis-Menten kinetics with the intercept of the Lineweaver-Burk plot indicating the maximum rate for the reaction at maximum occupancy of surface sites.

The proposed mechanistic scheme was adopted during the present study to extend the findings of Johnston *et al.* [101] concerning the oxidation of H_2O_2 on a solid platinum rotating-disc electrode over a range of concentrations and rotation rates so that the extent of diffusion control and nature of the surface kinetics could be evaluated.

4.2 Experimental Conditions

4.2.1 Reagents and Electrodes

All chemicals, reagents, electrodes and electrochemical equipment used in this study are described in Chapter 2 (sections 2.2 – 2.4). All experiments were performed at 20 ± 0.1 °C in 0.100 mol L^{-1} phosphate buffer solution at pH 7.28.

4.2.2 Electrochemical Methodology

Chronoamperometric measurements for the oxidation of H_2O_2 were made by stepping the potential of the working electrode from +200 mV to +600 mV vs Ag/AgCl. This potential was identified in the preliminary experiments, described in Chapter 3 and demonstrated in Fig. 3.1, where a maximum rate for the oxidation of H_2O_2 was achieved. In addition, this selected potential is consistent with previously reported values [54] and that commonly employed in biosensors [94,151,152].

The anodic potential was held for 20 s by which time the current had adopted a steady-state value. The last second of digitized data (50 points) was averaged for each experiment and the mean value and standard deviation recorded. In all cases reported here, the maximum standard deviation was 5×10^{-5} mA cm^{-2} and, thus, deviations are too small to include as error bars in the figures. Average responses and standard deviations were calculated and collated using the software package EVARY, developed for this work (Chapter 2, Section 2.9).

Chronoamperometric measurements were made over the bulk H_2O_2 concentration range 0 - 80 mM and for rotation rates, ω, of 630, 1000, 1585, 2500, 4000, 6300 and 10000 rpm. These rotation rates were selected so that they were evenly spaced in $\omega^{-1/2}$.

The problem of O_2 bubbles diminishing the area of the inverted electrode exposed to the electrolyte was avoided by rapidly increasing the rotation rate of the RDE to the maximum rate possible (10000 rpm) immediately prior to the potential step sequence by application of an external analog signal to the BAS RDE-1.

4.3 Chronoamperometric Response

The steady-state response of a Pt rotating disk electrode to H_2O_2 for a range of bulk concentrations and rotation rates is shown in Fig. 4.1. It should be noted that the data was collected for a single series of experiments with no electrode conditioning (either physical or electrochemical) between successive concentrations or rotation rates. Previous workers have shown that oxidation of H_2O_2 on Pt is dependent on the oxidation of the surface [52,148,149], the primary electron transfer being the re-oxidation of Pt formed as a consequence of reduction by H_2O_2 [52,73]. The experimental conditions in the present work involve establishing a reproducible electrode surface by cyclic voltammetry, as described in sections 2.3.1, in the potential region in which surface oxides will form [63].

All subsequent chronoamperometric measurements involved stepping from a potential close to the open circuit value to the anodic region for a sufficient time so that steady-state conditions were achieved. This approach minimised the extent to which the number of surface sites will change during successive additions of H_2O_2.

At each rotation rate the current exhibited linear dependence on bulk [H_2O_2] in the range 0–10 mM. The current response increases from 0.60 mA cm^{-2} mM^{-1} at 630 rpm to 1.75 mA cm^{-2} mM^{-1} at 10000 rpm indicated that the process involves diffusion.

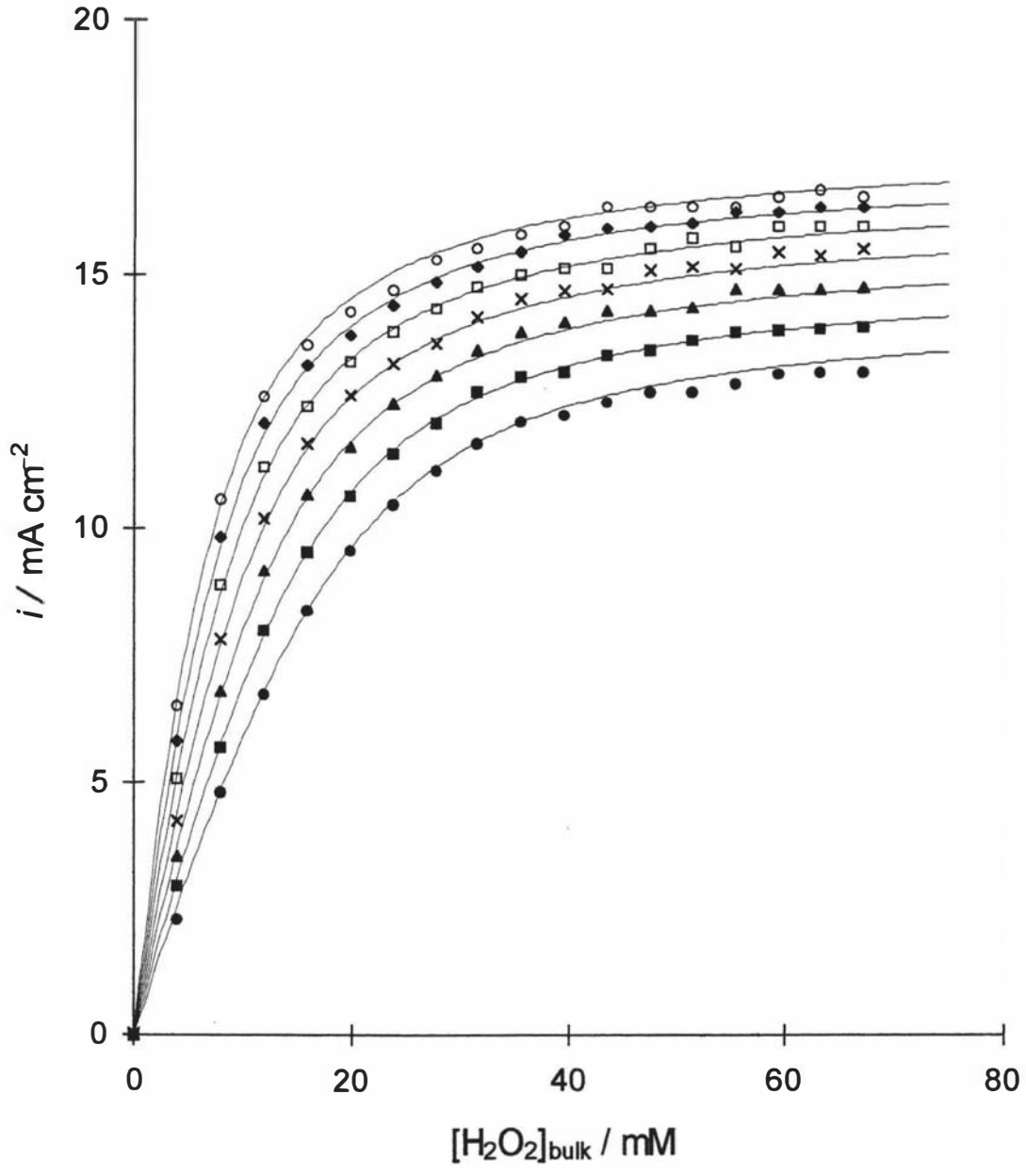

Fig. 4.1 Steady-state current responses (E = +600 mV vs Ag/AgCl) as a function of bulk hydrogen peroxide at 0.100 mol L^{-1} phosphate buffer solution of pH 7.28 and 20 °C for a range of rotation rates. ● 630 rpm, ■ 1000 rpm, ▲ 1585 rpm, × 2500 rpm, □ 4000 rpm, ◆ 6300 rpm and ○ 10000 rpm.

Smooth curves are the synthetic responses calculated using the model and parameters developed in this study.

The linear dependence was progressively curtailed so that for $[H_2O_2] > 50$ mM a limiting current was approached at all rotation rates with the limiting current being greater for higher rotation rates. This increase in current with rotation rate was expected as the mass transport of bulk H_2O_2 species to the electrode surface is increased, and the thickness of double layer becomes thinner, which facilitates the approach of H_2O_2 to the electrode surface and subsequent electrochemical reaction.

Given that the electrode response exhibited dependence on rotation rate, a range of models that incorporate consideration of mass transfer was explored.

4.4 Levich Study

The simplest model involving mass transport is the Levich model [120]. For situations where the surface concentration of an electroactive species is zero, the relationship between the limiting current density and the rotation rate is given by the Levich equation that was stated in Chapter 2 (Eq. 2.5)

$$i_L = 0.620nFD^{2/3}\omega^{1/2}\nu^{-1/6}c_b \qquad (2.5)$$

This expression indicates that the limiting current density is proportional to the bulk concentration, c_b, and is entirely mass transport controlled. A plot of i_L vs. $\omega^{1/2}$ should be linear and pass through the origin. The slope of such a plot may be used to estimate the diffusion coefficient of the electroactive species.

Figure 4.2 shows the current density for a selection of bulk H_2O_2 concentrations, $[H_2O_2]_{bulk}$, as a function of the square root of angular velocity, $\omega^{1/2}$, in $(\text{rad s}^{-1})^{1/2}$. Although current increases with $\omega^{1/2}$ for each H_2O_2 concentration, the plot exhibits non-linearity indicating the reaction is not entirely controlled by mass transport process. This suggests some other kinetic limitations may control the electrode reactions besides that of mass transport.

In addition to the deviation in linearity, the data presented in Fig. 4.2 do not extrapolate to the origin. Therefore, it is inappropriate to evaluate the diffusion coefficient of H_2O_2, $D_{H_2O_2}$, using this method.

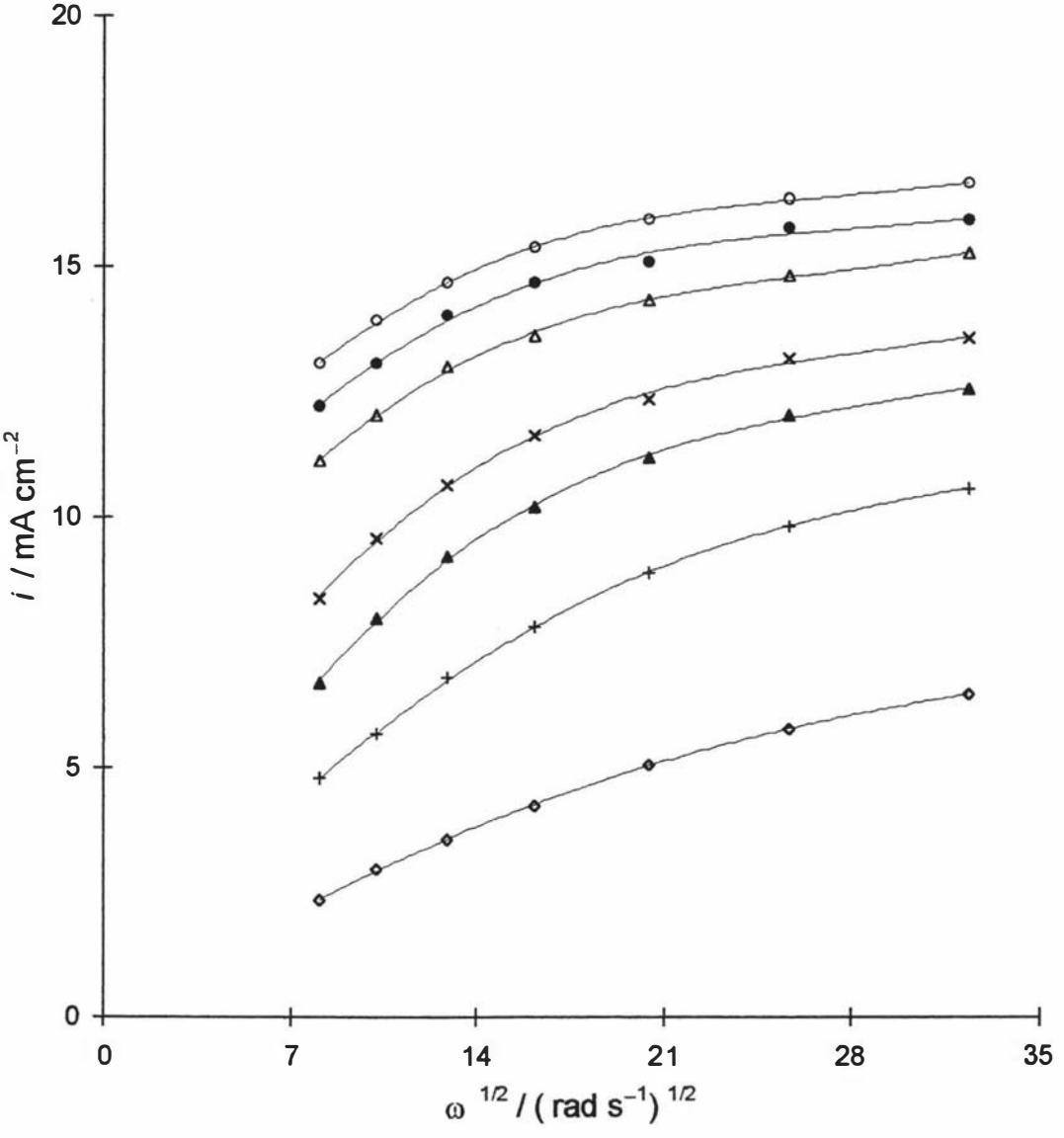

Fig. 4.2 Steady-state current responses (E = +600 mV vs. Ag/AgCl) as a function of $\omega^{1/2}$ using 0.100 mol L^{-1} phosphate buffer of pH 7.28 at 20 °C for a range of $[H_2O_2]_{bulk}$; □ 3.95, + 7.95, ▲ 11.92, × 15.89, Δ 27.77, ● 39.62 and O 63.24 mM.

4.5 Koutecky-Levich Study

The Koutecky-Levich model is a modification to the Levich model that permits rate control by both mass transport and electron transfer processes [153].

For irreversible electrode process, the current-potential wave can be divided into three regions:

i) in the limiting current plateau region, the current density depends only on the rate of mass transport (as in the Levich equation) and i_L will be proportional to $\omega^{1/2}$;

ii) at very low current density, the current density is totally determined by the kinetics of electron transfer, and the rate of mass transport will not affect the current density and hence i is independent of ω; and

iii) in the intermediate zone, called the mixed control region, the current density is controlled by both the electron transfer and mass transport processes. Since the current density is partially mass transport controlled, i must vary with ω in this region.

The current density at any potential in the region of mixed control is given by both mass transport and electron transfer kinetics.

The current density of electron transfer is given by

$$i = nFk_f c_s \tag{4.9}$$

where k_f is the heterogeneous electron transfer rate constant, and c_s is the surface concentration. The current may also be related to the bulk concentration, c_b, and the Nernst diffusion layer layer which was described in Chapter 2 (Eq. 2.2)

$$i = nFD\,\frac{c_b - c_s}{\delta} \tag{2.2}$$

Hence, eliminating i, one obtains

$$c_s = \frac{D\,c_b}{k_f\delta + D} \tag{4.10}$$

Substituting Eq. 4.10 into 4.9 and inverting gives

$$\frac{1}{i} = \frac{\delta}{nFDc_b} + \frac{1}{nFk_f c_b} \tag{4.11}$$

The diffusion layer thickness variation with rotation rate is given by Eq. 2.4

$$\delta = 1.61 D^{1/3} \omega^{-1/2} \nu^{1/6} \tag{2.4}$$

and substitute of Eq. 2.4 into 4.11 gives the Koutecky-Levich equation

$$\frac{1}{i} = \frac{1}{nFk_f c_b} + \frac{1}{0.620 nF D^{2/3} \nu^{-1/6} c_b} \frac{1}{\omega^{1/2}} \tag{4.12}$$

This may be separated into contributions from kinetic and mass transfer control. The general relationship for such a process can be written by the following form

$$\frac{1}{i} = \frac{1}{i_k} + \frac{1}{i_d} \tag{4.13}$$

For the present experimental conditions, the kinetic current , i_k, would be given by

$$i_k = nFk_f[H_2O_2]_{bulk} \tag{4.14}$$

where $[H_2O_2]_{bulk}$ is the bulk concentration in mol m^{-3}. The diffusion current, i_d, would be given by

$$i_d = 0.620 nF [H_2O_2]_{bulk} D_{H_2O_2}^{2/3} \nu^{-1/6} \omega^{1/2} \tag{4.15}$$

where ν is the kinematic viscosity (taken to be 1.00×10^{-6} m^2 s^{-1}) [154] and ω is the angular velocity in rad s^{-1}.

Thus, for kinetic and mass transfer controlled reactions a Koutecky-Levich plot of $1/i$ vs $1/\omega^{1/2}$ for each concentration should result in linear relationships with intercept equivalent to the inverse of i_k and a slope, from which the heterogeneous electron transfer rate constant and diffusion coefficient may be evaluated.

Previous workers [146] have analyzed the oxidation of H_2O_2 using Koutecky-Levich plots [120] where the electrode reaction is treated as an irreversible process involving both kinetic and mass transfer components.

Figure 4.3. displays Koutecky-Levich plot for the experimental data shown in Fig. 4.1 in the concentration range 0 - 30 mM (data above this are omitted for clarity). Predominantly linear relationships are observed with the slopes decreasing with increasing $[H_2O_2]_{bulk}$ in agreement with that expected by the form of the Koutecky-Levich relationship and consistent with those observed by Zhang and Wilson [146]. The intercepts, however, appear to have similar values at the $1/i$ axis. This is in marked

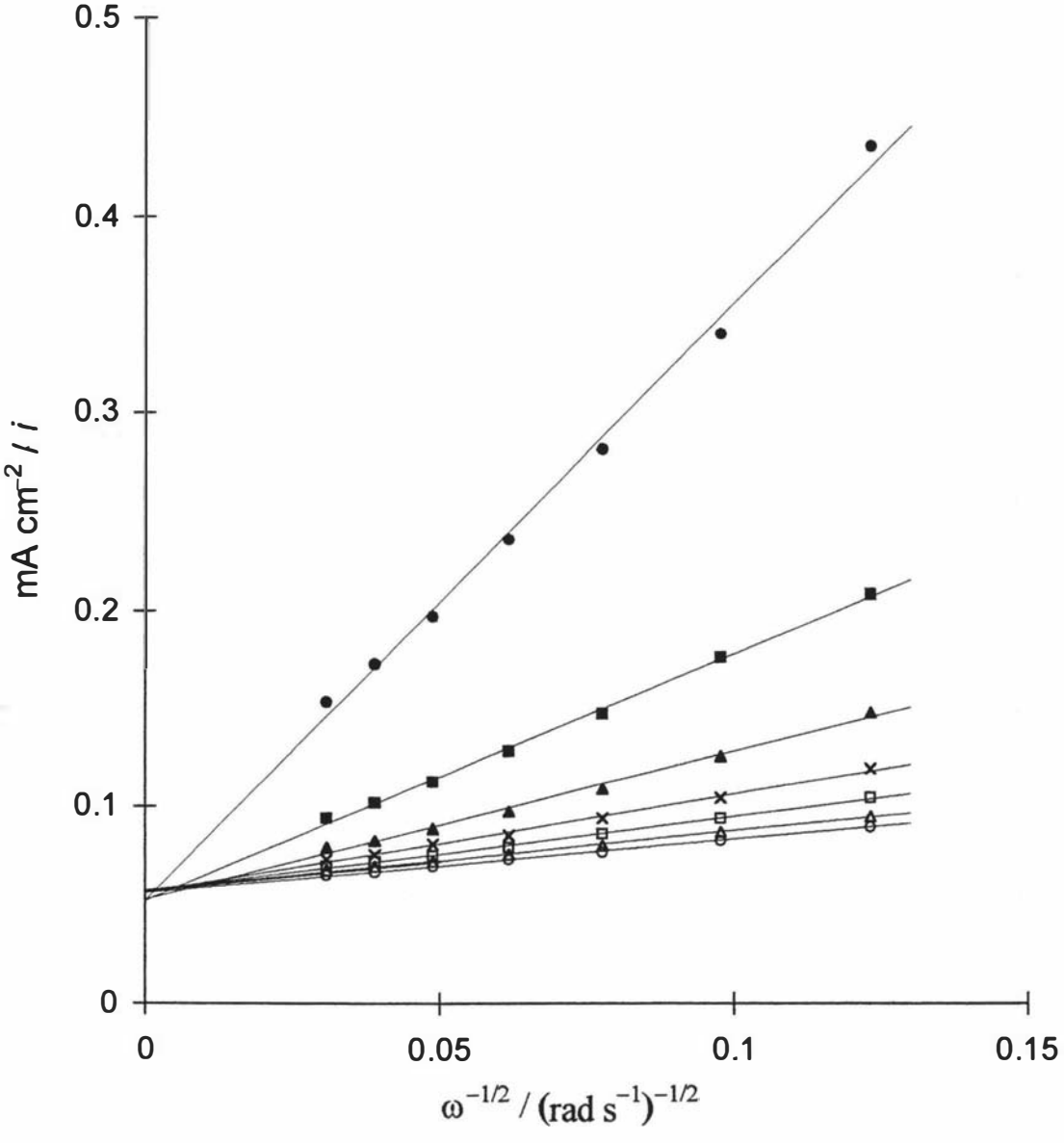

Fig. 4.3 Koutecky-Levich plots of the data presented in Fig. 4.1 for a selection of bulk hydrogen peroxide concentrations (higher concentrations omitted for clarity); ● 4.0, ■ 8.0, ▲ 11.9, × 15.9, □ 19.9, Δ 23.8 and O 27.8 mM, using 0.100 mol L^{-1} phosphate buffer of pH 7.28 at 20 °C.

contrast to that found by Zhang and Wilson [146] where the intercepts were inversely proportional to $[H_2O_2]_{bulk}$.

Linear regression analysis for Koutecky-Levich data for the intercepts and the error in the intercept as a function of the entire range of $[H_2O_2]$ are given in Table 4.1. The calculated values of the rate constant k_f are plotted against $[H_2O_2]_{bulk}$ in Fig. 4.4 with the positive and negative errors of k_f as the error bars. At $[H_2O_2]_{bulk}$ greater than 20 mM, these error bars are very small compared with the values of k_f.

If Koutecky-Levich behaviour is followed, it would be apparent that the electron transfer process is influenced by $[H_2O_2]_{bulk}$ in two different regions,

i) at low $[H_2O_2]_{bulk}$, the calculated rate constant has greatest values, which could mean that the electron transfer process proceeds at a faster rate,

ii) at high $[H_2O_2]_{bulk}$, the rate constant decreases rapidly and approaches a constant value (ca. 1.0×10^{-5} m s^{-1}) so that the electron transfer process apparently proceeds at a slow rate.

Linear regression analysis for Koutecky-Levich data for the slopes and errors in slope as a function of the entire range of $[H_2O_2]_{bulk}$ are given in Table 4.2. Diffusion coefficients for H_2O_2 were evaluated using Eq. 4.15 and the slopes of the linear relationships shown in Fig.4.3 (together with those not plotted for reasons of clarity). This parameter should be invariant with concentration at constant temperature. Inspection of the plot of $D_{H_2O_2}$ as a function of $[H_2O_2]$ in Fig.4.5 shows, however, that the apparent diffusion coefficient varies greatly and exhibits values of ca. 0.6×10^{-9} m^2 s^{-1} at both extremes of the concentration range explored and a maximum of 1.3×10^{-9} m^2 s^{-1} at 30 mM. Previous workers have used the hydrodynamic response for the oxidation of H_2O_2 at Pt to determine the diffusion coefficient for this species. Recently van Stroe-Biezen *et al.* [155] reported a value of 1.43×10^{-9} m^2 s^{-1} at 25°C and at an unspecified H_2O_2 concentration. Whilst this value is similar to those found by Prabhu *et al.* [54] for the reduction of H_2O_2 by chronoamperometric and chronopotentiometric techniques in quiescent solutions and also that found by Borggaard [156] using polarography, it is suggested here that use of these values should be treated with caution in light of these findings.

Furthermore, close inspection to Fig. 4.4 and to data represented in Tables 4.1, reveals that Koutecky-Levich plot illustrated in Fig. 4.3 is not entirely linear and display more

$[H_2O_2]$ / mM	intercept / $10^{-2}\,A^{-1}\,m^2$	error in intercept / $10^{-3}\,A^{-1}\,m^2$	k_f / $10^{-5}\,ms^{-1}$	(+) error / $10^{-5}\,ms^{-1}$	(−) error / $10^{-5}\,ms^{-1}$
3.98	5.22	7.19	24.96	3.988	3.022
7.95	5.26	2.22	12.39	0.547	0.503
11.92	5.34	2.27	8.14	0.362	0.332
15.89	5.64	1.22	5.78	0.128	0.123
19.85	5.74	0.89	4.54	0.072	0.069
23.81	5.77	0.67	3.77	0.044	0.043
27.77	5.69	0.33	3.28	0.019	0.019
31.72	5.67	0.51	2.88	0.026	0.026
35.67	5.64	0.43	2.58	0.020	0.019
39.62	5.55	0.54	2.36	0.023	0.022
43.57	5.54	0.62	2.15	0.024	0.024
47.51	5.50	0.34	1.98	0.012	0.012
51.45	5.47	0.50	1.84	0.017	0.017
55.38	5.50	0.65	1.70	0.020	0.020
59.31	5.44	0.44	1.61	0.013	0.013
63.24	5.41	0.22	1.51	0.006	0.006
67.17	5.43	0.50	1.42	0.013	0.013

Table 4.1 Analysis of the Koutecky-Levich plot listing the intercept and error in intercept as a function of $[H_2O_2]_{bulk}$ together with the calculated values of rate constant, k_f, and the positive and negative errors in k_f, (+) error and (−) error, respectively.

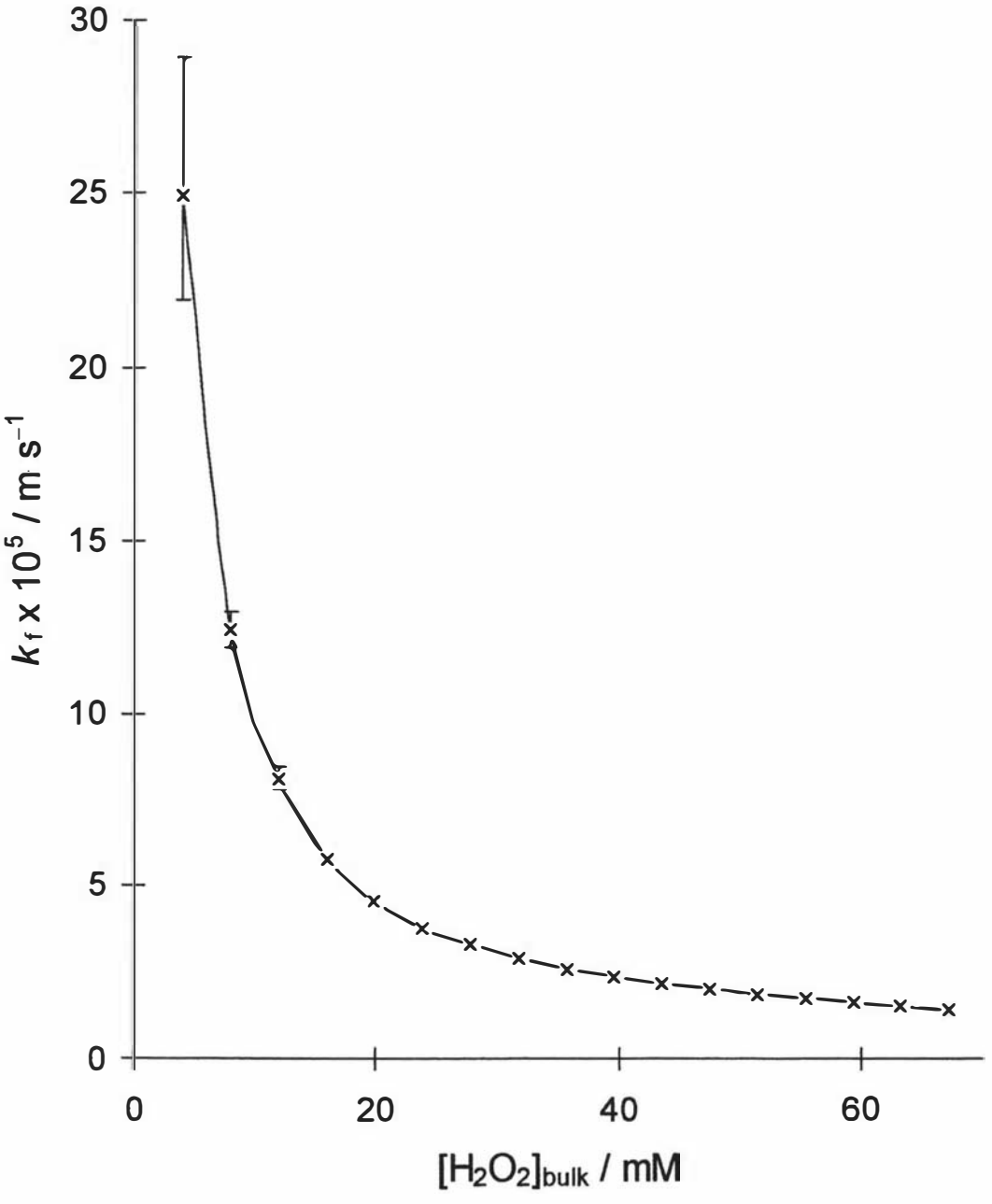

Fig. 4.4 Heterogeneous rate constant for H_2O_2 as a function of bulk concentration calculated using Eq. 4.14 from the intercept of Koutecky-Levich plots presented in Fig. 4.3 (including data omitted for clarity). The error bars were calculated from the estimated error in the Koutecky-Levich intercepts and listed in Table 4.1.

$[H_2O_2]_{bulk}$	slope	error in slope	$D_{H_2O_2}$	(+)error in $D_{H_2O_2}$	(–)error in $D_{H_2O_2}$
mM	$A^{-1} m^{-1} s$	$10^{-2} A^{-1} m^{-1} s$	$10^{-9} m^2 s^{-1}$	$10^{-9} m^2 s^{-1}$	$10^{-9} m^2 s^{-1}$
3.98	3.035	9.59	0.58	0.03	0.03
7.95	1.255	2.96	0.77	0.03	0.03
11.92	0.750	3.03	0.90	0.06	0.05
15.89	0.500	1.63	1.08	0.06	0.05
19.85	0.376	1.19	1.19	0.06	0.05
23.81	0.301	0.89	1.26	0.06	0.05
27.77	0.266	0.44	1.20	0.03	0.03
31.72	0.231	0.69	1.22	0.06	0.05
35.67	0.212	0.57	1.17	0.05	0.05
39.62	0.211	0.71	1.00	0.05	0.05
43.57	0.198	0.82	0.95	0.06	0.06
47.51	0.194	0.46	0.87	0.03	0.03
51.45	0.192	0.66	0.78	0.04	0.04
55.38	0.180	0.86	0.77	0.06	0.05
59.31	0.179	0.59	0.70	0.04	0.03
63.24	0.181	0.29	0.63	0.02	0.01
67.17	0.177	0.66	0.59	0.03	0.03

Table 4.2 Analysis of Koutecky-Levich plot listing the slope and error in slope as a function of $[H_2O_2]_{bulk}$ together with the calculated values of $D_{H_2O_2}$ and the positive and negative errors in $D_{H_2O_2}$, (+) error and (–) error, respectively.

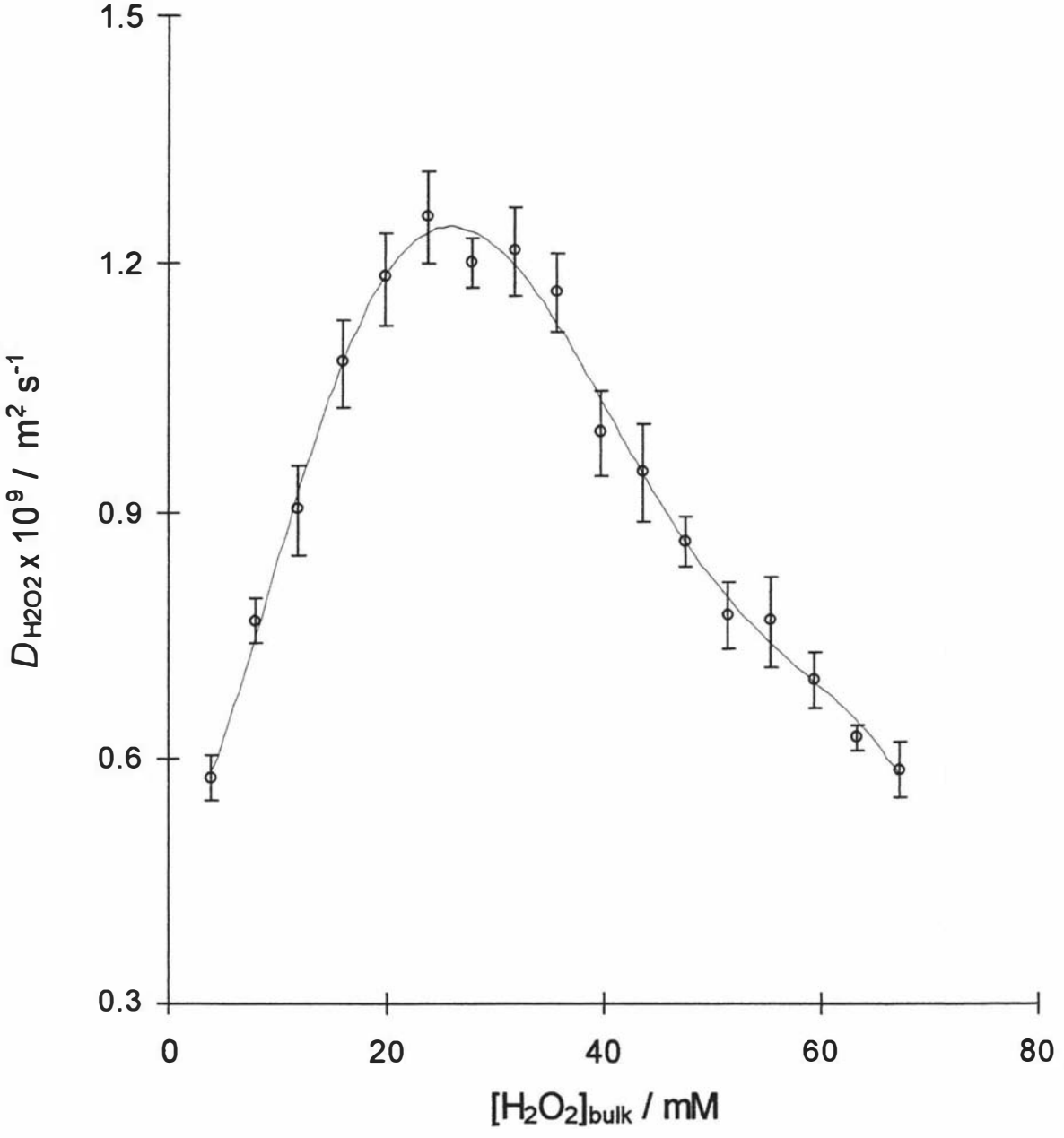

Fig. 4.5 Diffusion coefficients for H_2O_2 as a function of bulk concentration calculated using Eq. 4.15 from the slopes of the Koutecky-Levich plots presented in Fig. 4.3 (including data omitted for clarity). The error bars were calculated from the estimated error in the Koutecky-Levich slopes and are listed in Table 4.2.

parabolic departure from linearity with increasing $[H_2O_2]$. This indicates that Koutecky-Levich analysis is not sufficient to completely describe this electrode reaction.

The results shown in Figs. 4.3 and 4.4 strongly suggest that it is likely that the oxidation of H_2O_2 at Pt proceeds by a mechanism somewhat more complicated than electron transfer coupled with diffusion control. Accordingly, in the following sections the applicability of the Michaelis-Menten kinetic analysis employed by Johnston *et al.* [101] for the oxidation of H_2O_2 at Pd/Au thin-films is assessed for the present work. This will lead to the development of a kinetic model incorporating the features identified by Johnston *et al* [101] together with previously suggested features of both H_2O_2 and O_2 binding on an oxidized Pt surface.

4.6 Michaelis-Menten Study

The rate of enzyme-catalyzed reactions was studied by Michealis and Menten in the early twentieth century [157]. The reaction mechanism involves a single reaction of a substrate species, S, that binds to an enzyme active site, E, to form an enzyme-substrate intermediate, ES. This dissociates to give the reaction product, P, together with the release of the free enzyme. The sequence of these steps can be written as

$$S + E \overset{K_1}{\rightleftharpoons} ES \xrightarrow{k_2} E + P \tag{4.16}$$

where the equilibrium constant for the formation of the enzyme-substrate intermediate, K_1, is given by the ratio of forward to reverse reactions

$$K_1 = \frac{k_1}{k_{-1}} \tag{4.17}$$

The second step is a first-order reaction with a rate constant k_2, so that the reaction rate, j, to form the product is given by

$$j = \frac{d[P]}{dt} = k_2[ES] \tag{4.18}$$

A steady-state is approached in which the concentration of the intermediate is constant and does not build up to significant proportions. Therefore, an expression for the rate of change of intermediate may be written

$$\frac{d[ES]}{dt} = k_1[S][E] - k_{-1}[ES] - k_2[ES] = 0 \tag{4.19}$$

The term [E] used in this equation is the concentration of the enzyme that is free to catalyze the reaction. The initial enzyme concentration, $[E]_o$, added at the beginning of the reaction is equal to the sum of the concentration of the free enzyme plus that bound in the enzyme-substrate intermediate form:

$$[E]_o = [E] + [ES] \tag{4.20}$$

or

$$[E] = [E]_o - [ES] \tag{4.21}$$

Substituting Eq. 4.21 into 4.19 and solving for [ES] gives

$$[ES] = \frac{k_1[S][E]_o}{k_{-1} + k_2 + k_1[S]} \tag{4.22}$$

Combining Eqs. 4.18 and 4.22 gives the theoretical rate equation for the product in terms of both substrate and initial enzyme concentrations:

$$j = \frac{k_2 k_1[S][E]_o}{k_{-1} + k_2 + k_1[S]} \tag{4.23}$$

Equation 4.23 can be arranged to give the general form of Michaelis-Menten equation

$$j = \frac{j_{max}[S]}{K_M + [S]} \tag{4.24}$$

where j_{max} is the maximum rate under enzyme saturation conditions (all enzyme is in the ES form) and equivalent to $k_2[E]_o$, while K_M is referred to as the Michaelis constant and equal to $(k_{-1} + k_2) / k_1$, which is in part inversely proportional to the binding equilibrium constant, K_1.

Johnston *et al* [101] used the Michaelis-Menten equation to investigate the form of H_2O_2 oxidation on sputtered Pd/Au electrodes. The experimental results of the present study have also been analyzed in terms of Michaelis-Menten kinetics using the Hanes plot method [158] in preference to the Lineweaver-Burk approach [159] since the latter method suffers from undue weighting on low concentration data.

The first step in this model is the mass transport of hydrogen peroxide in the bulk, $H_2O_{2(bulk)}$, to the electrode surface by diffusion

$$H_2O_{2(bulk)} \xrightarrow{\text{diffusion}} H_2O_2 \tag{4.1}$$

where H_2O_2 (with no subscript denoted) represents the H_2O_2 at the surface in this and all subsequent models unless otherwise stated.

The second step is the adsorption of H_2O_2 onto the platinum binding sites, labelled $Pt(OH)_2$ to maintain consistency with sites identified by Johnston *et al* [101], to form the Pt(II)/ H_2O_2 surface site,

$$Pt(OH)_2 + H_2O_2 \overset{K_1}{\rightleftharpoons} Pt(OH)_2{\cdot}H_2O_2 \tag{4.2}$$

where the adsorption constant K_1 is given by

$$K_1 = \frac{\theta_{Pt(OH)_2 \cdot H_2O_2}}{[H_2O_2]\theta_{Pt(OH)_2}} \tag{4.25}$$

where θ_i refers to the fractional surface coverage of each species i in this and following expressions.

The third step involves internal charge transfer with the complex binding site, resulting in reduction of the Pt(II) centre and liberation of O_2,

$$Pt(OH)_2.H_2O_2 \xrightarrow{k_2} Pt + 2H_2O + O_2 \tag{4.3}$$

with the rate, j, given by

$$j = k_2 N \theta_{Pt(OH)_2 \cdot H_2O_2} \tag{4.26}$$

where N is the total number of binding sites per unit area.

The binding site is then regenerated electrochemically giving rise to the observed current

$$Pt + 2H_2O \xrightarrow{k_3} Pt(OH)_2 + 2H^+ + 2e^- \tag{4.4}$$

with j given by

$$j = k_3 N \theta_{Pt} \tag{4.27}$$

The mass balance equation for the fractional surface coverages is described by

$$1 = \theta_{Pt(OH)_2} + \theta_{Pt(OH)_2 \cdot H_2O_2} + \theta_{Pt} \tag{4.28}$$

By applying the steady-state approximation for all adsorbed species, substituting Eqs. 4.25, 4.26 and 4.27 into Eq. 4.28, a relationship can be solved for j

$$j = \frac{k_2 N K_1 [H_2O_2]}{1 + K_1[H_2O_2]\left(1 + \frac{k_2}{k_3}\right)} \tag{4.29}$$

The term (k_2 / k_3) in the denominator may be ignored as a sufficiently anodic potential is applied so that $k_3 >> k_2$ and θ_{Pt} approaches zero and, hence, should not been involved in the mass balance equation. Accordingly, Eq. 4.29 can be arranged to give the general form of Michaelis-Menten equation in terms of binding sites

$$j = \frac{k_2 N [H_2O_2]}{(1/K_1) + [H_2O_2]} \tag{4.30}$$

where the term K_M is equivalent to (1 / K_1) and j_{max} is equal to k_2N.

The general form of the Hanes plot for Michaelis-Menten kinetics is given by

$$\frac{[H_2O_2]}{j} = \left(\frac{1}{j_{max}}\right)[H_2O_2] + \frac{K_M}{j_{max}} \tag{4.31}$$

where j is the rate (mol m^{-2} s^{-1}) given by

$$j = \frac{i}{nF} \tag{4.32}$$

The Hanes plots for the steady-state data plotted in Fig. 4.1 are shown in Fig. 4.6. It is apparent that Michaelis-Menten kinetics is only approached at all concentrations for the highest rotation rates explored, with pronounced deviations evident at lower rotation rates in the concentration region 0 – 15 mM. Linear regions may be identified at all rotation rates at higher concentrations indicating that some form of Michaelis-Menten kinetics may have some role in the overall kinetics (although some deviation is also observed at high concentrations for low rotation rates).

Table 4.3 lists apparent Michaelis constants ($K_{M\ app}$) and j_{max} values (together with the maximum current, i_{max} calculated using Eq. 4.32) at each rotation rate for the linear regions identified by the solid lines in Fig. 4.6. The maximum rates and Michaelis constants are found to be consistent with estimated values obtainable from the data in Fig. 4.1, indicating that appropriate linear regions have been selected and are consistent with some form of Michaelis-Menten kinetics operating.

A decrease in $K_{M\ app}$ with increase in rotation rate might have been predicted for a reaction where some element of diffusion control is exhibited. Here, forced transport by electrode rotation would act to replenish the depletion of H_2O_2 at the electrode surface afforded by the reaction

$$H_2O_2 \xrightarrow{\text{electrode}} O_2 + 2H^+ + 2e^- \tag{1.12}$$

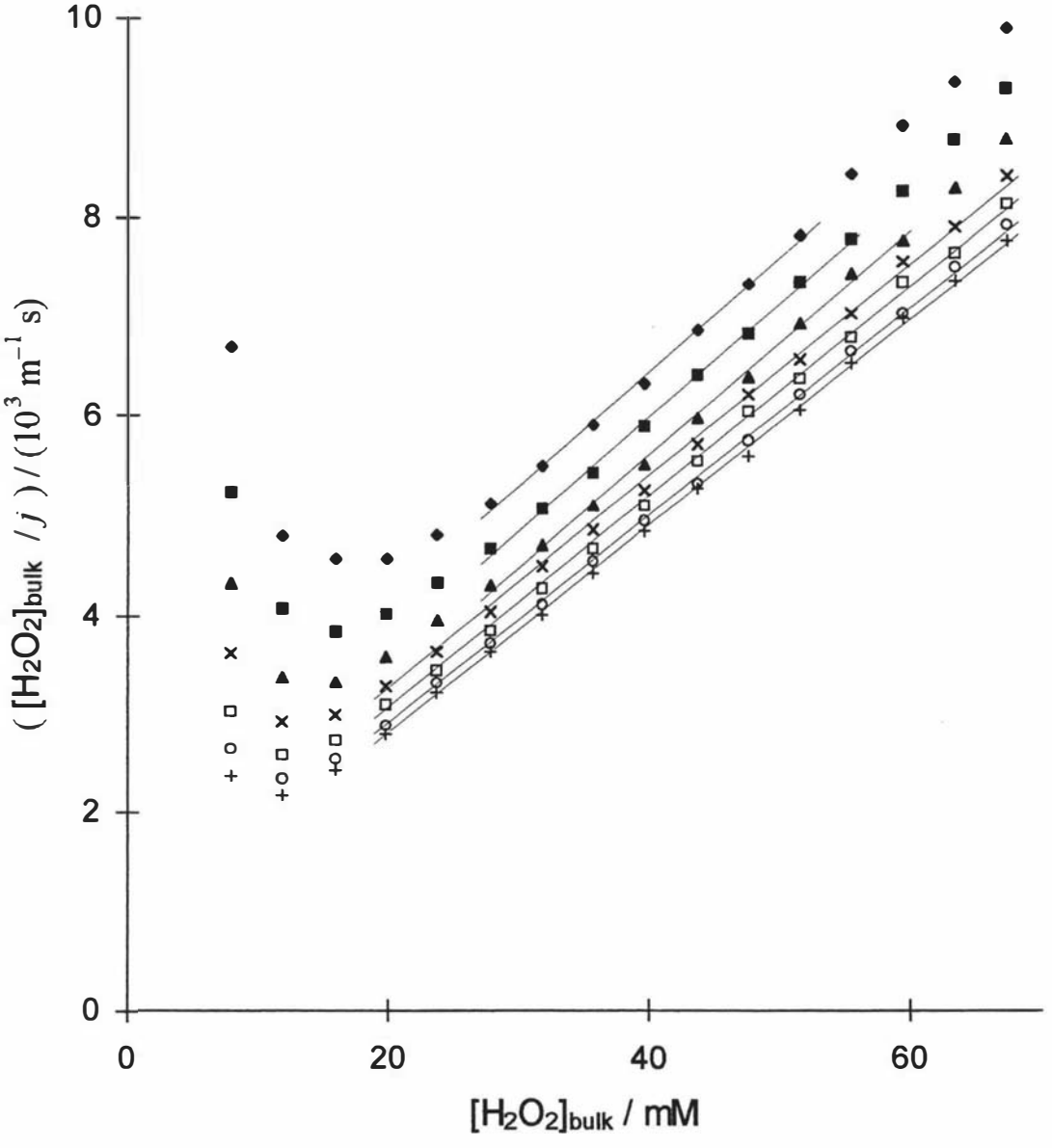

Fig. 4.6 Hane's plots for the data presented in Fig. 4.1 as a function of rotation rates. Regions selected for determination of $K_{M\,app}$ and j_{max} are indicated by solid lines.
ω: ◆ 630, ■ 1000, ▲ 1585, × 2500, □ 4000, O 6300 and + 10000 rpm.

ω / rpm	630	1000	1585	2500	4000	6300	10000
$K_{M\,app}$ / mol m^{-3}	15.8	12.3	9.9	10.4	8.8	7.6	6.8
$j_{max} \times 10^3$ / mol m^{-2} s^{-1}	0.863	0.871	0.886	0.932	0.938	0.948	0.954
i_{max} / mA cm^{-2}	16.7	16.8	17.1	18.0	18.1	18.3	18.4

Table 4.3 Kinetic parameters for simple Michaelis-Menten kinetics calculated from the selected linear regions identified in Fig. 4.6.

In this way, the bulk concentration required for half-saturation of the electrode (half the limiting current at which K_M is equivalent to the bulk concentration) would decrease with increased rotation rate. If this were the only effect of rotation, then the series of Hanes plots would exhibit linear responses with common slope and successively lower intercepts with increasing rotation rate.

Instead, deviations from linearity are observed at low rotation rates and low concentrations indicating that another process operates in this region to decrease the rate of reaction from that expected.

A further unexpected result is evident in the data tabulated in Table 4.3 (and displayed in Fig. 4.1) in that if rotation were only to aid transport of H_2O_2 to the electrode, then variation of j_{max} should not be observed. Instead, j_{max} is found to increase with rotation rate.

These results may be interpreted in terms of a mechanism involving Michaelis-Menten kinetics where the deviations in the Hanes plots at low concentrations and low rotation rates are due to a transient inhibition of the binding site by a reaction product and that another form of inhibition, also involving a reaction product, prevails at all concentrations as indicated by a variation in j_{max}.

The inhibition involves the reaction products since increasing the rotation rate increases the rate through forced removal of these species. Coupled with these effects is the enhanced reaction rate with delivery of the reactant to the binding site as shown by a decrease in K_{Mapp} with an increase in rotation rate in Table 4.3.

The steady-state current response results shown in Fig. 4.1 were analyzed to establish an appropriate mechanistic model for the oxidation of H_2O_2 at platinum electrodes, based upon the assumption that H_2O_2 follows some form Michaelis–Menten kinetics.

4.7 A Product-Inhibited Michaelis-Menten Mechanism

The mechanistic model described in Section 4.6 was assumed to follow Michaelis-Menten kinetics. This was shown to be too simplistic and incapable of describing all features revealed in Figs. 4.1 and 4.6. It was inferred that some form of product inhibition takes place. A number of candidate product-inhibition mechanisms were assessed and rejected for their failure to qualitatively describe the experimental results shown in Figs. 4.1 and 4.6. These rejected mechanisms are listed in Appendix A.

In this section, the final and successful model is presented in greater detail. This extends beyond qualitative analysis and full quantitative analysis is presented including consideration of mass transport terms. In the models presented in Sections 4.5 and 4.6, mass transport was not included.

It should be noted that the sequence of reaction steps and the structure of platinum binding site in the proposed simple model are exactly the same as that given by Johnston *et al.* [101] for palladium binding sites. This simple model is considered and described once again in this section as the fundamental scheme for constructing a model capable of describing the results shown in Figs. 4.1 and 4.6.

4.7.1 Modified Michaelis-Menten Mechanism

Bulk H_2O_2 diffuses to the electrode and is adsorbed onto Pt(II) binding sites according to a Langmuir isotherm to form the Pt(II)/H_2O_2 complex site in a similar manner to that reported by Johnston *et al.* [101] for Pd/Au sites

$$H_2O_2 + Pt(OH)_2 \overset{K_1}{\rightleftharpoons} Pt(OH)_2 \cdot H_2O_2 \tag{4.2}$$

where the adsorption constant K_1 is given by

$$K_1 = \frac{\theta_{Pt(OH)_2 \cdot H_2O_2}}{[H_2O_2]\,\theta_{Pt(OH)_2}} \tag{4.25}$$

In this and following expressions concentrations of species are those at the surface of the electrode unless otherwise stated.

Following adsorption, the complex undergoes internal electron transfer with the formation of a zero oxidation Pt site and the release of the products H_2O and O_2

$$Pt(OH)_2 \cdot H_2O_2 \xrightarrow{k_2} Pt + 2H_2O + O_2 \tag{4.3}$$

The binding site is regenerated electrochemically, giving rise to the observed current

$$Pt + 2H_2O \xrightarrow{k_3} Pt(OH)_2 + 2H^+ + 2e^- \tag{4.4}$$

Two inhibiting side reactions are proposed to occur in this mechanism. The first involves competitive binding of the reaction product O_2 to the Pt(II) binding site so that reaction 4.2 is blocked

$$Pt(OH)_2 + O_2 \overset{K_4}{\rightleftharpoons} Pt(OH)_2 \cdot O_2 \tag{4.33}$$

where the competitive inhibition binding constant K_4 is given by

$$K_4 = \frac{\theta_{Pt(OH)_2 \cdot O_2}}{[O_2]\theta_{Pt(OH)_2}} \tag{4.34}$$

The second involves reversible protonation of the surface Pt(II)/H_2O_2 complex where the protons are the product of reaction 4.4

$$Pt(OH)_2 \cdot H_2O_2 + H^+ \overset{K_5}{\rightleftharpoons} Pt(OH)_2 \cdot H_2O_2 \cdot H^+ \tag{4.35}$$

The protonation constant K_5 is given by

$$K_5 = \frac{\theta_{Pt(OH)_2 \cdot H_2O_2 \cdot H^+}}{[H^+]\theta_{Pt(OH)_2 \cdot H_2O_2}} \tag{4.36}$$

A sufficiently anodic potential is employed in the experiments reported here so that reaction 4.4 is not rate limiting and $\theta_{Pt} \rightarrow 0$. Thus, the steady-state rate, j, is given by the rate at which the surface Pt(II)/H_2O_2 complex undergoes internal electron transfer

$$j = k_2 N \theta_{Pt(OH)_2 \cdot H_2O_2} \tag{4.26}$$

where N is the number of binding sites per m^2.

Given that $\theta_{Pt} \rightarrow 0$, the fractional surface coverage balance equation is described by

$$1 = \theta_{Pt(OH)_2} + \theta_{Pt(OH)_2 \cdot H_2O_2} + \theta_{Pt(OH)_2 \cdot O_2} + \theta_{Pt(OH)_2 \cdot H_2O_2 \cdot H^+} \tag{4.37}$$

Applying the steady-state approximation to the adsorbed species and substitution of Eqs. 4.25, 4.26, 4.34 and 4.36 into Eq. 4.37 and then solving for j yields the product-inhibited Michaelis-Menten rate equation

$$j = \frac{k_2 N K_1 [H_2O_2]}{1 + K_4[O_2] + K_1[H_2O_2](1 + K_5[H^+])} \tag{4.38}$$

Inspection of Eq. 4.38 reveals that this product inhibited rate equation does not readily simplify to either first order kinetics at low [H_2O_2] or zero kinetics at high [H_2O_2]. This rate equation qualitatively allows for the variation in j_{max} with ω (in Fig. 4.1 and Table 4.3) and also transient inhibition at low [H_2O_2] seen in Fig. 4.6.

4.7.2 Incorporation of Mass Transport

The form of the rate equation is further complicated by recognition that the terms $[H_2O_2]$, $[O_2]$ and $[H^+]$ relate to the concentration of these species *at the electrode surface*.

Under steady-state conditions, the surface concentration may be related to the bulk concentration, the diffusion layer thickness and the rate at which the species is either being consumed or produced at the overall reaction, by application of Fick's First Law. Thus the surface concentrations of H_2O_2, O_2 and H^+ are given by

$$[H_2O_2] = [H_2O_2]_{bulk} - j k_D D_{H_2O_2}^{-2/3} \omega^{-1/2} \tag{4.39}$$

$$[O_2] = [O_2]_{bulk} + j k_D D_{O_2}^{-2/3} \omega^{-1/2} \tag{4.40}$$

$$[H^+] = [H^+]_{bulk} + 2j k_D D_{H^+}^{-2/3} \omega^{-1/2} \tag{4.41}$$

where k_D is given by

$$k_D = 1.61 \nu^{1/6} \tag{4.42}$$

$[O_2]_{bulk}$ and $[H^+]_{bulk}$ refer to the bulk concentrations of O_2 and H^+ respectively and D_{O_2} and D_{H^+} are the diffusion coefficients for these species. Substitution of the rate- and diffusion-dependent expressions 4.39 to 4.42 into the product-inhibited Michaelis-Menten rate Eq. 4.38 yields a third-order polynomial in rate in terms of the bulk concentrations of the reactant and products.

$$0 = \alpha j^3 + \beta j^2 + \chi j + \delta \tag{4.43}$$

where the polynomial coefficients are given by

$$\alpha = -2K_1K_5k_D^2 D_{H_2O_2}^{-2/3} D_{H^+}^{-2/3} \omega^{-1} \tag{4.44}$$

$$\beta = K_4 k_D D_{O_2}^{-2/3} \omega^{-1/2} + 2K_1K_5[H_2O_2]_{bulk} k_D D_{H^+}^{-2/3} \omega^{-1/2} - K_1 k_D D_{H_2O_2}^{-2/3} \omega^{-1/2} \left(1 + K_5[H^+]_{bulk}\right) \tag{4.45}$$

$$\chi = 1 + K_4[O_2]_{bulk} + k_2 N K_1 k_D D_{H_2O_2}^{-2/3} \omega^{-1/2} + K_1[H_2O_2]_{bulk} \left(1 + K_5[H^+]_{bulk}\right) \tag{4.46}$$

$$\delta = -k_2 N K_1 [H_2O_2]_{bulk} \tag{4.47}$$

Ascertaining the validity of the mechanism and evaluating the kinetic parameters requires comparison of the roots of this third-order polynomial with the experimental data.

4.7.3 Optimization of Parameters for Modified Michaelis-Menten Mechanism

The three real roots for a third-order polynomial in variable x of the general form

$$0 = x^3 + Ax^2 + Bx + C \tag{4.48}$$

where A, B and C are real, can be solved using Viète's method [160] in terms of an angle, ϕ, calculated by

$$\phi = \cos^{-1}\left(\frac{2A^3 - 9AB + 27C}{2\left(A^2 - 3AB\right)^{3/2}}\right) \tag{4.49}$$

The three roots λ_1, λ_2 and λ_3 are given by

$$\lambda_1 = -2\left(\frac{A^2 - 3B}{9}\right)^{1/2} \cos\left(\frac{\phi}{3}\right) - \frac{A}{3} \tag{4.50}$$

$$\lambda_2 = -2\left(\frac{A^2 - 3B}{9}\right)^{1/2} \cos\left(\frac{\phi + 2\pi}{3}\right) - \frac{A}{3} \tag{4.51}$$

$$\lambda_3 = -2\left(\frac{A^2 - 3B}{9}\right)^{1/2} \cos\left(\frac{\phi + 4\pi}{3}\right) - \frac{A}{3} \tag{4.52}$$

The rate equation polynomial given by Eq. 4.43 was transformed into the general form required for Viète's method by division of each of the polynomial coefficients by α. These operations were encoded in a purpose written computer program [161] incorporating a SIMPLEX [127-129,162] optimization routine as described in Section 2.9. Inspection of Eqs. 4.44 to 4.47 reveals that four mechanistic parameters require optimization; K_1, K_4, K_5 and the product k_2N. Values for D_{O_2} and D_{H^+} were obtained from the literature and taken as 1.93×10^{9} m^2 s^{-1} [155] and 9.31×10^{-9} m^2 s^{-1} [163] respectively. In light of the range of values for the diffusion coefficient of H_2O_2 obtainable from a series of Koutecky-Levich plots (as shown in Fig. 4.5), it was thought prudent to optimize this parameter together with the kinetic and binding constant

parameters in the SIMPLEX calculation. The SIMPLEX procedure was forced to deal with positive values of the parameters through optimization of the natural logarithm of each parameter.

The SIMPLEX procedure was primed with experimental rate values for each concentration and rotation rate shown in Fig. 4.1 with a constant bulk dissolved oxygen concentration of zero (given that the system was degassed rigorously before and during experimentation) and a bulk hydrogen ion concentration dictated by the electrolyte pH.

Initial optimization studies revealed that only one of the polynomial roots, λ_3, afforded positive real values for j. This significantly simplified the goal-seeking implicit in the SIMPLEX process. The parameters for the data set were optimized on this basis and a minimum in the sum of residuals, r_s, was obtained within 1000 iterations where r_s is given by

$$r_s = \sum (j - \lambda_3)^2 \tag{4.53}$$

for each data point (126 data points in the data set, i.e. 7 rotation rates × 18 values for $[H_2O_2]_{bulk}$). The average deviation between the observed and calculated current densities, $\bar{d}_{av}$, is given by

$$\bar{d}_{av} = nF\sqrt{\frac{r_s}{126}} \tag{4.54}$$

The optimized parameters are listed in Table 4.4 and synthetic i vs. $[H_2O_2]_{bulk}$ curves based on these values and transformed from rate using Eq. 4.32 are shown together with the experimental data in Fig. 4.1.

The synthetic response curves are in good agreement with the experimental data with small $\bar{d}_{av}$ (0.8% of maximum current density) and exhibiting no systematic deviations for any rotation rate or H_2O_2 concentration.

4.7.4 Interpretation of Optimised Parameters

Replicate sets of experimental data show equally good fits with small differences in the optimised parameters consistent with the expected variation in active surface area of the electrode.

The mechanism reported here is extremely sensitive to the diffusion coefficient for H_2O_2, with the sum of residuals exhibiting a sharp minimum for the optimised value. This value

Parameter	Value
K_1	0.357 m^3 mol^{-1}
k_2N	1.01×10^{-3} mol m^{-2} s^{-1}
K_4	0.149 m^3 mol^{-1}
K_5	0.054 m^3 mol^{-1}
$D_{H_2O_2}$	0.66×10^{-9} m^2 s^{-1}
r_s	5.45×10^{-9} (mol m^{-2} s^{-1})^2
$\bar{d}_{av}$	0.127 mA cm^{-2}

Table 4.4 Optimised parameters for the product-inhibited Michaelis-Menten mechanism given in Section 4.7.

is somewhat lower than those reported predominantly in the literature [54,155,156,164], a summary of which is presented in Table 4.5.

In this study an optimal value of $D_{H_2O_2}$ is found to be 0.66×10^{-9} m^2 s^{-1} whereas interpolation of the data presented in Table 4.4 would suggest a value approximately twice this at 20°C.

The methods used by these previous workers rely upon the assumption that the electrochemical reaction with H_2O_2 (either oxidation or reduction) is taking place under conditions where the reaction is entirely diffusion limited. The work presented here for the oxidation of H_2O_2 at platinum shows that this assumption is inappropriate and consequently affords misleading values for $D_{H_2O_2}$ from Koutecky-Levich plots. This is demonstrated in Fig. 4.5 where, depending on H_2O_2 concentration, $D_{H_2O_2}$ can be found in the range $0.6 - 1.4 \times 10^{-9}$ m^2 s^{-1}. These effects may be accounted for by inspection of the plot of calculated surface concentration data for H_2O_2, H^+ and O_2 in Fig. 4.7 at the lowest rotation rate explored as a function of bulk $[H_2O_2]$ based upon Eqs. 4.39 to 4.42 and the optimised rate parameters. It is clear that the surface concentration of H_2O_2 only approaches zero (and hence overall diffusion control) at low bulk concentrations; above 20 mM the surface concentration increases linearly and adopts a value some 18 mM below that of the bulk. The surface concentration of both O_2 and H^+ increase gradually and approach a plateau at above 40 mM of $[H_2O_2]_{bulk}$.

The surface concentration of these species at the highest rotation rate explored is plotted in Fig. 4.8 as a function of $[H_2O_2]_{bulk}$. The surface concentration of H_2O_2 increases rapidly and shows almost linear dependence with $[H_2O_2]_{bulk}$ except at the lowest concentrations. The slope and intercept of the linear curve were 0.9592 and –3.42 mM, respectively. It is clear that at this higher rotation rate the mass transport of H_2O_2 from bulk to electrode surface is increased. Simultaneously, the depletion of reaction products from electrode surface is also increased. The surface concentration of O_2 and H^+ species are significantly lower at 10000 rpm than at 630 rpm and approach a plateau at above 5 mM $[H_2O_2]_{bulk}$.

Both Figs. 4.7 and 4.8 clearly demonstrate that the earlier assumption of pure mass transport limitation is erroneous.

Honda et al. [165] have used a value for $D_{H_2O_2}$ of 0.5×10^{-9} m^2 s^{-1} which is similar to that found here and is ascribed to a report by Littauer and Tsai [166] on studies of H_2O_2

Workers	$\frac{D_{H_2O_2} \times 10^{-9}}{m^2 s^{-1}}$	$\frac{T}{°C}$	Methods
van Stroe-Biezen *et al.* [155]	1.43	25	Koutecky-Levich
van Stroe-Biezen *et al.* [155]	1.83	37	Koutecky-Levich
Brestovisky *et al.* [164]	1.2	not stated	Reverse Pulse Polarography
Prabhu *et al.* [54]	1.21 – 1.61	25	Chronoamperometry
Prabhu *et al.* [54]	1.07 – 1.56	25	Chronopotentiometry
Borggaard [156]	0.88	10	Polarography
Borggaard [156]	1.35	20	Polarography
Borggaard [156]	1.75	30	Polarography
Borggaard [156]	2.20	40	Polarography
this work	0.66	20	Michaelis-Menten kinetics

Table 4.5 Reported values for the diffusion coefficient of hydrogen peroxide.

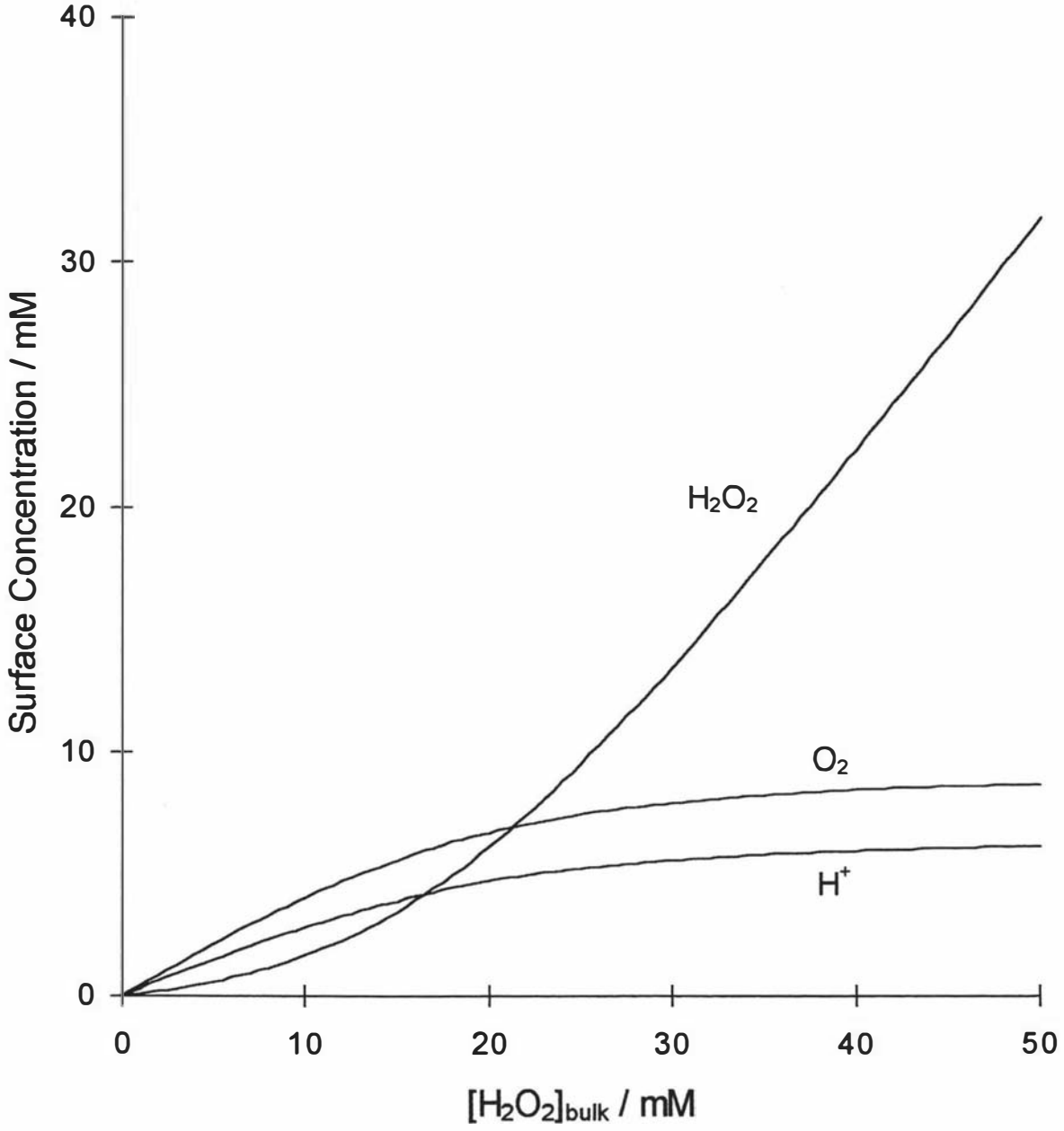

Fig. 4.7 Calculated surface concentrations for H_2O_2, O_2 and H^+ as a function of $[H_2O_2]_{bulk}$ based on the optimized model parameters for a rotation rate of 630 rpm.

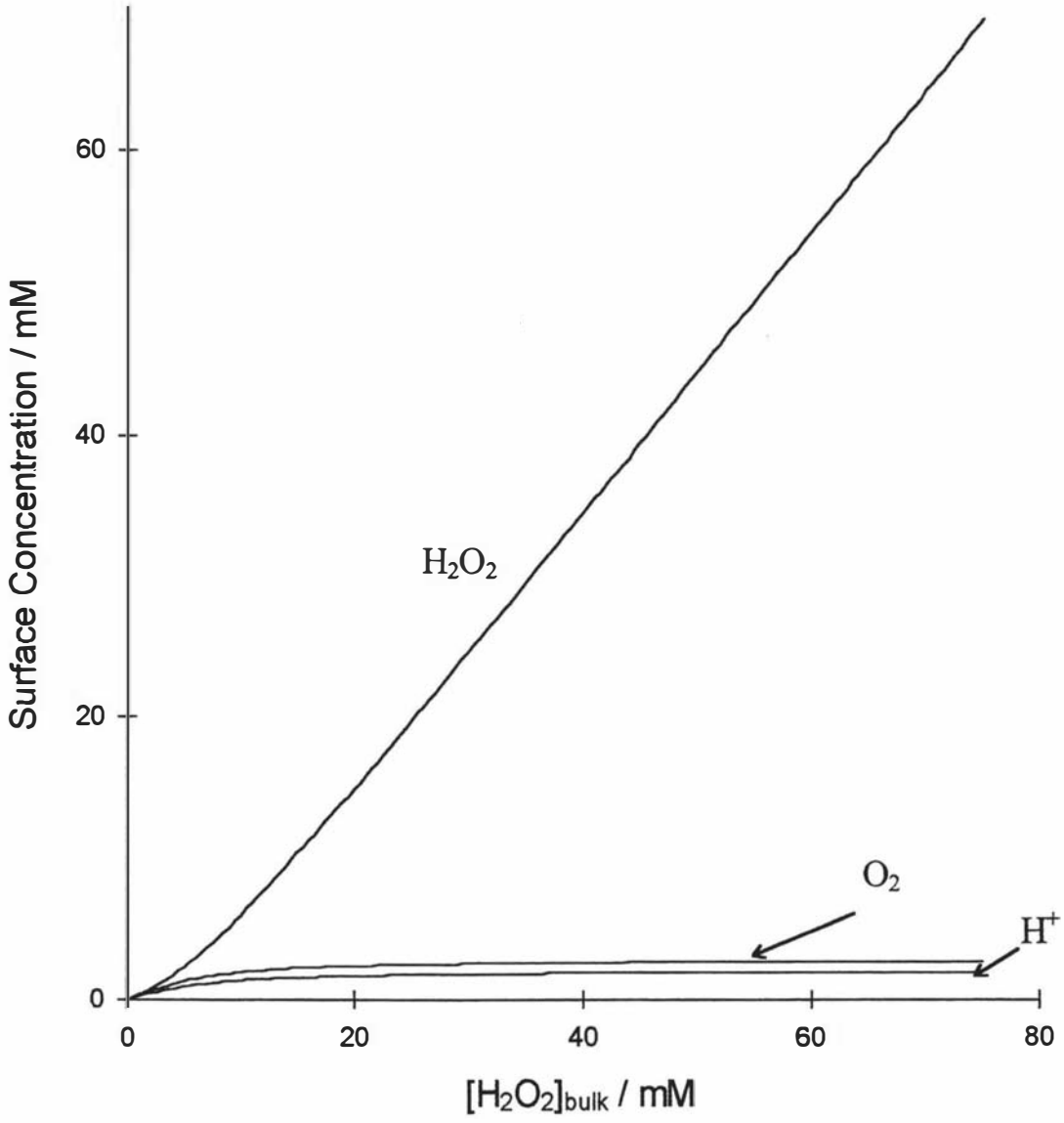

Fig. 4.8 Calculated surface concentrations for H_2O_2, O_2 and H^+ as a function of $[H_2O_2]_{bulk}$ based upon the optimized model parameters for a rotation rate of 10000 rpm.

in alkaline solutions. Inspection of the article by Littauer and Tsai [166], however, reveals this value was interpreted as being appropriate for the perhydroxy ion rather than H_2O_2 and cannot be taken as supporting evidence for the value reported in this study.

Whilst a single new value for $D_{H_2O_2}$ is reported here that accounts for both surface reaction kinetics and non-diffusion limited conditions, validation of this new value is desirable through some independent means.

Figures 4.9 and 4.10 display the calculated fractional coverages for each surface species in this mechanism as a function of bulk H_2O_2 concentration at the highest and lowest rotation rates respectively. At all rotation rates the fractional coverage of the binding site, $Pt(OH)_2$, decreases rapidly with increasing $[H_2O_2]_{bulk}$ with a concomitant increase in coverage of the $Pt(OH)_2.H_2O_2$ complex. This increase continues until a plateau is achieved which corresponds to the maximum observed reaction rate according to Eqs. 4.3 and 4.26. The coverage at the plateau is determined by the extent of inhibition at each rotation rate. The two inhibiting reactions prevail over two separate concentration regions.

Dioxygen inhibition forms a transient surface species at low concentrations through complexation with the binding site in competition with H_2O_2. This is particularly pronounced at low rotation rates where there is a greater surface concentration of O_2 than at higher rotation rates. This inhibition is the predominant cause for the dependence on ω for the linear response at low $[H_2O_2]_{bulk}$ as shown in Fig. 4.1. The ratio of the binding constants for H_2O_2 and O_2, K_1/K_4, is such that surface complexation of H_2O_2 is favoured. Consequently, a maximum for surface coverage by O_2 inhibition is evident as $[H_2O_2]_{bulk}$ is increased, the maxima having greatest values at low rotation rates as shown in Figs.4.9 and 4.10. This behaviour accounts for the pronounced deviation at low rotation rates and low $[H_2O_2]_{bulk}$ in the series of Hanes plots shown in Fig. 4.6.

Inhibition by protonation of the $Pt(OH)_2{\cdot}H_2O_2$ complex follows the development of this species due to the requirement for prior formation of the complex and the consummate increase in surface concentration of H^+ with increasing oxidation rate. Thus, a plateau in surface coverage of the protonated $Pt(OH)_2{\cdot}H_2O_2$ complex is evident with greatest coverage at low rotation rates.

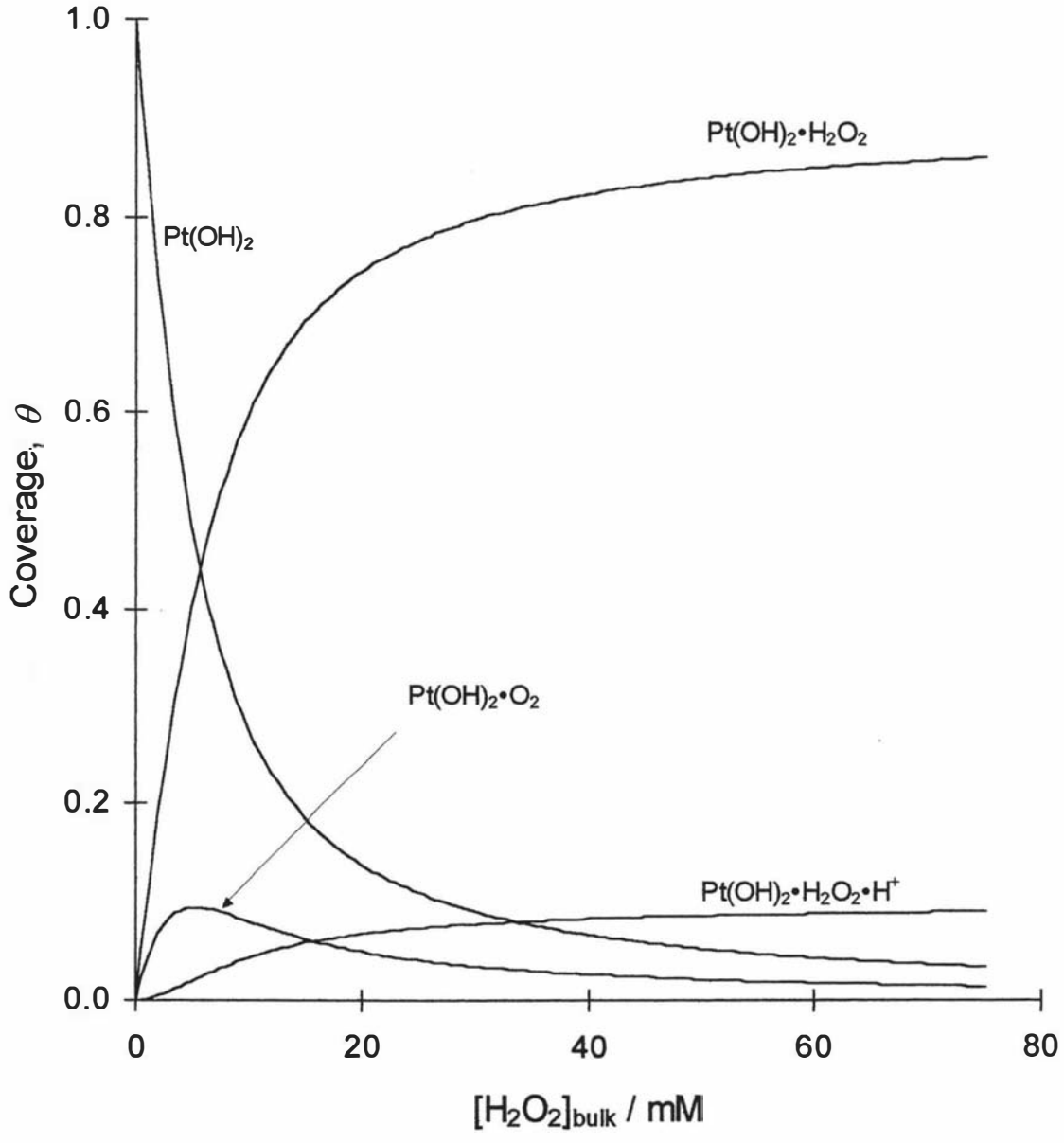

Fig. 4.9 Calculated surface coverages of all surface species involved in the mechanism as a function of $[H_2O_2]_{bulk}$ based on the optimised model parameters for a rotation rate of 10000 rpm.

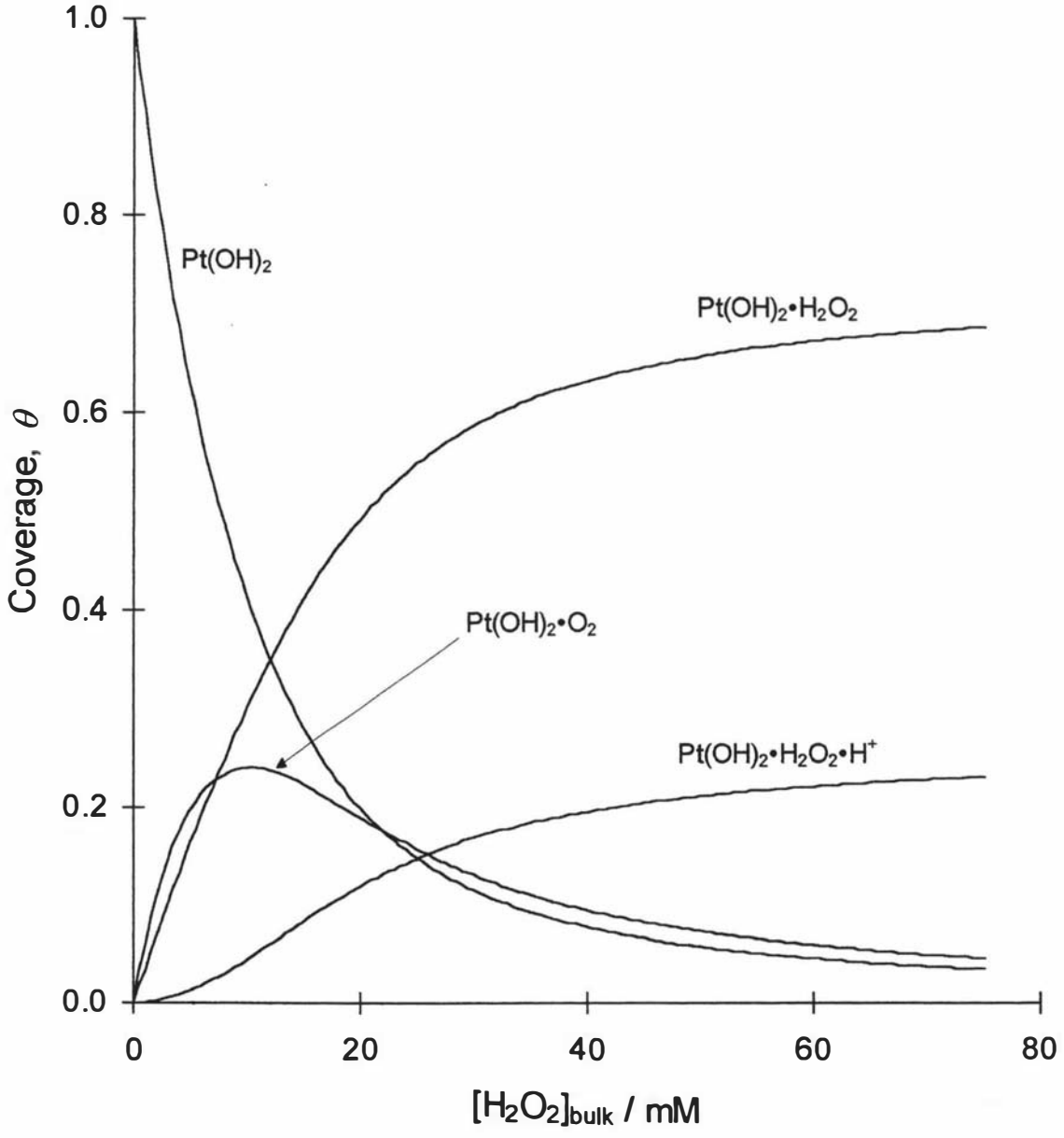

Fig. 4.10 Calculated surface coverages of all surface species involved in the mechanism as a function of $[H_2O_2]_{bulk}$ based on the optimised model parameters for a rotation rate of 630 rpm.

An operational value for K_M may be evaluated for each rotation rate. This parameter does not directly relate to the binding constant K_1 due to the combination of the two inhibiting equilibria.

The rate equation for the product-inhibited Michaelis-Menten stated in Eq. 4.38 can be rearranged and rewritten in the form of a Hanes plot as

$$\frac{[H_2O_2]}{j} = \frac{1+K_4[O_2]}{k_2NK_1} + \frac{1+K_5[H^+]}{k_2N}[H_2O_2] \tag{4.55}$$

The slope and intercept are given by

$$\text{slope} = \frac{1+K_5[H^+]}{k_2N} \tag{4.56}$$

$$\text{intercept} = \frac{1+K_4[O_2]}{k_2NK_1} \tag{4.57}$$

At high rotation rates when $\omega \rightarrow \infty$, the surface concentrations of species involved in product inhibition approach zero leading to the theoretical Michaelis-Menten mechanism in the absence of product inhibition (the simplest model) given in Section 4.6 where

$$j_{max} = k_2N \tag{4.58}$$

and

$$K_M = \frac{1}{K_1} \tag{4.59}$$

Otherwise, at lower rotation rates, the term K_M should involve the two product inhibition equilibrium constants given by division of Eq. 4.57 by Eq. 4.56

$$K_M = \frac{1+K_4[O_2]}{K_1(1+K_5[H^+])} \tag{4.60}$$

Consequently, inspection of Figs. 4.9 and 4.10 reveals that K_M (defined as the concentration for half coverage by the $Pt(OH)_2{\cdot}H_2O_2$ complex) has a value of 20.5 mM at 630 rpm which decreases to 7.1 mM at 10000 rpm. The latter value approaches the theoretical value of 2.8 mM given by the inverse of the optimal K_1 (given in Table 4.4) for an infinitely high rotation rate where the two inhibiting reactions would be absent.

4.8 Conclusions

A mechanistic model (reactions 4.2 – 4.4, 4.33 and 4.35) based on modified Michaelis-Menten kinetics for the electrochemical oxidation of H_2O_2 at platinum electrode is proposed which incorporates inhibition modes caused by both reaction products, O_2 and H^+. This study has demonstrated the need for controlling mass-transport conditions for this reaction, since these determine the extent of product-inhibition.

Whilst a mechanism is proposed based on interpretation of experimental data collected over a wide range of $[H_2O_2]$ and rotation rates, there is no reason to expect this not to follow at the low concentrations likely to be encountered in biosensors. Maximum electrode response and sensitivity can only be obtained under conditions where the products are rapidly removed from the vicinity of the electrode. The validation of this model must be examined for a range of potentials, since the electrode reaction proceeds in several consecutive steps, each of which may have potential-dependent electrochemical rate constants.

CHAPTER FIVE

The Effect of Potential on the Electrochemical Oxidation of Hydrogen Peroxide at Platinum Electrodes

5.1 Introduction

A mechanism for the electrochemical oxidation of H_2O_2 at platinum rotating disc electrodes employing a chronoamperometric (CA) method was described in the previous chapter to account for the steady-state current response as a function of both $[H_2O_2]$ and electrode rotation rate.

The CA method employed was based upon the application of a constant potential step to the electrode, and showed that the oxidation of H_2O_2 is both kinetically and mass transport controlled, involving both the reactant and the two products.

The proposed mechanism incorporated the binding of H_2O_2 to a platinum (II) binding site with two inhibition modes caused by the reaction products O_2 and H^+.

The main reaction scheme is summarised as follows:

$$H_2O_2 + Pt(OH)_2 \overset{K_1}{\rightleftharpoons} Pt(OH)_2 \cdot H_2O_2 \qquad (4.2)$$

$$Pt(OH)_2 \cdot H_2O_2 \xrightarrow{k_2} Pt + 2H_2O + O_2 \qquad (4.3)$$

$$Pt + 2H_2O \xrightarrow{k_3} Pt(OH)_2 + 2H^+ + 2e^- \qquad (4.4)$$

H_2O_2 near the electrode surface is in rapid equilibrium with the Pt(II) binding site as described in reaction 4.2. The binding site could well involve Pt(IV) since Anson and Lingane [63] have detected this oxidation state together with Pt(II) on the surface of platinum. If this were the case in the present study, then reaction 4.3 would involve the two electron reduction of Pt(IV) to Pt(II). This would not alter the form of the ensuing kinetic analysis. The adsorption constant K_1 for this process is given by

$$K_1 = \frac{\theta_{Pt(OH)_2 \cdot H_2O_2}}{[H_2O_2]\,\theta_{Pt(OH)_2}} \qquad (4.25)$$

where θ_i refers to the fractional surface coverage of each species i and the concentration is that at the surface of the electrode unless otherwise identified as bulk concentration in this and following expressions.

It was assumed that a sufficiently anodic potential was applied (+600 mV vs. Ag/AgCl) so that $k_3 >> k_2$ and reaction 4.3 became rate limiting and the overall reaction was given by

$$j = k_2 N \theta_{Pt(OH)_2 \cdot H_2O_2} \tag{4.26}$$

where N is the number of binding sites per m^2. Saturation and a maximum current is exhibited as $\theta_{Pt(OH)_2 \cdot H_2O_2} \rightarrow 1$.

Two inhibiting binding modes were identified. The first involves competitive binding of O_2 to the Pt(II) site so that reaction 4.2 is inhibited

$$Pt(OH)_2 + O_2 \overset{K_4}{\rightleftharpoons} Pt(OH)_2 \cdot O_2 \tag{4.33}$$

where the competitive inhibition binding constant K_4 is given by

$$K_4 = \frac{\theta_{Pt(OH)_2 \cdot O_2}}{[O_2]\,\theta_{Pt(OH)_2}} \tag{4.34}$$

The second involves reversible protonation of the surface $Pt(OH)_2 \cdot H_2O_2$ complex where the protons are the product of reaction 4.4

$$Pt(OH)_2 \cdot H_2O_2 + H^+ \overset{K_5}{\rightleftharpoons} Pt(OH)_2 \cdot H_2O_2 \cdot H^+ \tag{4.35}$$

The protonation constant K_5 is given by

$$K_5 = \frac{\theta_{Pt(OH)_2 \cdot H_2O_2 \cdot H^+}}{[H^+]\,\theta_{Pt(OH)_2 \cdot H_2O_2}} \tag{4.36}$$

Given that $\theta_{Pt} \rightarrow 0$ under these condition, applying the steady-state approximation and solving for j yielded the product-inhibited rate equation in terms of the surface concentration of each solution species.

$$j = \frac{k_2 N K_1 [H_2O_2]}{1 + K_4[O_2] + K_1[H_2O_2]\left(1 + K_5[H^+]\right)} \tag{4.38}$$

Since steady-state conditions prevailed, the surface concentrations were related to bulk concentrations through use of Fick's First Law and the Nernst diffusion layer thickness

controlled by the rotation rate. Substitution of these rate-dependent expressions into Eq. 4.38 resulted in a third-order polynomial in terms of bulk concentrations and electrode rotation rates. The validity of the mechanism was tested, and evaluation of kinetic and equilibrium parameters achieved, using a SIMPLEX [127-129,162] optimisation of the most positive root of this polynomial calculated directly using Viète's method [160]. In addition to determining the applicability of this new mechanism, a new value of the diffusion coefficient for H_2O_2 ($D_{H_2O_2} = 0.66 \times 10^{-9}$ m^2 s^{-1}) was evaluated.

Since the proposed mechanism proceeded in several consecutive steps with potential-dependent rate constants, the validity of this mechanism should be tested at steady-state conditions over a range of potentials.

This chapter, therefore, is concerned with the possibility that the electrochemical re-oxidation of surface sites described by reaction 4.4 may become the rate limiting step at less anodic potentials than used in the previous chapter. In addition, the rate equation for surface species concentration given by Eq. 4.38 could be modified to involve both potential-dependent rate constants.

To achieve this requirement, a pulse-step method was accomplished by using staircase potentiometery (SCP) technique to monitor the oxidation current response. This technique was described in Chapter 3, Section 3.3.

5.2 Experimental Conditions

5.2.1 Reagents and Electrodes

All chemicals, reagents, electrodes and electrochemical equipment used in this study are outlined in the previous chapter, Section 4.2 and in Chapter 2.

5.2.2 Electrochemical Methodology

Chronoamperometric measurements of the oxidation of H_2O_2 were made using staircase potentiometry over the potential range +232 to +712 mV. Potentials more anodic than this upper limit were not considered due to the likely interference from competitive oxidation of the solvent. The time for a steady-state response to be attained was found to be a complex function of H_2O_2 concentration, electrode rotation rate and anodic potential. It was established in preliminary work that a step height of 32 mV and depth of

8 s permitted steady-state measurements at the end of each step (the response for the last 17 ms is reported in this study). The step depth is substantially shorter that the 20 s used for the single potential step experiments reported in the previous chapter since each step in the staircase intrinsically involves less reaction rate alteration to achieve a steady-state than in stepping from +200 to +600 mV in CA experiments.

The electrochemical measurements were made over the $[H_2O_2]$ range 0 – 80 mM and for rotation rates, ω, of 630, 1000, 1585, 2500, 4000, 6300 and 10000 rpm.

The constants for the model were optimized using a SIMPLEX [127-129,162] algorithm encoded in the software package [161] (further modified during this work to give the program EVARY).

5.3 Steady–State Current Response

The steady-state current response of a platinum rotating disc at +584 mV vs Ag/AgCl and 20 °C to a range of $[H_2O_2]_{bulk}$ and electrode rotation rates is shown in Fig. 5.1. This figure is plotted in a similar manner to Fig. 4.1 in Chapter 4 using the CA method. The current response increases linearly with $[H_2O_2]_{bulk}$ in the range 0–10 mM and adopts a limiting value at $[H_2O_2]_{bulk}$ > 50 mM. The limiting current also shows rotation rate dependency as a result of increasing the mass transport of bulk H_2O_2.

5.4 Potential Dependence

The steady-state responses for the oxidation of bulk H_2O_2 for a series of anodic potentials at a single rotation rate are shown in Fig. 5.2. The current responses for potential amplitude at +232 mV are not included in this diagram since cathodic currents were recorded. The data presented in this figure represents 1/7 of that collected (7 rotation rates) for a single series of experiments with no intervening electrode conditioning (either physical or electrochemical) between successive concentrations or rotation rates. The current increases with $[H_2O_2]_{bulk}$ in a similar manner to that observed in Fig. 5.1 and approaches a limiting current. The concentration at which limiting currents are reached increases in an approximately linear fashion with applied potential. At each anodic potential, the dependence of current on electrode rotation rate is observed identically to that shown in Fig. 5.1, although the relative increase in response between high and low rotation rates becomes more pronounced with higher potentials.

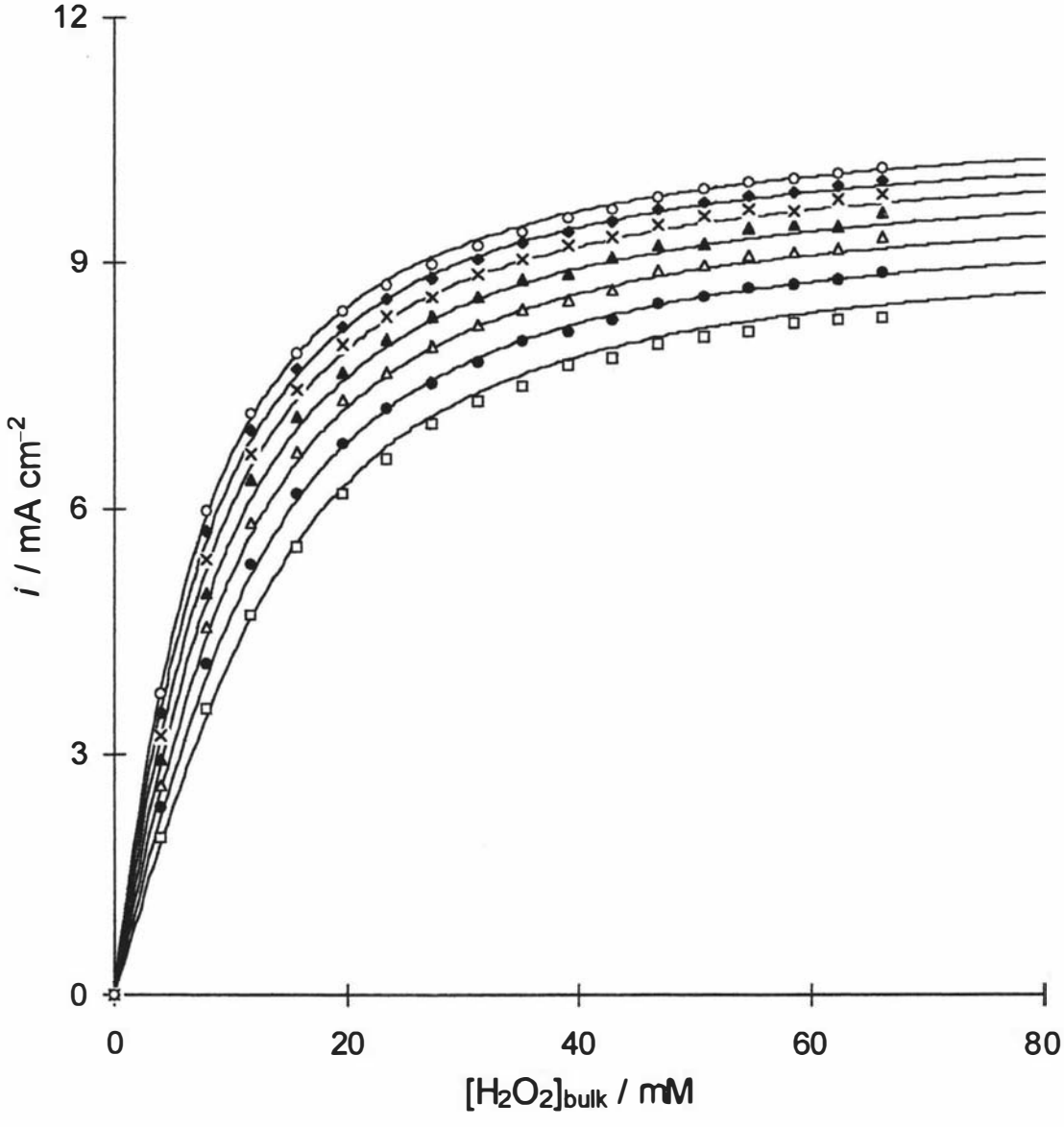

Fig. 5.1 Steady-state current response at +584 mV vs Ag/AgCl as a function of $[H_2O_2]_{bulk}$ for a range of rotation rates; □ 630, ● 1000, Δ 1585, ▲ 2500, × 4000, ◆ 6300 and O 10000 rpm. Smooth curves are the synthetic responses calculated using the model and parameters developed during this study.

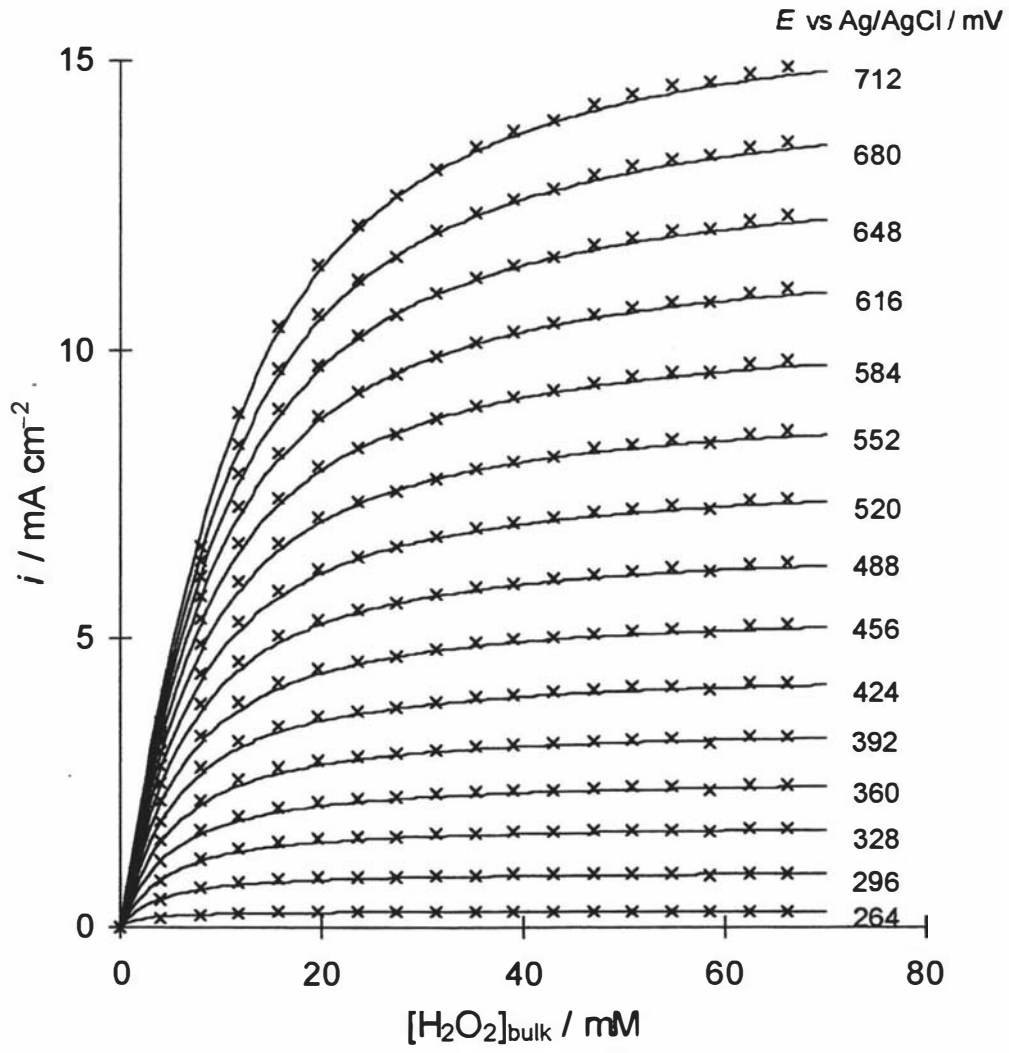

Fig. 5.2 Steady-state current responses (×) at a fixed rotation rate (ω = 4000 rpm) and constant temperature (T = 20 °C) as a function of $[H_2O_2]_{bulk}$ for a range of anodic potentials. Smooth curves are the synthetic responses calculated using the model and parameters developed in this study.

This is to be expected, since the mechanism proposed in Chapter 4 involves product inhibition and the extent of this inhibition increases with overall reaction rate.

In the derived rate equation for a fixed anodic potential given by Eq. 4.38 it was assumed that the rate of re-oxidation of surface sites described by reaction 4.4 was rapid. Since this process involves the flow of electrons into the bulk of the electrode, the possibility exists at less anodic potentials that reaction 4.4 becomes comparable in rate with the preceding reduction of the H_2O_2 bound site given in reaction 4.3. If this were the case then the steady-state assumption that $\theta_{Pt} \rightarrow 0$ would be invalid and the overall rate would be described by

$$j = k_3 N \theta_{Pt} \tag{4.27}$$

as well as by Eq. 4.26. The fractional surface coverage mass-balance expression would now be given by

$$1 = \theta_{Pt(OH)_2} + \theta_{Pt(OH)_2 \cdot H_2O_2} + \theta_{Pt} + \theta_{Pt(OH)_2 \cdot O_2} + \theta_{Pt(OH)_2 \cdot H_2O_2 \cdot H^+} \tag{5.1}$$

Applying the steady-state conditions to the adsorbed species, substitution of Eqs. 4.25-4.27, 4.34, 4.36 into 5.1 and solving for j yields

$$j = \frac{k_2 N K_1 [H_2O_2]}{1 + K_4[O_2] + K_1[H_2O_2]\left(1 + K_5[H^+] + k_2/k_3\right)} \tag{5.2}$$

This modified rate equation simplifies to Eq. 4.38 under conditions where $k_3 >> k_2$ at high anodic potentials. Inspection of Eq. 5.2 reveals that the ratio k_2 / k_3 is an inseparable term in a similar manner to k_2N. However, from these the term k_3N can be evaluated.

Substitution of Fick's First Law expressions relating surface to bulk concentrations in terms of electrode rotation rate (described in previous chapter) yields a third order polynomial in terms of the bulk concentrations of the reactant and products in mol m^{-3}, electrode rotation rate ω in rad s^{-1} and diffusion coefficients for each solution species in $m^2\ s^{-1}$.

$$0 = \alpha j^3 + \beta j^2 + \chi j + \delta \tag{4.43}$$

where the polynomial coefficients are given by

$$\alpha = -2 K_1 K_5 k_D{}^2 D_{H_2O_2}{}^{-2/3} D_{H^+}{}^{-2/3} \omega^{-1} \tag{4.44}$$

$$\beta = K_4 k_D D_{O_2}^{-2/3} \omega^{-1/2} + 2K_1 K_5 [H_2O_2]_{bulk} k_D D_{H^+}^{-2/3} \omega^{-1/2} - K_1 k_D D_{H_2O_2}^{-2/3} \omega^{-1/2} \left(1 + K_5 [H^+]_{bulk} + k_2 / k_3\right) \quad (5.3)$$

$$\chi = 1 + K_4 [O_2]_{bulk} + k_2 N K_1 k_D D_{H_2O_2}^{-2/3} \omega^{-1/2} + K_1 [H_2O_2]_{bulk} \left(1 + K_5 [H^+]_{bulk} + k_2 / k_3\right) \quad (5.4)$$

$$\delta = -k_2 N K_1 [H_2O_2]_{bulk} \quad (4.47)$$

The diffusion constant k_D is given by

$$k_D = 1.61 \nu^{1/6} \quad (4.42)$$

where ν is the kinematic viscosity and is taken to be 1.00×10^{-6} m^2 s^{-1} [154].

5.5 Optimization of Parameters Involved in the Modified Rate Equation

The kinetic and equilibrium parameters were evaluated in an identical manner to that reported in Chapter 4 by optimisation of the most positive root of this polynomial determined by Viète's method [160]. The optimisation was a two-stage process. One routine controlled the optimisation of the potential-invariant parameters for the complete data set and initiated the second optimisation for the potential-dependent parameters at each anodic potential.

Two distinct objectives were identified in the present work. The first was to establish whether the assumed potential-invariant parameters (binding constants K_1, K_4 and K_5 and the diffusion coefficients) were able to satisfactorily account for the experimental data over all the potential range explored. Inspection of Fig. 5.2 reveals that the limiting current is dependent on potential, a strong indication that k_2N is varying with potential. The second was to ascertain whether significant improvement in fitting to the experimental data is obtained if the re-oxidation of the reduced surface site is considered through the use of Eq. 5.2 rather than the simpler form given by Eq. 4.38.

The data set consisted of 1890 steady-state values (7 rotation rates × 18 concentrations × 15 potentials) used for optimising common potential-invariant values for K_1, K_4 and K_5.

The values for D_{O_2} and D_{H^+} were identical to those used previously in Chapter 4 and were 1.93×10^{-9} m^2 s^{-1} [155] and 9.31×10^{-9} m^2 s^{-1} [163] respectively.

There is a discrepancy between the values for $D_{H_2O_2}$ reported previously [54,155,156, 164] (determined using erroneous techniques) and the low value evaluated by the proposed mechanism given in Chapter 4, Table 4.5. Consequently, this parameter was included in the optimisation procedure as a potential–invariant parameter also.

Table 5.1 lists the optimised equilibrium and diffusion parameters with and without consideration of the ratio k_2 / k_3 in the optimisation ($k_2 / k_3 = 0$ and k_2 / k_3 optimised respectively). The sum of residuals r_s for each of the two models is given by

$$r_s = \sum (j - \lambda_3)^2 \tag{4.53}$$

where λ_3 is the most positive root of the polynomial expression 4.43 given by Viète's method and the average deviations d_{av},

$$d_{av} = nF\sqrt{\frac{r_s}{n_p}} \tag{4.54}$$

(where the number of points n_p = 1890), are also listed in Table 5.1.

Inspection of Table 5.1 reveals that the first objective of this work is met. Irrespective of whether k_2 / k_3 is included as a potential dependent parameter or not, the average deviation is comparable to (and slightly lower than) that reported in Chapter 4 (0.127 mA cm^{-2}) even though single values for each K_1, K_4, K_5 and $D_{H_2O_2}$ are employed over 15 anodic potentials simultaneously. This result offers further supporting evidence for the new mechanism.

The sum of residuals is clearly decreased with the inclusion of k_2 / k_3. In general, one should adopt the simplest model that adequately describes the experimental data. The question to be answered is whether the decrease in the sum of residuals is sufficient to warrant inclusion of this extra parameter. The use of the variance ratio F-test has been used to evaluate the statistical validity of adopting a more complex model over a simpler form [167-169]. The ratio F is calculated from Eq. 5.5

$$F(\phi_2 - \phi_1, \phi_1) = \frac{(r_{s2} - r_{s1})/(\phi_2 - \phi_1)}{r_{s1}/\phi_1} \tag{5.5}$$

where r_{s1} and r_{s2} are the sums of residuals and ϕ_1 and ϕ_2 are the degrees of freedom associated with the more complex and simple model respectively.

Parameter	Model	
	$k_2 / k_3 = 0$	k_2 / k_3 optimised
K_1 / m^3 mol^{-1}	0.206	0.177
K_4 / m^3 mol^{-1}	0.135	0.111
K_5 / m^3 mol^{-1}	0.063	0.073
$D_{H_2O_2}$ / 10^{-9} m^2 s^{-1}	0.53	0.55
r_s / 10^{-9} (mol m^{-2} s^{-1})^2	7.58	7.08
d_{av} / mA cm^{-2}	0.122	0.118

Table 5.1 Optimised equilibrium and diffusion parameters with and without consideration of k_2 / k_3 (n_p = 1890 data points).

The number of degrees of freedom are given by

$$\phi = n_p - p - 1 \tag{5.6}$$

where n_p is the number of steady-state measurements and p is the number of optimised parameters. The more complex model has $p_1 = 6$ (K_1, K_4, K_5, $D_{H_2O_2}$, k_2N and k_2 / k_3) whilst the simple model has $p_2 = 5$. The higher the value of the ratio F, the more unlikely it will be that the null hypothesis

$$H_o \equiv r_{s1} = r_{s2} \tag{5.7}$$

will be true and that the more likely that the complex model is the more appropriate one. Using the data presented in Table 5.1, F is calculated to be 133. The calculated value for F is markedly higher than the critical value $F_{0.999}(1,\infty) = 10.83$ for 99.9% confidence [170] (values for F are only tabulated to 120 degrees of freedom, hence use of $F_{0.999}(1,\infty)$), so that the more complex model incorporating k_2 / k_3 stated above by Eq. 5.2 should be used in all subsequent work.

5.6 Variation of Heterogeneous Rate Constants with Potential

The variation of k_2N and k_3N with potential is shown as a logarithmic plot in Fig. 5.3, where k_3N was calculated from k_2N and k_2 / k_3. This clearly shows that k_3N is greater than k_2N for most potentials and only becomes equal to k_2N at +271 mV. These values were used together with the third order polynomial rate expressions for the more complex model, Eqs. 4.42, 4.44, 4.47, 5.3 and 5.4 to calculate the smooth curves plotted together with the experimental data in Fig. 5.2. The agreement between these calculated responses and the steady-state measurements is very good, with only small systematic deviations at low concentrations, which may suggest some over-estimation of the transient O_2 inhibition. Plots generated for the other electrode rotation rates explored demonstrate similarly good fits.

One should be cautious when modeling kinetic data so as to avoid merely performing an exercise in multiparametric curve fitting. Indeed, it is likely that a general polynomial expression might be identified that affords a comparable fit to the experimental data to that reported here. In such empirical cases, the coefficients may not have any chemical significance.

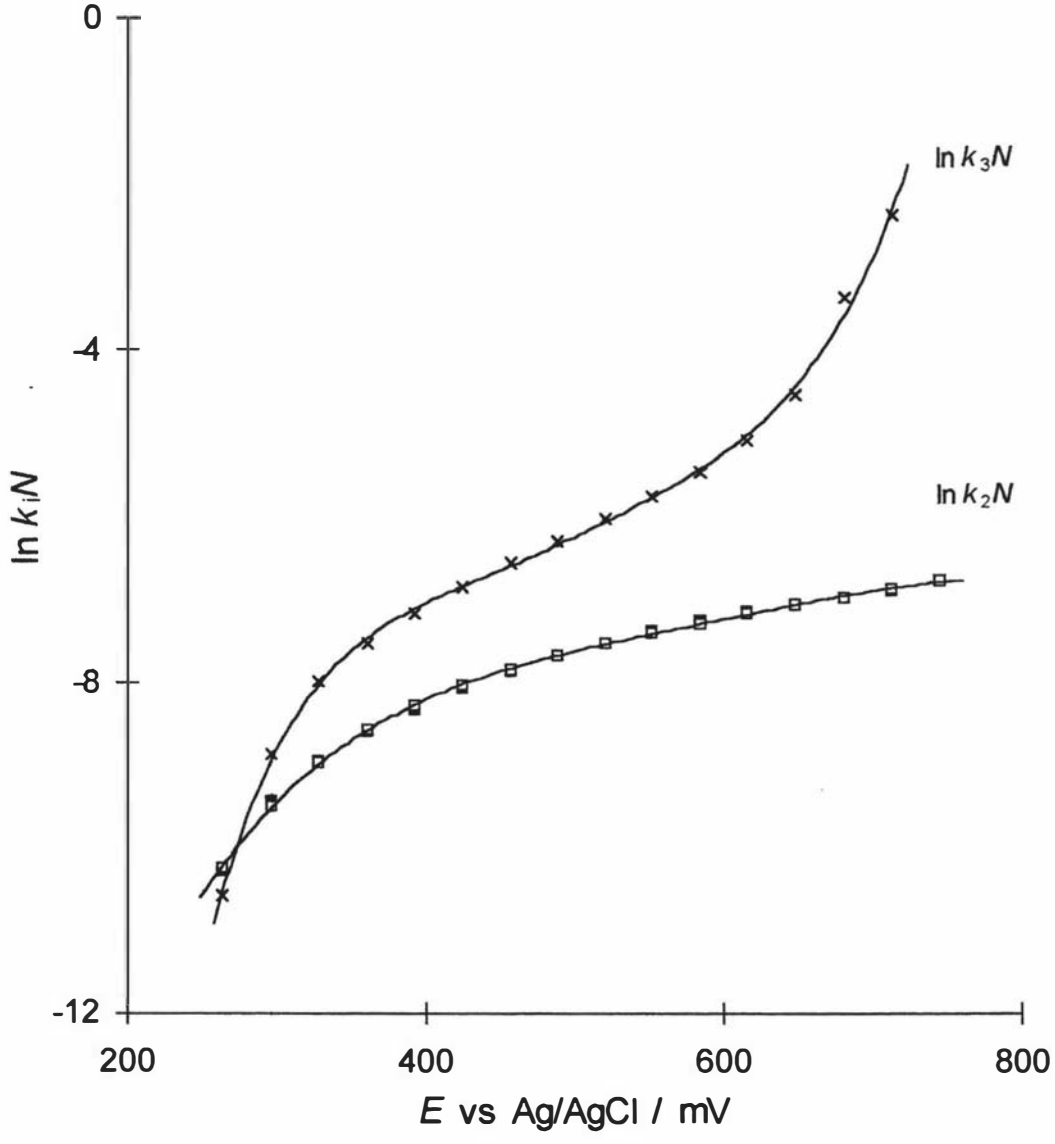

Fig. 5.3 Logarithmic plot of the optimised kinetic parameters k_2N and k_3N as a function of potential. Smooth curves are the empirical curves of best fit given by Eqs. 5.8 and 5.9.

In the present study, a strategy similar to that routinely employed in enzyme kinetic studies has been adopted. Equations arising from a series of proposed mechanistic steps were fitted. The fitted parameters are the accompanying kinetic and equilibrium constants and thus have chemical relevance.

At this stage there is no independent support for the optimised constants. The value for K_1 is similar, however, to that indicated by Johnston *et al.* [101] for the binding of H_2O_2 to evaporated gold/palladium composite electrodes. The variation of both k_2N and k_3N with potential are internally consistent with the extrapolated maximum currents obtained for high rotation rates.

Figure 5.4 shows the variation in current density as a function of anodic potential for a number of concentrations at a fixed rotation rate. Linear regression of the steady-state responses in the potential range +232 to +328 mV indicates an open circuit potential of +244 mV. The smooth curves are calculated again using the rate expressions 4.42, 4.44, 4.47, 5.3 and 5.4 together with continuous functions for k_2N and k_2 / k_3 derived from the data presented in Fig. 5.3. The simplest expression describing k_2N as a logarithmic function of potential is given by

$$\ln k_2N = 2.905 \times E - 8.916 - 0.288 \times \exp\left[11.272 \times (0.439 - E)\right] \tag{5.8}$$

whilst k_3N may be described by

$$\begin{aligned} \ln k_3N = {} & -21789E^6 + 67217E^5 - 84788E^4 + 56107E^3 \\ & - 20590E^2 + 3991.4E - 328.56 \end{aligned} \tag{5.9}$$

where the potential E is in volts vs. Ag/AgCl. The smooth curves in Fig. 5.4 show slightly poorer fit than those in Fig. 5.2 especially at the lower concentrations, consistent with the preceding observations on systematic deviations identified above. Hence the curve for the lowest concentration plotted in Fig. 5.4 indicates that the model under-estimates the response in the range +200 to +700 mV and over-estimates above this.

The rate limiting steps

$$Pt(OH)_2 \cdot H_2O_2 \xrightarrow{k_2} Pt + 2H_2O + O_2 \tag{4.3}$$

$$Pt + 2H_2O \xrightarrow{k_3} Pt(OH)_2 + 2H^+ + 2e^- \tag{4.4}$$

are unlikely to be true elementary steps since each involves significant bond-breaking and bond-making, coupled with the movement of two electrons. Thus, the values identified

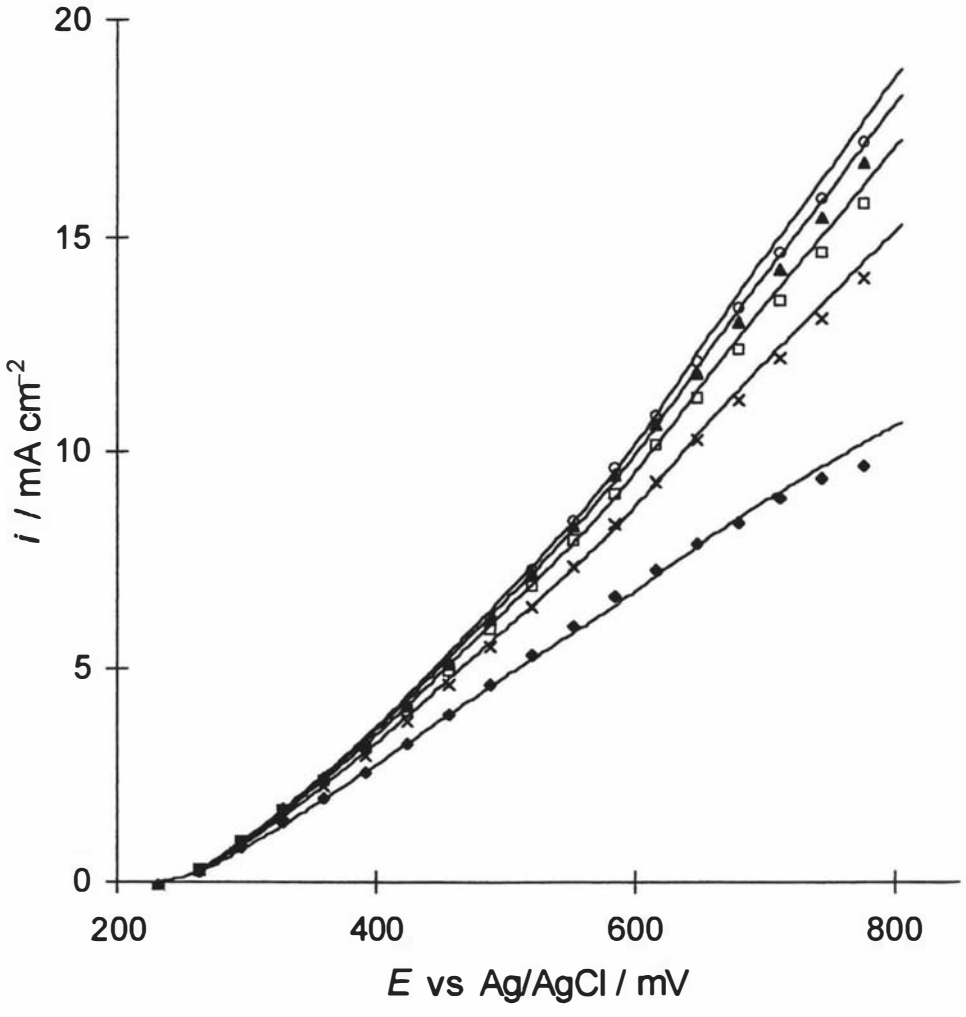

Fig. 5.4 Steady-state current responses at a fixed rotation rate (ω = 4000 rpm) as a function of potential for a selection of $[H_2O_2]_{bulk}$; ◆ 11.8 mM, × 23.5 mM, □ 35.2 mM, ▲ 46.9 mM and O 58.5 mM. Smooth curves are the synthetic responses calculated using the model and parameters developed in this study incorporating the empirical best fit relationships for k_2N and k_3N as a function of potential given by Eqs. 5.8 and 5.9.

for k_2N and k_3N must represent the rate of the slowest elementary steps in the processes that summate to give reactions 4.3 and 4.4. Furthermore, the ability to evaluate k_3N is also complicated by this parameter being derived from the optimised ratio k_2 / k_3. This ratio will inherently suffer in accuracy during optimisation at high potentials, where $k_2 / k_3 << 1$ since it is involved as a multiplying factor in Eqs. 5.3 and 5.4 as a term $\left(1 + K_5[\mathrm{H}^+]_{\mathrm{bulk}} + k_2 / k_3\right)$. Consequently, values for k_3N above +616 mV are not reported with any great confidence due to the low values of k_2 / k_3 optimised.

Despite reactions 4.3 and 4.4 being unlikely to be elementary steps, it is reasonable for both terms k_2N and k_3N to increase in exponential manner with potential. The plots of $\ln k_2N$ against potential in Fig. 5.3 demonstrate, however, that deviations from linearity are evident at low potentials. This deviation could be due to one of the following reasons. The first is that at anodic potentials close to the open circuit potential there is significant competition from simultaneous reduction of H_2O_2, and the observed value for k_2N may well represent the true value less the extent of reduction. The second possiblity is that k_2 changes exponentially over all potentials, whilst the number of sites, N, changes at low potentials. The latter interpretation can be explored further by inspection of the empirical expression for $\ln k_2N$ as a function of potential given by Eq. 5.8. The exponential component could describe the variation of the ratio N/N_{max}, where N_{max} is the maximum number of surface sites determined by the Pt lattice.

$$\ln N / N_{\mathrm{max}} = -0.288 \times \exp\left[11.272 \times \left(0.439 - E\right)\right] \qquad (5.10)$$

This function is shown in Fig. 5.5 modified to include $N/N_{\mathrm{max}} = 0$ at the open circuit potential of +244 mV. If this interpretation is correct then the response as a function of potential in the range +244 to +600 mV is predominantly due to development of the binding sites rather than the change in the rate constants k_2 and k_3. This concept is consistent with the earlier observations that oxidation of H_2O_2 is favoured on oxidised Pt surfaces [52,63,73,148,149].

5.7 The Fractional Surface Coverage Profile

The fractional surface coverages profile for each species at each potential, concentration and rotation rate is similar in form to Figs. 4.9 and 4.10 in the previous chapter.

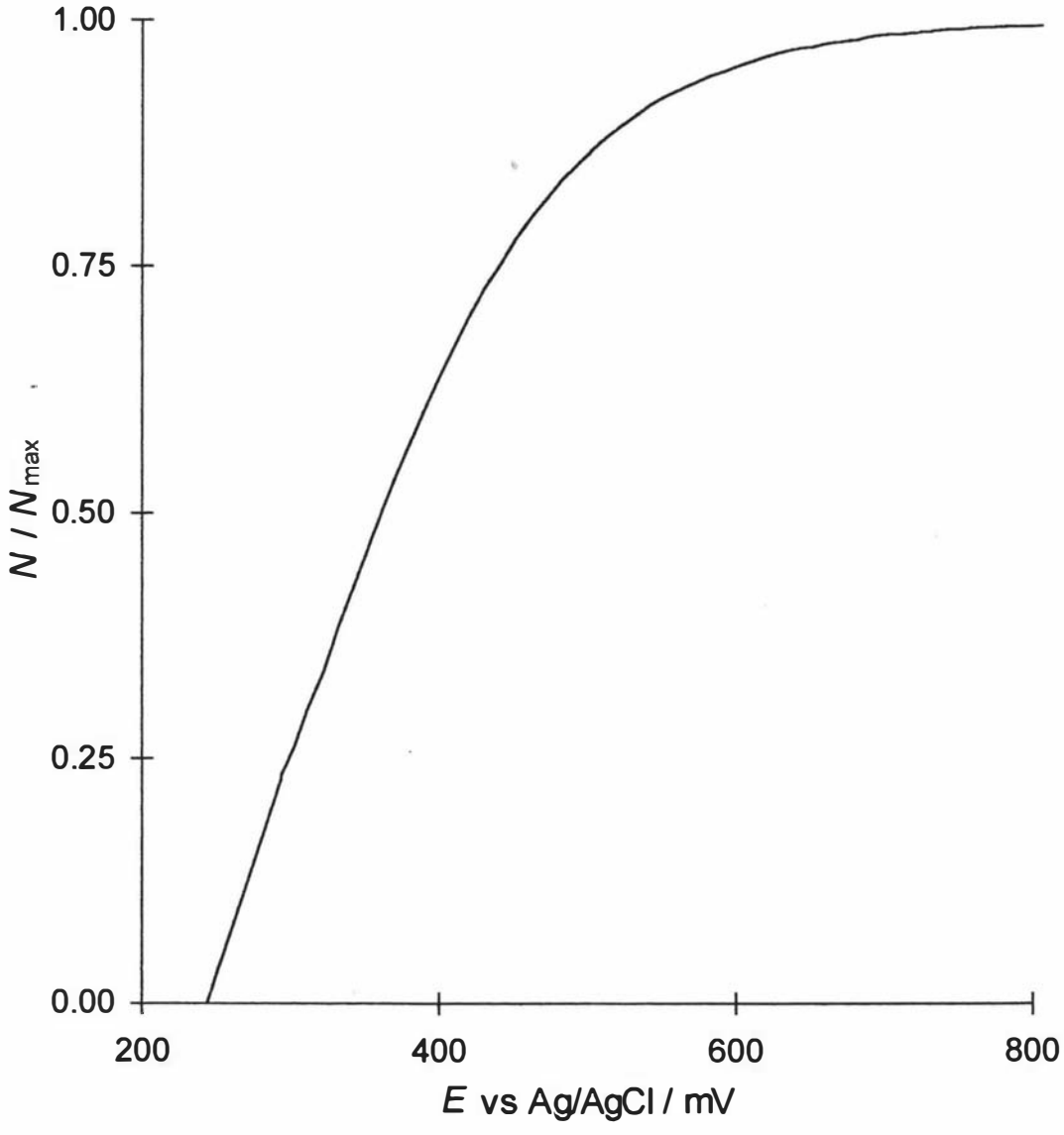

Fig. 5.5 N / N_{max} as a function of potential according to Eq. 5.10 derived using the assumption that k_2 varies exponentially with potential.

Of greater interest is the variation of these surface species as a function of potential as shown in Fig. 5.6 for a fixed rotation rate and $[H_2O_2]_{bulk}$. It should be noted that this figure shows the coverage as a fraction of N at each potential. Fractional surface coverage profiles are similar for other concentrations and rotation rates. At low anodic potentials the predominant surface species is that of the reduced binding site, Pt, which is to be expected if H_2O_2 acts as a reducing agent and the rate of re-oxidation is low. The coverage of this species initially decreases rapidly with potential as k_3N increases but this rate diminishes so that by +600 mV the coverage is still 0.1. The coverage of $Pt(OH)_2$ and $Pt(OH)_2{\cdot}H_2O_2$ increase rapidly with potential so that $\theta_{Pt} = \theta_{Pt(OH)_2 \cdot H_2O_2}$ at +271 mV, the point at which $k_2N = k_3N$. The increase in $Pt(OH)_2$ and $Pt(OH)_2{\cdot}H_2O_2$ diminishes by +328 mV so that relatively constant values with only slight potential dependence are exhibited. The coverage of the inhibiting species $Pt(OH)_2{\cdot}O_2$ and $Pt(OH)_2{\cdot}H_2O_2{\cdot}H^+$ simply follow the overall rate of reaction as shown in Fig. 5.4 for this concentration and rotation rate.

The optimised value for the diffusion coefficient in this work (0.55×10^{-9} m^2 s^{-1}) is less than that reported in Chapter 4 but is close to the value reported by Honda *et al.* [165] for the perhydroxy ion in alkaline solutions. Again the validation of these proposed low values for $D_{H_2O_2}$ is required through some independent methodology.

5.8 Conclusions

The modified rate equation for the electrochemical oxidation of H_2O_2 at platinum electrode over a range of potential given by Eq. 5.2 involves a new term, k_2 / k_3.

Both rate constants are found to increase with potential as shown in Fig. 5.3, and have equal value at potential +271 mV vs Ag/AgCl. At high anodic potentials the term k_2 / k_3 becomes insignificant and therefore the more simple rate equation described in Chapter 4 becomes valid.

The modified mechanism described in this Chapter builds upon on the work in Chapter 4 and further demonstrates the complex nature of the electrochemical oxidation of H_2O_2 at Pt. In addition, it demonstrates that the re-oxidation of the surface site is rapid at high anodic potentials only (E > +600 mV). It also has been demonstrated that the mechanism applies over a wide range of potentials and that only those parameters involving charge-transfer change with potential.

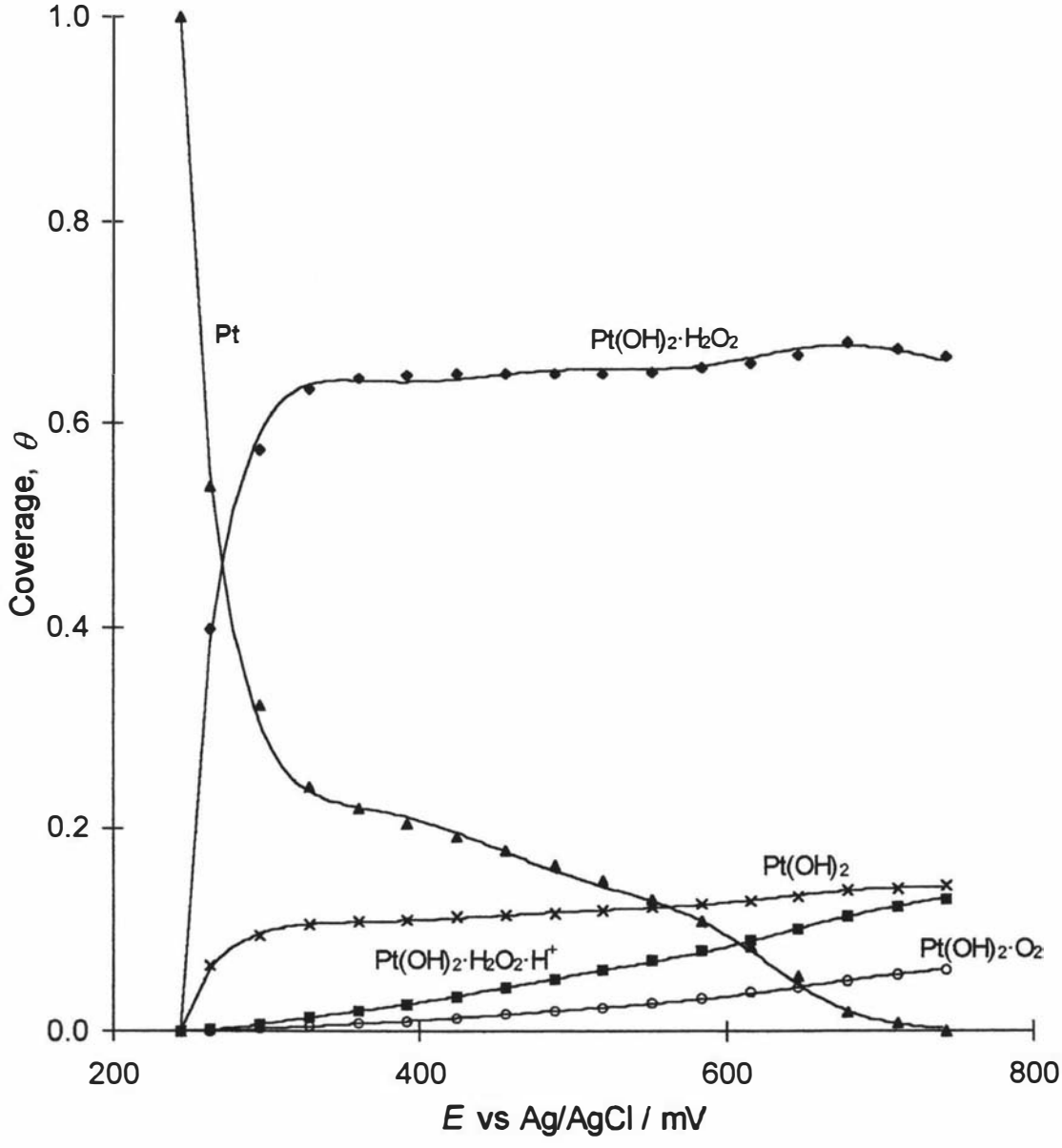

Fig. 5.6 Calculated surface coverages of all surface species involved in the mechanism as a function of potential based on the optimised model parameters for a rotation rate of 4000 rpm. The fractional surface coverages are: ▲θ_{Pt}, ◆$\theta_{Pt(OH)_2 \cdot H_2O_2}$, ×$\theta_{Pt(OH)_2}$, ■$\theta_{Pt(OH)_2 \cdot H_2O_2 \cdot H^+}$ and O$\theta_{Pt(OH)_2 \cdot H_2O_2 \cdot O_2}$.

CHAPTER SIX

The Effect of Temperature on the Electrochemical Oxidation of Hydrogen Peroxide at Platinum Electrodes

6.1 Introduction

In the previous two chapters a new model for the electrochemical oxidation of H_2O_2 at a platinum rotating disc electrode was developed that incorporates a binding site to account for the saturation kinetics when diffusion is not limiting. The mechanism involves reversible binding of H_2O_2 to electrochemically generated Pt(II) surface sites, followed by reduction of the site and competitive adsorption of the reaction products, i.e. O_2 and H^+.

The kinetic parameter products k_2N and k_3N were found to vary with potential in Chapter 5. At higher anodic potentials (E > +271 mV vs Ag/AgCl) $k_3N > k_2N$ and the rate for the reduction of the binding site given by reaction 4.3 is

$$j = k_2 N \theta_{Pt(OH)_2 \cdot H_2O_2} \tag{4.26}$$

While at low anodic potentials (E < +271 mV vs Ag/AgCl) $k_3N < k_2N$ and the rate for the regeneration of the binding site given by reaction 4.4 is

$$j = k_3 N \theta_{Pt} \tag{4.27}$$

At steady-state, the mass balance expression for all the surface species yields the rate expression in terms of surface concentration of the solution species

$$j = \frac{k_2 N K_1 [H_2O_2]}{1 + K_4[O_2] + K_1[H_2O_2]\left(1 + K_5[H^+] + k_2/k_3\right)} \tag{5.2}$$

where the term k_2 / k_3 was found to be significant over the potential range +200 to +600 mV vs Ag/AgCl.

The kinetic and equilibrium parameters were evaluated by SIMPLEX optimization [127-129,162] of the most positive root of this polynomial determined by Viète's method as described in Chapters 4 and 5.

It was established that a single set of potential-invariant parameters (binding constants K_1, K_4 and K_5 and the diffusion coefficients) satisfactorily accounted for the experimental

data over the $[H_2O_2]$ range 0 – 70 mM, rotation rate 630 – 10000 rpm and anodic potential +264 to +712 mV vs Ag/AgCl.

The vast majority of previous electrochemical studies for the oxidation of H_2O_2 were made at single temperatures. In this Chapter the temperature dependence of the kinetic model developed in Chapters 4 and 5 is tested.

The most likely effects of temperature on this model include alteration of the mass transport of reactants and products through modification to the diffusion coefficient and electrolyte viscocity, variation of the rate constants and variation of the equilibrium constants. Furthermore, the potential of the reference electrode will also alter with temperature [171].

This study was also an opportunity to test the robustness of the model developed in Chapters 4 and 5.

6.2 Experimental Conditions

6.2.1 Reagents and Electrodes

All chemicals, reagents, electrodes and electrochemical equipment used in this study are outlined in Chapter 4, Section 4.2.

6.2.2 Electrochemical Methodology

Steady-state measurements (n_p = 13230) were obtained over the $[H_2O_2]$ range 0 - 40 mM in 0.100 mol L^{-1} phosphate buffer at pH 7.28; rotation rates, 630, 1000, 1585, 2500, 4000, 6300 and 10000 rpm; potential range +232 to +712 mV vs Ag/AgCl (at the stated temperature) in 32 mV steps; and the temperature range 5 - 35 °C in 5 °C steps. Full *iR* compensation was employed in all measurements using the method of He and Faulkner [172] incorporated in the Bioanalytical Systems 100B/W potentiostat.

6.2.3 Viscosity and Density Measurements

The kinematic viscosity and the density of 0.100 mol L^{-1} and pH 7.28 phosphate buffer solution were determined at each temperature using the methods described in Chapter 2; Sections 2.7.1 and 2.7.2, respectively. The absolute viscosity of the buffer, η_{buffer}, at each

temperature was obtained by the product of the appropriate kinematic viscosity and density data.

6.2.4 Temperature Dependence of the Reference Electrode Potential

The temperature dependence of the 3 M NaCl Ag/AgCl reference electrode (Bioanalytical Systems, Indiana, USA) was calculated using the Nernst equation.

$$E_{\mathrm{Ag/AgCl},T} = E^{\circ}_{\mathrm{Ag/AgCl},T} - \frac{RT}{nF}\ln\left(m_{NaCl}\gamma_{\pm\,\mathrm{NaCl}}\right) \tag{6.1}$$

The formal potentials at each temperature, $E^{\circ}_{\mathrm{Ag/AgCl},T}$, were those reported by Harned and Owen [173]. Mean activity coefficients, $\gamma_{\pm\,\mathrm{NaCl}}$ were interpolated, using the cubic spline function of Mathcad, as a function of molality, m_{NaCl}, from data reported by Robinson for 5, 10, 15, 20, 30 and 35 °C [174] and by Harned and Nims for 25 °C [175]. These data are listed in Table 6.1 and shown together with the interpolated functions in Fig. 6.1.

Conversion from molarity (3 M NaCl at 25 °C) to molality was achieved using the lowest root for m in the quadratic relationship

$$c = m\rho - Am^2 \tag{6.2}$$

where ρ is the density of water in g ml^{-1} given in Chapter 2, Table 2.8, and the constant A as a function of temperature was taken from the literature [176]. For example, when $A = 0.0183$ at 25 °C so that $m_{\mathrm{NaCl}} = 3.197$ mol kg^{-1}. Accordingly, the reduction potentials are calculated employing Eq. 6.1 and listed in Table 6.2.

6.3 The Effect of Temperature on Mass Transport Process

Figures 6.2 and 6.3 show the steady state current responses of platinum rotating disc at +584 mV vs Ag/AgCl to a range of $[H_2O_2]_{\mathrm{bulk}}$ as a function of rotation rates at 5 and 35 °C, respectively. These plots are identical to that given by Fig. 5.1 in the previous chapter for the experimental temperature of 20 °C. The current densities in both figures increases with $[H_2O_2]_{\mathrm{bulk}}$ and are greater at higher temperatures. In addition, both show rotation rate dependency indicating that the process to some extent is diffusion controlled. As the temperature is increased, the diffusion coefficient of H_2O_2 is expected to increase while the viscosity of supporting electrolyte is expected to decrease, thus,

	$\gamma_{\pm NaCl}$						
$\frac{m_{NaCl}}{mol\,kg^{-1}}$	5 °C	10 °C	15 °C	20 °C	25 °C	30 °C	35 °C
0.1	0.7810	0.7810	0.780	0.779	0.778	0.777	0.776
0.2	0.7330	0.7340	0.734	0.733	0.732	0.731	0.729
0.5	0.6750	0.6770	0.678	0.679	0.679	0.679	0.679
1.0	0.6435	0.6490	0.652	0.654	0.656	0.657	0.657
1.5	0.6355	0.6425	0.648	0.652	0.655	0.658	0.660
2.0	0.6425	0.6520	0.659	0.665	0.670	0.674	0.676
2.5	0.6590	0.6670	0.677	0.684	0.691	0.695	0.697
3.0	0.6770	0.6910	0.702	0.711	0.719	0.724	0.725
3.5	0.7060	0.7210	0.735	0.744	0.752	0.756	0.759
4.0	0.7395	0.7570	0.772	0.783	0.791	0.797	0.800

Table 6.1 Interpolated mean activity coefficients, $\gamma_{\pm NaCl}$, for a range of temperatures as a function of molality, m_{NaCl}, calculated by employing Eq. 6.2.

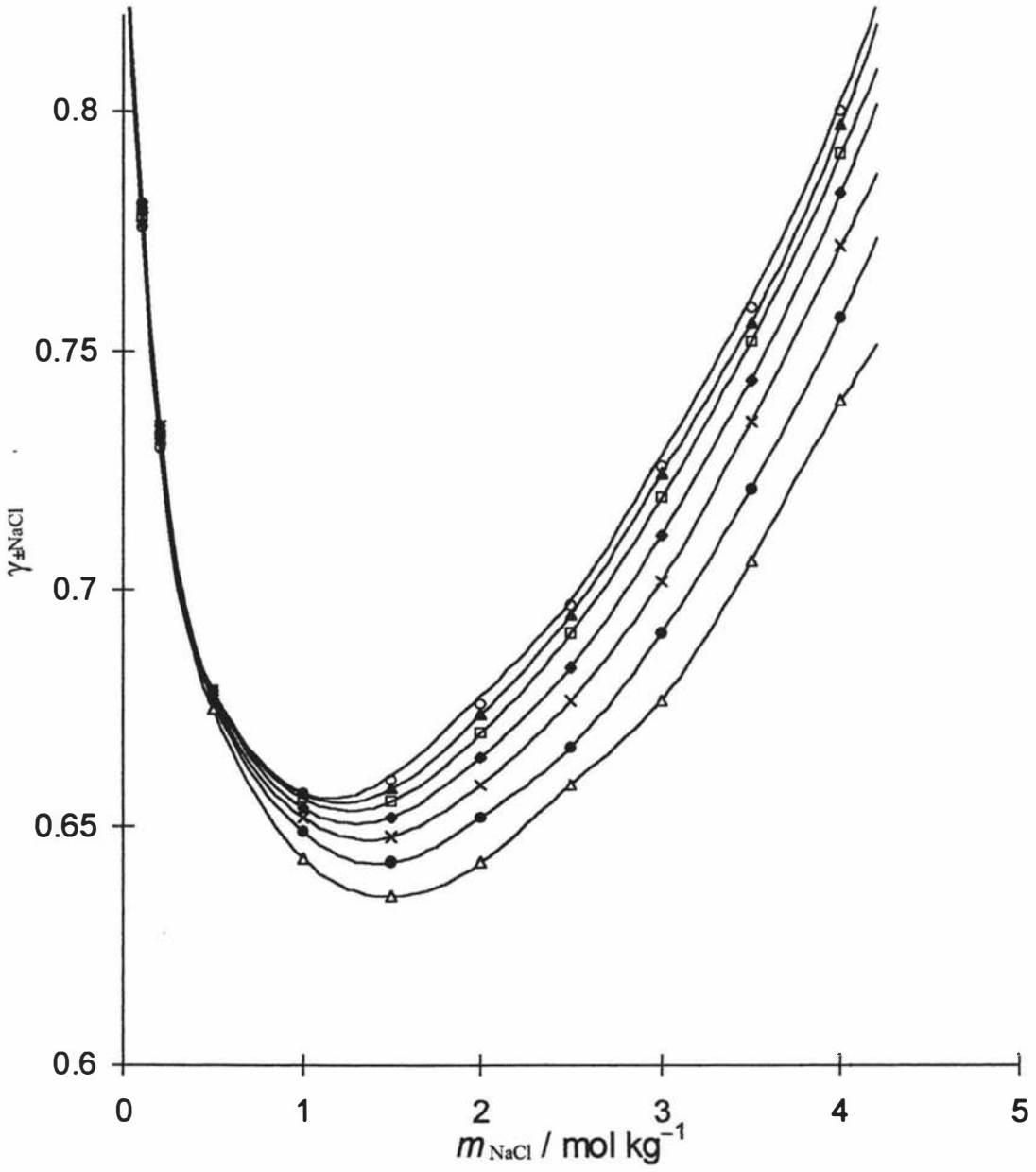

Fig. 6.1 The mean activity coefficient, $\gamma_{\pm\,NaCl}$, as a function of the molality, m_{NaCl}, for the data listed in Table 6.1 over a range of temperatures; Δ 5, ● 10, × 15, ◆ 20, □ 25, ▲ 30 and O 35 °C. Smooth curves are the interpolated mean activity coefficients calculated using the spline cubic function of Mathcad.

T / °C	$E^0_{Ag/AgCl}$ / V vs SHE	$\gamma_{\pm}$ (NaCl)	$E_{Ag/AgCl}$ / V vs SHE
5	0.23392	0.687 [a]	0.2175
10	0.23126	0.702 [a]	0.2141
15	0.22847	0.714 [a]	0.2107
20	0.22551	0.724 [a]	0.2071
25	0.22239	0.731 [b]	0.2035
30	0.21912	0.736 [a]	0.1997
35	0.21563	0.738 [a]	0.1958

[a] Ref. [174]

[b] Ref. [175]

Table 6.2 Formal potentials, $E^0_{Ag/AgCl}$, [173] and reduction potentials, $E_{Ag/AgCl}$, for the Ag/AgCl 3M NaCl reference electrode ($m = 3.197\ mol\ kg^{-1}$) as a function of temperature. Activity coefficients were interpolated from published data.

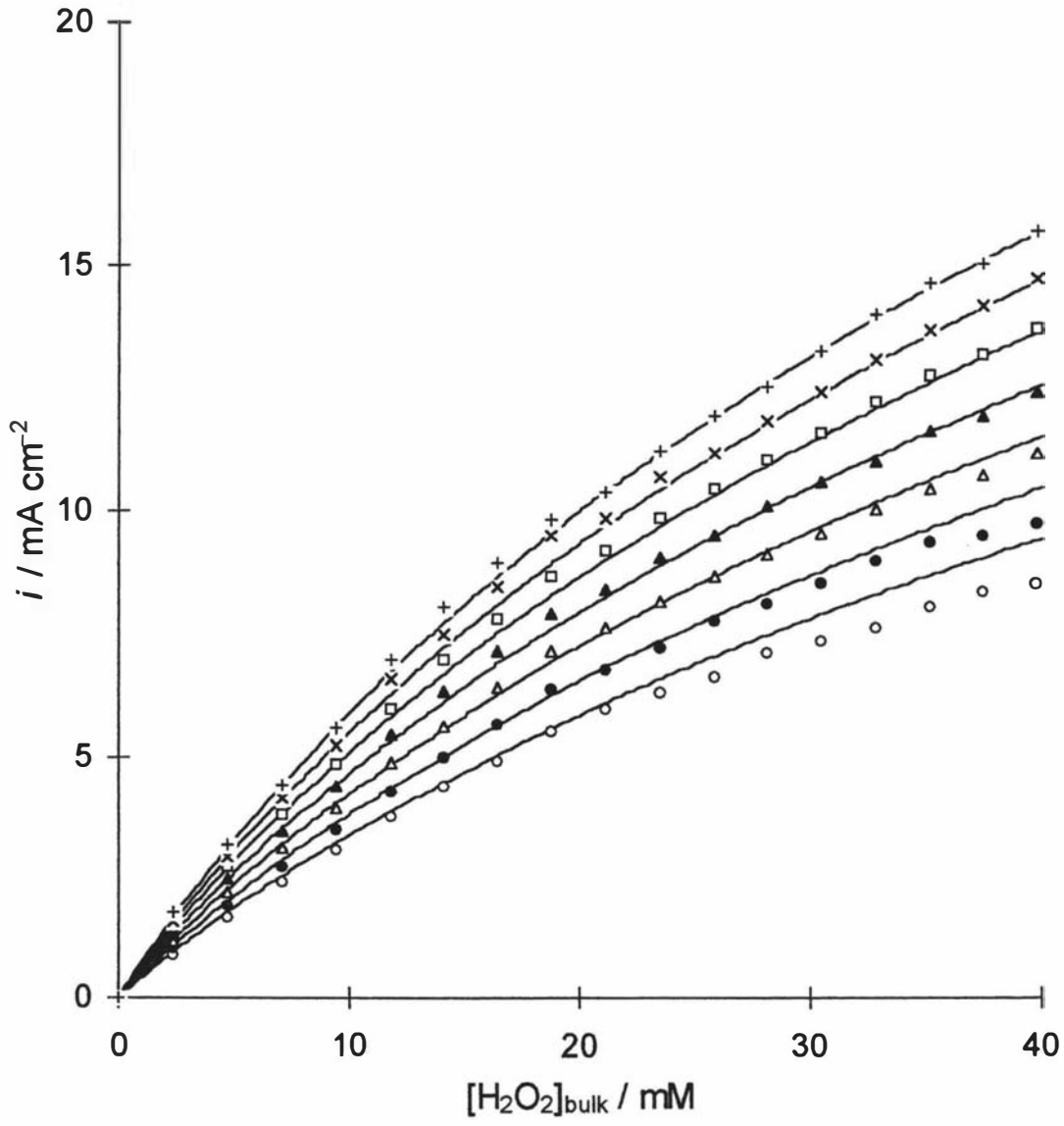

Fig. 6.2 Steady-state current response at +584 mV vs Ag/AgCl as a function of $[H_2O_2]_{bulk}$ at 5 °C for a range of rotation rates; O 630, ● 1000, Δ 1585, ▲ 2500, □ 4000, × 6300 and + 10000 rpm. Smooth curves are the synthetic responses calculated using the model and parameters developed during this study.

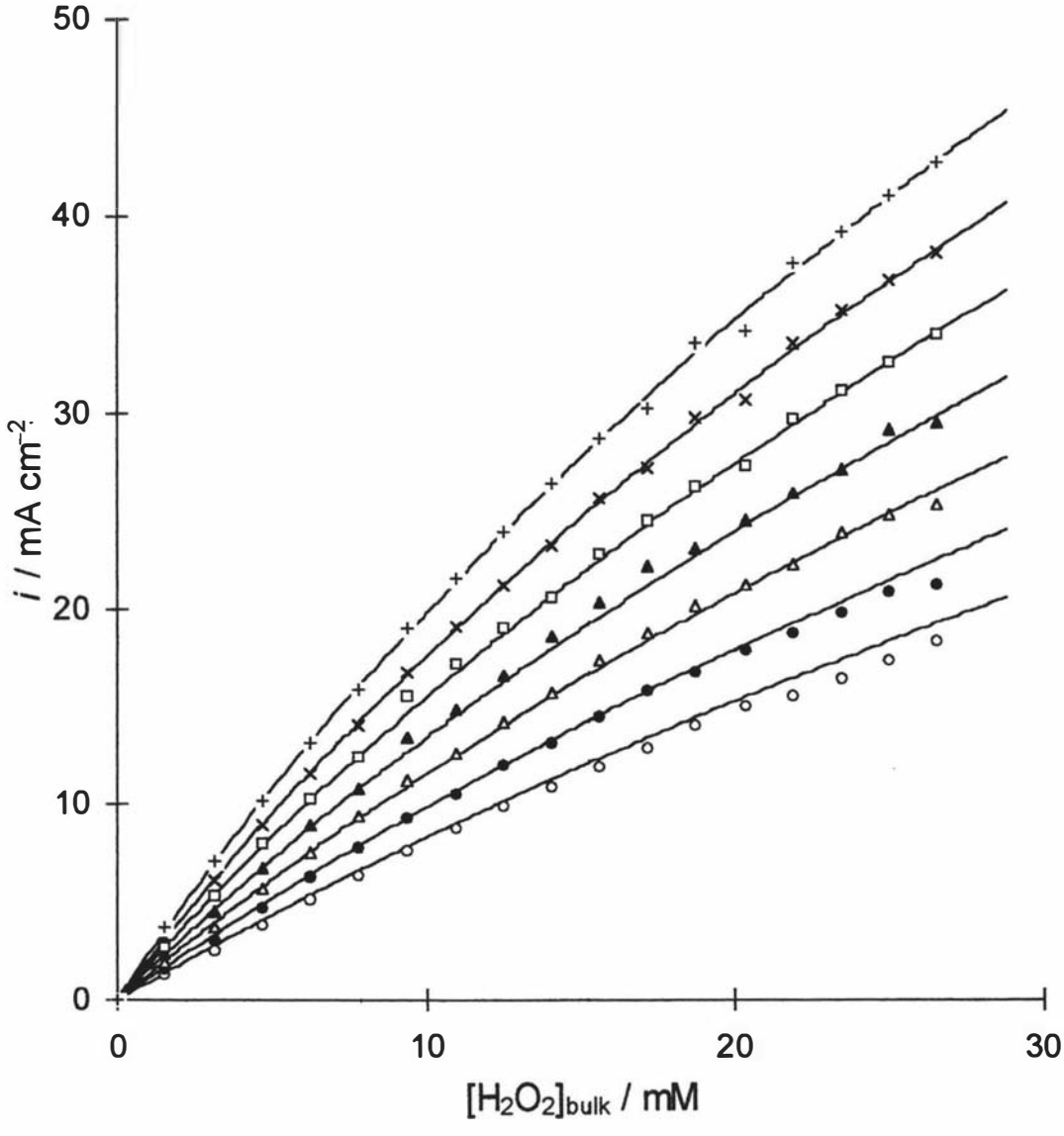

Fig. 6.3 Steady-state current response at +584 mV vs Ag/AgCl as a function of $[H_2O_2]_{bulk}$ at 35 °C for a range of rotation rates; O 630, ● 1000, Δ 1585, ▲ 2500, □ 4000, × 6300 and + 10000 rpm. Smooth curves are the synthetic responses calculated using the model and parameters developed during this study.

enhancing the mass transport of bulk H_2O_2 species to the electrode surface [177].

The approximate linear response region at lower $[H_2O_2]_{bulk}$ is narrower for experiments at low temperature. For example, in Fig. 6.2 at 5 °C pronounced deviation from linearity is evident at ca. 5 mM whilst in Fig. 6.3 at 35 °C this deviation occurs at ca. 10 mM.

It is likely that the low electrode response and its early saturation at lower temperatures is a result of a deficient mass transport of bulk H_2O_2 to the electrode surface and also lower numbers of binding sites.

In the case of experiments performed at higher temperatures, larger numbers of electrode binding sites may be present for occupation by more rapidly transported H_2O_2 from the bulk.

6.4 Steady-State Responses as a Function of Temperature

A selection of steady-state responses for the oxidation of a range of $[H_2O_2]_{bulk}$ at Pt rotating disc electrode over the temperature range 5 - 35 °C (at a fixed rotation rate and potential) are shown in Fig. 6.4. The data presented in this figure are 1/105 of that collected for the temperature dependence study (7 rotation rates in combination with 15 potential steps for 7 temperatures). The rotation rate and potential dependence have been described in Chapters 4 and 5. In general, larger currents are observed with greater temperature as demonstrated in the previous section. The rate constants k_2 and k_3 are also expected to increase with temperature to yield an increase in the rate according to Eqs. 4.26 and 4.27. A review of other parameters in the rate equation given in Eq. 5.2 identifies that these parameters may also be affected by temperature and hence would also influence the rate of reaction. An increase in K_1 with temperature (or indeed a decrease in either or both of the inhibition constants K_4 and K_5) might also afford an increase in rate, but only until saturation of all binding sites is achieved. Inspection of Fig. 6.4 indicates that the rate at which saturation occurs is less at lower temperatures. This suggests that an increase in the product k_2N with temperature may be the dominant effect rather than an increase in K_1.

The temperature variation of the diffusion constant, k_D, and the diffusion coefficients D_{O_2} and D_{H^+} required elucidation prior to optimization of the equilibrium and kinetic parameters. The kinematic viscosity of the buffer at each temperature is listed in Table 6.3 from which k_D was calculated using the equation:

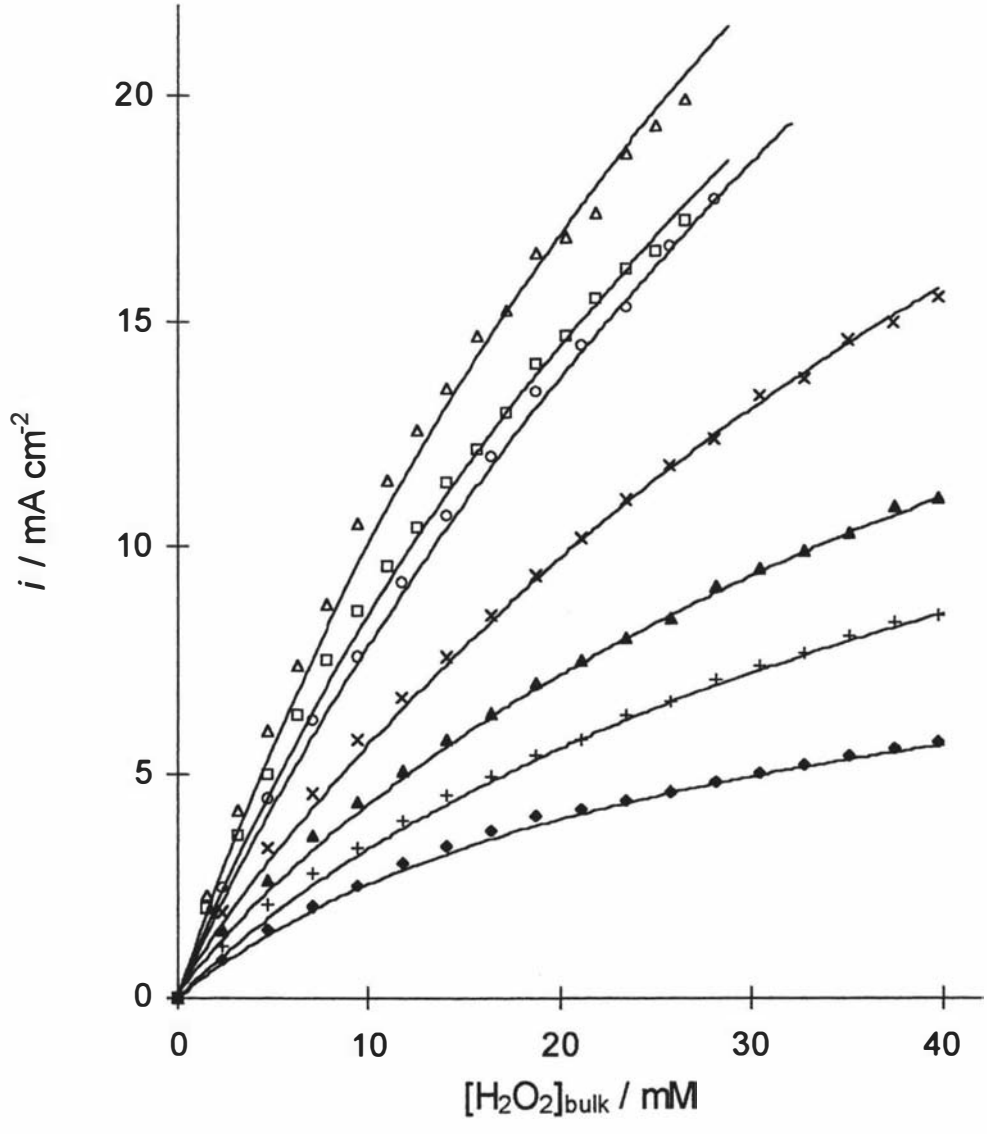

Fig. 6.4 Steady-state current responses at a fixed rotation rate ($\omega = 4000$ rpm) and potential ($E = +424$ mV vs Ag/AgCl) as a function of bulk hydrogen peroxide concentration at each temperature: ◆ 5 °C, + 10 °C, ▲ 15 °C, × 20 °C, O 25 °C, □ 30 °C and Δ 35 °C. Smooth curves are the synthetic responses calculated using the model and parameters developed in this study.

$\frac{T}{^{o}C}$	$\frac{\nu_{buffer} \times 10^{6}}{m^{2} s^{-1}}$	$\frac{\rho_{buffer} \times 10^{-3}}{kg\ m^{-3}}$	$\frac{\eta_{buffer} \times 10^{3}}{kg\ m^{-1} s^{-1}}$
5	1.5456	1.01338	1.5663
10	1.3369	1.01299	1.3543
15	1.1662	1.01216	1.1804
20	1.0304	1.01135	1.0421
25	0.9082	1.00997*	0.9173
30	0.8242	1.00819	0.8310
35	0.7787	1.00660	0.7839

* value verified at 25°C by an Anton Paar vibrating-tube density meter, where the measured value was $\rho_{25} = 1.00994 \times 10^{-3}$ kg m^{-3}.

Table 6.3 Kinematic viscosity, density and absolute viscosity of 0.100 mol L^{-1} phosphate buffer of pH 7.28.

$$k_D = 1.61\,\nu^{1/6} \tag{4.42}$$

The temperature dependence of D_{O_2} and D_{H^+} were assumed to follow the Stokes-Einstein equation, with a constant effective hydrodynamic radius, a, prevailing over the temperature range for each species.

$$D = \frac{kT}{6\pi\eta a} \tag{6.3}$$

where η is the absolute viscosity at each temperature as listed in Table 6.3.

The effective hydrodynamic radii for oxygen and protons were calculated using the reported diffusion coefficients at 25 °C; $D_{O_2} = 1.93 \times 10^{-9}$ m^2 s^{-1} [155] and $D_{H^+} = 9.31 \times 10^{-9}$ m^2 s^{-1} [163] so that $a_{O_2} =$ 1.23 pm and $a_{H^+} = 0.56$ pm. The resulting diffusion coefficients are listed in Table 6.4.

6.5 Optimization of Parameters as a Function of Temperature

Two approaches to optimization of fitting parameters were considered. The first involved optimization of K_1, K_4, K_5 and $D_{H_2O_2}$ for the data set at each temperature (i.e. combinations of steady-state measurements over a range of $[H_2O_2]$, potentials and rotation rates as in Chapter 5). The second tested the assumption that K_1, K_4 and K_5 are temperature-invariant whilst $D_{H_2O_2}$ varies with temperature. In either case, k_2N and k_2/k_3 vary with potential.

Consequently, initial optimization used the two-tiered fitting method described in Chapter 5. Inspection of the optimized equilibrium constants indicated no significant variation with temperature. This suggests that the enthalpy of formation for each process was close to zero. This finding, together with the principle of employing the minimum number of optimizing parameters to adequately describe experimental data, indicated the alternative approach to be more appropriate. This necessitated the development of a three-tier SIMPLEX optimization: The first tier optimized the potential-dependent parameters k_2N and k_2/k_3, the second optimized the temperature-dependent diffusion coefficient $D_{H_2O_2}$ and the third optimized the temperature- and potential-invariant parameters K_1, K_4 and K_5. The optimized equilibrium constants together with the sum of residuals, r_s

$\frac{T}{^{o}C}$	$\frac{D_{H_2O_2} \times 10^9}{m^2\ s^{-1}}$	$\frac{D_{O_2} \times 10^9}{m^2\ s^{-1}}$	$\frac{D_{H^+} \times 10^9}{m^2\ s^{-1}}$
5	0.70	1.05	5.09
10	0.60	1.24	5.99
15	0.64	1.45	6.99
20	0.63	1.67	8.06
25	0.83	1.93	9.31
30	1.02	2.17	10.45
35	1.17	2.45	11.81

Table 6.4 Optimized diffusion coefficients for H_2O_2 as a function of temperature together with the assumed diffusion coefficients for oxygen and the proton based upon the Stokes-Einstein equation.

$$r_s = \sum (j - \lambda_3)^2 \tag{4.53}$$

and average deviation, d_{av}

$$d_{av} = nF\sqrt{\frac{r_s}{n_p}} \tag{4.54}$$

are listed in Table 6.5.

The sum of residuals is not significantly higher than that found when permitting K_1, K_4 and K_5 to vary with temperature (6.48×10^{-6} (mol m^{-2} s^{-1})^2) indicating that this more simple case adequately describes the data. The values for the temperature-dependent $D_{H_2O_2}$ are listed in Table 6.4 and plotted in Fig. 6.5. This diffusion coefficient increases almost linearly with temperature in the range 20 - 35 °C. Below 20 °C no clear trend is evident, with $D_{H_2O_2}$ adopting a relatively constant value of ca. 0.6×10^{-9} m^2 s^{-1} in the range 10 – 20 °C and increasing to 0.7×10^{-9} m^2 s^{-1} at 5 °C. Subsequent re-optimization of the 5 °C data set fixing $D_{H_2O_2}$ at 0.6×10^{-9} m^2 s^{-1} failed to yield a satisfactory sum of residuals indicating that the value reported in Table 6.4 represents the best fit value and is not an artifact of the SIMPLEX process. Error bars are not included in Fig. 6.5 since in the optimization method these only represent the variation in this parameter in the final iterative steps (typically 0.002×10^{-9} m^2 s^{-1}) rather than reflecting the uncertainties in the primary data.

The series of smooth dashed curves in Fig. 6.5 are the relationships between diffusion coefficient and temperature if the Stokes-Einstein equation (Eq. 6.7) is followed for a number of fixed effective hydrodynamic radii. Clearly the optimized values for $D_{H_2O_2}$ do not follow the expected trend. There are two possible reasons for this. The first is that the effective hydrodynamic radius of H_2O_2 changes with temperature with a maximum of 325 pm at 20 °C decreasing above and below this temperature (175 pm and 250 pm at 5 °C and 35 °C respectively). The second is that the precise value for $D_{H_2O_2}$ at each temperature is influenced strongly by assumptions made in the optimization process. Namely, the enforcement of temperature-invariant values for K_1, K_4 and K_5 and rigid Stokes-Einstein behaviour for the diffusion of O_2 and H^+. It is proposed that the observed temperature-dependence in $D_{H_2O_2}$ arises from some combination of these two points. Consistent with the results reported in Chapters 4 and 5, the calculated value of

Parameter	Value
K_1 / 10^{-3} m^3 mol^{-1}	6.380
K_4 / m^3 mol^{-1}	0.128
K_5 / m^3 mol^{-1}	0.053
r_s / 10^{-6}(mol m^{-2} s^{-1})^2	6.520
d_{av} / mA cm^{-2}	0.430

Table 6.5 Optimized equilibrium constants and residual parameters (n_p = 13230 data points).

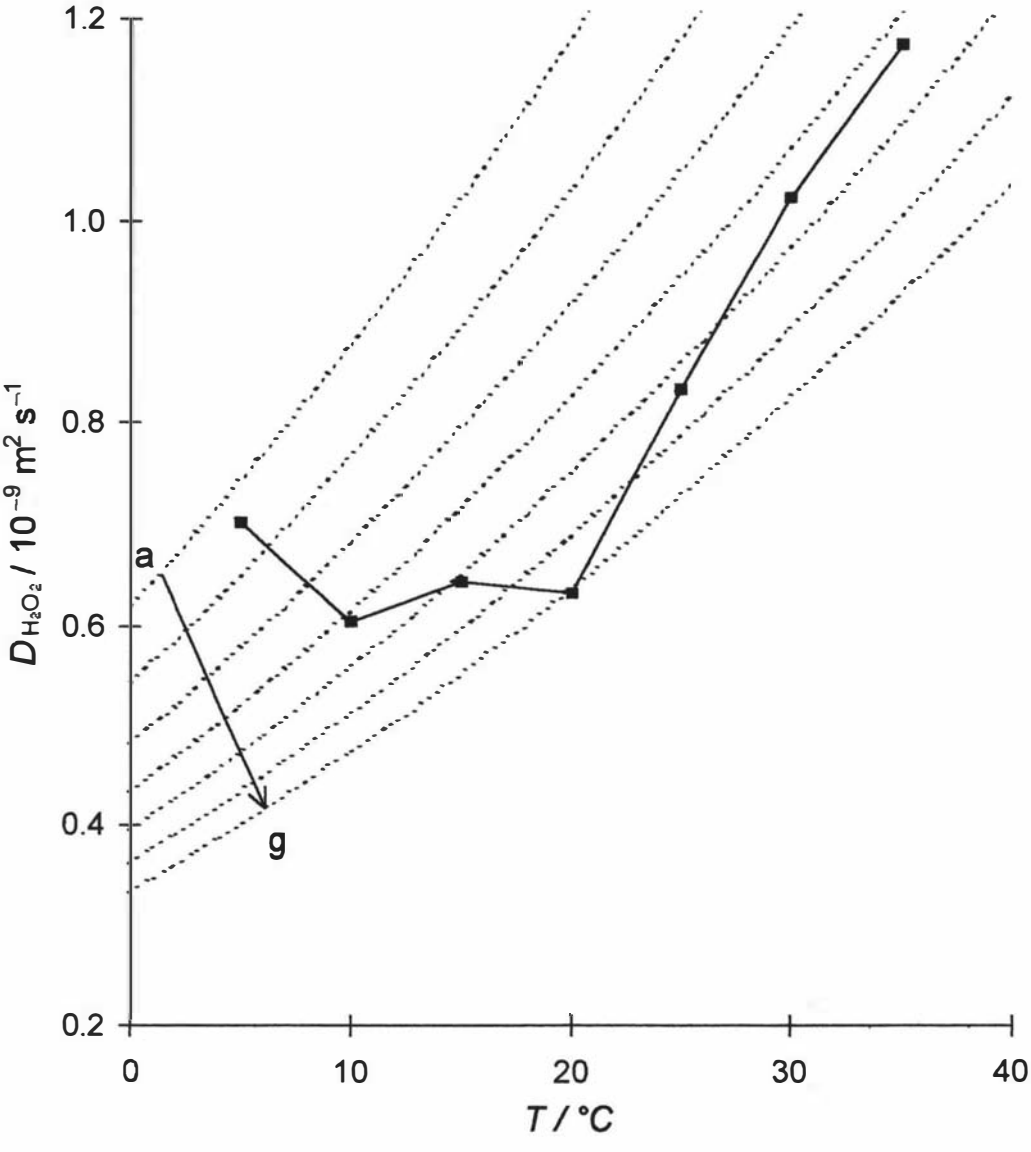

Fig. 6.5 Optimised diffusion coefficient for hydrogen peroxide (■) listed in Table 6.4 as a function of temperature. Dashed curves are those predicted by the Stokes-Einstein relationship given by Eq. 6.3 for a range of effective hydrodynamic radii; (a) 175, (b) 200, (c) 225, (d) 250, (e) 275, (f) 300 and (g) 325 pm.

$D_{H_2O_2}$ is found significantly lower than that reported previously [54,155,156,164].

6.6 The Variation of Rate Constants With Temperature

The variation of k_2N with both temperature and potential (converted to SHE) is shown as a logarithmic plot in Fig. 6.6. At each temperature k_2N varies in a manner similar to that reported in the previous chapter - the rate of increase in $\ln k_2N$ decreases with more anodic potentials. In Chapter 5, this was been interpreted as a combination of potential-dependence of each of the terms k_2 and N. The latter exhibits a marked increase as the potential approaches the point at which Pt(II) binding sites may be formed and the rate for this reaction, given in Eq. 4.3, increases due to the movement of electron density, within the surface complex $Pt(OH)_2{\cdot}H_2O_2$, towards the Pt(II) moiety becoming more favourable with anodic potential.

$$Pt(OH)_2.H_2O_2 \xrightarrow{k_2} Pt + 2H_2O + O_2 \qquad (4.3)$$

Temperature variation is also clearly shown in Fig. 6.6. In general, at any fixed potential, k_2N increases with temperature (although at large anodic potentials the data for 20 °C exceeds that for 25 °C) with a 20–fold increase in k_2N at +500 mV vs SHE over the range (5 – 35) °C diminishing to a 5–fold increase at +900 mV vs SHE. This increase in k_2N is consistent with the overall increase in the steady-state current shown in Fig. 6.4.

The potential- and temperature-dependence of k_3N calculated from the optimized k_2N and k_2/k_3 terms is shown in Fig. 6.7. In a similar manner to that shown for k_2N in Fig. 6.6, the increase in $\ln k_3N$ with potential diminishes with increasing anodic potential. This is again interpreted in terms of the number of binding sites increasing markedly at low potentials in combination with a steady increase in the rate constant. Data are not shown for the entire potential range since the term k_2/k_3 becomes unreliable when $k_2/k_3 << 1$ at high potentials during the optimization process.

The variation of k_3N with temperature is not as clear as that for k_2N with no distinguishable trend above 20°C although increases are observed at all potentials for the range (5 - 15) °C. This is attributed to the problems of reliably determining this parameter.

The potential- and temperature-dependent values for k_2N and k_2/k_3 together with the temperature-dependent values for $D_{H_2O_2}$ and K_1, K_4 and K_5 (temperature independent)

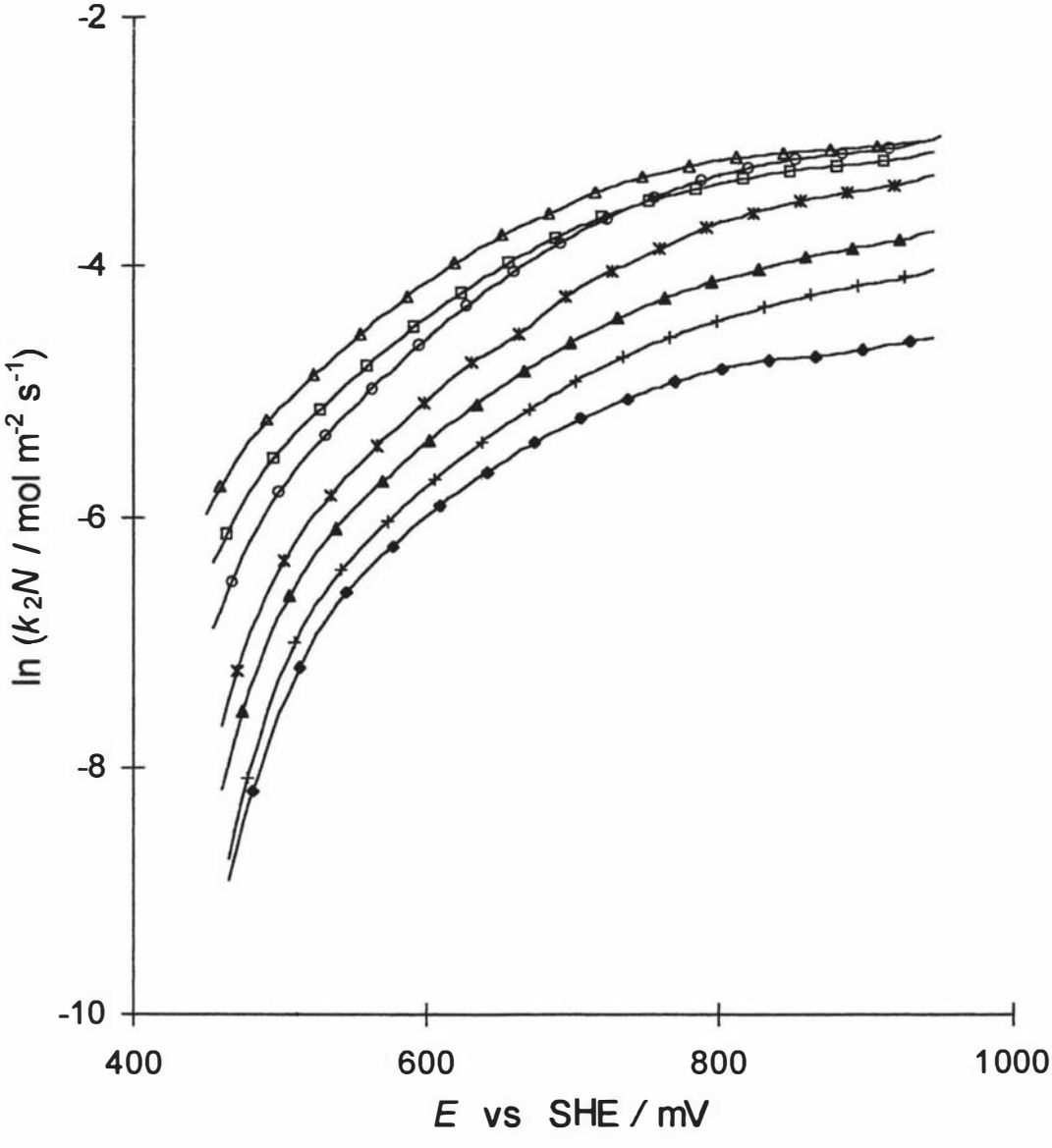

Fig. 6.6 Logarithmic plot of the optimised kinetic parameter k_2N as a function of potential for each temperature: ◆ 5 °C, + 10 °C, ▲ 15 °C, × 20 °C, O 25 °C, □ 30 °C and Δ 35°C.

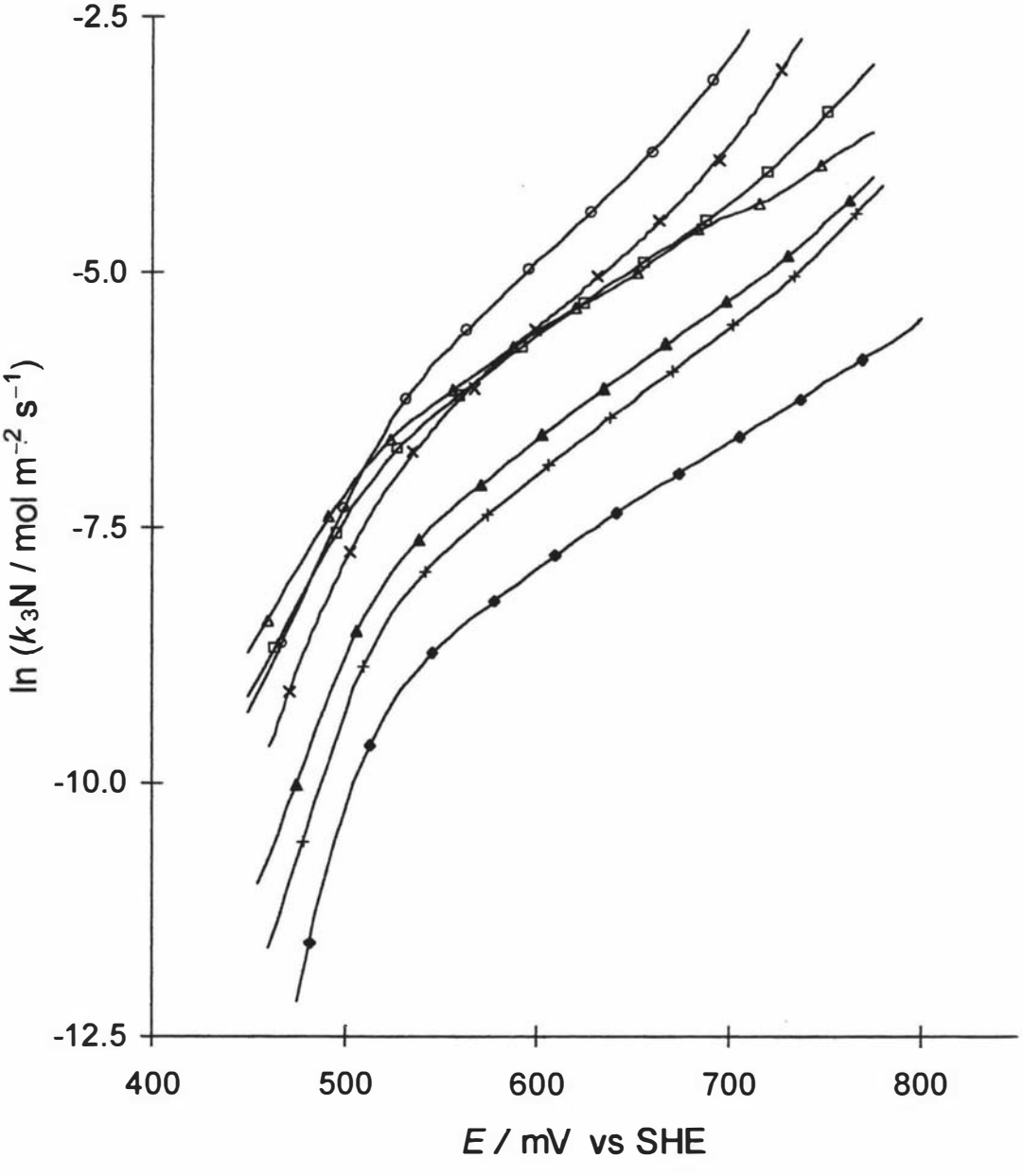

Fig. 6.7 Logarithmic plot of the optimised kinetic parameter k_3N as a function of potential for each temperature: ◆ 5 °C, + 10 °C, ▲ 15 °C, × 20 °C, O 25 °C, □ 30 °C and Δ 35 °C.

were used together with the third-order polynomial expressions 4.42, 4.44, 4.47, 5.3 and 5.4 given in Chapters 4 and 5, to calculate the smooth curves plotted together with the experimental data in Fig. 6.4. The calculated response is in good agreement with the steady-state measurements although the quality of agreement is inferior to that reported for a single temperature in Chapter 5. This is evident in the 3½ - fold increase in the average deviation, d_{av}, listed in Table 6.5 compared to that given in Table 5.1. The increase in the average deviation is considered as being inevitable in this study since a number of fundamental assumptions are now applied to the optimization process. Namely, that D_{O_2} and D_{H^+} follow Stokes-Einstein behaviour and K_1, K_4 and K_5 are independent of temperature. The large currents obtained at the higher temperatures increased the number of adherent O_2 bubbles at the electrode surface thus causing an increase in the scatter of the data in Fig. 6.4 at these temperatures.

6.7 Arrhenius Analysis

The variation in k_2N with temperature may be further explored by performing an Arrhenius analysis. This was not done for k_3N since no clear temperature-dependence was indicated. The k_2N data shown in Fig. 6.6 do not have common potential vs SHE (since they were obtained for a series of set potentials vs Ag/AgCl at each temperature and corrected to SHE using the data in Table 6.2).

Consequently, the Arrhenius plots shown in Fig. 6.8 are for a series of k_2N values interpolated from the data in Fig. 6.6 for a range of potentials vs SHE. Interpolation was achieved by first generating curves for k_2N as a function of E_{SHE} at each temperature and then using the cubic spline function incorporated in the software package Mathcad (MathSoft Inc., Massachusetts, USA) to determine k_2N for a number of potentials.

The Arrhenius slopes and intercepts are listed for a selection of these potentials vs SHE in Table 6.6 together with the errors in the slopes.

The Arrhenius slope may be related to a pseudo-activation energy using the logarithmic form of the Arrhenius equation [178]

$$\ln k_2N = -\frac{E_{A,k_2N}}{R}\cdot\frac{1}{T} + \ln A \qquad (6.4)$$

The variation in this activation energy as a function of potential vs SHE is shown in Fig. 6.9.

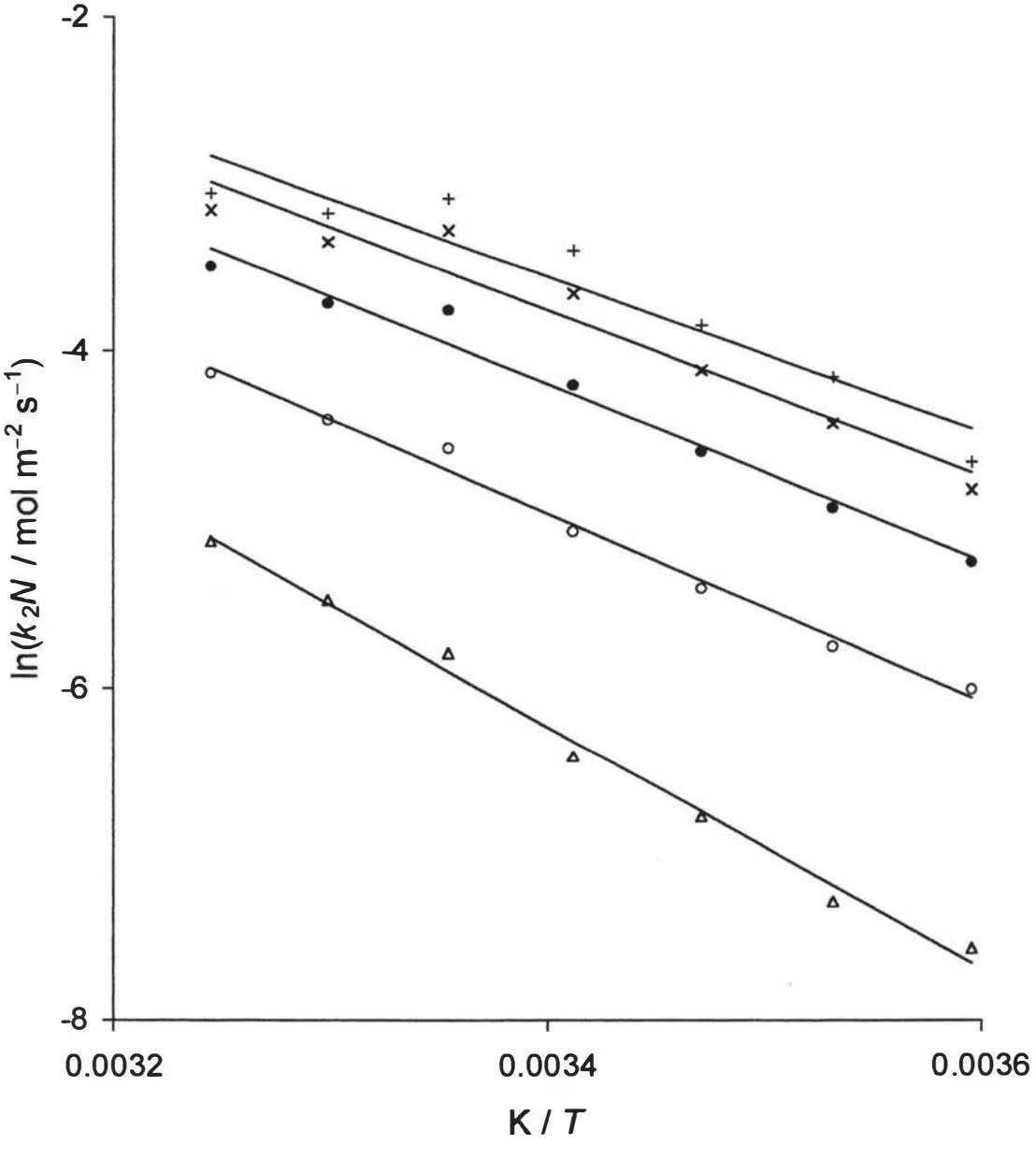

Fig. 6.8 Arrhenius plot showing the effect of temperature on the rate constant for the reduction of the complex binding site for a selection of potentials vs SHE; Δ 500, O 600, ● 700, × 800 and + 900 mV.

E vs SHE / mV	Slope / K	Error in slope / K	E_{A,k_2N} / k J mol^{-1}
450	−11761.3	866.0	97.8
475	−9131.4	456.1	75.9
500	−7324.3	281.5	60.9
525	−6268.6	238.1	52.1
550	−5840.4	246.0	48.6
575	−5707.2	247.3	47.4
600	−5600.2	250.0	46.6
625	−5508.1	261.9	45.8
650	−5424.9	285.9	45.1
675	−5315.2	315.8	44.2
700	−5240.5	350.7	43.6
725	−5177.0	379.7	43.0
750	−5090.1	420.8	42.3
775	−5011.0	478.0	41.7
800	−4940.6	532.0	41.1
825	−4866.6	570.8	40.5
850	−4800.1	616.0	39.9
875	−4731.6	647.9	39.3
900	−4646.9	659.4	38.6
925	−4576.4	675.0	38.0
950	−4552.3	729.3	37.8

Table 6.6 Arrhenius plot data regression shows the slopes and error in slopes with the calculated values of activation energy for the reduction of complex binding site.

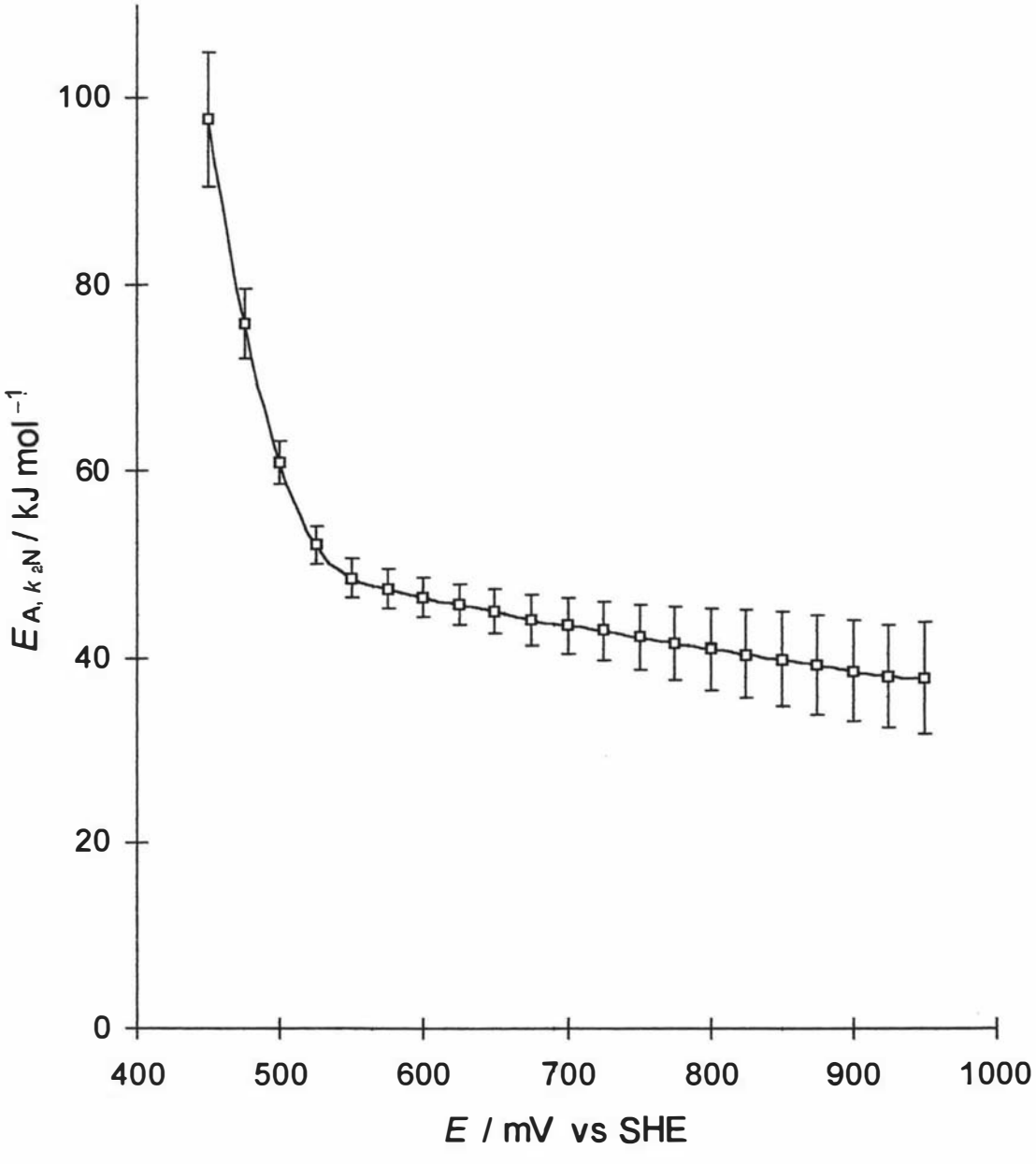

Fig. 6.9 Plot of the pseudo-activation energy for the kinetic parameter k_2N, E_{A,k_2N}, as a function of potential. E_{A,k_2N} were determined by Arrhenius regression of the data listed in Table 6.6, and error bars are the uncertainty in the regression slope.

The parameter E_{A,k_2N} is a pseudo-activation energy since it encompasses changes to both k_2 and N. In the previous chapter the variation of k_2 and N with potential was identified, with a marked increase in N taking place over the range +450 to +650 mV vs SHE. Inspection of Figs. 6.4 and 6.6 shows that the product k_2N increases with temperature. Unfortunately, the term k_2N is inseparable during the optimization and thus, the temperature variation is open to interpretation. One possible interpretation is that the number of binding sites, $Pt(OH)_2$, varies with potential which implies that there must be some precursor site, Pt_{PS}. If these species are in equilibrium at each potential then

$$Pt_{PS} \overset{K_{BS}}{\rightleftharpoons} Pt(OH)_2 \tag{6.5}$$

where K_{BS} is the equilibrium constant which becomes larger with more anodic potential. An expression for N may be written in terms of N', the total number of binding and precursor sites per m^2.

$$N = \frac{N'K_{BS}}{1 + K_{BS}} \tag{6.6}$$

If it is assumed that K_{BS} obeys the van't Hoff equation [179] at each potential and assuming that $K_{BS} << 1$, (which will certainly be the case at low potentials) then

$$N_E = N'_E \exp\left(\frac{-\Delta H_{BS,E}}{RT}\right) \tag{6.7}$$

where the subscript E denotes fixed potential and ΔH_{BS} is the enthalpy of formation of the binding site. If a rise in temperature were to increase N then ΔH_{BS} will be endothermic.

The Arrhenius expression may be written for k_2 (again with subscript E denoting fixed potential).

$$k_{2,E} = A_{k_2,E} \exp\left(\frac{-E_{A,k_2,E}}{RT}\right) \tag{6.8}$$

where $E_{A,k_2,E}$ and $A_{k_2,E}$ are the activation energy and Arrhenius frequency factor for reaction 4.3. Combination of Eqs. 6.7 and 6.8 affords the expected temperature variation of $\ln k_2N$ at fixed potential, $\ln (k_2N)_E$.

$$\ln(k_2 N)_E = \ln(A_{k_2,E} N'_E) - \frac{\left(E_{A,k_2N,E} + \Delta H_{BS,E}\right)}{RT} \quad (6.9)$$

Hence, the pseudo-activation energy at each potential shown in Fig. 6.9 is a combination of the activation energy for reaction 4.3, i.e. the formation of the reduced platinum form sites, and the enthalpy of formation of the binding site.

The formation of the binding site is likely to involve an oxidation process, so that if ΔH_{BS} were to be endothermic, then this parameter could reasonably be expected to decrease at more anodic potentials. Thus, the large decrease in pseudo-activation energy at low potentials in Fig. 6.9 may be attributed to a progressive decrease in the endothermic formation of binding sites, whilst at higher potentials the relatively invariant values are predominantly due to k_2.

6.8 Conclusions

The data presented in this chapter demonstrates that the mechanism developed in the previous two chapters, Eq. 5.2, for the oxidation of hydrogen peroxide at platinum may be used satisfactorily to account for the temperature-dependence of steady-state responses.

The equilibrium constants K_1, K_4 and K_5 are shown to be temperature-invariant indicating that the enthalpy of formation for each process is close to zero. The diffusion coefficient of H_2O_2 is maintained at lower values than those reported in the literature, although it increases with temperature but does not approach previously reported values [54,155,156,164] even at the highest temperature. The nature of the binding site has been further explored with the variation in the kinetic product k_2N with both potential and temperature. The number of binding sites, N, exhibited a pronounced increase at potential close to the formation of Pt(II) binding sites and the rate constant, k_2, increased due to internal electron transfer occurring at the Pt(II) moiety, that became faster at more positive potentials. At fixed potential, the term k_2N also exhibited a marked increase with temperature consistent with the overall increase in the steady-state response. This dependence in temperature was also interpreted in terms of the development of the binding site from a precursor.

CHAPTER SEVEN

Effect of Phosphate Buffer Concentration and pH on the Electrochemical Oxidation of Hydrogen Peroxide at Platinum Electrodes

7.1 Introduction

The catalytic activity of platinum on the oxidation of H_2O_2 was studied in previous chapters to account for the steady-state responses as a function of a range of $[H_2O_2]_{bulk}$ and rotation rates (Chapter 4), potential (Chapter 5) and temperature (Chapter 6). In these studies, a mechanistic model was developed incorporating platinum binding sites in the form of hydrous oxides labelled as $Pt(OH)_2$. Support for the existence of an oxidized binding site not only arises from the fit of the mechanism to the experimental data, but also from earlier work by others showing that oxidation of H_2O_2 is favoured on oxidized Pt surfaces [52,148,149]. This was based upon linking the potential at which H_2O_2 first oxidizes to that for platinum oxide film formation [63].

The number of binding sites per electrode area at 20 °C was proposed in Chapter 5 to increase with potential above +244 mV vs Ag/AgCl and increasing to a maximum at ca. +650 mV. This was found to be the case for all experiments performed over a range of temperatures between 5 to 35 °C described in Chapter 6.

The phosphate buffer employed in studying the oxidation of H_2O_2 described in previous chapters was maintained at 0.100 mol L^{-1} and pH 7.3. This was adopted as a standard since these conditions are widely used in enzyme-based sensor devices [81,100,180-184]. For the purpose of mechanistic studies, it is appropriate to deviate from these conditions. Therefore, in this chapter, the proposed mechanism was extended over a wider range of phosphate concentrations and pH. This was performed to investigate the role of the electrolyte in forming binding sites and to further investigate the inhibition by the proton according to

$$Pt(OH)_2 \cdot H_2O_2 + H^+ \overset{K_5}{\rightleftharpoons} Pt(OH)_2 \cdot H_2O_2 \cdot H^+ \qquad (4.35)$$

7.2 Experimental Conditions

7.2.1 Reagents and Electrodes

All chemicals and electrochemical equipment were as detailed in Chapter 5, Section 5.2. Two series of phosphate buffer solutions were prepared as outlined in Chapter 2, Sections 2.6.1 and 2.6.2. All experiments were performed at 20 ± 0.1 °C.

7.2.2 Electrochemical Methodology

Steady-state measurements at a platinum rotating disc electrode were made using the regimen of rotation rates and anodic potentials established in Chapters 4 and 5. Full *iR* compensation was employed for all rotating disc electrode experiments using the method of He and Faulkner [172] incorporated in the Bioanalytical 100B/W potentiostat.

Platinum microelectrodes were employed to examine low phosphate concentration buffers so as to avoid *iR* artifacts. Experimental details are given in Chapter 2, Section 2.3.2.

Flow injection analysis (FIA) using a thin layer flow cell was performed to study the reversibility of the platinum electrode to alteration in both pH and concentration of phosphate buffer solution. Experimental details are given in Chapter 2, Section 2.3.3.

7.3 Steady-State Current Responses

A selection of steady-state responses for the oxidation of $[H_2O_2]_{bulk}$ at a Pt rotating disc electrode as a function of total phosphate buffer concentration, $[PO_4^{3-}]_{tot}$, is shown in Fig. 7.1. These responses were selected at an electrode rotation rate of 4000 rpm and potential of +584 mV vs Ag/AgCl. The current response dependence upon rotation rate, potential and temperature has been described in Chapters 4, 5 and 6, respectively. Two main features are identified in Fig. 7.1. First, the rate of H_2O_2 oxidation (at any given potential, rotation rate and $[H_2O_2]_{bulk}$) increases with buffer concentration. This cannot be attributed to changes in *iR* artifacts since full *iR* compensation was employed throughout these experiments. Secondly, the saturation or the limiting current is approached at lower $[H_2O_2]_{bulk}$ for lower phosphate buffer concentrations. These features may be interpreted in terms of the mechanism for H_2O_2 oxidation developed in Chapters 4 – 6. Both new features exhibited in Fig. 7.1 may be accounted for if the total

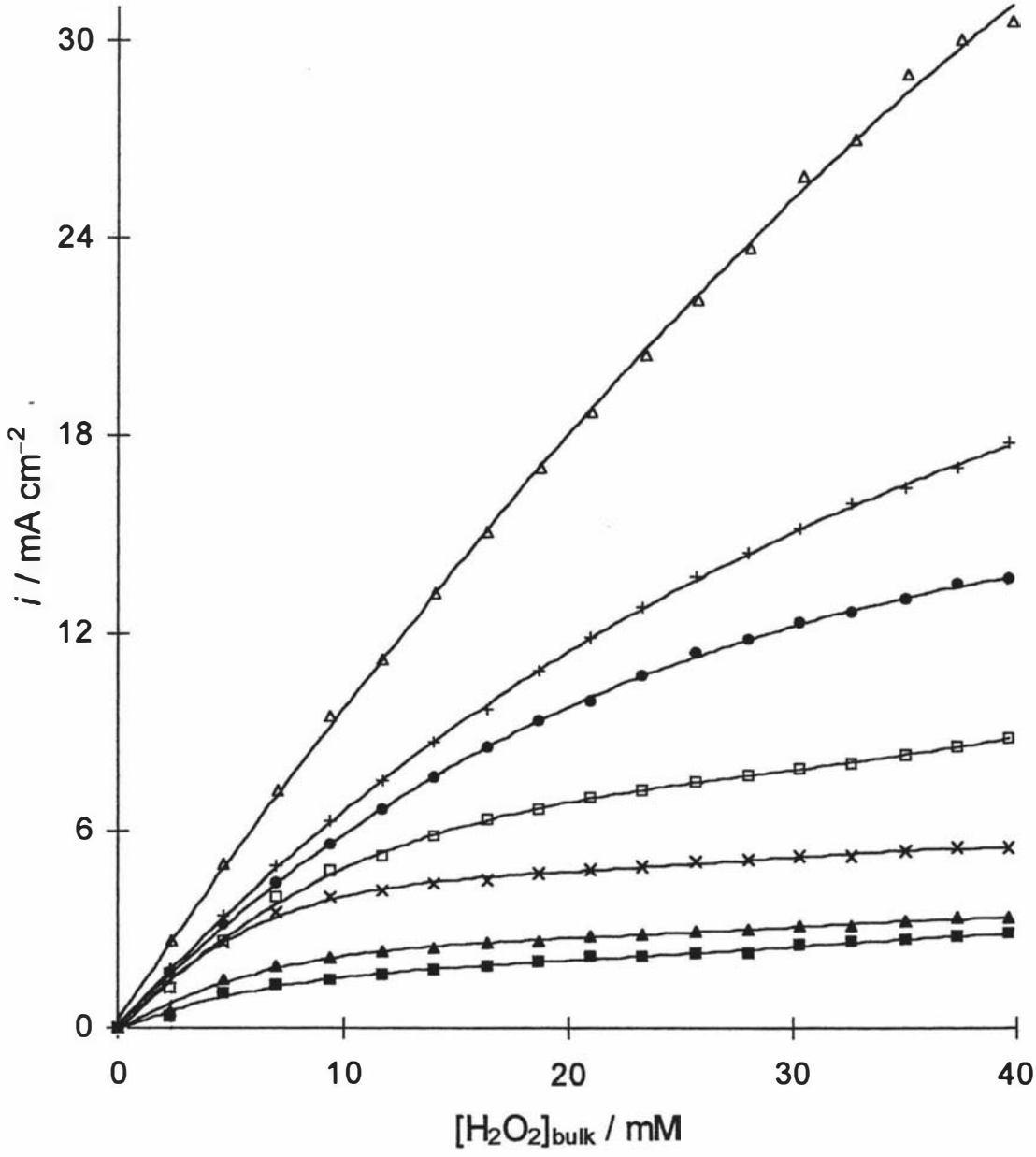

Fig. 7.1 Steady-state response at a platinum rotating disc electrode at a fixed rotation rate (ω = 4000 rpm), potential (E = +584 mV vs Ag/AgCl), temperature (20 °C) and pH 7.3 as a function of $[H_2O_2]_{bulk}$ for a range of $[PO_4^{3-}]_{tot}$: ■ 2, ▲ 5, × 10, □ 25, ● 50, + 75 and Δ 100 mM.

number of surface sites (occupied, unoccupied and reduced) per unit area, N, were to increase with $[PO_4^{3-}]_{tot}$. In addition, the existence of some precursor site, Pt_{PS}, was proposed in the previous chapter to account for the potential-dependence of N (increasing with more anodic potential) with an incompletely defined equilibrium given by reaction 6.5

$$Pt_{PS} \overset{K_{BS}}{\rightleftharpoons} Pt(OH)_2 \tag{6.5}$$

Reaction 6.5 does not give any evidence for the involvement of phosphate as a reactant, hence, the formation of the binding site needs to be investigated under the present conditions. Furthermore, the rate constant k_2 given in Eq. 4.26 for the reduction reaction of binding site described in reaction 4.3 is possibly increased with $[PO_4^{3-}]_{tot}$. However, this could not fully account for the buffer concentration-dependence since if N were to remain constant while k_2 increases, then increasing $[PO_4^{3-}]_{tot}$ would result in saturation occurring to the same extent with bulk $[H_2O_2]$ for each curve in Fig. 7.1 (although the current at saturation would be greater at higher $[PO_4^{3-}]_{tot}$).

7.4 The Current-Dependence Based on Buffer Concentration

To assist with interpretation of the buffer concentration-dependence a selection of the data presented in Fig. 7.1 is shown as a function of $[PO_4^{3-}]_{tot}$ in Fig. 7.2. In addition to displaying the previously noted trend that rate increases with $[PO_4^{3-}]_{tot}$, a number of significant features are evident in this view of the data. First, the relative increase in response with $[PO_4^{3-}]_{tot}$ is greater for higher $[H_2O_2]_{bulk}$. For example, for 5 mM H_2O_2 the response increases by a factor of 1.9 from 25 mM to 100 mM phosphate, whilst for 40 mM H_2O_2 the factor is 3.5 increase over the same range of $[PO_4^{3-}]_{tot}$. This could be attributed to a balance of equilibria between formation of the binding site from some precursor and the binding of H_2O_2 to the Pt(II) active site. Secondly, the increase in rate with $[PO_4^{3-}]_{tot}$ does not follow the expected saturation kinetics if reversible formation of a binding site from a precursor site were to occur according to

$$Pt_{PS} + H_xPO_4^{x-3} \overset{K_{BS}}{\rightleftharpoons} Pt_{BS} \tag{7.1}$$

where $H_xPO_4^{x-3}$ is the particular phosphate species involved in the interaction and Pt_{BS} is the label for the binding site (instead of $Pt(OH)_2$) in this and all subsequent expressions

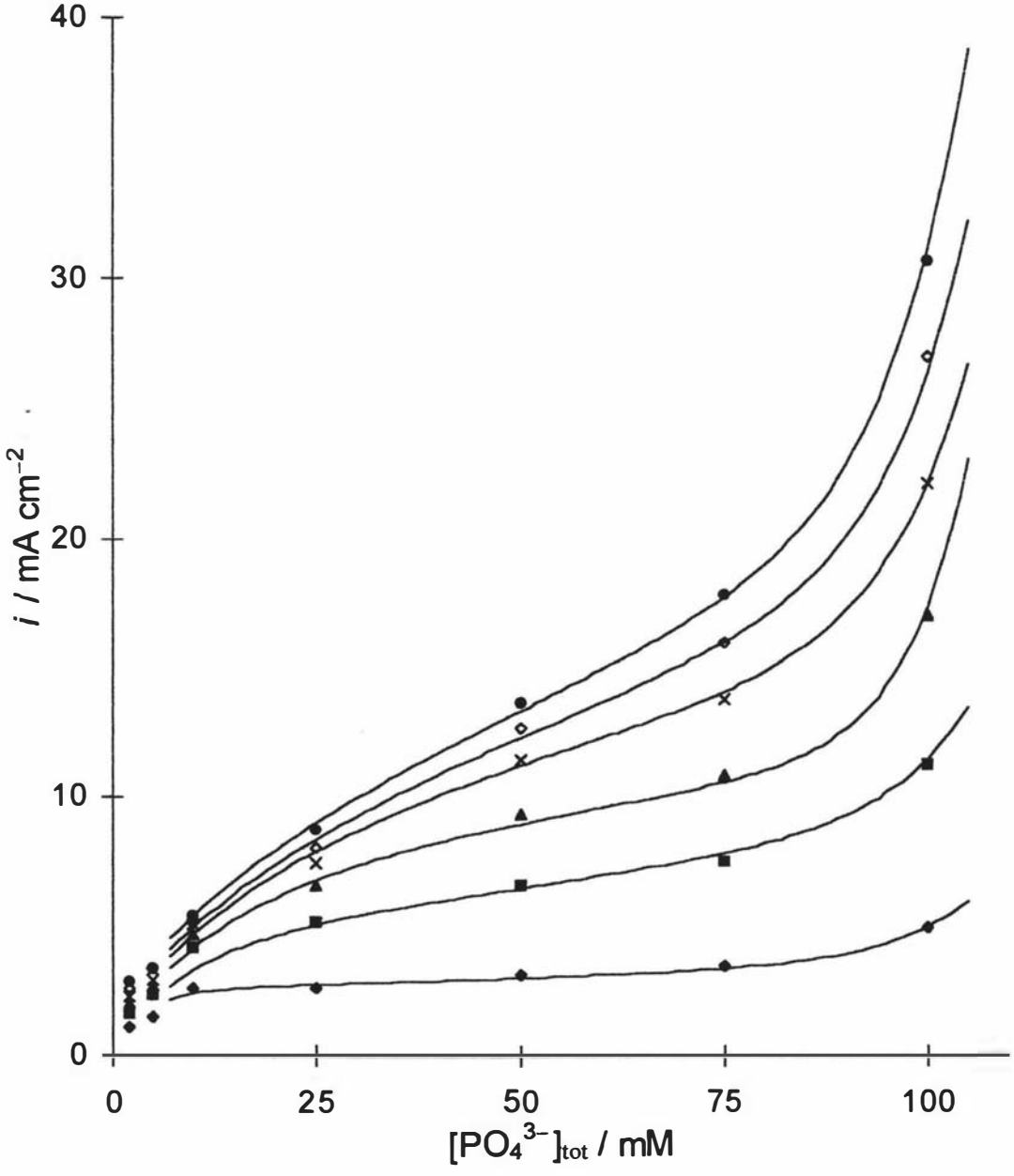

Fig. 7.2 A selection of data from Fig. 7.1 plotted as a function of $[PO_4^{3-}]_{tot}$ at pH 7.3 for fixed $[H_2O_2]_{bulk}$: ◆ 5, ■ 12, ▲ 19, × 26, □ 33 and ● 40 mM.

since the precise composition is not completely defined.

The large increase in rate over the $[PO_4^{3-}]_{tot}$ range 75 - 100 mM may be suggestive of further interaction of phosphate with the binding site

$$Pt_{BS} + H_xPO_4^{x-3} \overset{K_{BS2}}{\rightleftharpoons} Pt_{BS2} \tag{7.2}$$

where it is conceivable that the oxidation state for Pt in Pt_{BS2} is higher than that for Pt_{BS}. A quantitative analysis is not readily obtainable in the present study. Where this analysis was undertaken in previous chapters, it is necessary to include consideration of a number of inhibiting reactions. It was proposed that the reaction product O_2 interferes with the oxidation of H_2O_2 by competitive inhibition of the binding site according to

$$Pt_{BS} + O_2 \overset{K_4}{\rightleftharpoons} Pt_{BS}\cdot O_2 \tag{7.3}$$

where $Pt_{BS}\cdot O_2$ represents the species previously labeled $Pt(OH)_2\cdot O_2$. The proton also inhibits through uncompetitive inhibition of the occupied site (now written as $Pt_{BS}\cdot H_2O_2$)

$$Pt_{BS}\cdot H_2O_2 + H^+ \overset{K_5}{\rightleftharpoons} Pt_{BS}\cdot H_2O_2\cdot H^+ \tag{7.4}$$

The overall rate equation was shown to be

$$j = \frac{k_2 N K_1 [H_2O_2]}{1 + K_4[O_2] + K_1[H_2O_2]\left(1 + K_5[H^+] + k_2/k_3\right)} \tag{5.2}$$

If the simplest case for phosphate-dependence according to reaction 7.1 were considered (ignoring the possibility of higher phosphate species) then the equilibrium constant for binding site formation would be given by

$$K_{BS} = \frac{\theta_{Pt_{BS}}}{[H_xPO_4^{x-3}]\theta_{Pt_{PS}}} \tag{7.5}$$

where $\theta_{Pt_{BS}}$ and $\theta_{Pt_{PS}}$ are the fractional surface coverages for the binding and precursor sites respectively.

Provided the solution pH is held constant, the concentration of the particular phosphate species involved in binding site formation could be assumed to be directly proportional to the total phosphate concentration. Furthermore, the bulk concentration, $[PO_4^{3-}]_{tot,\,bulk}$, is appropriate since this remains constant throughout any experiment. The equilibrium may now be written

$$K'_{BS} = \frac{\theta_{Pt_{BS}}}{[PO_4^{3-}]_{tot,\,bulk}\ \theta_{Pt_{PS}}} \tag{7.6}$$

where K'_{BS} would be expected to exhibit pronounced pH-dependence.

Applying steady-state conditions to all surface species and solving for rate, yields the rate equation involving with the new term for bulk $[PO_4^{3-}]_{tot}$

$$j = \frac{k_2 N K_1 [H_2O_2]}{1 + K_4[O_2] + \dfrac{1}{K'_{BS}\,[PO_4^{3-}]_{tot,\,bulk}} + K_1[H_2O_2]\left(1 + K_5[H^+] + k_2/k_3\right)} \tag{7.7}$$

Quantitative analysis of the experimental data to afford rate and equilibrium constants in the manner taken Chapters 4 and 5 is believed to be inappropriate in this situation. In the previous chapters the SIMPLEX optimization techniques was used for the iterative solution of the rate polynomials that arise from Eq. 5.2 once diffusion effects are accounted for. A similar polynomial expression could be identified for the rate equation, Eq. 7.7, that incorporates the involvement of phosphate species. It is believed that meaningful results would not be obtained from such an analysis. The new term $(K'_{BS}\,[PO_4^{3-}]_{tot,\,bulk})^{-1}$ is likely to dominate the contribution from the terms $K_4[O_2]$ and $K_5[H^+]$ leading to low precision results for K_4 and K_5. This situation would not be ameliorated by varying rotation rate since there are no mass-transport considerations for phosphate. Another major concern is that the possibility of higher phosphate species forming as described in reaction 7.2 would prevent reliable optimization.

Hesitation to undertake optimization is related to the final observation for the data presented in Fig. 7.2. If simple formation of the binding site were to occur according to reaction 7.1 and the species Pt_{BS} were requisite for any oxidation of H_2O_2, then a response would not be expected in the absence of phosphate. Extrapolation of the data presented in Fig. 7.2 does not satisfactorily indicate whether this is the case. It was not possible to conduct rotating disc electrode experiments for $[PO_4^{3-}]_{tot} < 2$ mM whilst maintaining full *iR* compensation due to increased electrolyte resistance. Therefore, this $[PO_4^{3-}]_{tot}$ region was explored using microelectrodes where *iR* artifacts do not prevail. Furthermore, the loss of rotation rate-dependence information is not an issue since quantitative analysis was deemed to be futile and moreover, the decrease in O_2 and H^+ inhibition afforded by hemispherical diffusion is advantageous in clarifying the

dependence on buffer concentration.

7.5 Steady-State Responses at Microelectrodes

The current response of a Pt microelectrode for fixed $[H_2O_2]_{bulk}$ and over a range of $[PO_4^{3-}]_{tot}$ as a function of potential is shown in Fig. 7.3. Two distinct patterns of response are evident, depending on the total phosphate concentration. For all experiments with $[PO_4^{3-}]_{tot} > 5$ mM, a maximum rate develops (or appears to be approached) with increasing anodic potential. The current at the maximum appears to increase with increasing $[PO_4^{3-}]_{tot}$ and the open circuit potential is common at $E = +244$ mV vs Ag/AgCl, consistent with that found for rotating disc experiments in Chapter 5. The increase in maximum response with $[PO_4^{3-}]_{tot}$ is consistent with the observation in the present work that phosphate is incorporated in the binding site. The data for experiments with $[PO_4^{3-}]_{tot} < 5$ mM exhibit a markedly different profile. Here, exponential increases in response with potential are observed, with higher response for the lower $[PO_4^{3-}]_{tot}$. The open circuit potential is shifted anodically to $E = +282$ mV vs Ag/AgCl in the absence of phosphate.

The exponential potential-dependence is such that at the highest potential explored the rate of oxidation is greatest in the absence of phosphate. In general a minimum response at each potential is found in the range 1 mM $< [PO_4^{3-}]_{tot} <$ 2 mM. These observations indicate that the phosphate species is not absolutely necessary for the oxidation of H_2O_2 to proceed. The minima are more readily seen by presenting the data in Fig. 7.3 as a function of $[PO_4^{3-}]_{tot}$. These relationships are shown in Fig. 7.4 for a selection of anodic potentials. At low potentials ($E < +458$ mV vs Ag/AgCl) minima are not observed at low $[PO_4^{3-}]_{tot}$, whilst at higher anodic potentials progressively more pronounced minima occur on the phosphate range 1 mM $< [PO_4^{3-}]_{tot} <$ 2 mM. This behaviour can be described in terms of two distinct mechanisms for the oxidation of H_2O_2 at platinum. At physiological concentrations of phosphate the mechanism described in Chapters 4 and 5 predominates. As the concentration of phosphate changes to lower levels an alternative mechanism begins to operate, in particular at high anodic potentials (where the reaction proceeds more rapidly than in the presence of phosphate). Furthermore, the phosphate-free mechanism is impaired by low concentrations of phosphate and it is only when sufficient binding sites involving phosphate are formed that higher oxidation rates are

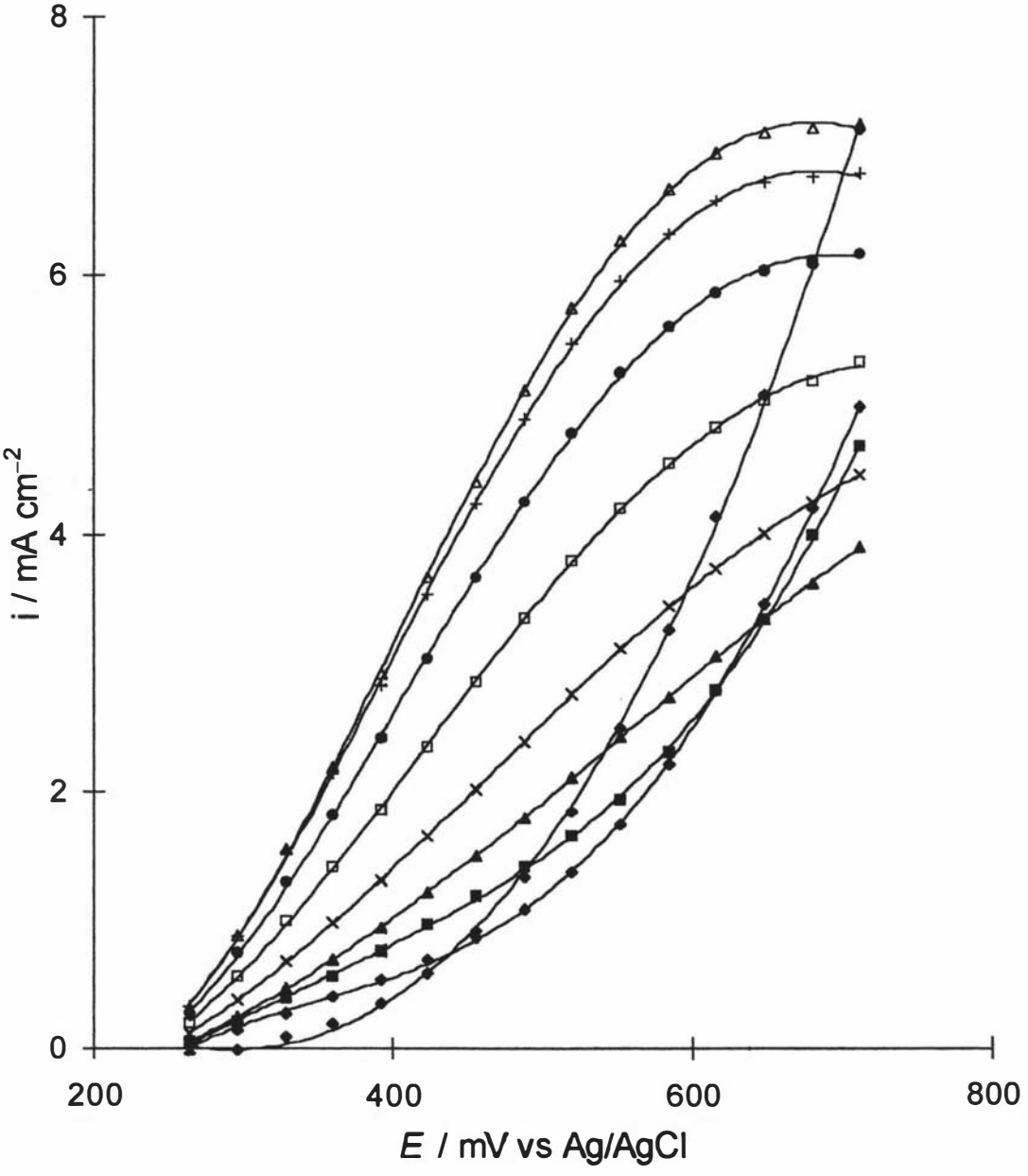

Fig. 7.3 Steady-state response at a platinum microelectrode at $[H_2O_2]_{bulk} = 5$ mM as a function of potential for a range of $[PO_4^{3-}]_{tot}$ at pH 7.3; ◆ 0 mM, O 1 mM, ■ 2 mM, ▲ 5 mM, × 10 mM, □ 25 mM, ● 50 mM, + 75 mM and Δ 100 mM.

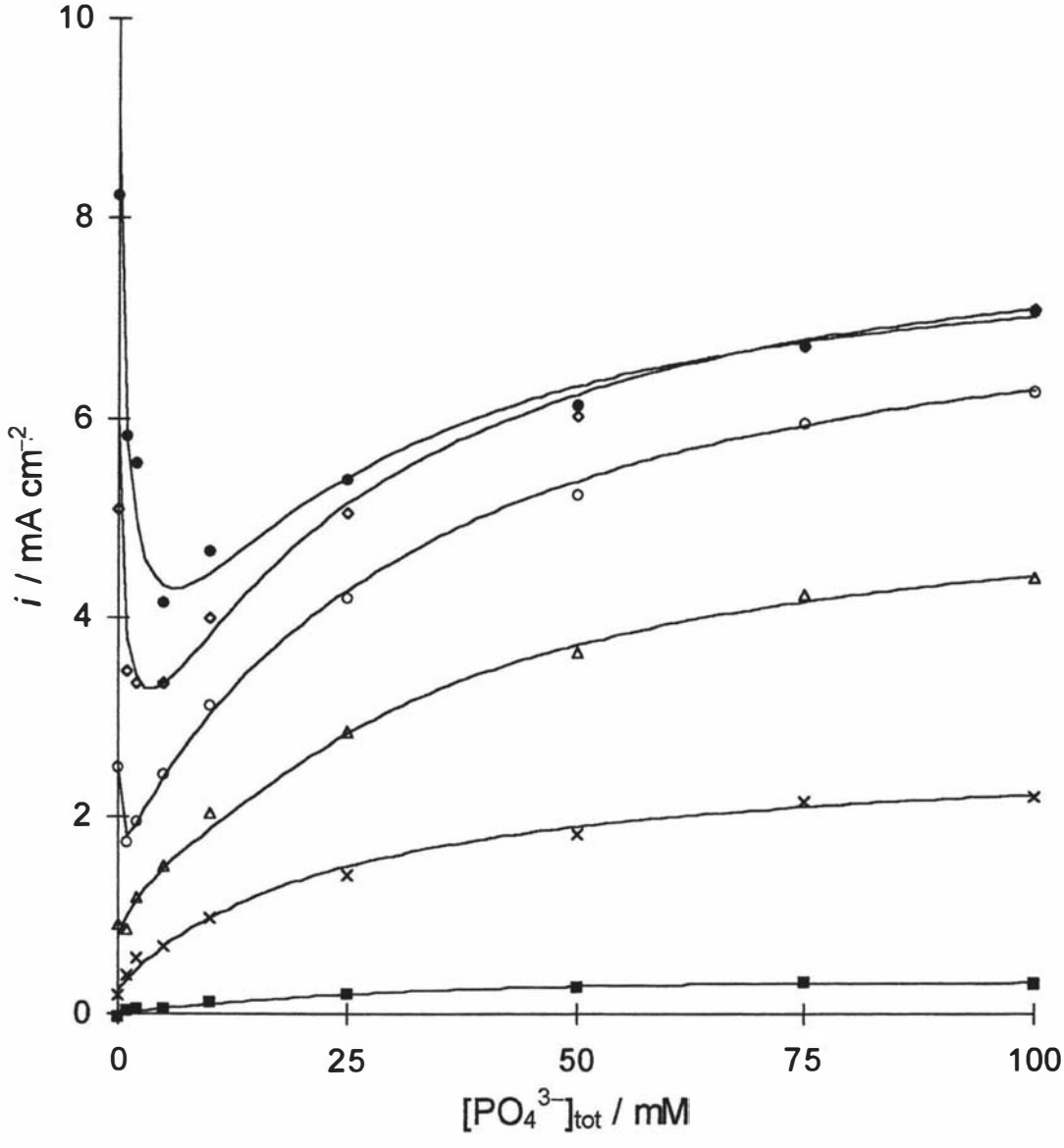

Fig. 7.4 A selection of data from Fig. 7.3 plotted as a function of $[PO_4^{3-}]_{tot}$ at pH 7.3 for fixed potentials vs Ag/AgCl: ■ 264 mV, × 360 mV, Δ 456 mV, O 552 mV, □ 648 mV and ● 744 mV.

observed. In contrast, at low potentials the phosphate-mediated mechanism is more rapid at all concentrations of phosphate.

The nature of the phosphate-free mechanism on Pt microelectrodes was examined in the $[H_2O_2]_{bulk}$ range 0 – 25 mM and for potentials +232 mV to +744 mV vs Ag/AgCl using staircase potentiometry and the data are shown in Fig. 7.5. In a similar manner to that reported for phosphate buffer systems, in this study and studies given in previous chapters, saturation kinetics are observed at all potentials in Fig. 7.5 with greater response at more anodic potentials. It is important to note that no response is observed at all potentials in the absence of H_2O_2 indicating that the potential-dependence exhibited in the phosphate-free curve in Fig. 7.3 can not be attributed to oxidation of the solvent.

In a similar manner to the initial qualitative analysis of binding site kinetics given in Chapter 4, a Hanes plot [158] given in Fig. 7.6 for the data presented in Fig. 7.5, shows linear regions similar to that found in Fig. 4.6. This is consistent with a binding site mechanism operating also in the phosphate-free system with maximum rate (at saturation) and binding constants, K_M, increasing with potential. Exact Michaelis-Menten kinetics are not exhibited at low $[H_2O_2]_{bulk}$ where the reaction rate is lower than expected, a phenomenon that was demonstrated in Chapter 4 to due to competitive inhibition of the binding site by O_2. There is no evidence obtainable from Fig. 7.5 to support any hypothesis for accompanying uncompetitive inhibition by H^+ since mass-transport variation by rotation rate is not available.

7.6 Steady-State Responses in Phosphate-Citrate Buffer

There is the possibility that the phosphate-dependence of both rotating disc and microelectrodes arise, in part, from diminished buffering capacity of the electrolyte adjacent to the electrode surface as $[PO_4^{3-}]_{tot}$ decreases. The predicted consequence of any failure of buffering would be to exacerbate the non-competitive inhibition by the proton according to reaction 7.4. The significance of electrolyte buffer capacity on the phosphate-dependence was assessed by conducting a second series of microelectrode experiments with the inclusion of 0.100 mol L^{-1} citrate buffer at pH 7.3 throughout whilst varying $[PO_4^{3-}]_{tot}$. The response of a Pt microelectrode to $[PO_4^{3-}]_{tot}$ in this mixed phosphate-citrate buffer is shown in Fig. 7.7 as a function of $[H_2O_2]_{bulk}$. At all anodic potentials examined the trend shown in Fig. 7.7 is maintained with saturation kinetics

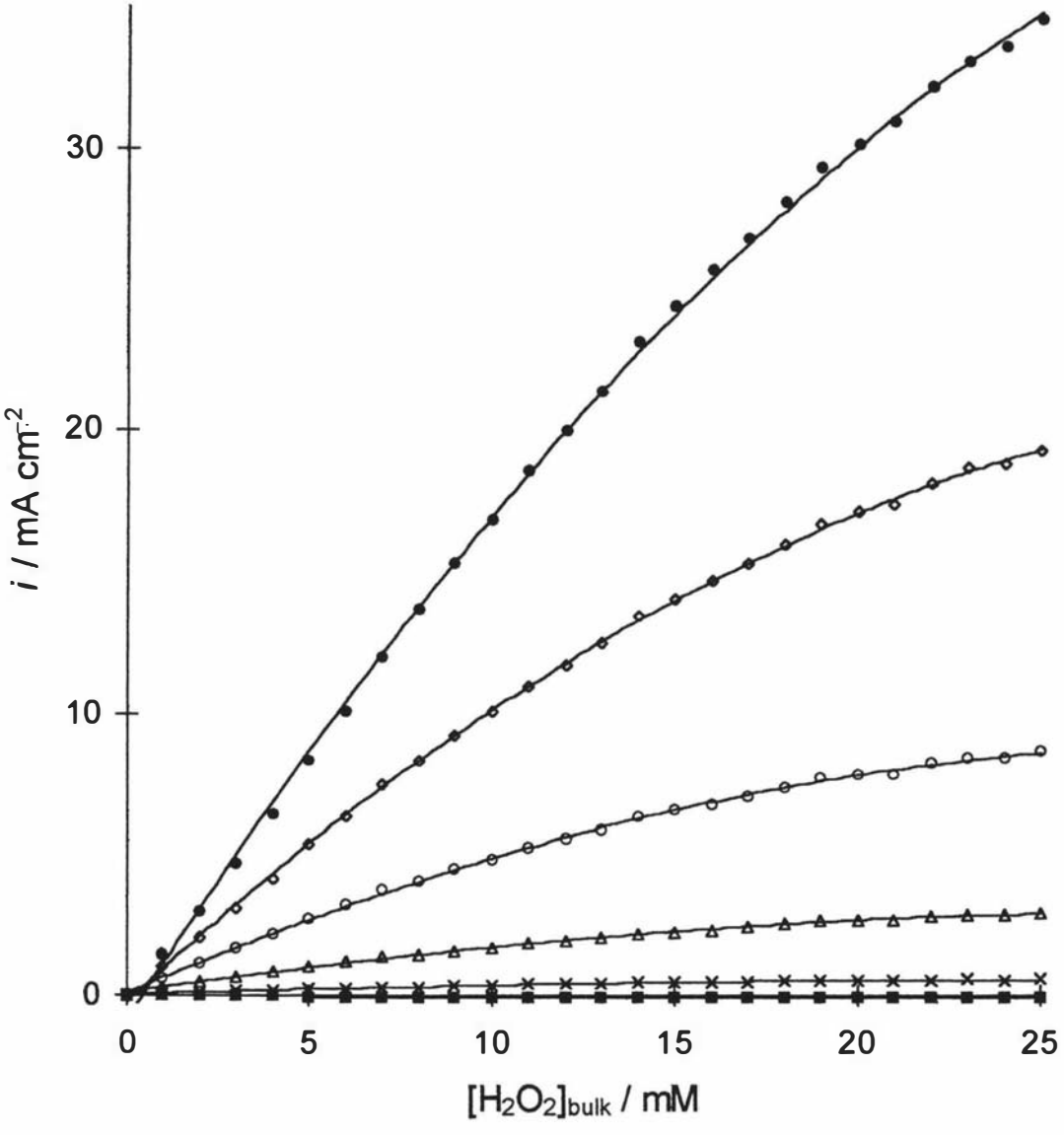

Fig. 7.5 Steady-state response at a platinum microelectrode as a function of $[H_2O_2]_{bulk}$ in water (with no phosphate buffer or supporting electrolyte) for a range of potentials vs Ag/AgCl: ■ 264 mV, × 360 mV, Δ 456 mV, O 552 mV, □ 648 mV and ● 744 mV.

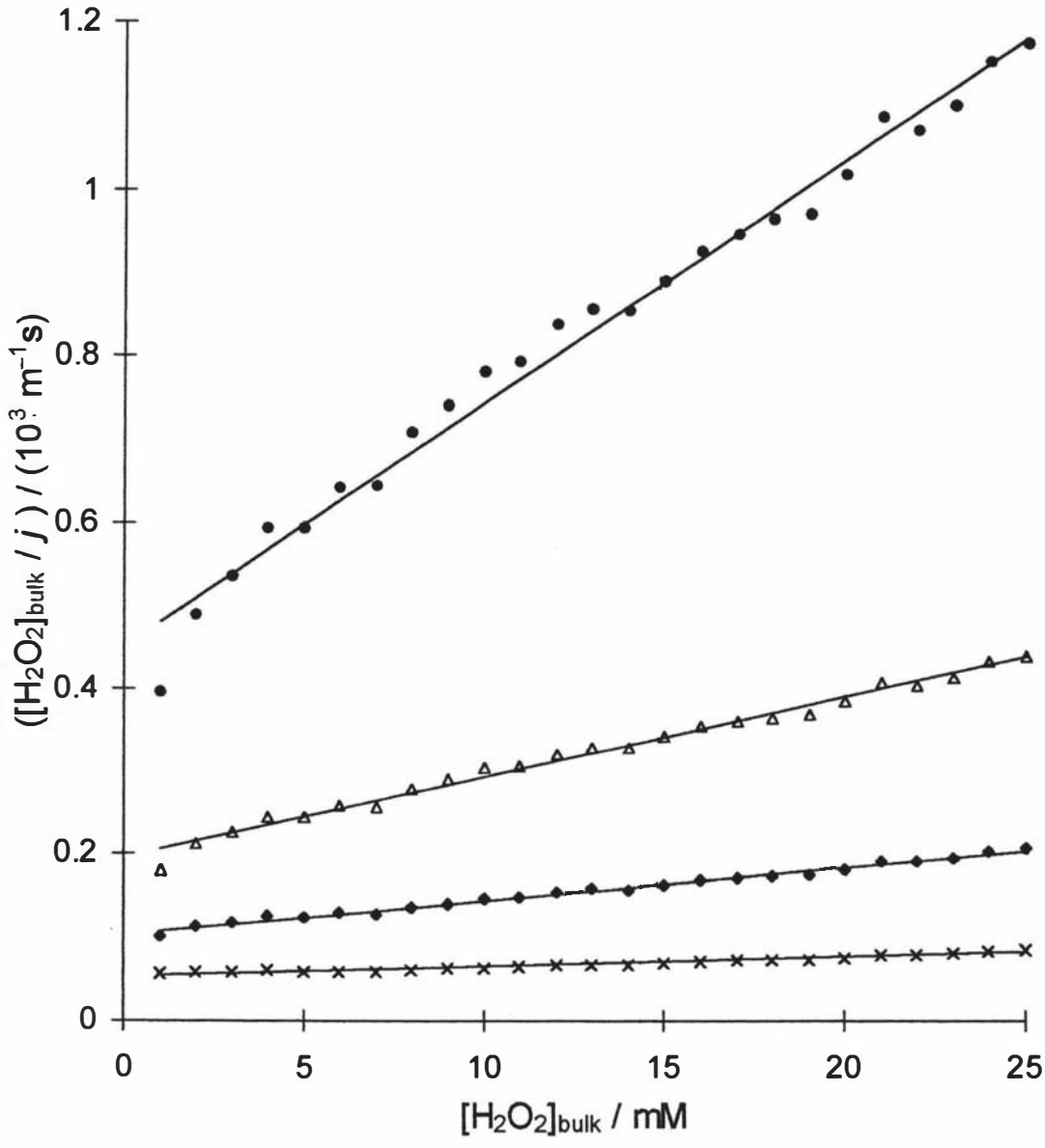

Fig. 7.6 Hanes plots for the data presented in Fig. 7.5 for a selection of electrode potentials: ● 392, Δ 456, ◆ 520 and × 616 mV vs Ag/AgCl.

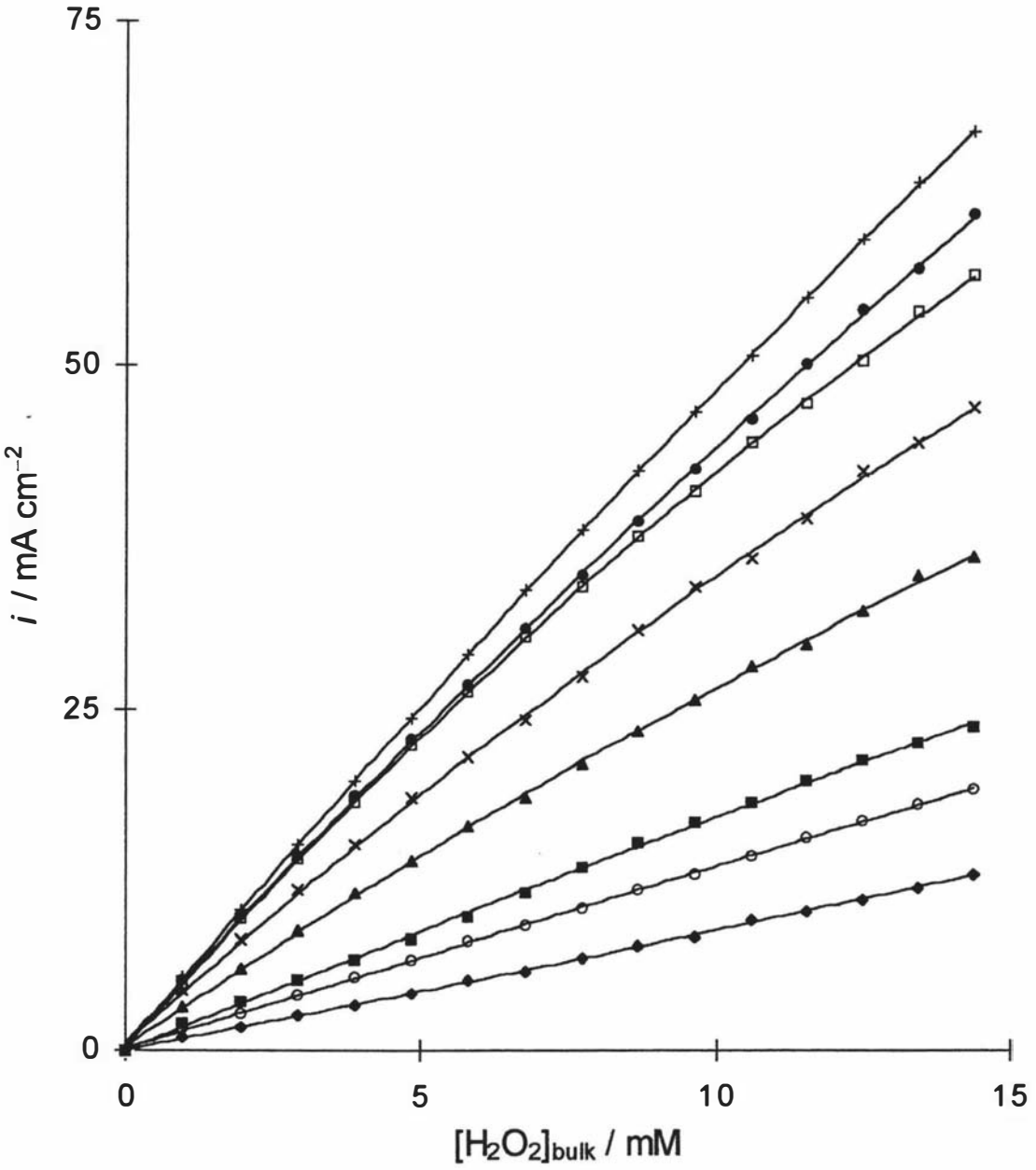

Fig. 7.7 Steady-state response at a platinum microelectrode at fixed potential (E = +584 mV vs Ag/AgCl) with 0.100 mol L^{-1} citrate buffer at pH 7.3 maintained throughout for a range of $[PO_4^{3-}]_{tot}$: ◆ 0 mM, O 1mM, ■ 2 mM, ▲ 5 mM, × 10 mM, □ 25 mM, ● 50 mM and + 75 mM.

exhibited with a greater response for higher $[PO_4^{3-}]_{tot}$ and no minima at low $[PO_4^{3-}]_{tot}$. This is consistent with the interpretation discussed above that phosphate is involved in a binding site and the dependence can not be attributed solely to a loss of buffer capacity at low $[PO_4^{3-}]_{tot}$.

Two further observations may be made on the data shown in Fig. 7.7. First, the current obtained at any given phosphate and H_2O_2 concentration is greater in the presence of citrate indicating that the enhanced buffer capacity may play some part. Secondly, in the absence of phosphate, the oxidation process does not revert to the high rate shown in Figs. 7.3 and 7.4. This may indicate that citrate inhibits the rapid phosphate-free mechanism to some extent.

7.7 The Electrode Reversibility With Varying Buffer Concentration and pH

The reversibility of an electrode (within a single polishing and pretreatment regime) to a series of test solutions with varying phosphate concentration was determined. This was achieved using a thin-layer flow cell containing a planar Pt electrode connected to an FIA system. The response of the thin-layer flow cell electrode as a function of $[H_2O_2]$ shown in Fig. 7.8 is similar to that demonstrated for rotating disc electrodes in Chapters 4-6. However, lower current densities and more pronounced saturation kinetics are exhibited due to the relatively low solution velocity across the face of the electrode in the thin-layer flow cell (akin to low rotation rates in rotating disc experiments) resulting in poor removal of the inhibiting species O_2 and H^+. Of greater interest is the ability to investigate a series of increasing and decreasing $[PO_4^{3-}]_{tot}$ with fixed $[H_2O_2]_{bulk}$ in a rapid sequence of experiments. Figure 7.9 shows the relative response to 10 mM H_2O_2 in 50 and 100 mM phosphate buffer. The sequence is carried out by passing a series of 5 replicate 50 mM phosphate solutions through the thin-layer flow cell followed by a series of 5 × 100 mM buffer, 5 × 50 mM buffer and then finally 5 × 100 mM buffer.

The extent of any carry over of H_2O_2 is negligible since the response returns to zero after every sample is swept out of the thin layer cell by the carrier phosphate buffer ($0.100\ mol\ L^{-1}$). The average response for replicates at each phosphate concentration demonstrates that the effect of varying phosphate is reversible and indicate that the kinetics for attaining steady-state conditions for Eq. 7.1 are relatively rapid. The spread in peak maximum values in each set of replicates relates to the reproducibility of the FIA

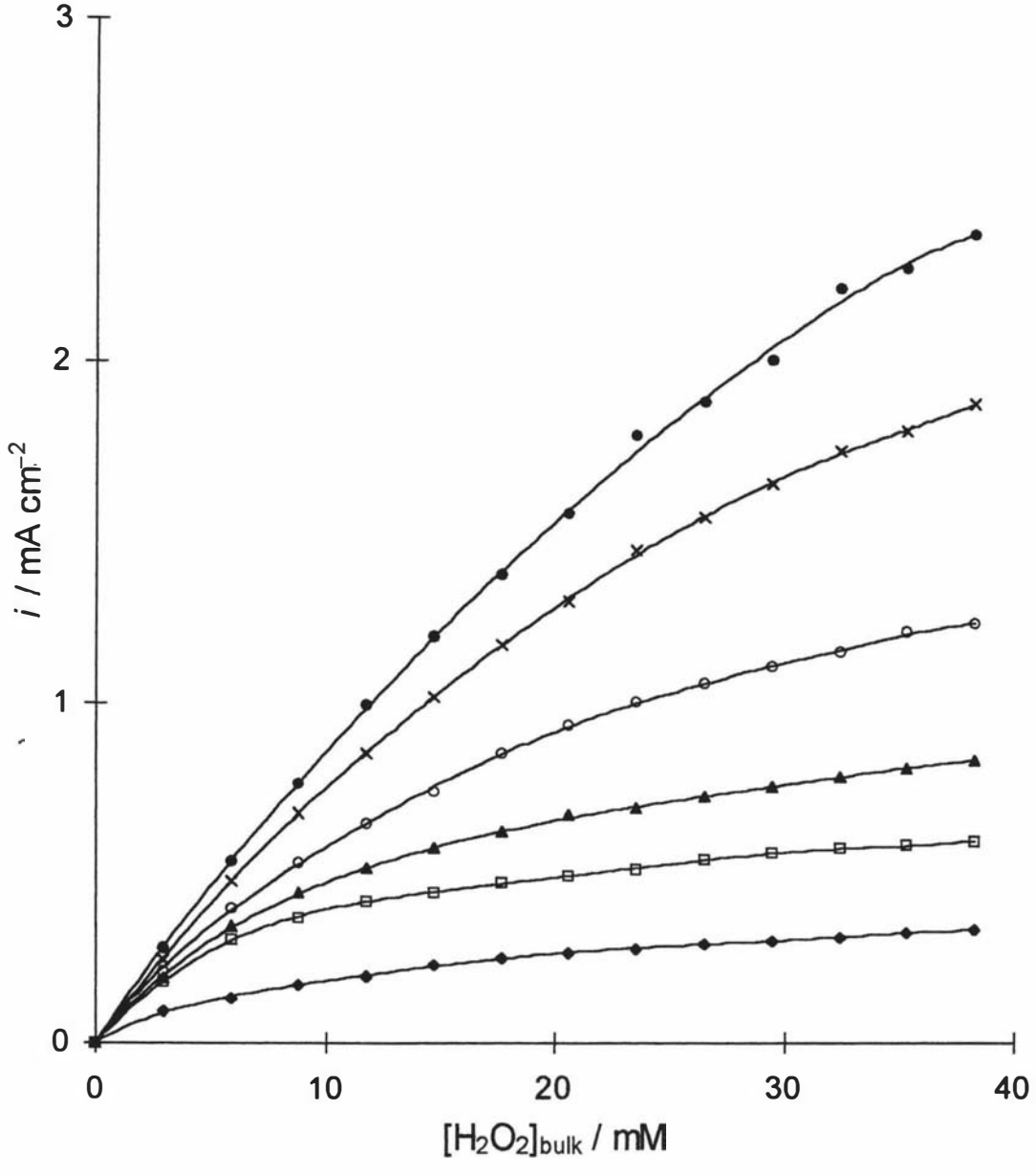

Fig. 7.8 The response of the thin layer flow cell electrode at +600 mV vs Ag/AgCl as a function of $[H_2O_2]_{bulk}$ over a range of $[PO_4^{3-}]_{tot}$: ◆ 10, □ 25, ▲ 50, O 75, × 100 and ● 125 mM. The carrier reagent concentration was the same $[PO_4^{3-}]_{tot}$ for each experiment.

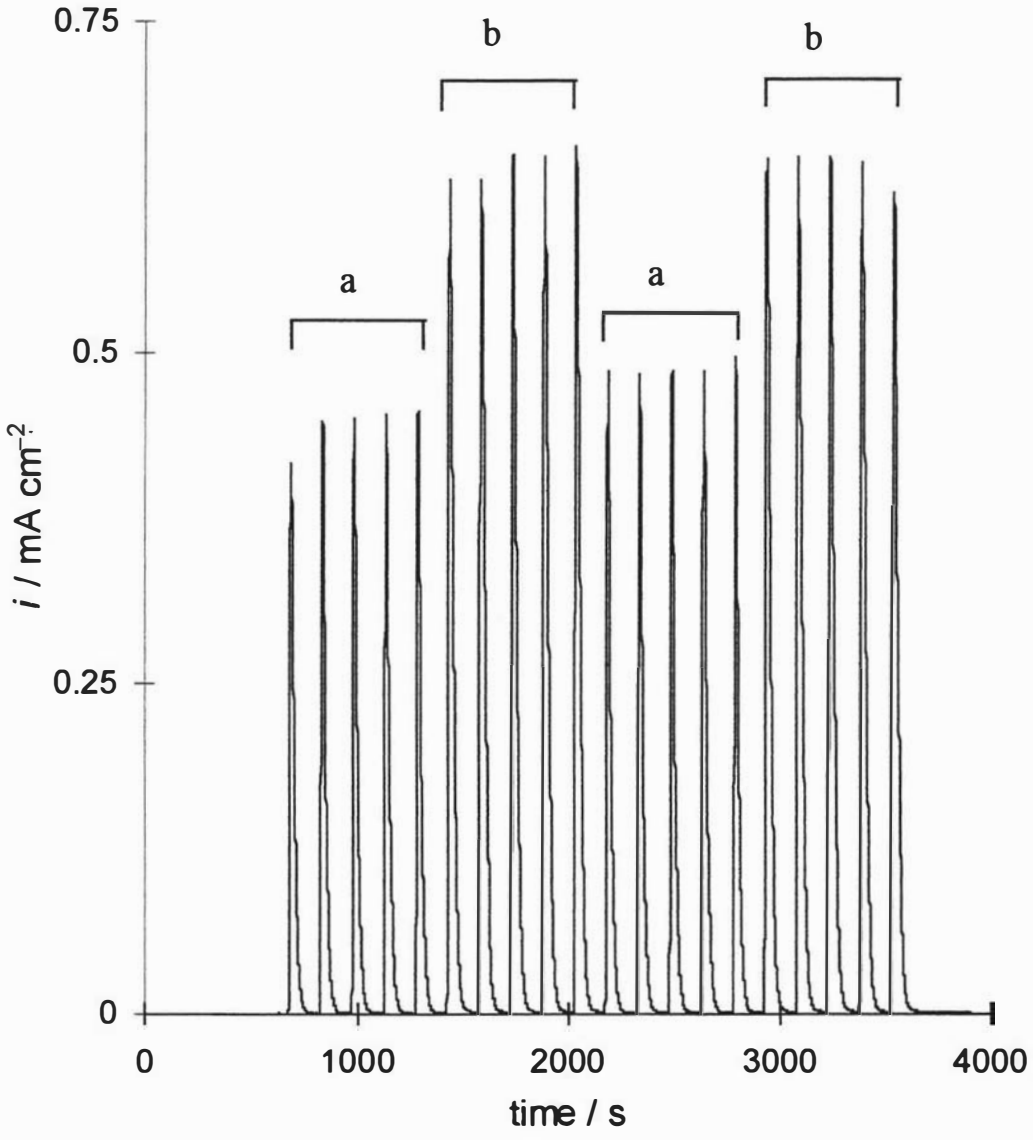

Fig. 7.9 A series of responses for a platinum electrode in a thin-layer flow cell at a fixed potential (E = +600 mV vs Ag/AgCl) connected to an FIA system for two series of test solutions at pH 7.3. Series **a**: 5 replicates of 10 mM H_2O_2 and 50 mM phosphate. Series **b**: 5 replicates of 10 mM H_2O_2 and 100 mM phosphate. 100 mM phosphate buffer at pH 7.3 used as a carrier solution at flow rate 250 ± 10 μL/min.

system. The flow cell is not compensated for *iR* effects since the solution resistance is inherently varying during the sequence of test solutions. The solution resistance in the flow cell is too small to be the cause for the 50 mM phosphate having lower response than the 100 mM.

7.8 Steady-State Responses as a Function of Buffer pH

The steady-state response of a Pt microelectrode to $[H_2O_2]_{bulk}$ at +584 mV vs Ag/AgCl in a range of phosphate buffers with $[PO_4^{3-}]_{tot} = 0.100$ mol L^{-1} and varying pH is shown in Fig. 7.10. In general, for pH > 6.4 the H_2O_2 concentration-dependence profiles were similar to those shown for a rotating disc electrode at pH 7.3 given in Chapter 5, Fig. 5.2. At lower pH, however, the saturation kinetics profiles are not as distinct with development of sigmoidal responses. A selection of these responses as a function of pH for a fixed potential and $[H_2O_2]_{bulk}$ is shown in Fig. 7.11. The maximum oxidation rate occurs at pH 6.8, decreasing markedly under more basic or acidic conditions so that half the maximum response is attained at pH 6.0 and pH 7.5.

The potential-dependence for each pH at a fixed $[H_2O_2]_{bulk}$ is shown in Fig. 7.12. The profiles for pH > 6.4 are similar to the 100 mM phosphate curve in Fig. 7.3 (although the magnitude of the response varies as shown in Fig. 7.12), with maxima developing ca. +600 mV vs Ag/AgCl. The potential-dependence for pH < 6, however, is similar to the exponential profiles for the low $[PO_4^{3-}]_{tot}$ curves in Fig. 7.3, with the response decreasing markedly with decreasing pH. The potential-dependence is further complicated by the open-circuit potential shifting to more anodic potentials with decreasing pH. This is consistent with the linear sweep voltammetry experiments for H_2O_2 on Pt reported by Guilbault and Lubrano [185] where similar shifts were found. Interpolation of the present data, however, does not reveal clear Nernstian behaviour of the open-circuit potential.

The results presented in Figs. 7.11 and 7.12 can be interpreted in two parts. At all pHs, it is proposed that $H_2PO_4^-$ is the required species for binding site formation. The rapid drop in response above pH 6.8 is consistent with the decrease in $[H_2PO_4^-]$ given $pK_{a2} = 7.3$ [186]. Thus, reaction 7.1 may now be written

$$Pt_{PS} + H_2PO_4^- \overset{K_{BS}}{\rightleftharpoons} Pt_{BS} \qquad (7.8)$$

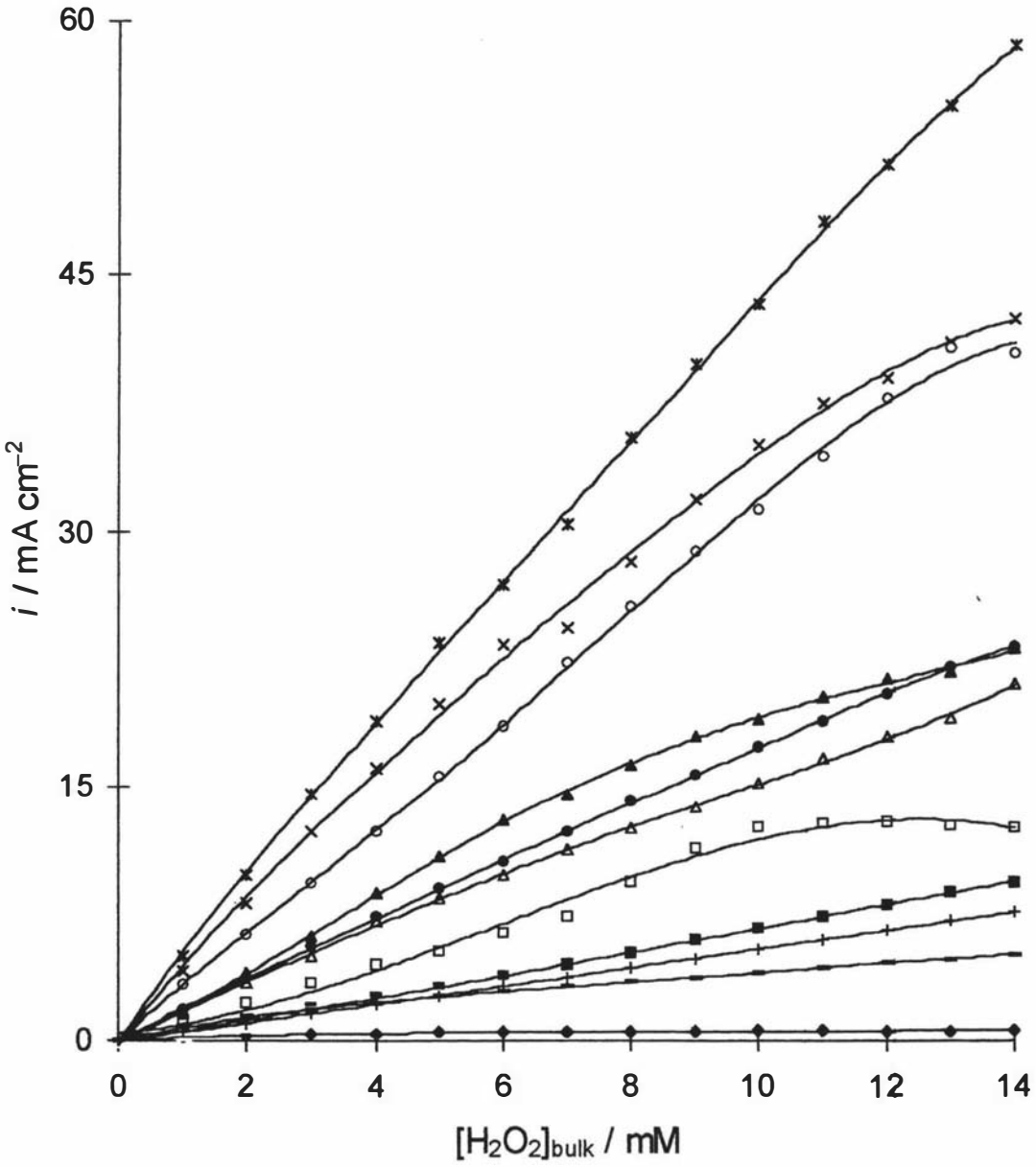

Fig. 7.10 Steady-state responses at platinum microelectrode as a function of $[H_2O_2]_{bulk}$ at + 584 mV vs Ag/AgCl and in $[PO_4^{3-}]_{tot}$ = 100 mM for a range of buffer pHs; ◆ 4.1, □ 5.3, ▲ 6.0, × 6.4, ✳ 6.8, ○ 7.3, ● 7.5, Δ 7.8, ■ 8.2, + 9.2 and – 10.1.

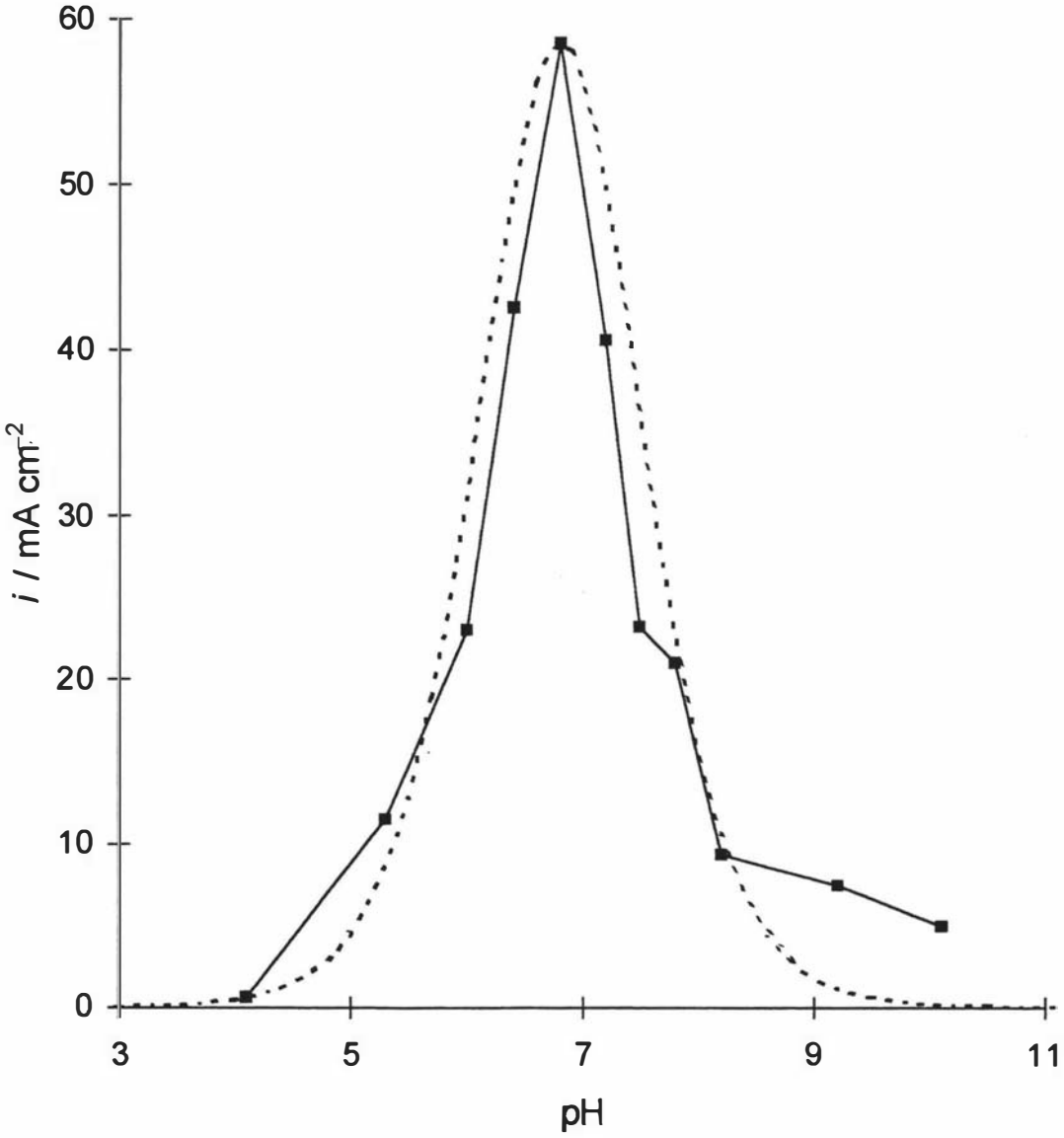

Fig. 7.11 Steady-state responses (■) at a platinum microelectrode at fixed potential (E = +584 mV vs Ag/AgCl) with $[PO_4^{3-}]_{tot}$ = 100 mM and $[H_2O_2]_{bulk}$ = 14 mM for a range of buffer pHs. The smooth dashed curve is the best fit for Eq. 7.10 to the experimental data.

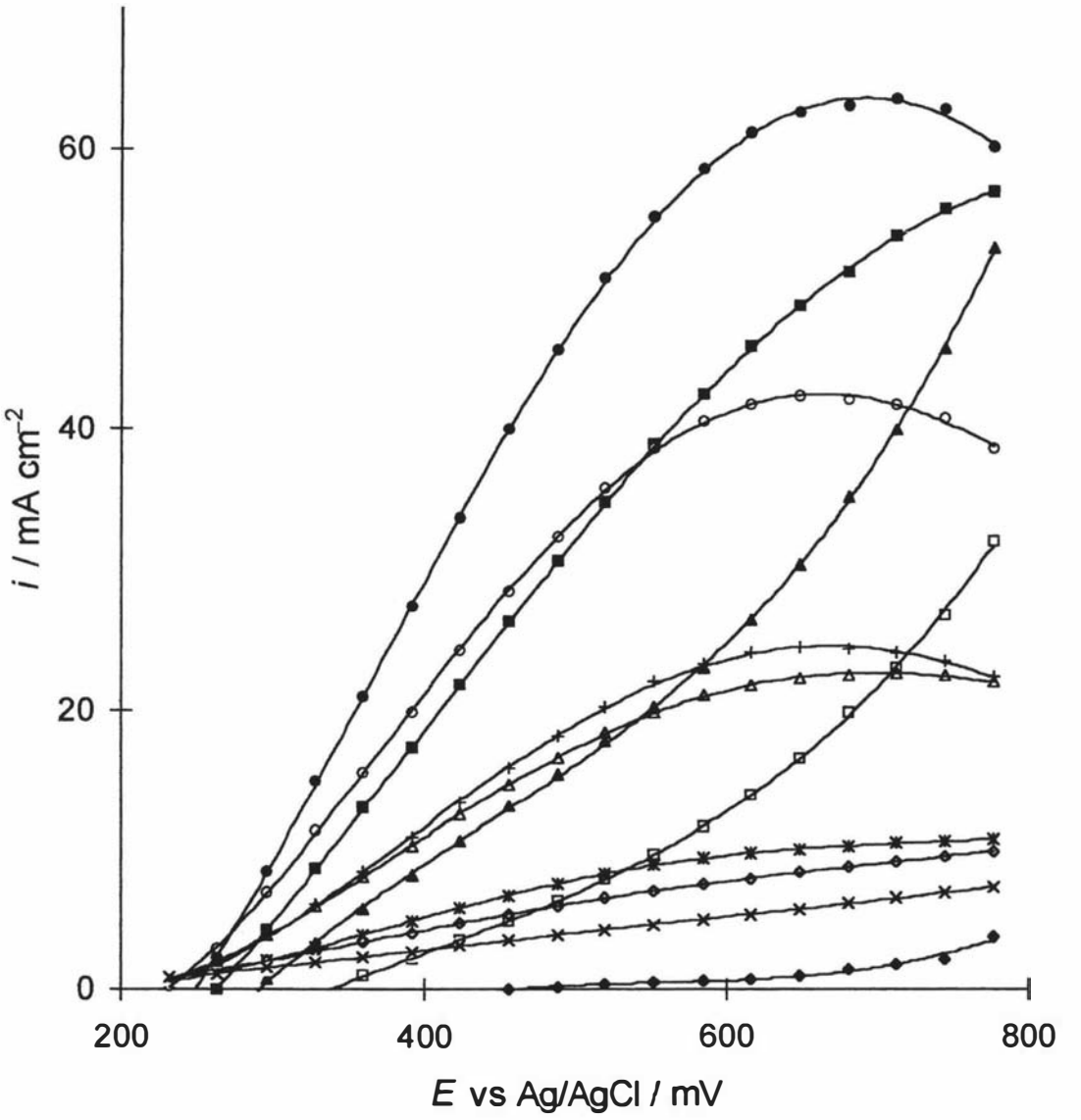

Fig. 7.12 Steady-state responses at a platinum microelectrode for the oxidation of 14 mM H_2O_2 in $[PO_4^{3-}]_{tot}$ = 100 mM as a function of potential (vs Ag/AgCl) for a range of pH: ◆ 4.1, □ 5.3, ▲ 6.0, ■ 6.4, ● 6.8, ○ 7.3, + 7.5, Δ 7.8, ✳ 8.2, ◇ 9.2 and × 10.1.

This is consistent with the FTIR studies of phosphate adsorption on Pt at pH 6.8 reported by Ye *et al.* [187] where it was found that $H_2PO_4^-$ was the species interacting with the surface.

The decrease in response at pH < 6.8 is greater than that expected if the non-competitive inhibition by the proton according to reaction 7.4 where to be the sole pH effect. It is calculated that the bulk pH must fall below pH 3 before even a 5% decrease would occur based upon the kinetic and equilibria data reported in the previous chapter. This marked decrease in response over the range pH 6.8 to pH 5 can also not be attributed to decrease in $[H_2PO_4^-]$ at low pH since $pK_{a1} = 2.15$ [186]. Accordingly, this low pH inhibition mode must act to hinder the formation of the binding site in reaction 7.8. The simplest possibility is that the precursor site, Pt_{PS}, undergoes protonation to give an inactive site

$$Pt_{PS} + H^+ \overset{K_H}{\rightleftharpoons} Pt_{PS}{\cdot}H^+ \tag{7.9}$$

The exponential potential-dependence in Fig. 7.12 at pH < 6.4 could be ascribed to a progressive decrease in K_H with more anodic potential. Incorporation of this equilibrium into a mass-balance expression for all surface species (excluding $Pt_{BS}{\cdot}H_2O_2{\cdot}H^+$ and $Pt_{BS}{\cdot}O_2$ since their contributions under microelectrode conditions are assumed to be negligible) yields a modified rate equation.

$$j = \frac{k_2 N K_1[H_2O_2] K_{BS}[H_2PO_4^-]}{1 + K_H[H^+] + K_1[H_2O_2] K_{BS}[H_2PO_4^-]} \tag{7.10}$$

The predicted form of this response can be compared with the experimental data using the value for K_1 reported in the previous chapter (Table 6.5) and $[H_2PO_4^-]$ calculated from pK_{a1}, pK_{a2} and pK_{a3} for phosphate [186]. The optimized fit of Eq. 7.10 to the experimental data is shown as a smooth dashed curve in Fig. 7.11 and is for $K_H = 2.5 \times 10^3$ m^3 mol^{-1} and $K_{BS} = 0.1$ m^3 mol^{-1}. There is a good qualitative agreement between the experimental data and the best fit for Eq. 7.10 which indicates that the proposed inhibition of the precursor site is not inconsistent with the experimental data.

7.9 Conclusions

The data presented in this chapter indicates that the mechanism proposed in previous chapters was not complete and the binding site labeled as $Pt(OH)_2$ was not entirely

appropriate. This leads to a modification of the proposed mechanism by involvement of $H_2PO_4^-$ in forming the active binding site. This does not detract, however, from the utility of the general model in describing the oxidation of H_2O_2 at Pt electrodes in phosphate buffer solutions at fixed concentration and pH. Furthermore, the present study demonstrates that there is a relationship between phosphate buffer concentration and the number of binding sites at the electrode surface and hence the overall rate, with saturation kinetics exhibited at all $[PO_4^{3-}]_{tot}$. In the absence of phosphate, saturation kinetics are also observed for H_2O_2 oxidation and at high anodic potentials this mechanism operates at a higher rate than in the presence of phosphate. $H_2PO_4^-$ has been inferred to be the species involved in the formation of the binding site based upon the pronounced pH-dependence exhibited at pH > 6.8. A new form of proton inhibition of the precursor site has also been proposed to account for the depression in response at pH < 6.8. The modified mechanism is summarized in Fig. 7.13.

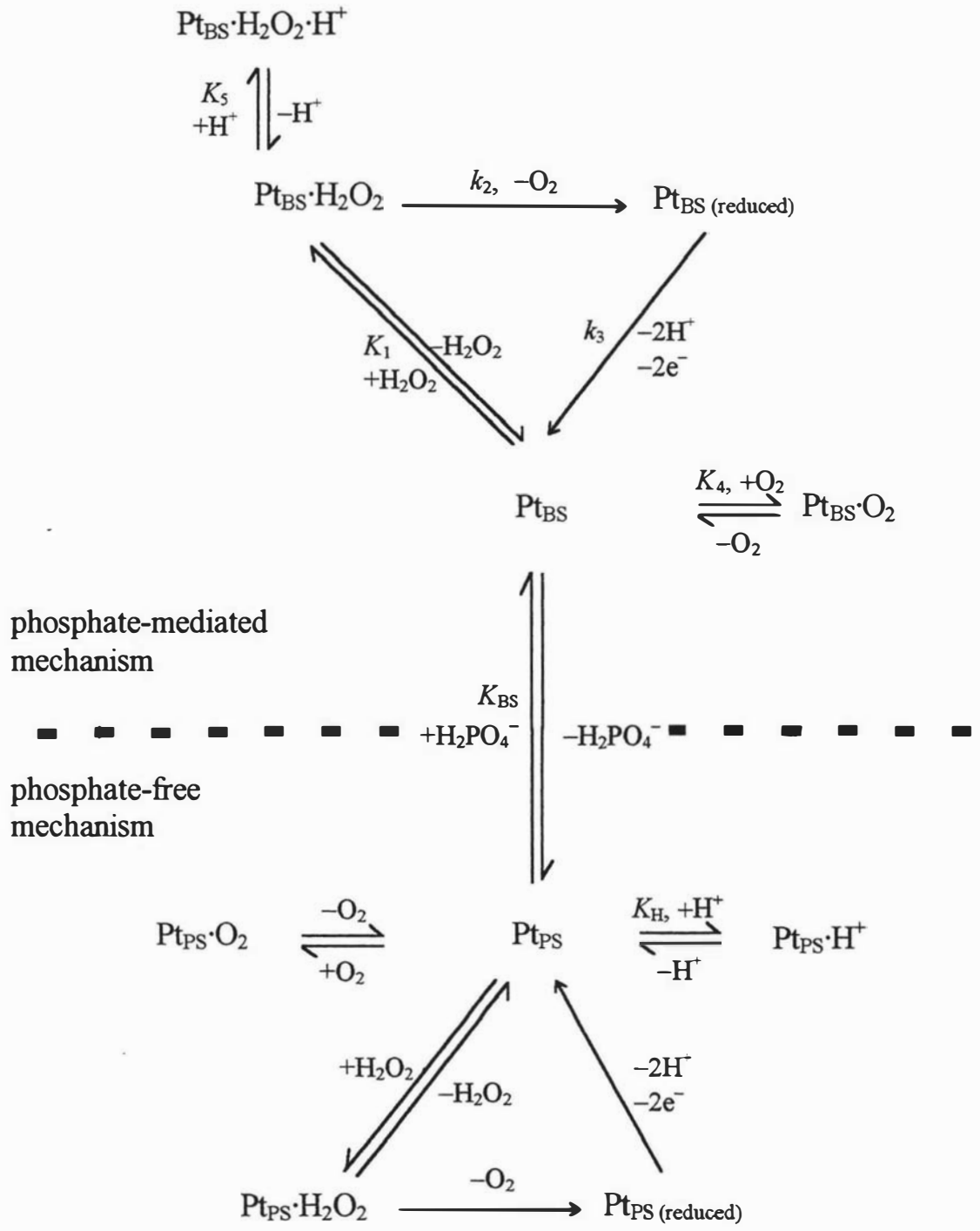

Fig. 7.13 Summary of the mechanism for the oxidation of H_2O_2 at both phosphate-mediated binding site, Pt_{BS}, and phosphate-free precursor site, Pt_{PS}. The mechanism above the dashed line is that which predominates in phosphate buffer under physiological conditions as in Chapters 4-6. Below the dashed line the mechanism is that found in phosphate-free system.

CHAPTER EIGHT

The Inhibitory Effect of Chloride Ions on the Electrochemical Oxidation of Hydrogen Peroxide at Platinum Electrodes

8.1 Introduction

In the previous chapters 4-7, a comprehensive mechanism has been established for the oxidation of H_2O_2 at platinum electrodes. This mechanism takes account into variation in hydrodynamic conditions, potential, temperature and formation of the central binding site by incorporation of solution species. One novel feature of the mechanism is the inhibition exhibited by the reaction products, O_2 and H^+.

The focus of this chapter is to provide an initial investigation to explore the susceptibility of the H_2O_2 oxidation reaction to inhibitors not directly involved in either the overall reaction or in forming the binding sites.

Since the electrode kinetics have been shown in previous chapters to be similar in form to that exhibited by enzymes, it is appropriate to discuss inhibition in terms of the terminology used in describing enzyme kinetics.

In general, an inhibitor (I) may interfere with an enzyme (E) mediated reaction for the conversion of a substrate (S) to products (P) by either complexing with the enzyme binding site or by binding to the enzyme-substrate complex (ES). The first may prevent the formation of the enzyme-substrate complex, whilst the second may inactivate the complex towards formation of the products.

In enzyme kinetics, three distinct modes of inhibition are observed: competitive, non-competitive and uncompetitive inhibition. These modes are shown schematically in Fig. 8.1.

Competitive inhibition is the most frequently encountered inhibition mode observed in enzyme kinetics [188]. As shown in Fig. 8.1(a), inhibition is afforded through the inhibitor binding to the active site and hence blocking the binding of the substrate. Thus, increasing the concentration of the inhibiting species decreases the overall rate.

Non-competitive inhibition also involves binding of the inhibitor to the enzyme. However, the sites for substrate and inhibitor binding are different (represented by different shapes in Fig. 8.1 (b)) so that the concentration of inhibitor does not influence

a) Competitive Inhibition

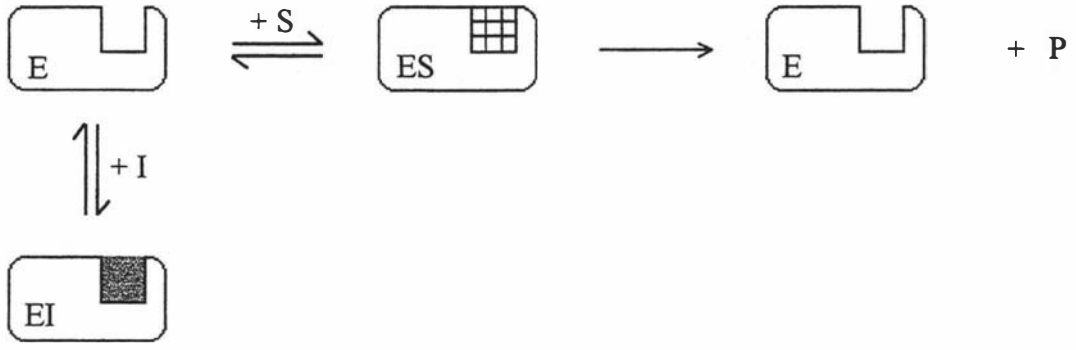

b) Non-competitive Inhibition

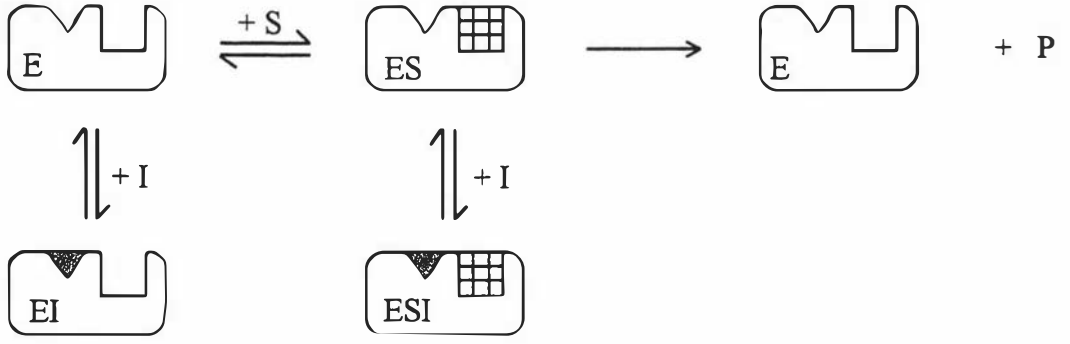

c) Uncompetitive Inhibition

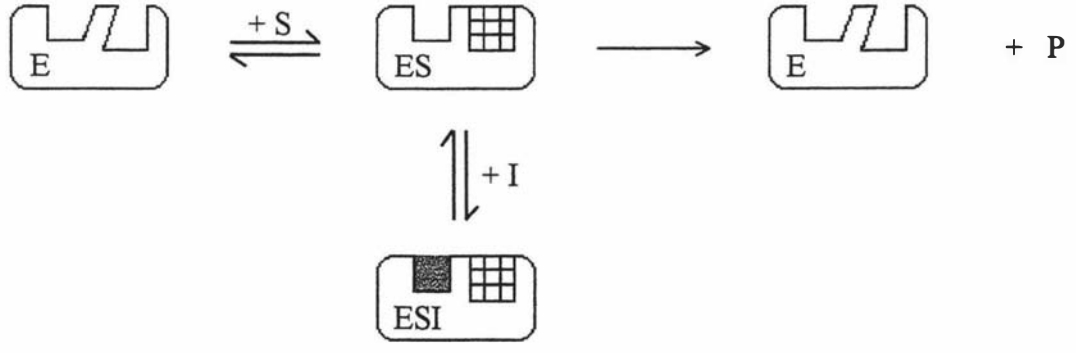

Fig. 8.1 Schematic mechanisms for the three different modes of reversible inhibition exhibited between an enzyme (E), substrate (S) and inhibitor (I).

the extent of enzyme-substrate complex formation. Furthermore, since the sites are different, a complex between the enzyme and both substrate and inhibitor is possible. Inhibition arises since this latter complex is assumed to be totally inactive towards forming the products.

Uncompetitive inhibition (Fig. 8.1(c)) is similar in form to competitive inhibition with the important exception that no enzyme-inhibitor complex forms. Consequently, in a paradoxical manner, increasing the inhibitor concentration acts to increase the rate of reaction by shifting the equilibrium to form the enzyme-inhibitor-substrate complex via the active enzyme-substrate complex.

Using this enzyme kinetics terminology, the inhibition by O_2 in the mechanism for the oxidation of H_2O_2 developed in this work (reaction 4.33) would be termed competitive, while the inhibition by the proton (reaction 4.35) could be described as non-competitive.

Chloride ions were selected for this study, since earlier reports by other workers [141,189] have shown that the rate of electrochemical oxidation of H_2O_2 at platinum decreases markedly in the presence of chloride. This was attributed to the formation of a $PtCl_2$ barrier film on the electrode surface. The influence of chloride on complete biosensors may be further complicated by its reported inhibition of the kinetics of glucose oxidation [190].

Oungpipat *et al* [85] employed a sensor based on asparagus tissue (acting as a source of peroxidase) and ferrocene mediator for H_2O_2 detection. They observed that the enzyme electrode response to H_2O_2 decreased in the presence of chloride ions and attributed this to the inhibition of asparagus peroxidase by chloride. This was consistent with the results previously gained by Cruess *et al* [191].

The formation of Pt(II) or Pt(IV) films on platinum electrodes that is central to the mechanism described in Chapters 4-7 and previously postulated by other researchers [52,73,192], also appears to be affected by the adsorption of chloride ions, with the formation potential of platinum oxide being found to shift to more positive values [193]. This observation was supported by Polta and Johnson [194] who concluded that the oxide suppression is large in the presence of cyanide or chloride ions, both of which exhibit pronounced adsorption on platinum electrodes in alkaline solutions. This is also accompanied, in the case of chloride, by tarnishing of the platinum electrode surface [195].

Clavilier [196] has also shown that anion adsorption on platinum is sensitive to the surface structure and electrode pre-treatment. In addition to the surface structure dependency, anions have been proposed to be engaged in competitive chemisorption with water decomposition products, mainly hydrated surface species [197] (presumably species such as Pt_{BS} in the present work).

A schematic diagram for the electrochemical oxidation of H_2O_2 at platinum electrodes was developed in the previous chapter (Fig. 7.13). The mechanism involves the interaction of $H_2PO_4^-$ species with a precursor site, Pt_{PS}, to form the active binding sites, Pt_{BS}, as given in Eq. 7.8

$$Pt_{PS} + H_2PO_4^- \overset{K_{BS}}{\rightleftharpoons} Pt_{BS} \tag{7.8}$$

where K_{BS} is the equilibrium constant for the formation of binding site given by

$$K_{BS} = \frac{\theta_{Pt_{BS}}}{[H_2PO_4^-]\theta_{Pt_{PS}}} \tag{8.1}$$

These binding sites were found to determine the rate of H_2O_2 oxidation, so that the amperometric signal was progressively increased with increasing the concentration of $H_2PO_4^-$ according to

$$j = \frac{k_2 N K_1 [H_2O_2]}{1 + K_4[O_2] + \dfrac{1}{K_{BS}[H_2PO_4^-]_{bulk}} + K_1[H_2O_2]\left(1 + K_5[H^+] + k_2/k_3\right)} \tag{8.2}$$

This chapter is devoted to demonstrating the effect of chloride ions on the oxidation of H_2O_2 at platinum electrodes under physiologically relevant conditions, where the phosphate buffer concentration was maintained at 0.100 mol L^{-1} and pH 7.3 at 20 °C.

8.2 Experimental Conditions

8.2.1 Reagents and Electrodes

All chemicals and electrochemical equipment were as detailed in Chapter 5, Section 5.2. Potassium chloride (BDH Limited, Poole, England) was added directly to the electrochemical cell (containing 250 cm^3 phosphate buffer) as solid, in small accurately weighed portions for the rotating disc experiments. In the microelectrode experiments,

successive 100 μL additions of 3 mol L^{-1} KCl stock solution were made to a 50 cm^3 phosphate buffer. This KCl stock solution was also used to prepare a range of chloride concentrations by dilution with the phosphate buffer for the flow-injection analysis (FIA) experiments.

8.2.2 Electrochemical Methodology

Steady-state measurements at platinum rotating disc electrode were made using the regimen of rotation rates and anodic potentials established in Chapters 4 and 5. Full *iR* compensation was employed for all rotating disc electrode experiments using the method of He and Faulkner [172] incorporated in the Bioanalytical 100B/W potentiostat.

Platinum microelectrodes were employed to avoid *iR* artefacts for the whole range of chloride concentrations. Experimental details are given in Chapter 2, Section 2.3.2.

A thin layer flow cell for FIA was performed to examine the reversibility of response changes to a range of KCl concentrations. Experimental details are given in Chapter 2, Section 2.3.3.

8.3 Steady-State Responses as a Function of Chloride

The inhibitory effect of chloride ion concentrations on the steady-state response to the oxidation of 10 mM H_2O_2 at +584 mV vs Ag/AgCl over a range of rotation rates is shown in Fig. 8.2. The steady-state response for the chloride-free electrolyte exhibits a pronounced increase as a function of rotation rate which is consistent with the experimental results described in Chapters 4-6. At each rotation rate, the electrode response decreases with increasing chloride ion concentration. This may be due to either of the following electrode surface reactions:

i) An adsorption interaction of chloride ions to the binding sites, Pt_{BS}, may take place in a similar reversible fashion to the competitive inhibition caused by O_2 described in the previous chapters. With increasing concentration of chloride this would progressively block the binding sites according to the equilibrium

$$Pt_{BS} + Cl^- \overset{K_i}{\rightleftharpoons} Pt_{BS}{\cdot}Cl^- \qquad (8.3)$$

where K_i represents the inhibition equilibrium constant given by

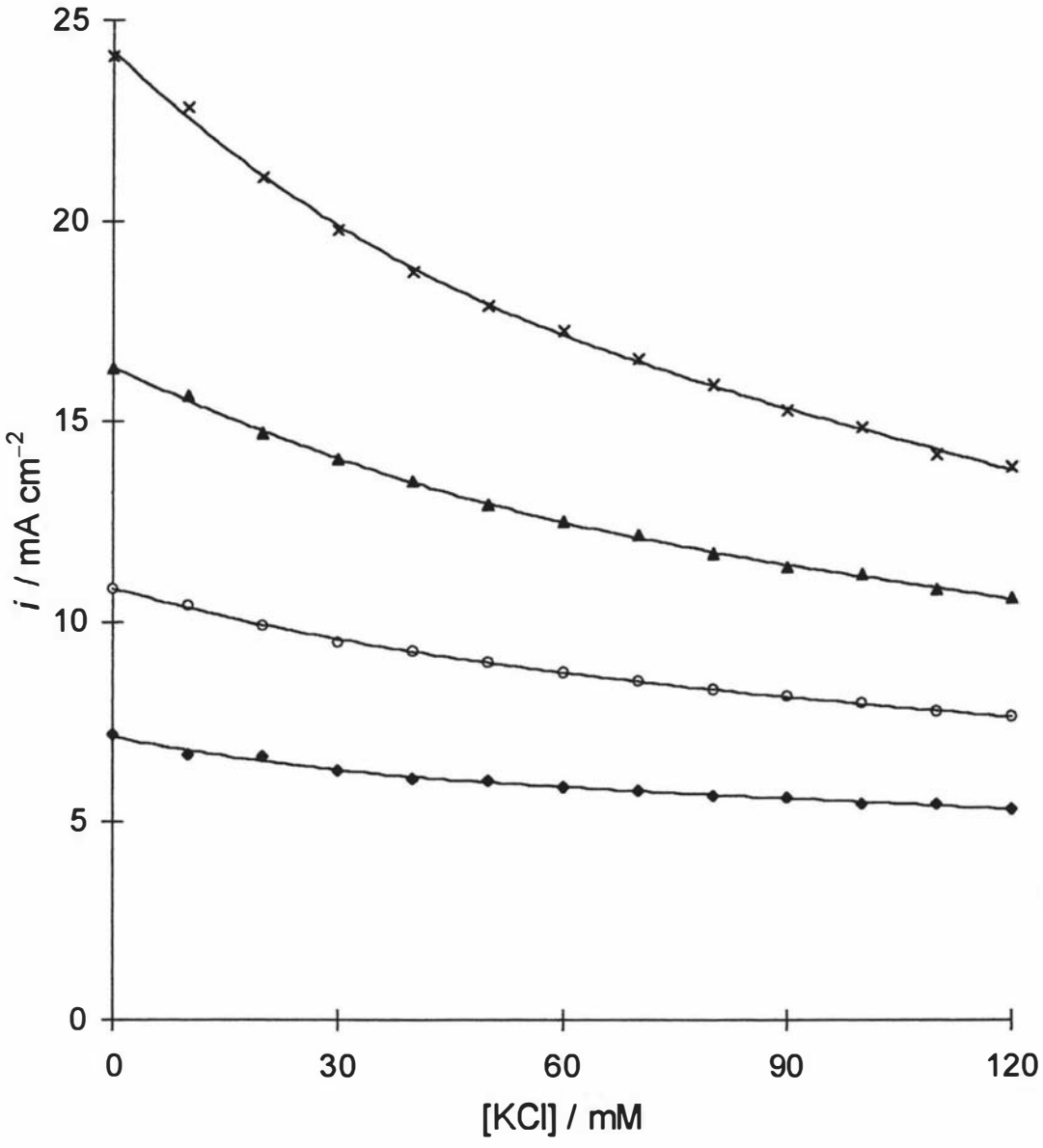

Fig. 8.2 Steady-state response to the oxidation of 10 mM H_2O_2 at +584 mV vs Ag/AgCl on a rotating disc electrode over a range of [KCl] as a function of electrode rotation rate: ◆ 630 rpm, O 1585 rpm, ▲ 4000 rpm and × 10000 rpm.

$$K_i = \frac{\theta_{Pt_{BS}\cdot Cl^-}}{[Cl^-]\theta_{Pt_{BS}}} \tag{8.4}$$

In enzyme kinetics terminology, this mode of inhibition is called competitive inhibition. If this mode of inhibition was to operate, rate equation 8.2 would be modified to involve reaction 8.3 to give

$$j = \frac{k_2 N K_1 [H_2O_2]}{1 + K_4[O_2] + K_i[Cl^-] + \dfrac{1}{K_{BS}\,[H_2PO_4^-]_{bulk}} + K_1[H_2O_2]\left(1 + K_5[H^+] + k_2/k_3\right)} \tag{8.5}$$

Consequently, the rate in part would become inversely related to $[Cl^-]$.

ii) An alternative mode of inhibition could be the interaction of chloride ions with the precursor sites to hinder the formation of the binding site given by Eq. 7.8.

$$Pt_{PS} + Cl^- \overset{K'_i}{\rightleftharpoons} Pt_{PS}\cdot Cl^- \tag{8.6}$$

In this mode, the inhibition is termed non-competitive and K'_i is the non-competitive inhibition equilibrium constant.

For this case, the rate equation given in Eq. 8.2 could be written in the form

$$j = \frac{k_2 N K_1 [H_2O_2]}{1 + K_4[O_2] + \dfrac{1 + K'_i\,[Cl^-]}{K_{BS}\,[H_2PO_4^-]_{bulk}} + K_1[H_2O_2]\left(1 + K_5[H^+] + k_2/k_3\right)} \tag{8.7}$$

In a similar manner to the competitive inhibition described in Eqs. 8.3-8.6, the rate is in part inversely proportion to $[Cl^-]$.

Polynomial expressions could be identified for Eqs. 8.5 and 8.7 to incorporate mass transport terms, in a similar manner to that described in Chapters 4-6. However, it is not appropriate here to attempt SIMPLEX optimisation of the kinetic and thermodynamic parameters due to the involvement of phosphate species in the denominator which dominate the contribution from the other terms, leading to low precision results for K_4 and K_5. Moreover, the introduction of the new term, $K_i[Cl^-]$ may complicate the optimisation process. Both rate equations, Eqs. 8.5 and 8.7, however, qualitatively fit the

data shown in Fig. 8.2.

In the absence of optimisation of the kinetic and thermodynamic parameters, it is difficult to ascertain which of the two inhibition modes described above operate. Indeed it is possible that both modes operate to some extent and hence a qualitative interpretation of the results are discussed.

8.4 The Inhibitory Effect as a Function of H_2O_2 Concentration

The steady-state responses for the oxidation of a range of $[H_2O_2]$ at +584 mV vs Ag/AgCl and 4000 rpm as a function of chloride concentration is shown in Fig. 8.3. The electrode response in chloride-free electrolyte exhibits a pronounced increase with $[H_2O_2]$ which is consistent with the experimental results described in Chapters 4-7. In the presence of chloride the electrode response decreases markedly to the extent that the rate of oxidation decreases by 30% at 115 mM chloride for each $[H_2O_2]$. This qualitative analysis is consistent with the non-competitive inhibition mode, since increasing the $[H_2O_2]$ should not affect the degree of inhibition.

Similar experiments were conducted employing a platinum microelectrode for the oxidation of a range $[H_2O_2]$. Figure 8.4 shows the steady-state response for the oxidation of a range $[H_2O_2]$ at +584 mV vs Ag/AgCl as a function of chloride concentration. The electrode response exhibits a pronounced increase with $[H_2O_2]$ in chloride-free electrolyte consistent with the experimental results demonstrated in previous chapters.

This dependence on $[H_2O_2]$ is curtailed in the presence of chloride, where the electrode response decreases to a value dependent on the chloride concentration. For the selected range of $[H_2O_2]$, the electrode loses about 26% of its activity in the presence of 115 mM chloride. These observations are consistent with the non-competitive inhibition inferred in the RDE experiments discussed above.

8.5 The Inhibitory Effect as a Function of Potential

The data presented in Fig. 8.2 was converted to inhibition percentage, % *Inh*, a function used in enzyme kinetics to describe inhibition [198], given by

$$\% \, Inh = \left(\frac{i_o - i_i}{i_o} \right) \times 100 \tag{8.11}$$

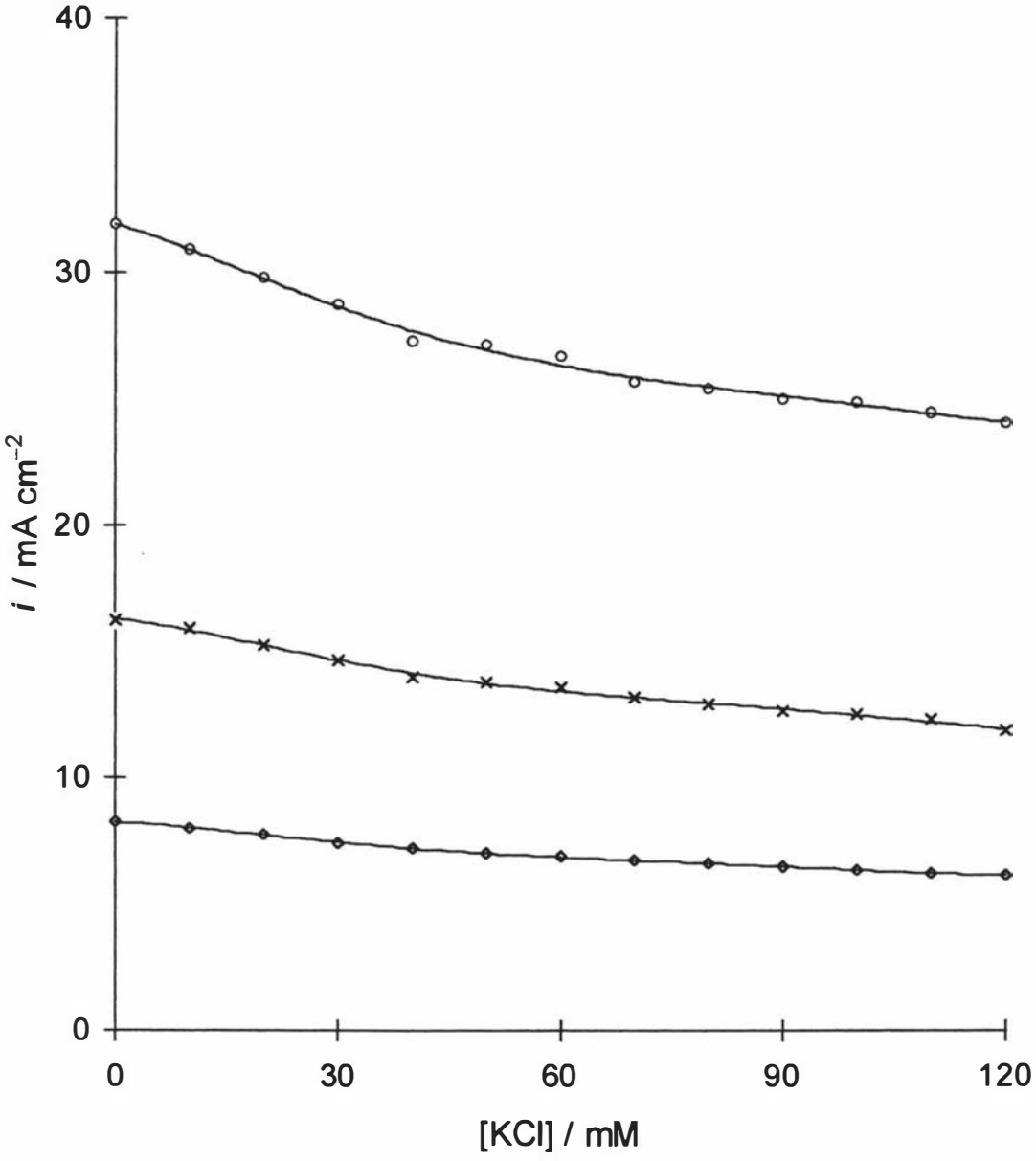

Fig. 8.3 Steady-state oxidation response for a range of bulk $[H_2O_2]$ at +584 mV vs Ag/AgCl and 4000 rpm as a function of [KCl] on a platinum rotating disc electrode. $[H_2O_2]$ range: □ 5 mM, × 10 mM and Δ 20 mM.

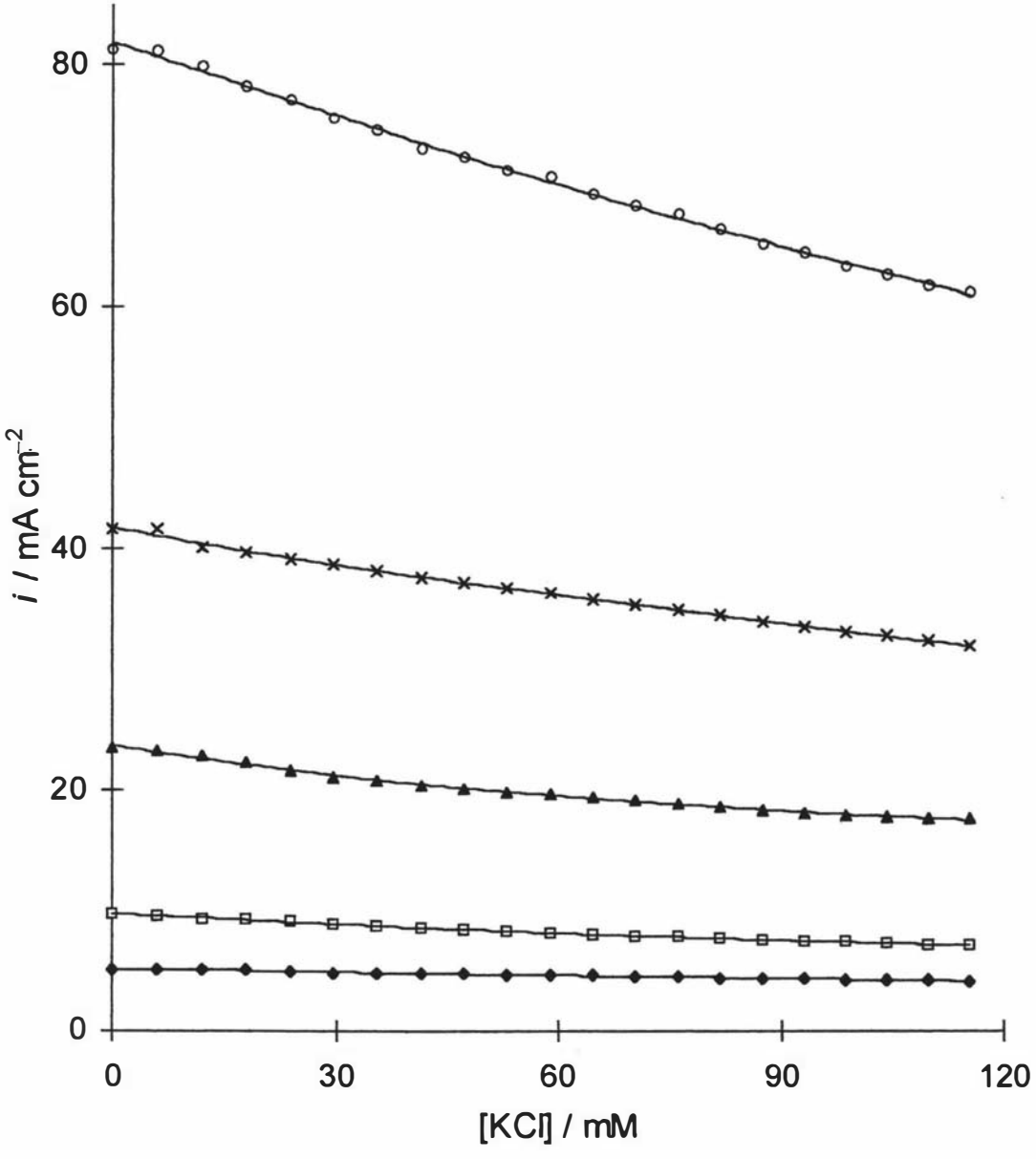

Fig. 8.4 Steady-state response to the oxidation of a range of $[H_2O_2]$ on a platinum microelectrode at +584 mV vs Ag/AgCl as a function of [KCl].

$[H_2O_2]$ range: ◆ 1 mM, □ 2 mM, ▲ 5 mM, × 10 mM ○ and 20 mM.

where i_o and i_i are the observed current densities in the absence and presence of chloride respectively.

Figure 8.5 shows % *Inh* for the oxidation of 10 mM H_2O_2 at 4000 rpm as a function of chloride concentration over a range of selected electrode potentials. For each potential % *Inh* increases with increasing chloride concentration consistent with the experimental results shown in Figs. 8.2 and 8.3 for the depression in the steady-state response at +584 mV. Excursion of the electrode to more positive potentials tends to decrease the degree of inhibition. For example, at 115 mM chloride the electrode loses about 65% and 26% of its activity at +264 mV and +744 mV respectively. These observations may be attributed in part to a decrease in the formation of platinum chloride surface species described by reaction 8.6. At more anodic potentials the formation of the binding site is favoured over this inhibition reaction. In addition, the platinum oxide formation is expected to occur at more anodic potentials since the presence of chloride shifts this to more positive potentials [193,194] and at lower potentials fewer binding sites are formed.

Figure 8.6 shows the steady-state response on an platinum microelectode to the oxidation of 10 mM H_2O_2 as a function of electrode potential for a range of chloride concentrations. The electrode response increases linearly with anodic potential between +232 to +616 mV vs Ag/AgCl which is consistent with the experimental results given in Chapter 5. The electrode exhibits a greater response to the oxidation of 10 mM H_2O_2 for chloride-free electrolyte and is depressed by increasing the concentration of chloride over the entire range of applied potential.

At fixed chloride concentration, % *Inh* as a function of electrode potential (not shown) is similar to that shown in Fig. 8.5 for the rotating disc electrode, where the potential excursion tends to decrease % *Inh*.

8.6 The Inhibitory Effect as a Function of Rotation Rate

The data presented in Fig. 8.2 is shown as a function of inhibition percentage, % *Inh*, in Fig. 8.7, where the electrode exhibits a maximum inhibition with highest rotation rate at each chloride concentration. This increase in % *Inh* with rotation rate cannot be attributed to mass transport if it is assumed that chloride is not an electroactive species. As in the case for phosphate described in Chapter 7, the surface concentration of

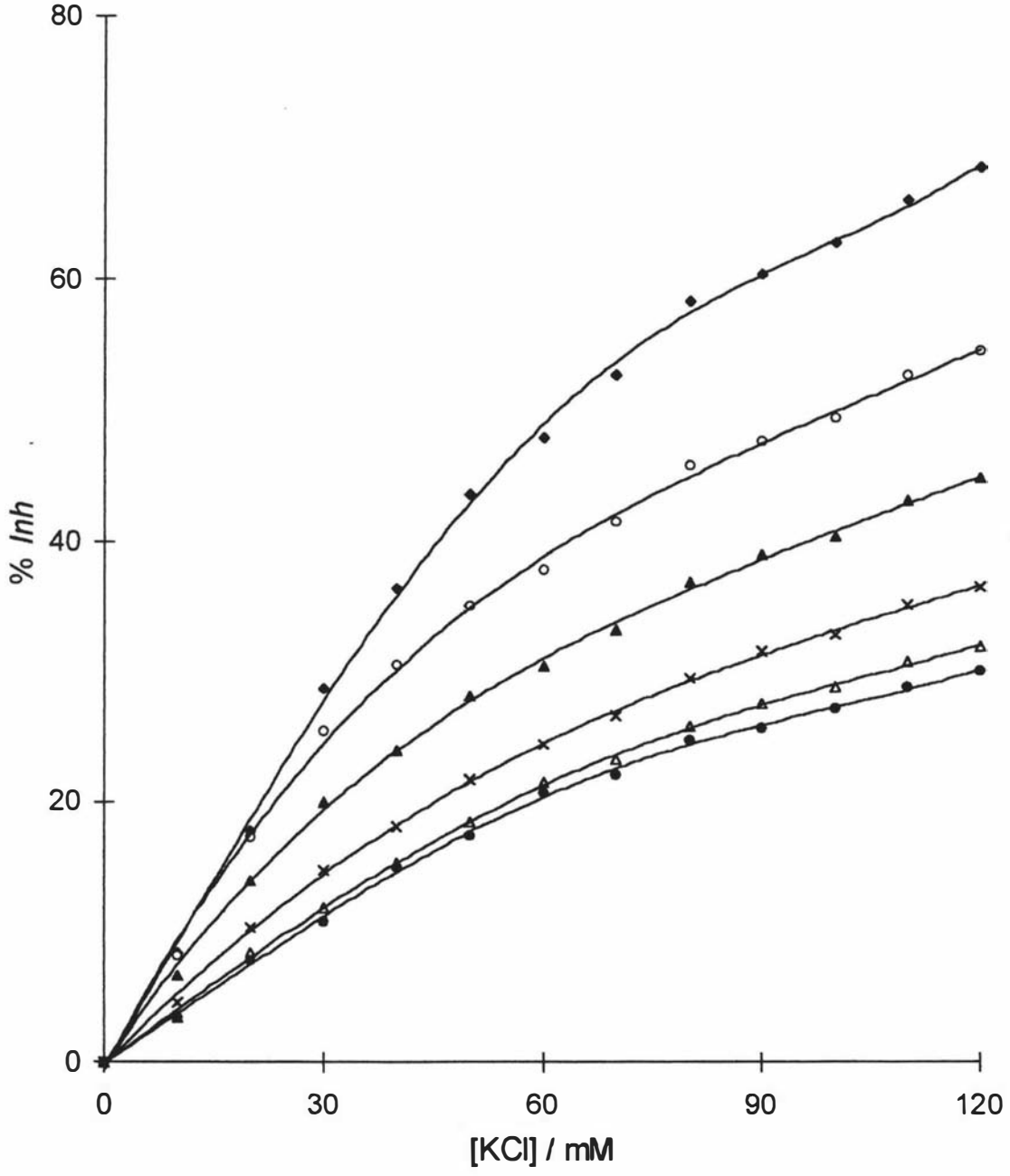

Fig. 8.5 % *Inh* for the oxidation of 10 mM H_2O_2 at 4000 rpm as a function of [KCl] on a platinum rotating disc electrode over a range of applied potential vs Ag/AgCl: ◆ 264 mV, O 360 mV, ▲ 456 mV, × 552 mV, Δ 648 mV and ● 744 mV.

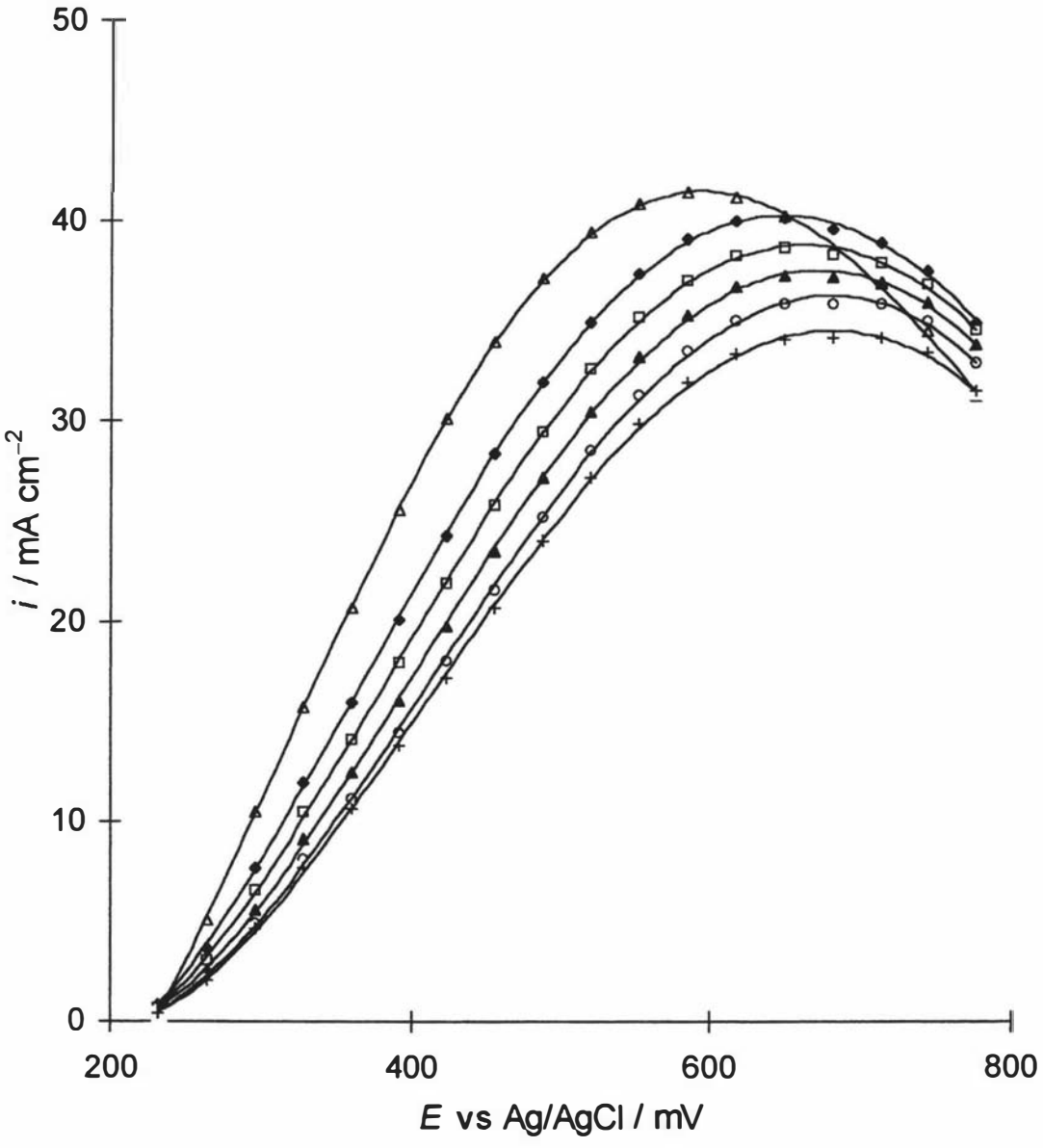

Fig. 8.6 Steady-state response to the oxidation of 10 mM H_2O_2 on a platinum microelectrode over a range of applied potential and as a function of a selected range of chloride concentration: Δ zero, ◆ 23.81 mM, □ 47.24 mM, ▲ 70.31 mM, O 93.02 mM and + 115.38 mM.

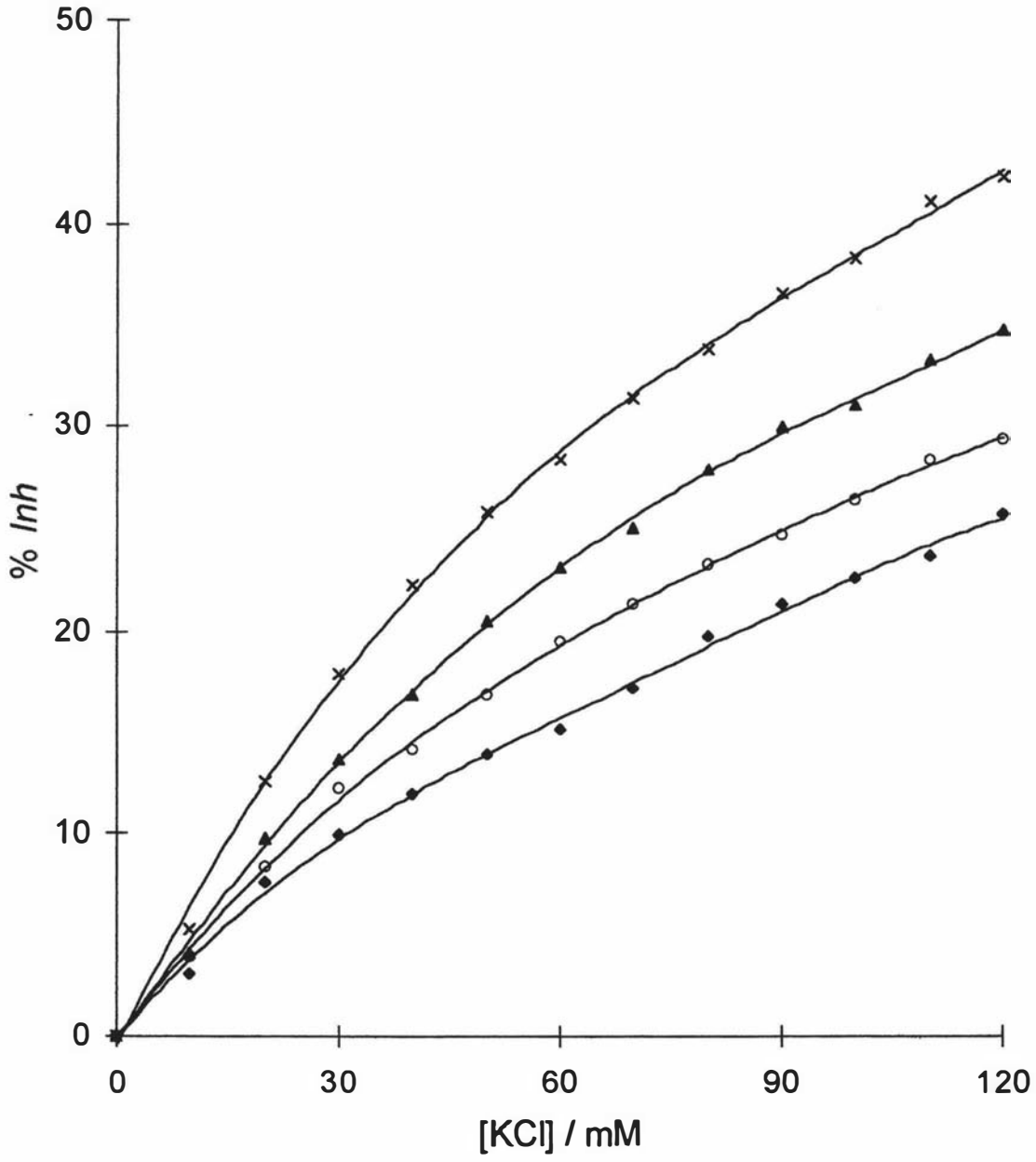

Fig. 8.7 % *Inh* as a function of chloride concentrations for the data presented in Fig. 8.2 at 10 mM H_2O_2 for a range of electrode rotation rates: ◆ 630 rpm, O 1585 rpm, ▲ 4000 rpm and × 10000 rpm.

chloride could be assumed to remain at the bulk concentration and hence should be invariant with electrode rotation rate. Clearly, this not the case and chloride must be involved in some surface reaction as a reactant. This cannot merely be inhibition of the binding site, Pt_{BS}, or prevention of the formation of Pt_{BS} from the precursor site, Pt_{PS} identified in reactions 8.3 and 8.6, since these should not exhibit rotation rate dependence.

It is proposed that the simplest sequence of events to account for rotation rate dependence is that chloride forms a soluble chloro complex with either Pt_{BS} or Pt_{PS}, such as $PtCl_4^{2-}$ or $PtCl_6^{2-}$. Increasing the rotation rate will act to increase both the rate of formation and departure of these soluble complexes from the electrode-solution interface and hence act to decrease the overall number of binding sites. This is also consistent with the observed tarnishing of platinum electrodes in chloride medium [195]. Indeed, in some long term experiments, tarnishing was observed at the Pt-RDE in this work.

8.7 Flow-Injection Analysis Experiments

In these experiments a set of standard chloride solutions was prepared by diluting a concentrated chloride stock-solution with the carrier reagent, i.e. 0.100 mol L^{-1} phosphate buffer at pH 7.3. Hydrogen peroxide was maintained at 20 mM for the entire set of chloride solutions. It should be noted, that the compensation of *iR* effects is not possible in this electrochemical cell.

The steady-state response to the oxidation of H_2O_2 at +600 mV vs Ag/AgCl over a range of chloride concentration is shown in Fig. 8.8. The electrode response exhibits a pronounced increase with increasing chloride concentration. This is in contrast with the experimental results shown for rotating disc and microelectrodes discussed in previous sections, where a decrease in response is observed. This behaviour may be explained as being due to an increase of electrolyte conductivity with increasing chloride concentration. Table 8.1 lists the conductivity of chloride solutions mixed with 20 mM H_2O_2 which is linearly proportional to chloride concentration. Therefore, the observed response is probably a combination of the increase in H_2O_2 oxidation inhibition together with a decrease in *iR* effects by increasing chloride concentration. Thus, the response is fraught with artifacts and not appropriate for mechanism interpretation. Tarnishing was

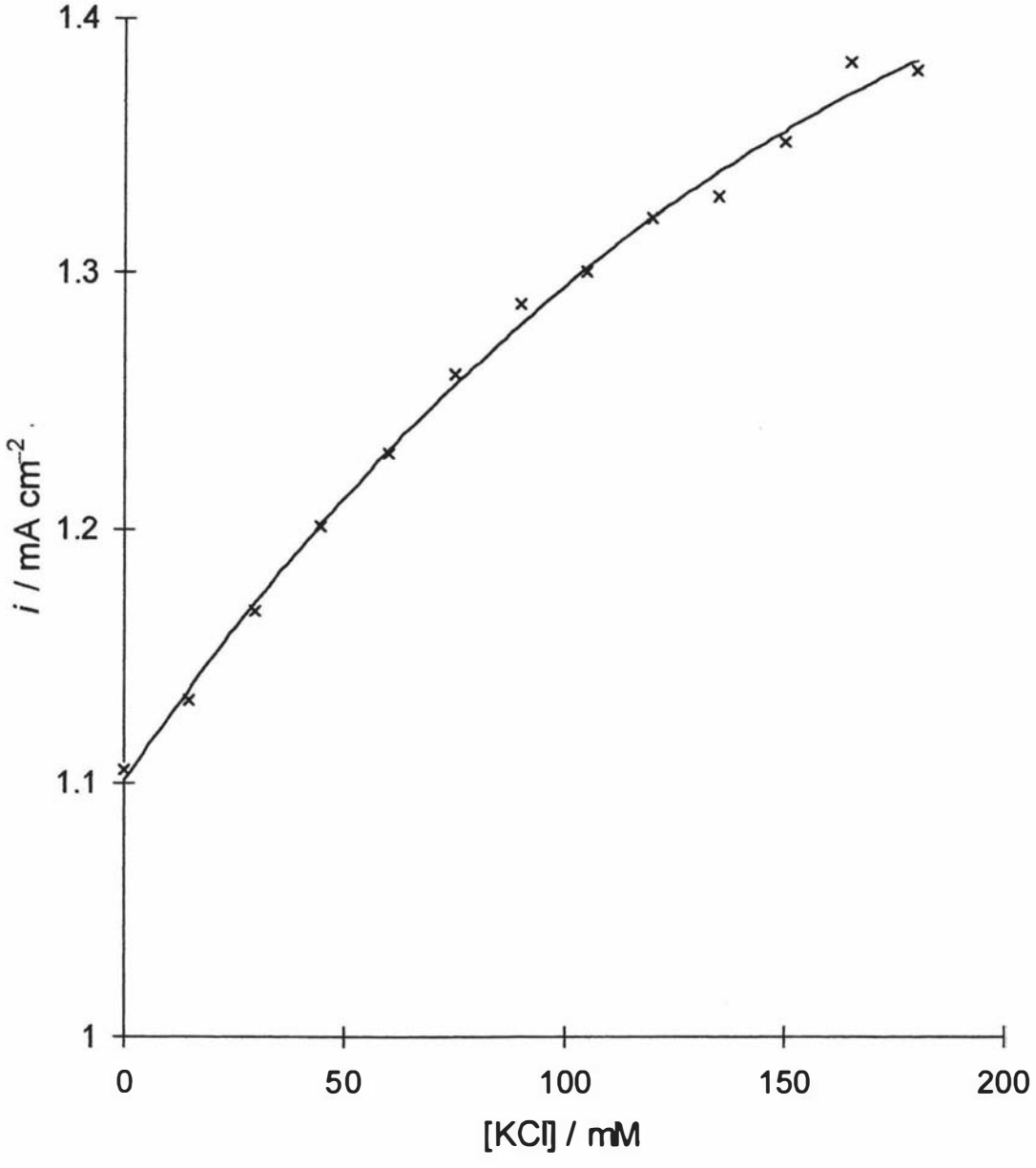

Fig. 8.8 The response of a platinum electrode in a thin-layer flow cell to the oxidation of 20 mM H_2O_2 at +600 mV vs Ag/AgCl over a range of [KCl].

[KCl] mM	Conductivity mS
0	14.78
15	16.42
30	18.15
45	19.83
60	20.80
75	22.50
90	24.20
105	25.70
120	27.40
135	29.20
150	30.60
165	31.80
180	33.60

Table 8.1 Conductivity for a set of chloride solutions with $[H_2O_2]$ = 20 mM throughout.

also observed on the FIA electrode, and the electrode required polishing after each experiment to regenerate a smooth and bright surface.

8.8 Conclusions

The qualitative experimental results described for the platinum rotating disc and microelectrodes show the inhibitory nature of chloride ions to the catalytic oxidation of H_2O_2. The degree of inhibition is found to depend on the chloride concentration in the test solution. Two possible inhibition modes were proposed to involve the interaction of chloride ions to either the binding sites or/and the precursor sites. In the first case, a number of binding sites are blocked by chlorides that hinder H_2O_2 binding, while in the second case, a number of precursor sites interact with chlorides to hinder the formation of binding sites. The nature of the electrode inhibition was found to follow the second mode, which is identified as a non-competitive, since an increase in $[H_2O_2]$ does not decrease the degree of inhibition.

The rotation rate experiments suggest the formation of a soluble chloro-platinum species as a further side reaction, so that increasing the rotation rate decreases the overall number of binding sites.

The electrode response for FIA experiments were complicated by the inability to compensate for *iR* artifacts. The increase in response, which is associated with marked decrease in solution resistance, is found for increasing chloride concentrations. This strongly indicates that chloride should not be present in oxidase enzyme-based biosensors. However, it is common practice to include chloride in the carrier stream for biosensors so as to provide a constant potential for screen-printed Ag/AgCl reference electrodes [199,200]. Clearly, in this case, it is not only essential to rigidly maintain chloride concentration for the reference electrode, but also to maintain a constant extent of inhibition of the H_2O_2 oxidation. Furthermore, biosensors are inherently used with blood samples where chloride content is in the range 100-106 mM [201]. Therefore it would seem that is impossible to avoid chloride in these situations. Nevertheless, chloride should be avoided, if at all possible, when accurate oxidation rates for H_2O_2 oxidation on platinum are required.

CHAPTER NINE

Summary and Conclusions

9.1 Introduction

The aim of this study was to investigate the electrochemical oxidation of H_2O_2 on platinum electrodes in phosphate buffer solutions.

This reaction has been a field of interest for many researchers during this century, and most of the published articles have been concerned with elucidating an appropriate mechanistic model to describe the events that occur at the electrode surface as well as to evaluate the kinetic parameters of the electrode reaction.

The findings of the previous studies have been significantly enhanced by the new work presented in this thesis, with the development of a model that accounts for the effects of concentration, rotation rate, potential, temperature and buffer composition.

The sections that follow in this chapter summarise the major findings of the experimental chapters in this thesis and demonstrate the new concepts that have been used to interpret the electrode reaction kinetics. Cross-referencing to relevant figures and sub-sections is provided.

9.2 Concentration and Rotation Rate Dependence

In these experiments the potential of the working electrode was stepped from +200 to +600 mV vs Ag/AgCl employing the chronoamperometric technique (Chapter 3, Fig. 3.1). This technique was used to illustrate the adsorption-controlled mechanism for the oxidation of H_2O_2 on a platinum rotating disc electrode in 0.100 mol L^{-1} phosphate buffer solution and pH 7.3 at T = 20 °C (Chapter 4).

i) The steady-state responses to the oxidation of H_2O_2 for a range of rotation rates was found to increase linearly at low $[H_2O_2]_{bulk}$ (Section 4.3, Fig. 4.1). The linear dependence was curtailed for $[H_2O_2]_{bulk}$ > 50 mM, where limiting currents were approached at all rotation rates (greatest for the highest rotation rate). This experiment indicated that the electrode reaction involved mass transport processes (diffusion-limited).

ii) The data shown in Fig. 4.1 were analysed according to the Levich equation (Section 4.4, Fig. 4.2). The Levich plot showed a non-linear relationship between the current density and the square root of the angular velocity, indicating that the reaction is not entirely controlled by mass transport processes.

iii) The experimental data represented in Fig. 4.1 were further analysed adopting the Koutecky-Levich method (Section 4.5, Fig. 4.3). Linear relationships were observed with slopes decreasing with increasing $[H_2O_2]_{bulk}$ and intercepts appearing to have similar values.

The diffusion coefficient for H_2O_2 was calculated from the slopes (listed in Table 4.2) and apparently found to vary with $[H_2O_2]_{bulk}$ (Fig. 4.5). The heterogeneous rate constants were determined from the intercepts (Table 4.1) and found to be inversely proportional to $[H_2O_2]_{bulk}$ (Fig. 4.4).

The data listed in Table 4.1 and the plot of Fig. 4.3 were inspected to justify the appropriateness of the Koutecky-Levich analyses in describing the electrode kinetics. It was found that the plot of Fig. 4.3 was not rigidly linear and displayed parabolic departure from linearity with increasing $[H_2O_2]_{bulk}$. Therefore, the Koutecky-Levich study was deemed inappropriate to describe the electrode kinetics.

iv) The steady-state data plotted in Fig. 4.1 were further analysed employing the Michaelis-Menten relationship (Section 4.6). These data were represented in Fig. 4.6 in the form of Hanes plots (Eq. 4.31). Linear regions were identified at all rotation rates for higher $[H_2O_2]_{bulk}$, while an extreme deviation from linearity was observed at lower rotation rates in the region of low $[H_2O_2]_{bulk}$.

The maximum rate and Michaelis constant were determined from the linear regions of Hanes plots and listed in Table 4.3. The maximum rate was found to increase with rotation rate which was consistent with that observed in Fig. 4.1. This could not be accounted for by simple Michaelis-Menten kinetics. Therefore, the observed deviation from linearity and the dependence of maximum rate on rotation rates suggested a form of product-inhibition in the Michaelis-Menten kinetics.

v) A mechanistic model was proposed involving binding sites on the surface of the electrode and incorporating with two inhibition modes (Section 4.7.1). A rate equation was derived (Eq. 4.38) to describe the reaction kinetics of this model.

vi) The validation of the proposed mechanism was tested by optimising the kinetic parameters using a SIMPLEX program developed during the present study (Sections 2.9.1 and 4.7.3). A new optimised value for the diffusion coefficient of H_2O_2 was evaluated, 0.66×10^{-9} m^2 s^{-1}, and found to be lower than those reported in the literature (Table 4.5).

9.3 Potential–Dependence

The potential of the platinum rotating disc electrode was stepped between +232 to +744 mV employing staircase potentiometry (Section 3.2.3, Fig. 3.7). These experiments were conducted to test the validity of the proposed mechanism over a range of applied potentials, determine the rate limiting steps and to modify the derived rate equation given in Eq. 4.38.

i) The steady-state responses as a function of anodic potential over a range of $[H_2O_2]_{bulk}$ at fixed rotation rate (Fig. 5.2) indicated that the electrode reaction is potential-dependent. For each anodic potential step, the response increased with $[H_2O_2]_{bulk}$ and approached a limiting current that was greater for higher anodic potentials.

ii) The fractional surface coverage for all surface sites involved in the proposed mechanism was considered in building the modified rate equation (Eq. 5.2). The kinetics and equilibrium constants involved in the rate equation were optimised employing a SIMPLEX program (Sections 2.9.1 and 5.5) and are given in Table 5.1. The optimised value for the diffusion coefficient of H_2O_2, 0.55×10^{-9} m^2 s^{-1}, still lower than those reported in the literature (Table 4.5).

iii) The optimised kinetic parameters, k_2N and k_3N, were found to increase exponentially with potential (Fig. 5.3) and approached the same value at +271 mV vs

Ag/AgCl. At higher anodic potentials the term k_2 / k_3 in the modified rate equation (Eq. 5.2) became insignificant as k_3 became large compared to k_2 and, hence, the more simple rate equation (Eq. 4.38) could be applied.

The deviation from linearity at low potentials for the plot of ln k_2N as a function of potential in Fig. 5.3 was attributed to the competition from the simultaneous reduction of H_2O_2 and that the number of binding sites, N, would change at low potential whilst k_2 changed exponentially over all potentials. Therefore, the response as a function of potentials between +244 to +600 mV was suggested as being due to the development of binding sites rather than the rate constants. This was consistent with the earlier observations that the oxidation of H_2O_2 is favoured on oxidised platinum surfaces.

9.4 Temperature–Dependence

The validity of the proposed mechanism was tested over a range of experimental temperatures.

i) The steady-state responses as a function of $[H_2O_2]_{bulk}$ over a range of temperatures between 5 to 35 °C (Fig. 6.4) indicated that the electrode reaction is temperature-dependent.

ii) The optimisation process for all parameters involved in the rate equation (Section 6.5) showed that the equilibrium constants, K_1, K_4 and K_5, were temperature-invariant (Table 6.5). While the optimised values for the diffusion coefficient of H_2O_2 listed in Table 6.4 were found to vary with temperature (Fig. 6.5), this parameter did not behave according to the Stoke-Einstein equation (Eq. 6.3). This unexpected trend of $D_{H_2O_2}$ was attributed, in part, to the effective hydrodynamic radius of H_2O_2 changing with temperature, with a maximum at 20 °C and decreasing below and above 20 °C.

iii) The variation of rate constant, k_2N, with temperature as a function of potential (Fig. 6.6) showed that this parameter is temperature-dependent also. The increase in k_2N with temperature was consistent with the overall increase in the steady-state response shown in Fig. 6.4. The variation of k_3N with temperature (Fig. 6.7) was not as clear as that for k_2N due to the problems of reliably determining this parameter.

iv) Arrhenius analysis was used (Fig. 6.8) to determine the pseudo-activation energy for the reduction reaction of the surface complex Pt(II)/H_2O_2 site employing Eq. 6.4. The pseudo-activation energies listed in Table 6.6 and plotted in Fig. 6.9 over a range of potentials were found to decrease at low potentials and adopt a constant value at high anodic potentials. This behaviour was thought to be due to a combination of the activation energy for the formation of the reduced platinum site with the enthalpy of formation of the binding site (Eq. 6.9). Thus, the large drop in the pseudo-activation energy at low potentials was attributed to the decrease in the endothermic formation of the binding site while the relatively constant value at higher potentials were predominantly due to k_2.

9.5 Buffer–Dependence

These experiments were performed under non-physiological conditions to extend the proposed mechanism over a range of buffer concentrations and pH.

i) The steady-state responses as a function of $[PO_4^{3-}]_{tot}$ over a range of $[H_2O_2]_{bulk}$ at fixed rotation rate (Fig. 7.1) showed that the oxidation of H_2O_2 is dependent on buffer concentration. This was related to the development of the number of binding sites with increasing $[PO_4^{3-}]_{tot}$. The data given in Fig. 7.1 were further analysed (Fig. 7.2) over the range of $[PO_4^{3-}]_{tot}$, where at high bulk $[H_2O_2]$ the responses were greatly increased while slightly increased at low bulk $[H_2O_2]$. This behaviour was attributed to the balance in equilibria between the formation of the binding site from a precursor site and the binding of H_2O_2.

ii) Two features were observed for the oxidation of 5 mM H_2O_2 at a platinum microelectrode as a function of potential over a range of $[PO_4^{3-}]_{tot}$ (Fig. 7.3). At $[PO_4^{3}]_{tot}$ > 5 mM, the response approached a maximum that was greater for the higher $[PO_4^{3-}]_{tot}$ indicating buffer concentration dependence consistent with the earlier findings presented in Fig. 7.1. For $[PO_4^{3-}]_{tot}$ < 5 mM, the response exhibited exponential increase with potential and was greater for the lower $[PO_4^{3-}]_{tot}$. Inspecting these data at fixed $[H_2O_2]$ and for a selected potential range (Fig. 7.4), the minima in response were not observed at low potentials whilst at high potentials the minima were progressively more

pronounced at low $[PO_4^{3-}]_{tot}$. Accordingly, two linked mechanisms were identified. First, at physiological conditions the response increases with potential in similar fashion to that described in Chapters 4 and 5. Secondly, at low $[PO_4^{3-}]_{tot}$, an alternative mechanism operates, particularly at high potentials where the reaction proceeded more rapidly.

iii) The phosphate-free mechanism was further studied by performing the experiment in the absence of buffer (Fig. 7.5) where the response to the oxidation of H_2O_2 was observed to increase with potential. An important feature of this experiment was that the response was nil in the absence of H_2O_2 over the entire potential range, so that the potential dependence exhibited in the phosphate free mechanism (Fig. 7.3) can not be attributed to the oxidation of the solvent. Further experiments were performed in citrate buffer (Fig. 7.7) to demonstrate that proton inhibition was not the cause for the decrease in response at low $[PO_4^{3-}]_{tot}$.

iv) The effect of buffer pH was studied and presented in Figs. 7.10 and 7.11 where the maximum response was approached at pH 6.8 and decreased markedly under more basic or acidic conditions. The maximum response was suggested as being due to the involvement of $[H_2PO_4^-]$ species in the formation of the binding sites (reaction 7.8) consistent with the FTIR studies of phosphate adsorption [187] on Pt at pH 6.8. The decrease in response at pH > 6.8 was described as being due to the decrease in $[H_2PO_4^-]$ since $pK_{a2} = 7.3$. The decrease in response at pH < 6.8 was suggested as being due to the inhibition of the precursor site by protons (reaction 7.9) that would hinder the formation of binding sites stated in reaction 7.8.

9.6 Inhibition By Chloride

These experiments demonstrated the effect of chloride ions on the oxidation of H_2O_2 at platinum electrodes.

i) The steady-state responses for the oxidation of H_2O_2 at the platinum rotating disc exhibited a pronounced decrease with increasing chloride concentration at all rotation rates (Fig. 8.2). Two possible inhibition modes were proposed involving the interaction

of chloride ions either with the binding sites (reaction 8.3) to form $Pt_{BS}{\cdot}Cl^-$ or with the precursor sites (reaction 8.6) to form $Pt_{PS}{\cdot}Cl^-$.

ii) The steady-state responses on both rotating disc and microelectrodes for a range of $[H_2O_2]_{bulk}$ (Figs. 8.3 and 8.4) were observed to decrease with increasing chloride concentrations. The inhibition mode was identified as non-competitive, since an increase in $[H_2O_2]_{bulk}$ does not decrease the degree of inhibition.

iii) The inhibitory effect was found to decrease when applying more anodic potentials (Fig. 8.5) due to a positive potential shift for the oxide film formation.

iv) Inhibition by chloride was found to be more pronounced at higher rotation rates where chloride was proposed to form soluble chloro complexes with either Pt_{BS} or Pt_{PS}, such as $PtCl_4^{2-}$ or $PtCl_6^{2-}$. The effect of rotation rate in this case was assumed to increase both the formation and removal of chloro complexes from the electrode-solution interface and therefore decrease the overall number of binding sites.

Chloride ions were not treated as electroactive species at these experiments, since the applied potential was below that for chloride oxidation.

This work strongly suggests that care should be taken to avoid chloride when studying the electrochemistry of H_2O_2.

9.7 Publications

This study has resulted in a number of publications. The first [112], covers the work presented in Chapter 4, whilst the second, third and fourth report the work presented in Chapters 5,6 and 7 respectively [113-115]. A fifth paper [116] on the chloride inhibition work in Chapter 8 has been submitted for publication.

REFERENCES

1. L. Chalmers, "*Domestic and Industrial Chemical Specialties*", Leonard Hill, London, 1966, pp. 67-69.

2. BP, 549,362, I.C.I.,1942.

3. J. F. Van Oss "*Chemical Technology*", Vol.1, edited by Barnes and Noble Inc., New York, 1968, pp. 195-201.

4. F. A. Lowerheim and M. K. Moran "*Industrial Chemicals*", Faith, Keys and Clark's, 4th. edn., John Wiley Inc., 1975, pp. 487-495.

5. F. A. Cotton and G. Wilkinson "*Advanced Inorganic Chemistry*", 5th. edn., John Wiley Inc., 1988, pp. 456-458.

6. U.S., 2,392,733, E.I., *du Pont du Nemours*, 1946.

7. W. C. Schumb, C. N. Satterfield and R. L. Wentworth, "*Hydrogen Peroxide*", Reinhold, New York, 1955.

8. U. Kirner, *Melliand Textilber*, 1970 (51) 1069.

9. K. Schliefer, *Melliand Textilber*, 1989 (70) 856.

10. S. T. Test and S. J. Weiss, *Biol. Chem.*, 1984 (259) 399.

11. P. Jolliet, *Crit. Care Med.*, 1994 (22) 157.

12. S. Penkett, B. Jones, K. Brice and A. Eggleton, *Atmos. Environ*, 1979 (13) 123.

13. D. Moller, *Atmos. Environ*, 1980 (14) 1067.

14. H. P. Van Egmond, "*Mycotoxins in Dairy Products*", Elesevier Applied Science, London and New York, 1989, p. 144.

15. R. K. Robinson, "*The Microbiology of Milk Products*", Elesevier Applied Science, 2nd edn., vol. 2, London and New York, 1989, p. 210.

16. B. Strausak, W. Schoch; *European Patent Application*, 10 April 1985, Bulletin 85/15, EP 0136973.

17. J. Wang, Y. Lin and L. Chen, *Analyst*, 1993 (118) 277.

18. A. Y. Tamine and R. K. Robinson "*Yogurt Science and Technology*", Pergamon, Oxford, 1985, pp. 206-221.

19. J. Bassett, R. C. Denney, G. H. Jeffry and J. Mendham "*Vogel's Text Book of Quantitative Inorganic Analysis*", Longman, London, 4th. edn., 1978, p. 355.

20. R. M. Seller, *Analyst*, 1980 (105) 950.

21.. M. S. Abdel-Latif and G. G. Guilbault, *Anal. Chem.*, 1988 (60) 2671.

22. K. Hool and T. A. Neiman, *Anal. Chem.*, 1988 (60) 834.

23. T. R. Holm, G. K. George and M. J. Barcelona, *Anal. Chem.*, 1987 (59) 582.

24. L. C. Clark and C. Lyons, *Ann. N.Y. Acad. Sci.*, 1962 (105) 20.

25. S. J. Updick and G. P. Hicks, *Nature*, 1967 (214) 986.

26. L. C. Clark, *US Patent* 3534955, 1970.

27. P. T. Kissinger and W. R. Heineman "*Laboratory Techniques in Electroanalytical Chemistry*", Marcel Dekker, Inc., 2nd. Edn., 1996.

28. N. C. Foulds and C. R. Lowe, *Anal. Chem.*, 1988 (60) 2473.

29. B. A. Gregg and A. Heller, *Phys. Chem.*, 1991 (95) 5976.

30. G. Galiasatos, Y. Ikariyama, J. E. Mark and W. H. Heineman, *Biosens. Bioelect.*, 1990 (5) 47.

31. H. Gunasingham and C. B. Tan, *Electroanalysis*, 1989 (1) 223.

32. I. M. Christie, P. Treloar and P. Vaolgama, *Anal. Chim. Acta*, 1992 (269) 65.

33. F. Moussy, D. J. Harrison, D. O'Brien and R. Rajotte, *Anal. Chem.*, 1993 (65) 2072.

34. J. Wang and H. Wu, *Anal. Chim. Acta*, 1993 (283) 683.

35. Y. Zhang, Y. Hu, G. Wilson, D. Moatti-Sirat, V. Poitout and G. Reach, *Anal. Chem.*, 1994 (66) 1183.

36. A. Mulchandaui, C. L. Wang and H. H. Weetall, *Anal. Chem.*, 1995 (67) 94.

37. P. C. Pandey, A. M. Kayastha and V. Pandey, *Appl. Biochem. Biotechnol.*, 1992 (33) 139.

38.. Y. Liu, H. Liu, J. Qian, J. Deng and T. Yu, *Electrochim. Acta*, 1995 (41) 77.

39. P. D. Sanchez, P. T. Blanco, J. M. F. Alvarez, M. R. Smyth and R. O'Kennedy, *Electroanalysis*, 1990 (2) 303.

40. L. Bifulco, C. Cammaroto, J. D. Newman and A. P. F. Turner, *Anal. Lett.*, 1994 (27) 1443.

41. H. Liu, J. Qian, Y. Liu, T. Yu and J. Deng, *Talanta*, 1996 (43) 111.

42. G. A. Somorjai, "*Chemistry in Two Dimensions: Surfaces*", Cornell University Press, 1981.

43. Y. Tong, C. Belrose, A. Wieckowski and E. Oldfield, *Am. Chem. Soc.*, 1997 (119) 11709.

44. J. Bucher, J. Buttet, J. Van der Klink and M. Graetzel, *Surf. Sci.*, 1989 (214) 347.

45. D. C. Johnson, J. A. Polta, T. Z. Polta, G. G. Neuburger, J. Johnson, A. Tang, I-H.Yeo and J. Baur, *Chem.Soc., Faraday Trans.*, 1986 (82) 1081.

46. D. Gilory, *Electroanal. Chem.*, 1977 (83) 329.

47. S. G. Roscoe and B. E. Conway, *Electroanal. Chem.*, 1987 (224) 163.

48. N-H. Li, S-G. Sun, S-P. Chen, *Electroanal. Chem.*, 1997 (430) 57.

49. W. Bold and M. W. Breiter, *Electrochim. Acta*, 1961 (5) 145.

50. M. W. Breiter, *Electrochim. Acta*, 1963 (8) 447.

51. J. E. Vitt, L. A. Larew and D. C. Johnston, *Electroanalysis*, 1990 (2) 21.

52. J. J. Lingane and P .J. Lingane, *Electroanal. Chem.*, 1963 (5) 411.

53. M. Honda; T. Kodera and H. Kita, *Electrochim. Acta*, 1983 (28) 727.

54. V. G. Prabhu, L. R. Zarapkar and R. G. Dhaneshwar, *Electrochim. Acta*, 1981 (26) 725.

55. H. Angerstein-Kozlowska, B. E. Conway and B. A. Sharp, *Electroanal. Chem.*, 1973 (43) 9.

56. B. E. Conway and S. Gottesfeld, *Chem. Soc. Faraday Trans.*, 1973 (69) 1090.

57. B. V. Tilak, B. E. Conway and H. Angerstein-Kozlowska, *Electroanal. Chem.*, 1973 (48) 1.

58. D. Gilory, *Electroanal. Chem.*, 1976 (71) 257.

59. L. D. Burke and J. K. Casey, *Electrochim. Acta*, 1992 (2) 21.

60. L. D. Burke and M. M. Murphy, *Electroanal. Chem.*, 1991 (305) 301.

61. L. D. Burke, J. K. Casey and J. A. Morrissey, *Electrochim. Acta*, 1993 (38) 897.

62. L. D. Burke and D. T. Buckley, *Electroanal. Chem.*, 1994 (366) 239.

63. F. C. Anson and J. J. Lingane, *Am. Chem. Soc.*, 1957 (79) 4901.

64. I. M. Kolthoff and N. Tanaka, *Anal. Chem.*, 1954 (26) 632.

65. J. K. Lee, R. N. Adams and C. E. Bricker, *Anal. Chim. Acta*, 1957 (17) 321.

66. L. D. Burke, J. F. Healy, K. J. O'Dwyer and W. A. O'Leary, *Electrochem. Soc.*, 1989 (136) 1015.

67. L. D. Burke and K. J. O'Dwyer, *Electrochim. Acta*, 1990 (35) 1821.

68. H. Angerstein-Kozlowska, B. E. Conway, A. Hamelin and L. Stoicovicin, *Electrochim. Acta*, 1986 (31) 1051.

69. H. Angerstein-Kozlowska, B. E. Conway and A. Hamelin, *Electroanal. Chem.*, 1990 (277) 233.

70. R. E. Roberts and D. C. Johnson, *Electroanalysis*, 1994 (6) 193.

71. I. M. Kolthoff and E. R. Nightingal, *Anal. Chim. Acta*, 1957 (17) 329.

72. D. G. Devis, *Talanta*, 1960 (3) 335.

73. A. Hickling and W. Wilson, *Electrochem. Soc.*, 1951 (98) 425.

74. B. Baker and W. Mac Nevin, *Am. Chem. Soc.*, 1953 (75) 1476.

75. F. C. Anson, *Anal. Chem.*, 1961 (33) 934.

76. F. C. Anson and D. M. King, *Anal. Chem.*, 1962 (34) 362.

77. F. Meiattini, "*In Methods of Enzymatic Analysis*" VCH, Weinheim, 3rd. Edn, 1985, Vol. 7, pp. 566-571.

78. G. G. Guilbault, "*Handbook of Enzymatic Methods of Analysis*", Dekker, New York, 1976.

79. C. Bourdillon, J. Bourgeois and D. Thomas, *Am. Chem. Soc.*, 1980 (102) 4231.

80. M. Lundbäck, G. Johansson and O. Holest, *Anal. Chim. Acta*, 1983 (155) 47.

81. G. J. Moody, G. S. Sanghera and J. D. R. Thomas, *Analyst*, 1986 (111) 605.

82. W. Kunnecka and R.D. Schmid, *Anal. Chim. Acta*, 1990 (234) 213.

83. Y. L. Huang, S. B. Khoo and M. G. S. Yap, *Anal. Chim. Acta*, 1993 (282) 763.

84. Z. Taha and J. Wang, *Electroanalysis*, 1991 (3) 215.

85. W. Oungpipat, P. Alexander and P. Southwell-Kelly, *Anal. Chim. Acta*, 1995 (309) 35.

86. X. Cia, B. Ogorevc, G. Tavcar and J. Wang, *Analyst*, 1995 (120) 2579.

87. R. N. Adams, *Anal. Chem.*, 1958 (30) 1576.

88. K. Kalcher, J. M. Kauffmann, J. Wang, I. Svancara, K. Vytras, C. Neuhold and Z. Yang, *Electroanalysis*, 1995 (7) 5.

89. M. E. Rice, Z. Galus and R. M. Adams, *Electroanal. Chem.*, 1983 (143) 89.

90. K. Kalcher, *Electroanalysis*, 1990 (2) 419.

91. J. Wang, N. Naser, L. Angnes, H. Wu and L. Chen, *Anal. Chem.*, 1992 (64) 1285.

92. M. F. Cardosi and S. W. Birch, *Anal. Chim. Acta*, 1993 (276) 69.

93. M. F. Cardosi, *Electroanalysis*, 1994 (6) 89.

94. S. F. White, A. P. F. Turner, R. D. Schmid, U. Bilitewski, and J. Bradley, *Electroanalysis*, 1994 (6) 625.

95. J. Wang, "*Analytical Electrochemistry*", VCH Inc., 1994.

96. K. Shimazu, D. Weisshaar and T. Kuwana, *Electroanal. Chem.*, 1987 (233) 223.

97. S. J. Mukerjee, *Appl. Electrochem.*, 1990 (20) 537.

98. H. P. Bennetto, D. R. DeKeyser, G. M. Delaney, A. Koshy, J. R. Mason, L. A. Razack, J. L. Sterling and C. F. Thurston, *Internal. Analyst*, 1987 (8) 22.

99. W. H. Mullen, *European Patent Application*, Pub. No. 0352925, 1989.

100. L. O. Gorton, *Anal. Chim. Acta*, 1985 (178) 247.

101. D. A. Johnston, M. F. Cardosi and D. H. Vanghan, *Electroanalysis*, 1995 (7) 520.

102. L. O. Gorton and T. Svensson, *J. Mol.Catal.*, 1986 (38) 49.

103. G. Johnsson and L. O. Gorton, *Anal. Lett.*, 1987 (20) 839.

104. J. D. Newman, A.P.F. Turner and G. Marrazza, *Anal. Chim. Acta*, 1992 (262) 13.

105. J. Kulys and E. D'Costa, *Anal. Chim. Acta*, 1991 (243) 173.

106. M. Gilmartin and J. P. Hart, *Analyst*, 1992 (117) 1299.

107. S. F. White, I. E. Tothill, J. D. Newman and A. P. F. Turner, *Anal. Chim. Acta*, 1996 (321) 165.

108. Y. Zhang and G. S. Wilson, *Electroanal. Chem.*, 1993 (345) 253.

109. J. A. Cox and R. K. Jaworski, *Electroanal. Chem.*, 1990 (281) 163.

110. Z. Gao, A. Ivaska, P. Li, K. Lui and J. Yang, *Anal. Chim. Acta*, 1992 (259) 211.

111. X. Cai, K. Kalcher, G. Kolbl, C. Neuhold, W. Diewald and B. Ogorevc, *Electroanalysis*, 1995 (7)3 40.

112. S. B. Hall, E. A. Khudaish and A. L. Hart, *Electrochim. Acta*, 1998 (43) 579.

113. S. B. Hall, E. A. Khudaish and A. L. Hart, *Electrochim. Acta*, 1998 (43) 2015.

114. S. B. Hall, E. A. Khudaish and A. L. Hart, *Electrochim. Acta*, 1999 (44) 2455.

115. S. B. Hall, E. A. Khudaish and A. L. Hart, *Electrochim. Acta*, 1999 (44) 4573.

116. S. B. Hall, E. A. Khudaish and A. L. Hart, *Electrochim. Acta*, submitted for publication.

117. A. A. Noyes and W. R. Whitney, *Z. Phys. Chem.*, 1897 (22) 689.

118. W. Nernst, *Z. Phys. Chem.*, 1904 (47) 52.

119. V. G. Levich "*Physiochemical Hydrodynamics*", Prentice-Hall, Englewood Cliffs, NJ., 1962, pp 62-70.

120. A. J. Bard and L. R. Faulkner "*Electrochemical Methods; Fundamentals and Applications*", Wiley, New York, 1980, pp 298-304.

121. R. N. Adams "*Electrochemistry at Solid Electrodes*", Marcel Dekker, 1969.

122. R. M. Wightman, *Anal. Chem.*, 1981 (53) 1125A.

123. K. R. Wehmeyer, M. R. Deakin and R. M. Wightman, *Anal. Chem.*, 1985 (57) 1913.

124. *C.R.C. Handbook of Chemistry and Physics*, 63rd. edn., 1982-1983, pp. D-154 and D-155.

125. *C.R.C. Handbook of Chemistry and Physics*, 63rd. edn., 1982-1983, pp. F-11 and F-40.

126. B. V. Tilak, R. S. Perkins, H. A. Koslowska and B. E. Conway, *Electrochim. Acta*, 1972 (17) 1447.

127. G. E. P. Box and K. B. Wilson, *Roy. Statist. Soc. ser. B*; 1951 (13) 1.

128. W. Spendley, G. R. Hext and F. R. Himsworth, *Technometric*, 1962 (4) 441.

129. J. A. Nadler and R. Mead, *Computer J.*, 1965 (7) 308.

130. S. B. Hall, J. R. Duffield, D. R. Williams, M. I. Barnett and A. G. Cosslett, *Nutrition*, 1992 (8) 167.

131. A. K. Burrell, B. M. Jones, S. B. Hall, D. L. Officer, D. C. W. Reid and K. Y. Wild, *J. Incl. Phenom.*, 1999 (in press).

132. D. K. Gosser, Jr. "*Cyclic Voltammetry Simulation and Analysis of Reaction Mechanism*", VCH Publisher Inc., 1993.

133. G. C. Barker, *Adv.Polarogr.*, 1960 (1) 144.

134. S. Stefani and R. Seeber, *Anal. Chem.*, 1982 (54) 2524.

135. M. F. Cardosi and A. P. F. Turner "*Advances in Biosensors*", Vol. 1, 1991, pp 125.

136. A. J. Appleby and M. Savy, *Electroanal.Chem.*, 1978 (92) 15.

137. J. Wilshire and D. T. Sawyer, *Acc. Chem. Res.*, 1979 (12) 105.

138. J. P. Hoare, *Electrochem. Soc.*, 1978 (125) 1768.

139. K. Schachi, H. Alemu, K. Kalcher, J. Jezkova, I. Svancara and K. Vytras, *Analyst*, 1997 (122) 985.

140. J. O'M. Bockris and L. F. Oldfield, *Trans. Faraday Soc.*, 1955 (51) 249.

141. J. E. Harrar, *Anal. Chem.*, 1963 (35) 893.

142. G. G. Guilbault and G. J. Lubranco, *Anal. Chim. Acta*, 1973 (64) 439.

143. M. Lundback and G. Johanson, *Anal. Chim. Acta*, 1981 (128) 141.

144. J. Wang, M. Pedrero, P. V. A. Pamidi and X. Cai, *Electroanalysis*, 1995 (7) 1032.

145. W. A. Collier, D. Janssen and A. L. Hart, *Biosens. Bioelectron.*, 1996 (11) 1041.

146. Y. Zhang and G. S. Wilson, *Electroanal. Chem.*, , 1993 (345) 253.

147. H. B. Urbach and R. J. Bowen, *Electrochim. Acta*, 1969 (14) 927.

148. J. J. Lingane, *Electroanal. Chem.*, 1961 (2) 296.

149. L. Miller, *Electroanal. Chem.*, 1968 (16) 531.

150. Y. L. Sandler and D. A. Pantier, *Electrochem. Soc.*, 1965 (112) 928.

151. W. H. Mullen, S. J. Churchouse, F. H. Keedy and P. M. Vadgama, *Clin. Chem.* 1986 (157) 191.

152. M. Mascini and G. Palleschi, *Selective Electrode Rev.*, 1989 (11) 191.

153. P. A. Christensen and A. Hamnett; "*Techniques and Mechanisms in Electrochemistry*", 1st edn., Alden Press, Oxford, UK, 1993.

154. C. T. Kingzett, *J. Chem. Soc.*, 1980 (37) 792.

155. S. A. M. van Stroe-Biezen, F. M. Everaerts, L. J. J. Janssen and R. A. Tacken, *Anal. Chim. Acta*, 1993 (273) 553.

156. O. K. Borggaard, *Acta Chem. Scand.*, 1972 (26) 3393.

157. A. Cornish-Bowden; "*Fundamentals of Enzyme Kinetics*", Portland Press, London, 1995.

158. C. S. Hanes, *Biochem. J.*, 1932 (26) 1406.

159. H. Lineweaver and D. Burk, *Am. Chem. Soc.*, 1934 (56) 658.

160. First appears in Francois Viète's treatise *De emendatione* published 1615. Quoted by W. H. Press, B. P. Flannery, S. A. Teulosky and W. T. Vetterling, *Numerical Recipes in Pascal*, p. 164, Cambridge University Press, Cambridge (1989).

161. Modified version of code written by A. Kucernak, Department of Chemistry, Imperial College of Science, Technology and Medicine, London, UK.

162. L. A. Yarbro and S. N. Deming, *Anal. Chim. Acta*, 1974 (73) 391.

163. P. W. Atkins "*Physical Chemistry*", p. 836 Oxford University Press, Oxford (1978).

164. A. Brestovisky, E. Kirowa-Eisner and J. Osteryoung, *Anal. Chem.*, 1983 (55) 2063.

165. M. Honda, T. Kodera and H. Kita, *Electrochim. Acta*, 1983 (28)727.

166. E. L. Littauer and K. C. Tsai, *Electrochim. Acta*, 1979 (24) 681.

167. R. G. Duggleby and D. T. Dennis, *J. Biol. Chem.*, 1974 (249) 167.

168. C. L. McMinn and J. H. Ottaway, *Biochem. J.*, 1977 (161) 569.

169. K. J. Ellis and R. G. Duggleby, *Biochem. J.*, 1978 (171) 513.

170. W. H. Beyer (Ed.) "*CRC Handbook of Mathematical Sciences*", 5th edn., CRC Press, Florida, 1978.

171. R. P. Van Duyne and C. N. Reilly, *Anal. Chem.*, 1972 (44) 142.

172. P. He and L. R. Faulkner, *Anal. Chem.*, 1986 (58) 517.

173. H. S. Harned and B. B. Owen "*The Physical Chemistry of Electrolytic Solutions*", Reinhold Publishing Corporation, New York, 1943, P. 330.

174. R. A. Robinson, *Trans. Faraday Soc.*, 1939 (35) 1222.

175. H. S. Harned and L. F. Nims, *J. Am. Chem. Soc.*, 1932 (54) 423.

176. H. S. Harned and M. A. Cook, *J. Am. Chem. Soc.*, 1939 (61) 495.

177. J. Hotlos and M. Jaskula, *Electroanal. Chem.*, 1988 (249) 125.

178. G. M. Barrow "*Physical Chemistry*", 2nd edn., McGrow-Hill, New York, 1966, PP. 486-490.

179. P. W. Atkins "*Physical Chemistry*", 6th. edn., Oxford University Press, Oxford, 1998, p 225.

180. D. S. Bindra and G. S. Wilson, *Anal. Chem.*, 1989 (61) 2566.

181. D. Wijesueiya, M. S. Lin and G. A. Rechnitz, *Anal. Chim. Acta*, 1990 (234) 453.

182. E. Csoregi, L. Gorton and G. Marko-Verga, *Anal. Chim. Acta*, 1993 (273) 59.

183. Q. Chi and S. Dong, *Anal. Chim. Acta*, 1993 (278) 19.

184. F. Mizutani, S. Yabuki and S. Izjima, *Electroanalysis*, 1995 (7) 706.

185. G. G. Guilbault and G. J. Lubrano, *Anal. Chim. Acta*, 1973 (64) 439.

186. M. A. Habib and J. O'M. Bockris, *J. Electrochem. Soc.*, 1985 (132) 108.

187. S. Ye, H. Kita and A. Amarata, *Electroanal. Chem.*, 1992 (333) 299.

188. "*Physical Chemistry: Principles of Chemical Change*", Topic Study 1, Prepared by the Open University, UK, 1985.

189. D.G. Peters and J. J. Lingane, *Electroanal. Chem.*, 1962 (4) 193.

190. L. Marincic, J. S. Soeldner, C. K. Cotton, J. Giner and S. J. Morris, *Electrochem. Soc.*, 1979 (126) 43.

191. W. V. Cruess and J. Sugihara, *Food Technol.*, 1949 (3) 370.

192. G. Bianchi, F. Mazza and T. Mussini, *Electrochim. Acta*, 1962 (7) 457.

193. H. Angerstein-Kozlowska, B. E. Conway, B. Barnett and J. Mozatta, *Electroanal. Chem.*, 1979 (100) 417.

194. J. A. Polta and D. C. Johnson, *Anal. Chem.*, 1985 (57) 1373.

195. J. Gulens, *Ion-sel. Electrode Rev.*, 1981 (2) 117.

196. J. Clavilier, *Electroanal. Chem.*, 1980 (107) 211.

197. K. Aljaaf-Golze, D. M. Kolb and D. Scherson, *Electroanal. Chem.*, 1986 (200) 353.

198. T-M. Park, E. I. Iwuoha and M. R. Smyth, *Electroanalysis*, 1997 (9) 1120.

199. W. A. Collier, P. Lovejoy and A. L. Hart, *Biosensors and Bioelectronics*, 1997 (13) 219.

200. J. Kulys, J. A. Munk, T. Buch-Rasmussen and H. E. Hansen, *Electroanalysis*, 1994 (6) 945.

201. D. S. Bindra and G. S. Wilson, *Anal. Chem.*, 1989 (61) 2566.

APPENDIX A

Other Possible Binding Site Models

A number of possible binding site models with their derived rate equations were investigated qualitatively to assess their appropriateness for describing the data presented in Chapter 4, Fig. 4.1. These are briefly described in terms of the product inhibition of Michaelis-Menten type kinetics deduced in Chapter 4, Section 4.6.

Model 1

The first two steps are the diffusion and adsorption of bulk H_2O_2 to the electrode binding sites. These form the core reactions for this and subsequent models,

$$H_2O_{2(bulk)} \xrightarrow{\text{diffusion}} H_2O_2 \tag{A.1}$$

$$Pt(OH)_2 + H_2O_2 \overset{K_1}{\rightleftharpoons} Pt(OH)_2{\cdot}H_2O_2 \tag{A.2}$$

In this model, the binding site is oxidized internally to higher oxidation platinum intermediate sites and the adsorbed H_2O_2 is reduced to water

$$Pt(OH)_2.H_2O_2 \xrightarrow{k_2} PtO_2 + 2H_2O \tag{A.3}$$

The intermediate is then reduced internally to form the reduced platinum zero site which is assumed to be in equilibrium with the oxidized form

$$PtO_2 \overset{K_3}{\rightleftharpoons} Pt + O_2 \tag{A.4}$$

where K_3 is the equilibrium constant given by

$$K_3 = \frac{\theta_{Pt}[O_2]}{\theta_{PtO_2}} \tag{A.5}$$

The binding site is regenerated electrochemically giving rise to the observed amperometric signal

$$Pt + 2H_2O \xrightarrow{k_4} Pt(OH)_2 + 2H^+ + 2e^- \tag{A.6}$$

so that the rate of reformation of binding site is given by

$$j = k_4 N \theta_{Pt} \tag{A.7}$$

The mass balance equation for the fractional surface coverage is described by

$$1 = \theta_{Pt(OH)_2} + \theta_{Pt(OH)_2 \cdot H_2O_2} + \theta_{Pt} + \theta_{PtO_2} \quad (A.8)$$

Substitution of the fractional surface coverage for all adsorbed species and solving for j gives the rate equation

$$j = \frac{k_2 N K_1 [H_2O_2]}{1 + K_1[H_2O_2]\left(1 + \frac{k_2}{k_4} + \frac{k_2[O_2]}{k_4 K_3}\right)} \quad (A.9)$$

The rate equation, A.9, can describe in part the product inhibition of the reaction kinetics shown in Fig. 4.1. In particular, it would permit increase in j_{max} with ω as the $[O_2]$ term in the denominator will decrease with increasing rotation rate. It does not, however, provide an explanation for rotation rate dependence at low $[H_2O_2]$ when $K_1[H_2O_2] << 1$.

Model 2

Model 2 incorporates the sequences of steps as described for Model 1 with the addition of a reversible inhibition of the regenerated Pt(II) binding site by the oxygen produced in reaction A.4

$$Pt(OH)_2 + O_2 \overset{K_5}{\rightleftharpoons} Pt(OH)_2.O_2 \quad (A.10)$$

where K_5 is the equilibrium constant for the reversible inhibition reaction, and is given by

$$K_5 = \frac{\theta_{Pt(OH)_2 \cdot O_2}}{\theta_{Pt(OH)_2}[O_2]} \quad (A.11)$$

The mass balance equation for the fractional surface coverage is given by

$$1 = \theta_{Pt(OH)_2} + \theta_{Pt(OH)_2 \cdot H_2O_2} + \theta_{Pt} + \theta_{PtO_2} + \theta_{Pt(OH)_2 \cdot O_2} \quad (A.12)$$

Substitution of the fractional surface coverage and solving for j, gives

$$j = \frac{k_2 N K_1 [H_2O_2]}{1 + K_5[O_2] + K_1[H_2O_2]\left(1 + \frac{k_2}{k_4} + \frac{k_2[O_2]}{k_4 K_3}\right)} \quad (A.13)$$

This is similar in form to the rate equation for Model 1 with the addition of a second $[O_2]$

form in the denominator and similarly could not account for the decreased kinetics.

Model 3

After diffusion and absorption of H_2O_2, the Pt(II)/ H_2O_2 binding site undergoes internal electron transfer giving rise to the reduced Pt site and the products water and oxygen

$$Pt(OH)_2{\cdot}H_2O_2 \xrightarrow{k_2} Pt + 2H_2O + O_2 \qquad (A.14)$$

The reduced form undergoes further reaction with the products to regenerate the binding site in a form suffering product inhibition by oxygen

$$Pt + 2H_2O + O_2 \xrightarrow{k_3} Pt(OH)_2{\cdot}O_2 + 2H^+ + 2e^- \qquad (A.15)$$

The last step would be reversible dissociation of the oxygen-inhibited binding site which is in equilibrium with the free binding site

$$Pt(OH)_2{\cdot}O_2 \overset{K_4}{\rightleftharpoons} Pt(OH)_2 + O_2 \qquad (A.16)$$

The mass balance equation for the fractional surface coverage of all adsorbed species

$$1 = \theta_{Pt(OH)_2} + \theta_{Pt(OH)_2\cdot H_2O_2} + \theta_{Pt} + \theta_{Pt(OH)_2\cdot O_2} \qquad (A.17)$$

and solving for j gives the rate equation

$$j = \frac{k_2 N K_1 [H_2O_2]}{1 + \frac{[O_2]}{K_4} + K_1[H_2O_2]\left(1 + \frac{k_2}{k_3[O_2]}\right)} \qquad (A.18)$$

This model, while, potentially offering product inhibition at low $[H_2O_2]$ with the $[O_2] / K_4$ term in the denominator, would not permit increase in j_{max} with ω. This is due to the second $[O_2]$ form in the denominator indicating that rate should increase with $[O_2]$.

Model 4

Model 4 incorporates features of Model 1. The occupied Pt(II)/H_2O_2 binding site is oxidized internally to Pt(VI) oxide and H_2O_2 reduced to water as in reaction A.3

$$Pt(OH)_2{\cdot}H_2O_2 \xrightarrow{k_2} PtO_2 + 2H_2O \qquad (A.3)$$

The oxidized form then undergoes reduction as described by reaction A.4

$$PtO_2 \overset{K_3}{\rightleftharpoons} Pt + O_2 \tag{A.4}$$

The binding site regenerates but in an oxygen inhibited form

$$Pt + 2H_2O + O_2 \xrightarrow{k_4} Pt(OH)_2.O_2 + 2H^+ + 2e^- \tag{A.15}$$

The free binding site is reformed in step described in reaction A.16

$$Pt(OH)_2.O_2 \overset{K_5}{\rightleftharpoons} Pt(OH)_2 + O_2 \tag{A.16}$$

The mass balance equation is given by

$$1 = \theta_{Pt(OH)_2} + \theta_{Pt(OH)_2 \cdot H_2O_2} + \theta_{PtO_2} + \theta_{Pt} + \theta_{Pt(OH)_2.O_2} \tag{A.19}$$

and solving for the rate, j, gives

$$j = \frac{k_2 N K_1 [H_2O_2]}{1 + \frac{[O_2]}{K_5} + K_1[H_2O_2]\left(1 + \frac{k_2}{k_4} + \frac{k_2[O_2]}{k_4 K_3}\right)} \tag{A.20}$$

This is identical in form to Model 2 and hence can not qualitatively fit the data shown in Fig. 4.1.

Model 5

The occupied Pt(II)/H_2O_2 binding site is oxidized internally to Pt(VI) oxide and the bound H_2O_2 reduced to water as in reaction A.3

$$Pt(OH)_2 \cdot H_2O_2 \xrightarrow{k_2} PtO_2 + 2H_2O \tag{A.3}$$

then the oxidized form undergoes reduction as described by reaction A.4

$$PtO_2 \overset{K_3}{\rightleftharpoons} Pt + O_2 \tag{A.4}$$

The binding site regenerates electrochemically as described in A.6

$$Pt + 2H_2O \xrightarrow{k_4} Pt(OH)_2 + 2H^+ + 2e^- \tag{A.6}$$

The mechanism suffers inhibition by protons released by reaction A.6 interacting with the unoccupied binding sites

$$Pt(OH)_2 + H^+ \overset{K_5}{\rightleftharpoons} Pt(OH)_2 \cdot H^+ \tag{A.21}$$

The mass balance equation is given by

$$1 = \theta_{Pt(OH)_2} + \theta_{Pt(OH)_2 \cdot H_2O_2} + \theta_{PtO_2} + \theta_{Pt} + \theta_{Pt(OH)_2 \cdot H^+} \quad (A.22)$$

and solving for j gives

$$j = \frac{k_2 N K_1 [H_2O_2]}{1 + K_5[H^+] + K_1[H_2O_2]\left(1 + \frac{k_2}{k_4} + \frac{k_2[O_2]}{k_4 K_3}\right)} \quad (A.23)$$

This is identical in form to Model 2 with the involvement of proton binding instead of oxygen in the second term in the denominator.

Model 6

The occupied Pt(II)/ H_2O_2 binding site undergoes internal electron transfer as stated in reaction A.14

$$Pt(OH)_2.H_2O_2 \xrightarrow{k_2} Pt + 2H_2O + O_2 \quad (A.14)$$

then the binding site is regenerated electrochemically as in reaction A.6

$$Pt + 2H_2O \xrightarrow{k_3} Pt(OH)_2 + 2H^+ + 2e^- \quad (A.6)$$

The binding site undergoes reversible inhibition by the proton as given in reaction A.21

$$Pt(OH)_2 + H^+ \overset{K_4}{\rightleftharpoons} Pt(OH)_2 \cdot H^+ \quad (A.21)$$

The mass balance equation is now written

$$1 = \theta_{Pt(OH)_2} + \theta_{Pt(OH)_2 \cdot H_2O_2} + \theta_{Pt} + \theta_{Pt(OH)_2 \cdot H^+} \quad (A.24)$$

and solving for the rate gives

$$j = \frac{k_2 N K_1 [H_2O_2]}{1 + K_4[H^+] + K_1[H_2O_2]\left(1 + \frac{k_2}{k_3}\right)} \quad (A.25)$$

This rate equation will not permit variation in j_{max} with ω at high $[H_2O_2]$ when $K_1[H_2O_2] >> 1$.

Model 7

The complex Pt(II)/H_2O_2 site undergoes electrochemical oxidation giving rise to the reaction products and regenerates the binding site in the free form

$$Pt(OH)_2{\cdot}H_2O_2 \xrightarrow{k_2} Pt(OH)_2 + 2H^+ + O_2 + 2e^- \quad (A.26)$$

The binding site undergoes reversible protonation by hydrogen ions produced in reaction A.26

$$Pt(OH)_2 + H^+ \overset{K_3}{\rightleftharpoons} Pt(OH)_2{\cdot}H^+ \quad (A.21)$$

The mass balance equation is given by

$$1 = \theta_{Pt(OH)_2} + \theta_{Pt(OH)_2\cdot H_2O_2} + \theta_{Pt(OH)_2\cdot H^+} \quad (A.27)$$

and solving for j gives

$$j = \frac{k_2 N K_1 [H_2O_2]}{1 + K_3[H^+] + K_1[H_2O_2]} \quad (A.28)$$

This is similar in form to Model 6 with an alteration to the form of the Michaelis constant and will also not allow for increase in j_{max} with ω.

Model 8

Model 8 has the same sequence as Model 7 except the final step is the protonation of the Pt(II)/H_2O_2 binding site instead of the free binding site

$$Pt(OH)_2{\cdot}H_2O_2 + H^+ \overset{K_4}{\rightleftharpoons} Pt(OH)_2{\cdot}H_2O_2{\cdot}H^+ \quad (A.29)$$

where the protonation constant, K_4, is given by

$$K_4 = \frac{\theta_{Pt(OH)_2\cdot H_2O_2\cdot H^+}}{[H^+]\theta_{Pt(OH)_2\cdot H_2O_2}} \quad (A.30)$$

The mass balance equation is the same as that given in Eq. A.27

$$1 = \theta_{Pt(OH)_2} + \theta_{Pt(OH)_2\cdot H_2O_2} + \theta_{Pt(OH)_2.H_2O_2.H^+} \quad (A.27)$$

and solving for the rate gives

$$j = \frac{k_2 N K_1 [H_2O_2]}{1 + K_1 [H_2O_2] \left(1 + \frac{1}{K_4 [H^+]}\right)} \qquad (A.31)$$

This model is inappropriate since it implies that rate will increase with $[H^+]$ rather than decrease.